

Long-range interacting quantum systems

Nicolò Defenu 

*Institute for Theoretical Physics, ETH Zürich,
Wolfgang-Pauli-Straße 27, 8093 Zürich, Switzerland*

Tobias Donner 

Institute for Quantum Electronics, ETH Zürich, Otto-Stern-Weg 1, 8093 Zürich, Switzerland

Tommaso Macrì 

*QuEra Computing, Inc., 1284 Soldiers Field Road, Boston, Massachusetts 02135, USA,
ITAMP, Harvard-Smithsonian Center for Astrophysics, Cambridge, Massachusetts 02138, USA,
and Departamento de Física Teórica e Experimental and International Institute of Physics,
Universidade Federal do Rio Grande do Norte, 59072-970 Natal, Brazil*

Guido Pagano 

*Department of Physics and Astronomy, Rice University,
6100 Main Street, Houston, Texas 77005, USA*

Stefano Ruffo 

*SISSA and INFN, Sezione di Trieste, Via Bonomea 265, I-34136 Trieste, Italy
and CNR-ISC, Via Madonna del Piano 10, I-50019 Sesto Fiorentino, Italy*

Andrea Trombettoni 

*Department of Physics, University of Trieste, Strada Costiera 11, I-34151 Trieste
and CNR-IOM DEMOCRITOS Simulation Centre and SISSA,
Via Bonomea 265, I-34136 Trieste, Italy*

 (published 29 August 2023)

In this review recent investigations are summarized of many-body quantum systems with long-range interactions, which are currently realized in Rydberg atom arrays, dipolar systems, trapped-ion setups, and cold atoms in cavities. In these experimental platforms parameters can be easily changed, and control of the range of the interaction has been achieved. The main aim of the review is to present and identify the common and mostly universal features induced by long-range interactions in the behavior of quantum many-body systems. Discussed are the case of strong nonlocal couplings, i.e., the nonadditive regime, and the one in which energy is extensive, but low-energy, long-wavelength properties are altered with respect to the short-range case. When possible, comparisons with the corresponding results for classical systems are presented. Finally, cases of competition with local effects are also reviewed.

DOI: [10.1103/RevModPhys.95.035002](https://doi.org/10.1103/RevModPhys.95.035002)

CONTENTS

I. Introduction	2	B. Cold atomic gases in cavities	8
A. Classification of long-range systems	3	1. Thermal ensembles with cavity-mediated interactions	8
B. Classical systems with long-range interactions	4	2. Quantum gases with cavity-mediated interactions	9
1. Strong long-range interactions	4	3. Mapping to spin models	10
2. Weak long-range interactions	5	4. Lattice models with cavity-mediated long-range interactions	11
3. Competing nonlocal interactions	5	C. Dipolar and Rydberg systems	13
II. Experimental Realizations	6	1. Dipolar interactions and dipolar gases	13
A. Trapped ions	6	2. Interactions between Rydberg atoms	14
1. Phonon-mediated interactions	6	3. Mapping to spin models	15
2. Mapping to spin models	7	III. Thermal Critical Behavior	17
		A. The weak long-range regime	18
		1. Competing momentum contributions	19
		2. Berezinskii-Kosterlitz-Thouless scaling	20

* ndefenu@phys.ethz.ch

B. Strong long-range regime	21
1. Ensemble inequivalence	21
2. Violation of hyperscaling	22
C. Competing nonlocal systems	22
IV. Quantum Critical Behavior	23
A. Quantum rotor models	23
1. Effective dimension approach	23
2. Beyond mean-field critical exponents	24
B. Kitaev chain	25
1. Finite-range couplings	27
2. Infinite-range pairing	27
3. The $\alpha = \beta$ case and its relation to the long-range Ising model	28
4. The general $\alpha \neq \beta$ case	29
C. XXZ models	30
D. Hard-core bosons in one dimension	31
E. Soft-core interactions	32
1. Quantum phases	34
2. Elementary excitations	36
F. Structural transitions in mesoscopic long-range systems	37
G. Flat interactions	38
1. Lipkin-Meshkov-Glick model	38
2. Self-organization phase transition in cavity QED	40
3. Discrete and continuous symmetry breaking	41
4. Criticality of the self-ordering phase transition	42
V. Dynamical Critical Behavior	42
A. Metastability and diverging equilibration times	42
B. Lieb-Robinson bound	45
1. Experimental observation	47
C. Kibble-Zurek mechanism	47
1. Kitaev chain	48
2. Lipkin-Meshkov-Glick model	50
3. Structural transitions	51
4. Cavity systems	52
D. Dynamical phase transitions	53
E. Confinement	55
F. Other dynamical phenomena	56
1. Many-body localization	56
2. Periodic drive	57
VI. Conclusion and Outlook	58
Acknowledgments	59
References	59

I. INTRODUCTION

The successful use of mathematical models in the theory of critical phenomena lies in the universal behavior of continuous phase transitions. Owing to universality, it is possible to describe different physical situations within the same theoretical framework. The $O(\mathcal{N})$ -symmetric models provided privileged tools to investigate the universal behavior occurring close to criticality in a large class of physical systems ranging from magnets and superconductors to biological systems and cold atom ensembles (Chaikin and Lubensky, 1995; Pelissetto and Vicari, 2002). Over the last century, intense investigations of the properties of $O(\mathcal{N})$ models, dating back to Ising's original paper (Ising, 1925), have provided the physics community with deep insight into the physics of phase transitions (Cardy, 1996; Mussardo, 2009; Nishimori and Ortiz, 2015).

For several decades such understanding has been limited mostly to the universal behavior of systems with local, short-range interactions, such as lattice systems with nearest-neighbor couplings or local ϕ^4 field theories. Only in more recent times has the overall picture of the universal phenomena appearing in classical systems due to long-range interactions been delineated. The range of the effective interactions among the constituents of a system is in general one of its main properties, and it can affect in many ways the phase diagram, the critical properties, and the dynamical behavior of physical observables. Therefore, a natural question to be asked for both classical and quantum systems is how the properties of the system are modified by increasing the range of the interactions V , or equivalently reducing the power exponent α , where $V(r) \sim 1/r^\alpha$ for large interconstituent distances r .

For classical systems, the effect of long-range interactions has been systematically investigated in both the equilibrium and out-of-equilibrium realms (Campa *et al.*, 2014). There the range of interactions in most of the cases is given, and one studies its consequences on, among others, ensemble equivalence and thermodynamic properties such as specific heat and the occurrence of quasistationary states, i.e., metastable configurations whose lifetime scales superlinearly with the system size. See the reviews by Dauxois, Ruffo *et al.* (2002), Campa, Dauxois, and Ruffo (2009), and Campa *et al.* (2014) for discussions and references on equilibrium and out-of-equilibrium properties of classical systems, including $O(\mathcal{N})$ models, with long-range interactions.

At the same time, the study of the influence of nonlocal couplings, and especially of the competition between local and long-range interactions, in quantum systems has seen a surge in the wake of several experimental realizations in atomic, molecular, and optical (AMO) systems; see Fig. 1 for an illustration. The same set of questions on how long-range interactions modify the properties of models when the

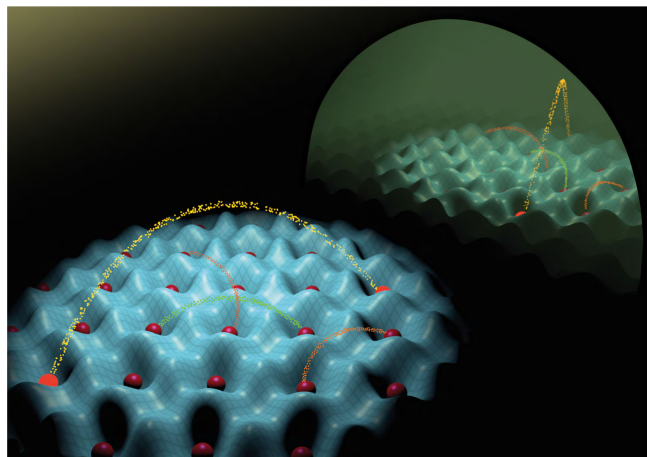


FIG. 1. Illustration of long-range interactions in quantum many-body systems. Atoms (red spheres) trapped in a potential landscape (blue) are coupled to the light field inside an optical cavity. Far distant atoms can interact with each other via the exchange of photons (yellow arc) confined in the cavity mode. Using diverse tools of AMO systems (such as those provided by trapped ions, Rydberg atoms, or dipolar atoms), other types of long-range interactions (colored arcs) can also be induced.

interactions are varied from the short-range limit to the strong long-range regime is present not only in classical systems but also in the quantum realm.

The recent interest in quantum long-range systems primarily derives from the desire to understand the fundamental physics of nonlocal systems and the interplay between local and long-distance properties, and how they are changed with respect to the classical counterpart. It is rooted as well in the role of long-range systems as powerful tools for efficient quantum computing and quantum simulation, as they allow highly entangled or correlated dynamical states to be realized (Jozsa and Linden, 2003; Vidal, 2003; Gyongyosi and Imre, 2019). Long-range interactions promise to play a crucial role in quantum technology applications since their prominent collective character promotes entanglement spreading and leads to novel forms of dynamical scaling, which cannot be observed in traditional systems with local interactions. As an example, the physics of long-range interacting atomic assemblies provides a clear route to circumventing the constraints imposed by thermal equilibrium, linear entanglement spreading, and fast decoherence.

Despite outnumbering investigations, the current literature still lacks a comprehensive perspective on long-range interacting quantum systems, making it difficult to place results in the existing framework. Indeed, most current results present their findings in comparison with the traditional ones on short-range systems, rather than with more recent but established results in the quantum long-range realm. While this has often helped to raise the interest of the physics community in these investigations, it eventually hinders the drawing of a comprehensive picture on long-range interacting quantum systems and the admission of this knowledge in the domain of general-interest physics.

In this review we construct an account of the phenomena arising due to long-range couplings in quantum systems, with a focus on the universal common features that may be observed in AMO experiments. After reviewing basic notions of classical long-range models and discussing the phases of nonlocal systems, we extend our understanding beyond the equilibrium properties and clarify paradigmatic questions regarding relaxation and thermalization dynamics. Long-range quantum systems as they are typically experimentally realized are mostly isolated, and their dynamics is governed by unitary time evolution. In this context, several open questions derive from the comparison with the conventional local interacting case, as motivated by recent progress in the experimental simulation of quantum long-range systems with a tunable range. At variance, the strong coupling to the environment is inevitable for cold atom ensembles in cavities, and the discussion about their properties necessarily connects with nonadditive classical systems.

The main motivation in this review, i.e., identifying the universal features induced by long-range interactions in quantum many-body systems, directly points to the overwhelming amount of research, appearing almost every day in the literature, featuring both theoretical results and state-of-the-art experimental measurements of the dynamical universal behavior of highly nonlocal interacting systems, such as trapped ions, cavity quantum electrodynamics, Rydberg atom arrays, and cold atoms. All these experimental platforms

present a high degree of complexity and the comprehensive picture, which we draw here, serves as a chart to set in a context both novel experimental realizations and recent theoretical findings.

Our ambition is not only to derive an all-in-one picture to direct outsiders in the realm of long-range-induced physical effects but also to pinpoint the most relevant and broad results in the field. This effort will provide a step toward the inclusion of the physics of long-range many-body systems in the inventory of university-taught physics. Given this purpose and the growing amount of publications in the field, we are necessarily limited to a selection of themes, and not all of the expected references are cited. For each topic, we include only the references relevant for our main goal of the discussion of universal properties of quantum long-range systems or the ones that are better suited to summarizing the previous literature on the issue. Whenever possible, we cite references containing accounts of previous efforts on the different topics.

The review is organized as follows: In the remainder of Sec. I, we start with a definition of what we refer to as a long-range interaction, and we present reminders on the behavior of classical long-range systems that are used in the subsequent presentation. We then move on to a classification of quantum systems in different groups. An account of the most relevant properties of each group is presented. In Sec. II, we discuss the most relevant experimental realizations of each of the aforementioned groups. Section III is devoted to the definition and identification of critical and universal behavior in classical many-body long-range systems, both at equilibrium and in the dynamical regime. The content of Sec. IV mainly concerns the equilibrium critical properties of long-range interacting quantum many-body systems, evidencing the analogies and differences with respect to the classical case. Finally, Sec. V focuses on the mosaics of dynamical critical scalings observed in long-range systems when they are driven out of their equilibrium state. Concluding remarks and an outlook are reported in Sec. VI.

A. Classification of long-range systems

Since the concept of long-range interactions encompasses nonlocal terms, beyond on-site or nearest-neighbor couplings, it is natural to classify long-range systems based on the shape of the considered interactions. This arrangement does not only reflect differences in the interaction shapes but indicates the radically different properties that appear in each class.

The word *long range* conventionally, but not universally, refers to couplings that, as a function of the distance r between the microscopic components, decay as a power law in the large r limit $r \rightarrow \infty$ as

$$V(r) \sim \frac{1}{r^\alpha}. \quad (1)$$

The exponent α is one of the main characters in this review, together with the related one

$$\sigma \equiv \alpha - d, \quad (2)$$

where d is the spatial dimension of the system.

A preliminary disclaimer is due at this point. The word long range is sometimes used to denote generic nonlocal couplings, which are beyond on-site or nearest-neighbor couplings, so that within this convention an exponentially decaying coupling would be called long range. In this review, for clarity we stick (and to a certain extent promote) the use of the word *nonlocal* for a generic coupling that is not local (exponential, finite range, power law, etc.) and *long range* for interactions that at large distances decay as a power law of the form of Eq. (1), i.e., $1/r^\alpha$, with an exponent α “small enough,” in a sense that is defined later.

An important result for the critical properties of classical systems with power-law interactions (Sak, 1973; Defenu *et al.*, 2020) is that if α is larger than a critical value α_* , then the critical behavior is indistinguishable from the short-range limit of the model, which is retrieved for $\alpha \rightarrow \infty$. Thus, for $\alpha > \alpha_*$ the behavior of the model is not “genuinely” long range and its universal behavior is the same as in the short-range limit. The specific value of α_* depends on the system and on the transition under study.

Among the unique effects produced by long-range interactions, notable features appear in the case α that are smaller than the dimension of the system d . There the interaction energy of homogeneous systems becomes infinite due to the diverging long-distance contribution of the integral $\int r^{-\alpha} d^d r$. Therefore, when $\alpha \leq d$ the energy is not extensive (Campa *et al.*, 2014).

Since α_* is larger than d , there is an interval of values of α for which the energy is extensive yet the long-distance properties of the system are altered by the long-range nature of the interactions.

Given this, for our presentation we employ the following classification.

- *Weak long-range interactions.*—These involve infinite-range interactions with power-law behavior (1) for large r and for α such that $d < \alpha < \alpha_*$.
- *Strong long-range interactions.*—These involve infinite-range interactions with power-law behavior (1) for large r and for $\alpha < d$.

Therefore, with short-range interactions we refer to the limit $\alpha \rightarrow \infty$ and, by extension, to α larger than α_* , bearing in mind that for $\alpha > \alpha_*$ it is the critical behavior to be of short-range type, but nonuniversal properties may also be affected.

In both of the previous definitions for weak and strong long-range interactions, by “infinite-range interactions with power-law behavior” we mean that the power-law decay is present for large distances, i.e., for the tails of the potential, regardless of the short-range structure of the interactions (Mukamel, 2008). To appropriately cover the cases in which there is competition between excitations on different length scales, for instance, between a certain long-range interaction and another one acting at short range, we use the following additional notation:

- *Competing nonlocal interactions.*—These involve finite- and/or infinite-range interactions with different signs.

Note that this classification has been introduced for ease of discussion, but it does not purport to be rigorous or perfect. Indeed, certain strong long-range systems may exhibit a critical scaling that is analogous to the general weak

TABLE I. Different applications where systems are governed by long-range (LR) interactions. These systems present interactions that remain long range up to the thermodynamics limit. Here the ratio α/d signaling how strong the long range is refers to $d = 3$ in the first four lines; see the text for a discussion of different d . Notice that for multimode cavity QED systems α is tunable.

System	α	α/d	Comments
Gravitational systems	1	1/3	Attractive forces, possibly nonhomogeneous states
Non-neutral plasmas	1	1/3	Some LR effects are also present in the neutral case
Dipolar magnets	3	1	Competition with local ferromagnetic effects
Dipolar gases	3	1	Anisotropic interactions
Single-mode cavity QED systems	0	0	Interactions mediated by cavity photons
Trapped-ion systems	$\sim 0-3$	$\sim 0-3$	Interactions mediated by crystal phonons

long-range case; in an infinite-range interacting system the dominant effect could be the creation of nonhomogeneous patterns so that its physics is more similar to the case of finite-range sign-changing interactions. Similarly, it could be that in a system with finite-range interaction plus a power-law interaction with power decay α , the long-range tail does not affect ground-state properties, so according to the classification the interaction could be long range and, nevertheless, the system would behave as a non-long-range system. Given a variety of situations, when needed for clarity of presentation we regroup the material according to the phenomena exhibited by the different systems. Nevertheless, when it is not misleading, we stick to the previous convention, which has the merit of classifying different interactions independently of further considerations and knowledge of the actual behavior of the quantity of interest studied in the particular models at hand.

In Table I we summarize physical systems governed by long-range interactions. Results for some of the interactions in the classical limit are summarized in the remaining part of this section and further discussed in the quantum case in Secs. III–V.

B. Classical systems with long-range interactions

In the rest of the section, we take account of the most established phenomena occurring in each of the previously introduced classes in the classical limit to lay the groundwork for the quantum case.

1. Strong long-range interactions

For $\alpha < d$, the common definitions of internal energy lead to a nonextensive energy and traditional thermodynamics does not apply. These properties are shared by a wide range of physical systems ranging from gravity to plasma physics; see Table I. Apart from the cases summarized there, the general results of strong long-range systems often also apply to mesoscopic systems, far from the thermodynamic limit, whose interaction range, even if finite, is comparable to the size of the system. In the perspective of quantum systems,

this situation is particularly relevant for Rydberg gases (Böttcher *et al.*, 2020).

Owing to the lack of extensivity, theoretical investigations in the strong long-range regime need a suitable procedure to avoid encountering divergent quantities. This has been obtained in the literature by scaling the long-range interaction term using a volume prefactor guaranteeing energy extensivity, i.e., the so-called Kac prescription (Kac, Uhlenbeck, and Hemmer, 1963).

The salient feature of the Kac prescription is that it allows a proper thermodynamic description of strong long-range systems without disrupting their key property, i.e., nonadditivity. Indeed, other possible regularizations where the long-range tails of the interactions are cut off exponentially or at a finite range tend to disrupt the peculiar physics of these systems. Similar cutoff regularizations are often employed in neutral Coulomb systems, where the $1/r$ potential tails are naturally screened by the presence of oppositely charged particles. However, even in the screened case the long-range tails of the interaction potential may give rise to finite corrections to thermodynamic quantities from the boundary conditions, which also remain finite in the thermodynamic limit (Lewin and Lieb, 2015).

Similarly, the appearance of nonadditivity in strong long-range systems is connected to a finite contribution of the system boundaries to the thermodynamic quantity, as in the prototypical case of fully connected systems where the boundary and bulk contributions are of the same order. It is in fully connected systems that most of the properties of strong long-range systems were first identified, such as *ensemble inequivalence* (Barré, Mukamel, and Ruffo, 2001). This is the property of nonadditive systems to produce different results when described with different thermodynamical ensembles, leading to apparently paradoxical predictions such as negative specific heat or susceptibility. These models also present the so-called quasistationary states (QSSs) in the out-of-equilibrium dynamics, i.e., metastable configurations whose lifetime scales super-linearly with the system size. Extensive accounts of the peculiar properties of long-range systems in the classical case were given by Dauxois, Ruffo *et al.* (2002) and Campa *et al.* (2014). In the following we focus only on the quantum case.

Based on the previous discussion, one may be tempted to exclusively relate peculiar properties such as ensemble inequivalence, negative specific heat, and QSSs to the nonextensive scaling of strong long-range systems in the thermodynamic limit. However, similar effects also appear in mesoscopic systems, where the interaction range is finite but of the same order as the system size, or for attractive systems where most of the density is localized within a finite radius (Thirring, 1970). To emphasize that effective strong long-range models with $\alpha = 0$ can also emerge when the couplings occur not between components separated in space but rather in another, “internal” space, we mention effective models of interacting neutrinos where the energy and the momentum dependence of the neutrinos enter a Heisenberg model in a magnetic field with $\alpha = 0$ (Pehlivan *et al.*, 2011).

2. Weak long-range interactions

The focus on short-range interactions in the theory of critical phenomena (Nishimori and Ortiz, 2015) is motivated

not only by simplicity but also by the resilience of the universal behavior upon the inclusion of nonlocal couplings, at least in homogeneous systems. Indeed, common wisdom states that universal properties close to a critical point depend not upon variations of the couplings between the microscopic components but instead on the symmetry of the order parameter and the dimension of the system under study. However, this statement is not generally true when long-range interactions are introduced into the system.

Indeed, while universal properties are insensible to the intermediate-range details of the interactions for critical systems with homogeneous order parameters, they are sensitive to the power-law decaying tails of long-range couplings (and, to be explicit, not on the strength of the interaction itself). For $\alpha < d$, the interaction energy diverges and the universal behavior typically belongs to the mean-field universality class. On the contrary, as a function of the parameter $\sigma \equiv \alpha - d > 0$ three different regimes can be found (Defenu *et al.*, 2020):

- For $\sigma \leq \sigma_{\text{mf}}$, where σ_{mf} can be calculated in the mean-field approximation, the mean-field approximation correctly describes the universal behavior.
- For $\sigma > \sigma_*$, the model has the same critical exponents as its short-range version, i.e., the $\sigma \rightarrow \infty$ limit.
- For $\sigma_{\text{mf}} < \sigma \leq \sigma_*$ the system exhibits peculiar long-range critical exponents, where the notation $\sigma_* \equiv \alpha_* - d$ has been used.

Therefore, there are a range of long-range decay exponents $0 < \sigma \leq \sigma_*$ where thermodynamics remains well defined and the critical behavior is qualitatively similar to the one appearing in the limit $\sigma \rightarrow \infty$. Nevertheless, the universal properties become σ dependent and loosely mimic the dependence of the short-range universal properties as a function of the spatial dimension d (Fisher, Ma, and Nickel, 1972). In other words, varying σ at fixed dimension is approximately equivalent to changing the geometric dimension in short-range systems. Notice that this equivalence is not expected to be exact in general, but it is at the Gaussian level, as one can explicitly see in the spherical model (Joyce, 1966).

While the boundary σ_{mf} can be exactly calculated by appropriate mean-field arguments, the location of the σ_* is the result of a complex interplay between long-range and short-range contributions to critical fluctuations. This interplay is at the root of several interesting phenomena that appear in a wide range of different critical systems upon the inclusion of long-range interactions in the weak long-range regime (Defenu, Trombettoni, and Codello, 2015; Defenu *et al.*, 2020). The appearance of novel effects is not limited to the equilibrium universal properties but instead extends to the out-of-equilibrium realm, whose plethora of interesting long-range phenomena has been only partially understood. Given these considerations, most of the focus of the discussion on weak long-range interacting systems concerns universal properties both at and out of equilibrium.

3. Competing nonlocal interactions

Systems with nonlocal interactions whose tails are rapidly decaying, with $\sigma > \sigma_*$, or exponentially decaying may still produce universal features due to the interplay with other local couplings or to the presence of frustration in the system.

Indeed, when long-range repulsive interactions compete with short-range attractive ones, the pertinent order parameter of the system can form spatial modulations in the form of lamellae, cylinders, or spheres. These *modulated phases* are ubiquitous in nature and emerge in a large variety of physical systems ranging from binary polymer mixtures, cold atoms, and magnetic systems to high-temperature superconductors (Seul and Andelman, 1995). Especially in two dimensions, modulated phases lead to rich phase diagrams with peculiar features that are currently far from being fully understood. In particular, the appearance of modulated phases has been invoked to describe several properties of strongly correlated electronic systems, including high-temperature superconductors and manganites with colossal magnetoresistance (Bustingorry, Jagla, and Lorenzana, 2005; Ortix, Lorenzana, and Castro, 2008).

At finite temperatures, another effect of modulated phases is the so-called inverse melting, which is a consequence of reentrant phases. Indeed, a modulated phase may be “too hot to melt” (Greer, 2000), which occurs when the system recovers the disordered state at low temperature after being in a symmetry-broken state in an intermediate temperature regime. The extension of this reentrance becomes appreciable for systems where the homogeneous and modulated phases present similar energy cost and the order parameter remains small, and it is thus strongly influenced by the form and intensity of nonlocal interactions (Mendoza-Coto, Nicolao, and Díaz-Méndez, 2019).

The study of the universal properties of modulated phases was initiated long ago (Brazovskii, 1975), but a comprehensive picture of their critical properties is still lacking, despite many investigations (Cross and Hohenberg, 1993), due to the difficulty of devising reliable approximation schemes. However, the increasing number of experimental realizations featuring striped phases could lead to a renovated interest in such problems within the framework of the physics of long-range interactions.

II. EXPERIMENTAL REALIZATIONS

As mentioned, the rising interest for long-range physics has been made pressing by the current developments of the experimental techniques for the control and manipulation of AMO systems. Indeed, long-range quantum systems are currently being realized in several experimental platforms, such as Rydberg atoms (Saffman, Walker, and Mølmer, 2010), dipolar quantum gases (Lahaye *et al.*, 2009), polar molecules (Carr *et al.*, 2009), quantum gases coupled to optical cavities (Ritsch *et al.*, 2013; Mivehvar *et al.*, 2021), and trapped ions (Blatt and Roos, 2012; Schneider, Porras, and Schaetz, 2012; Monroe *et al.*, 2021). Long-range interactions with a tunable exponent α can currently be realized using trapped ions off-resonantly coupled to motional degrees of freedom stored in a Paul trap (Islam *et al.*, 2013; Jurcevic *et al.*, 2014; Richerme *et al.*, 2014) or in a Penning trap (Dubin and O’Neil, 1999; Britton *et al.*, 2012), or neutral atoms coupled to photonic modes of a cavity (Douglas *et al.*, 2015; Vaidya *et al.*, 2018). Note also that the dependence of the decay at intermediate length scales can in turn be tuned, as in polar gases in one-dimensional lattices (Li *et al.*, 2020).

Based on the aforementioned classification, we focus our attention on three different classes of experimental systems: trapped ions, quantum gases in cavities, and dipolar systems, including, in particular, Rydberg states. All of these systems are quantum in nature and represent prototypical applications of recent investigations in long-range physics. Trapped ions present an almost unique possibility to experimentally realize long-range interactions with a decay exponent that may be tuned in the range $\alpha \in 0 - 3$, and then allow one to explore both the strong and weak long-range regimes. Conversely, cavity-mediated interactions between atoms are typically flat ($\alpha = 0$) and constitute the experimental counterpart of the Dicke or Lipkin-Meshkov-Glick (LMG) models (Dicke, 1954; Lipkin, Meshkov, and Glick, 1965; Hepp and Lieb, 1973), two real workhorses in long-range interactions. Finally, Rydberg states and dipolar atoms in general present several common features with thin magnetic films, which have been the traditional experimental setup for the study of modulated critical phenomena at finite temperatures (Selke, 1988).

Thus, each of these experimental platforms represents a realization of the peculiar physics in the long-range regimes. However, this statement should not be considered strictly, but instead mostly as a general guideline to ease our presentation. The reason for this disclaimer is that in the following we describe several examples violating this correspondence, such as the observation of QSSs in the strong long-range regime of trapped ions (Neyenhuis *et al.*, 2017), the presence of pattern formation in cavity systems (Baumann *et al.*, 2010; Landini *et al.*, 2018), and the realization of the LMG model in the fully blockade limit of Rydberg atoms (Henkel, Nath, and Pohl, 2010; Zeiher *et al.*, 2016).

A. Trapped ions

Laser-cooled ions confined in radio-frequency traps are one of the most advanced platforms for both quantum computing (Ladd *et al.*, 2010) and quantum simulation (Monroe *et al.*, 2021). In these systems, time-dependent electric fields create an effective harmonic, eV-deep potential (Dehmelt, 1968; Brown and Gabrielse, 1986; Paul, 1990) that allows a long storage time of collections of charged particles in vacuum systems (Pagano *et al.*, 2018). When laser cooled (Leibfried, Blatt *et al.*, 2003), the atomic ions form Wigner crystals whose equilibrium positions and vibrational collective modes are determined by the competition between the Coulomb interactions and the harmonic confinement induced by the trap. In this section, we review the experimental techniques used to realize spin models with tunable power-law interactions. In Secs. IV and V, we describe the experimental realizations of these models where the long-range character of the interaction allowed the observations of new physical phenomena in many-body quantum systems.

1. Phonon-mediated interactions

In trapped-ion systems, the spin degree of freedom can be encoded in two long-lived atomic states, either in the hyperfine ground-state manifold (Knight *et al.*, 2003) or using a metastable electronic state (Blatt and Wineland, 2008). Both approaches guarantee coherence time of the order of a

few seconds, near-perfect initialization via optical pumping (Happer, 1972), and high-fidelity detection via state-dependent fluorescence (Myerson *et al.*, 2008; Noek *et al.*, 2013; Christensen *et al.*, 2020).

Without any spin-motion coupling, the ion crystal can be described as a set of normal modes of motion (phonons) and an independent set of internal (spin) degrees of freedom, with the Hamiltonian

$$H = \sum_m \hbar \omega_m a_m^\dagger a_m + \sum_i \vec{B}_i \cdot \vec{\sigma}_i, \quad (3)$$

where a_m^\dagger (a_m) is the creation (annihilation) operator of the m th phonon mode with $[a_m, a_n^\dagger] = \delta_{mn}$ and $\vec{\sigma}_i = \{\mathbb{1}_i, \sigma_i^x, \sigma_i^y, \sigma_i^z\}$ and \vec{B}_i are the Pauli matrix vector and effective magnetic fields associated with the i th ion, respectively. The effective magnetic fields are implemented experimentally with microwaves or one-photon and two-photon laser-induced processes.

Laser-cooling and sub-Doppler techniques, such as resolved Raman sideband cooling (Monroe *et al.*, 1995) and electromagnetic-induced transparency cooling (Roos *et al.*, 2000; Lin *et al.*, 2013; Jordan *et al.*, 2019; Feng *et al.*, 2020), can prepare all motional states near their ground states, which is crucial for the simulation of the later-described spin models.

Quantum operations can be carried out by exerting a spin-dependent optical force on the ion crystal, coherently coupling the spin and the motional degrees of freedom. High-fidelity coherent spin-motion coupling can be realized with one-photon optical transitions in the case of optical qubits (Blatt and Wineland, 2008), two-photon stimulated Raman transitions in the case of hyperfine qubits (Kim *et al.*, 2009; Britton *et al.*, 2012; Harty *et al.*, 2014), and near-field microwaves (Ospelkaus *et al.*, 2011; Harty *et al.*, 2016; Srinivas *et al.*, 2021).

When the momentum $\hbar \Delta k$ imparted by the laser on the ions confined in a harmonic potential well is considered, the general light-atom Hamiltonian in the rotating frame of the qubit is

$$H = \frac{\hbar \Omega}{2} \sum_i [(\vec{\theta} \cdot \vec{\sigma}_i) e^{i(\Delta k X_i - \mu t - \phi)} + \text{H.c.}], \quad (4)$$

where Ω , μ , and ϕ are the Rabi frequency, the laser beat-note frequency, and the laser phase, respectively. The spin Pauli operators $\vec{\sigma}_i$ are multiplied by the complex coefficients $\vec{\theta} = \{\theta_0, \theta_1, \theta_2, \theta_3\}$, depending on the specific experimental configuration. The position operator can be written in terms of collective phononic modes as

$$X_i = \sum_m \eta_{im} (a_m^\dagger e^{i\omega_m t} + a_m e^{-i\omega_m t}), \quad (5)$$

with $\eta_{im} = \eta_m b_{im}$, where b_{im} is the normal mode transformation matrix¹ and $\eta_m = \Delta k \sqrt{\hbar/2m\omega_m}$ is the

Lamb-Dicke parameter associated with the m th normal mode at frequency ω_m .

2. Mapping to spin models

In the Lamb-Dicke regime, $\Delta k \langle X_i \rangle \ll 1$, the first-order term of the Hamiltonian (4) gives rise to spin-phonon couplings of the form $\sigma_i^{\pm,z} a_m e^{i\omega_m t} + \text{H.c.}$, where the spin operator depends on the experimental configuration. These terms generate an evolution operator under a time-dependent Hamiltonian that can be written in terms of Magnus expansions (Zhu, Monroe, and Duan, 2006). In the limit of $(\mu - \omega_m) \gg \eta_m \Omega$ for all m , the motional modes are only virtually excited, meaning that only the second-order term of the Magnus expansion is dominant and leads to the following pure spin-spin Hamiltonian:

$$H = \sum_{ij} J_{ij} \sigma_i^{\vec{\theta}} \sigma_j^{\vec{\theta}}, \quad (6)$$

where the choice of the Pauli spin operator $\sigma_i^{\vec{\theta}}$ is controlled by the laser configuration.² One common configuration $\{\theta_1 = 1/2, \theta_2 = i/2, \theta_0 = \theta_3 = 0\}$ leads to the so-called Mølmer-Sørensen gate (Sørensen and Mølmer, 1999), where two laser beat notes are tuned close to the motional mode transitions with the opposite detunings $\pm\mu$. In this configuration $\sigma_i^{\vec{\theta}} = \sigma_i^\phi = \sigma_i^x \cos(\phi) + \sigma_i^y \sin(\phi)$, where ϕ can be tuned by controlling the phases of the two laser beat notes (Monroe *et al.*, 2021). Another widely used laser configuration is $\{\theta_1 = \theta_2 = \theta_0 = 0, \theta_3 = 1\}$ (Leibfried *et al.*, 2003), where the ion motion is modulated by a spin-dependent light shift.³

The spin-spin interaction matrix J_{ij} can be explicitly calculated given the frequencies of the normal modes ω_m and the detuning μ as follows:

$$J_{ij} = \Omega^2 \omega_{\text{rec}} \sum_m \frac{b_{im} b_{jm}}{\mu^2 - \omega_m^2}, \quad (7)$$

where $\omega_{\text{rec}} = \hbar(\Delta k)^2/2M$ is the recoil frequency associated with the transfer of momentum $\hbar(\Delta k)$; see Fig. 2. The spin-spin interaction can be approximated with the following tunable power law:

$$J_{ij} = \frac{J_0}{|i-j|^\alpha}. \quad (8)$$

The approximate power-law exponent can be adjusted in the $0 < \alpha < 3$ range by tuning the detuning μ and the trap frequencies ω_m . In the limit $\mu \gg \Delta\omega$, with $\Delta\omega$ the typical mode separation, all modes contribute equally, and the spin-spin interaction decays with a dipolar power law, for instance, $J_{ij} \sim 1/|i-j|^3$. On the other hand, when μ is tuned close to $\omega_{\text{c.m.}}$ (see Fig. 2), the exponent α decreases.

²For a detailed derivation of Eq. (6), see Monroe *et al.* (2021).

³In the following, we often employ the conventions that the $\vec{\sigma}$'s are quantum spin operators and the \vec{S} 's are classical or collective spins.

¹ $\sum_i b_{im} b_{in} = \delta_{nm}$ and $\sum_m b_{im} b_{jm} = \delta_{ij}$.

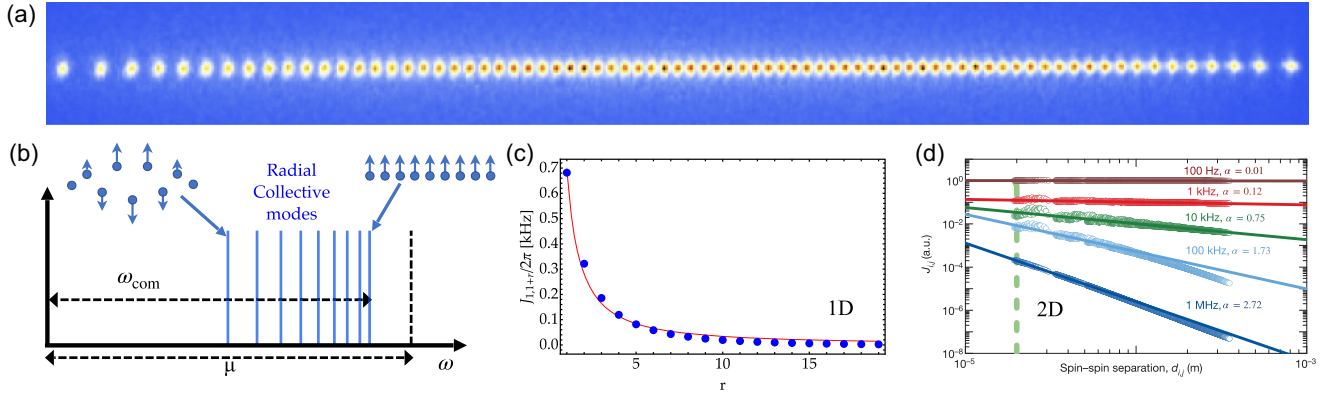


FIG. 2. Trapped-ion systems. (a) A 77 linear chain of $^{171}\text{Yb}^+$ ions. The harmonic confinement and Coulomb interactions cause the spacing between ions to be inhomogeneous, thereby breaking translational invariance. (b) A laser drive at frequency μ is detuned from the radial center-of-mass mode frequency $\omega_{\text{c.m.}}$ to create phonon-mediated spin-spin interactions. (c) Calculated spin-spin interaction (blue circles) for a 1D chain of 20 ions vs the distance from the edge ion. In this case $\delta = \mu - \omega_{\text{c.m.}} = 2\pi \times 100$ kHz and $J_{1,1+r} \sim 1/r^{1.3}$ (red solid line). (d) Calculated Ising couplings in a 2D crystal of 217 ions vs a sampling of the distance d_{ij} between ion pairs (empty circles). The solid lines are best-fit power-law exponents ($\alpha = 0.01, 0.12, 0.75, 1.73,$ and 2.72 from top to bottom) for various detunings from the center-of-mass (c.m.) mode of 795 kHz. Adapted from Britton *et al.*, 2012.

Note that in the quantum simulation regime large transverse fields ($\mu - \omega_{\text{c.m.}} \gg B_z \gg J_0$) have been used in the Mølmer-Sørensen configuration to tune the Hamiltonian (6) and experimentally realize the following long-range XY model:

$$H = \sum_{ij} J_{ij} (\sigma_i^x \sigma_j^x + \sigma_i^y \sigma_j^y) \equiv \sum_{ij} J_{ij} (\sigma_i^+ \sigma_j^- + \sigma_i^- \sigma_j^+). \quad (9)$$

Qualitatively, the large field B_z transverse to the interaction direction energetically suppresses the processes involving two spin flips ($\sim \sigma_i^+ \sigma_j^+ + \sigma_i^- \sigma_j^-$) of the Ising Hamiltonian (6) and retains only the spin preserving part ($\sim \sigma_i^+ \sigma_j^- + \sigma_i^- \sigma_j^+$). Note that some refer to the Hamiltonian (9) as an XX Hamiltonian rather than an XY one. In the following we use the two synonymously, depending on the specific reference that is being discussed.

B. Cold atomic gases in cavities

When microscopic interactions between particles are local, effective nonlocal models can also be realized by coupling the particles to the mode of microwave or optical resonators (Majer *et al.*, 2007; Leroux, Schleier-Smith, and Vuletić, 2010). Photons delocalized over the volume of a resonator can then mediate interactions between the particles, leading to highly tunable long-range or global-range interactions. Since the photons constantly decay from the resonator, these systems have to be externally driven. Depending on the parameters, the lossy character of the cavity can thus be made dominant such that the physics has to be effectively described by nonequilibrium, driven-dissipative models. In the following, we discuss how this basic scheme has been applied to cold thermal ensembles of atoms to realize effective spin interactions, and to quantum degenerate ensembles of atoms to realize effective density-density interactions.

1. Thermal ensembles with cavity-mediated interactions

Thermal ensembles of cold atoms coupled to optical cavities have proven to be a versatile platform for engineering long-range spin interactions. Nonlocal, tunable Heisenberg models and spin-exchange dynamics have been implemented using photon-mediated interactions in atomic ensembles, where the coupling between atomic sublevels is controlled via magnetic and optical fields.

For example, by coupling the clock transition of an ensemble of strontium atoms to a detuned narrow-linewidth optical resonator, photons mediate an effective spin-exchange interaction whose strength can be widely tuned since it scales inversely with the detuning between the drive and the cavity resonance (Norcia *et al.*, 2018). The long-range interactions featured in this system have been exploited to explore the nonequilibrium phase diagram of the LMG model with transverse and longitudinal fields (Muniz *et al.*, 2020); see also Sec. V.D.

Photon-mediated spin-exchange interactions have also been realized in a spin-1 system of Rb atoms (Davis *et al.*, 2019, 2020). Here a detuned four-photon Raman process is induced: A first atom absorbs a drive photon and emits it virtually into the cavity mode while changing its internal state. This virtual photon is absorbed by a second atom that then emits the photon back into the drive field while also changing its internal state, thereby realizing a “flip-flop interaction.” Since these processes depend via the Zeeman shift on the applied magnetic field, spatially dependent interactions can also be generated. Using multifrequency drives in conjunction with a magnetic field gradient, highly tailorable interactions in arrays of atomic ensembles within an optical cavity have recently been realized (Periwal *et al.*, 2021); see also Hung *et al.* (2016) for a theoretical proposal in crystal waveguides. This approach allowed a multitude of interesting structures, such as Möbius strips with sign-changing interactions or treelike geometries, to be generated. With these tools, models that exhibit fast scrambling connecting spins separated by distances that are powers of 2 were proposed by Bentsen *et al.* (2019), which neatly connects to 2-adic models (Gubser *et al.*, 2017).

2. Quantum gases with cavity-mediated interactions

Dilute quantum gases of neutral atoms are a powerful platform to study many-body physics (Bloch, Dalibard, and Zwerger, 2008). However, these gases typically interact only via collisional, short-range interactions. Nonlocal dipole-dipole interactions can nevertheless be implemented by employing either particles with a large static dipole moment (such as heteronuclear molecules or atomic species with large magnetic dipole moments) or with an induced dipole moment, such as Rydberg atoms. These approaches are discussed in Sec. II.C. A complementary route to exploit induced dipolar interactions is to couple the quantum gas to one or multiple modes of an optical cavity (Ritsch *et al.*, 2013; Mivehvar *et al.*, 2021). In this section, we first provide an introduction to the fundamental mechanism giving rise to cavity-mediated long-range interactions and then turn to experimental realizations of relevance to this review.

The basic setting is shown in Fig. 3. A Bose-Einstein condensate (BEC) is trapped by an external confining potential at the position of the mode of an optical cavity. The quantum gas is exposed to a standing-wave transverse pump laser field with a wave vector \mathbf{k}_p whose frequency ω_p is far detuned by $\Delta_a = \omega_p - \omega_a$ from the atomic resonance ω_a . In this dispersive limit, the atoms are not electronically excited but form a dynamical dielectric medium that scatters photons. At the same time, the resonance frequency ω_c of a cavity mode with wave vector \mathbf{k}_c (where $|\mathbf{k}_c| \approx |\mathbf{k}_p| = k$) is tuned close to the frequency of the transverse pump field, such that photons scattered off the atoms are preferentially scattered into the cavity mode. Compared to free space, such vacuum-stimulated scattering is enhanced by a factor proportional to the finesse of the optical cavity.

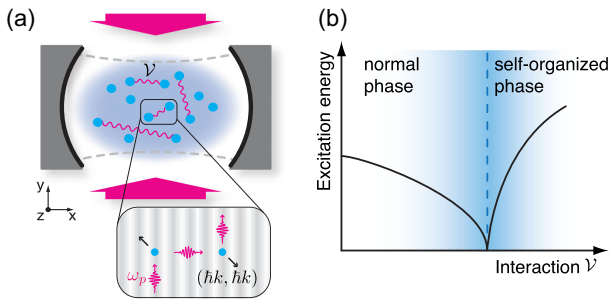


FIG. 3. Experimental scheme for realizing cavity-mediated interactions and mode softening at the superradiant phase transition. (a) A BEC (shaded cloud) inside an optical cavity is transversally illuminated by a far-red-detuned standing-wave laser field. In a quantized picture, atoms off-resonantly scatter photons from the pump field into a close-detuned cavity mode and back, creating and annihilating pairs of atoms in the superposition of momenta $(p_x, p_y) = (\pm\hbar k, \pm\hbar k)$ (one of four possible processes is shown schematically). This results in global interactions between all atoms. The interaction strength \mathcal{V} is controlled via the power of the transverse laser field and the detuning Δ_c . (b) The cavity-mediated atom-atom interaction causes a softening of a collective excitation mode with energy $\hbar\omega_s$ at the momenta $(\pm\hbar k, \pm\hbar k)$ and a diverging susceptibility (shaded area) at a critical interaction strength (dashed line). Adapted from Mottl *et al.*, 2012.

The scattering of a photon from the pump off a first atom into the cavity and then back into the pump off a second atom is the microscopic process mediating the interaction between two atoms. This photon scattering process imparts each one recoil momentum along the cavity direction and the pump field direction onto the atoms such that atoms initially in the zero-momentum BEC state $|\mathbf{p}_0\rangle = |p_x, p_y\rangle = |0, 0\rangle$ are coupled to a state $|\mathbf{p}_1\rangle$, which is the symmetric superposition of the four momentum states $|\pm\hbar\mathbf{k}_c, \pm\hbar\mathbf{k}_p\rangle$. Since the photon is delocalized over the cavity mode, this interaction is of global range. The strength of the interaction can be increased either by reducing the absolute value of the detuning $\Delta_c = \omega_p - \omega_c$ between the pump frequency and the cavity resonance or by increasing the power of the transverse pump field. The interaction inherits its shape from the interference of the involved mode structures of the transverse pump and cavity.

More formally, after adiabatically eliminating the electronically excited atomic states, a quantum gas driven by a standing-wave transverse pump field with mode function $\chi(\mathbf{r})$ and coupled to a linear cavity with the mode function $\xi(\mathbf{r})$ can be described using the second-quantized many-body Hamiltonian (Maschler, Mekhov, and Ritsch, 2008) $H = H_c + H_a + H_{ac}$, with

$$\begin{aligned} H_c &= -\hbar\Delta_c a^\dagger a, \\ H_a &= \int d^3\mathbf{r} \Psi^\dagger(\mathbf{r}) \left[\frac{\mathbf{p}^2}{2m} + V_p \chi^2(\mathbf{r}) + \frac{g}{2} \Psi^\dagger(\mathbf{r}) \Psi(\mathbf{r}) \right] \Psi(\mathbf{r}), \\ H_{ac} &= \int d^3\mathbf{r} \Psi^\dagger(\mathbf{r}) \hbar[\eta\chi(\mathbf{r})\xi(\mathbf{r})(a + a^\dagger) + U_0\xi^2(\mathbf{r})a^\dagger a] \Psi(\mathbf{r}), \end{aligned} \quad (10)$$

where H_c describes the dynamics of a single cavity mode with the photon creation (annihilation) operator $a^\dagger(a)$. The atomic evolution in the potential provided by the pump field with depth V_p is captured by the term H_a , where \mathbf{p} is the atomic momentum, m is the atomic mass, g describes the atomic contact interaction (Bloch, Dalibard, and Zwerger, 2008), and $\Psi(\mathbf{r})$ is the bosonic atomic field operator. The term H_{ac} describes the interaction between atoms and light fields. Its first term captures the photon scattering between the cavity and the pump fields at a rate given by the two-photon Rabi frequency $\eta = g_0\Omega_p/\Delta_a$, where g_0 is the maximum atom-cavity vacuum Rabi coupling rate and Ω_p is the maximum pump Rabi rate. The second term describes the dynamic dispersive shift of the cavity resonance, with $U_0 = g_0^2/\Delta_a$ the light shift of a single maximally coupled atom.

The atomic system evolves on a timescale given by the energy $\sim\hbar\omega_r$ of the excited momentum state, where $\omega_r = \hbar k^2/2m$ is the recoil frequency of the photon scattering and k is the cavity wave vector. If the cavity evolution is fast compared to this timescale (i.e., if the cavity decay rate $\kappa \gg \omega_r$), the cavity field can be adiabatically eliminated, which yields

$$a = \frac{\eta\Theta}{\Delta_c + i\kappa}, \quad (11)$$

where $\tilde{\Delta}_c = \Delta_c - U_0 \int d^3\mathbf{r} \Psi^\dagger(\mathbf{r}) \xi^2(\mathbf{r}) \Psi(\mathbf{r})$ is the dispersively shifted cavity detuning. Equation (11) shows that the cavity field is proportional to the order parameter operator $\Theta = \int d^3\mathbf{r} \Psi^\dagger(\mathbf{r}) \chi(\mathbf{r}) \xi(\mathbf{r}) \Psi(\mathbf{r})$, which measures the overlap between atomic density modulation and the mode structure of the interfering light fields. This relation is essential for the real-time observation of the atomic system via the light field leaking from the cavity.

Eliminating the steady-state cavity field in Eqs. (10) using Eq. (11), an effective Hamiltonian is obtained (Mottl *et al.*, 2012),

$$H_{\text{eff}} = H_a + \int d^3\mathbf{r} d^3\mathbf{r}' \Psi^\dagger(\mathbf{r}) \Psi^\dagger(\mathbf{r}') \mathcal{V}_{\text{lr}}(\mathbf{r}, \mathbf{r}') \Psi(\mathbf{r}) \Psi(\mathbf{r}'), \quad (12)$$

with the long-range interaction potential

$$\mathcal{V}_{\text{lr}}(\mathbf{r}, \mathbf{r}') = \mathcal{V} \chi(\mathbf{r}) \xi(\mathbf{r}) \chi(\mathbf{r}') \xi(\mathbf{r}'). \quad (13)$$

This periodic interaction potential with a strength $\mathcal{V} = \hbar\eta^2 \tilde{\Delta}_c / (\tilde{\Delta}_c^2 + \kappa^2)$ is of global range and favors a density modulation of the atomic system with a structure given by the interference of pump and cavity fields. For a standing-wave transverse pump field impinging on the BEC perpendicular to the cavity mode, this interference has a checkerboard shape of the form $\cos(kx) \cos(ky)$.

While integrating out the light field provides access to a simple description in terms of a long-range interacting quantum gas, it is important to keep in mind that the system is of a driven-dissipative nature. The excitations of the system are polaritons that share the character of both the atomic and photonic fields. Furthermore, as we later detail, in the sideband resolved regime $\kappa \lesssim \omega_r$, the cavity field can no longer be integrated out and the interaction becomes retarded (Klinger, Keßler, Wolke *et al.*, 2015).

The sign of the interaction \mathcal{V} can be chosen by a change in the detuning $\tilde{\Delta}_c$. For $\mathcal{V} < 0$, this interaction leads to density correlations in the atomic cloud favoring a λ -periodic density structure, where $\lambda = 2\pi/k$ is the wavelength of the pump laser field. This can also be understood by inspecting the first term in H_{ac} from Eqs. (10). A λ -periodic density structure would act as a Bragg lattice, enhancing the coherent scattering of photons between pump and cavity. The emerging intracavity light field interferes with the pump lattice and builds an optical potential in which the atoms can lower their energy. However, the long-range interaction favoring the density modulation competes with the kinetic energy term. Above a critical interaction strength, the system undergoes a quantum phase transition to a self-ordered state characterized by a density-modulated cloud and a coherent field in the cavity mode; see Sec. IV.G.2.

In addition, tunable-range interactions can be engineered by extending the previously described scheme to multimode cavities (Gopalakrishnan, Lev, and Goldbart, 2009; Gopalakrishnan, Lev, and Goldbart, 2010, 2011). In such cavities, a large number of modes with orthogonal mode functions (in theory an infinite number, in practice several thousands) are energetically quasidegenerate. An atom within the quantum gas will thus scatter the pump field into a

superposition of modes, with the weights set by the position of the atom and a residual detuning between the modes. These modes interfere at large distances destructively, such that only a wave packet localized around the scattering atom remains where constructive interference dominates. Accordingly, the effective atomic interaction acquires a finite-range set by the number of contributing modes.

Full degeneracy can be reached only in a multimode cavity that is either planar or concentric, both of which are marginally stable cavity configurations (Siegman, 1986). However, the experimentally stable confocal cavity configuration also supports a high degree of degeneracy where either all even or all odd modes are degenerate. The resultant effective atomic interaction also features a tunable short-range peak; see Fig. 4. This interaction has been experimentally realized (Kollár *et al.*, 2017; Vaidya *et al.*, 2018) and can be further employed to realize sign-changing effective atomic interactions (Guo *et al.*, 2019, 2020). Changing the range of the mediated interaction is also expected to impact the universality class of the self-ordering phase transition described in Sec. IV.G.2. With an increasing number of modes, the initially second-order phase transition is expected to develop into a weakly first-order phase transition (Gopalakrishnan, Lev, and Goldbart, 2009, 2010; Vaidya *et al.*, 2018).

3. Mapping to spin models

One of the most fundamental models in quantum optics is the Dicke model, which describes the collective interaction between N two-level atoms (captured as collective spin \mathbf{S}) with resonance frequency ω_0 and a single electromagnetic field mode at frequency ω (Dicke, 1954; Kirton *et al.*, 2019). The Dicke model exhibits for a sufficiently strong coupling Λ between matter and light $\Lambda > \Lambda_c \equiv \sqrt{\omega\omega_0}/2$ a quantum phase transition to a superradiant ground state (Hepp and

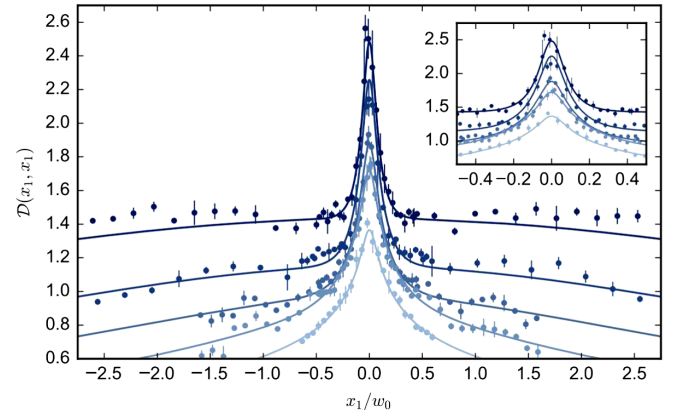


FIG. 4. Tunable-range cavity-mediated interaction in a multimode cavity. The dimensionless interaction strength $\mathcal{D}(x_1, x_1)$ as a function of BEC position in a mode with waist w_0 for five different cavities is indicated by the saturation of the color. The darkest data correspond to a confocal cavity at a high degeneracy of modes, while the brighter shades correspond to fewer interacting modes. Inset: enlargement near the cavity center illustrating how a larger number of interacting modes allows a more localized effective atomic interaction to be engineered. From Vaidya *et al.*, 2018.

Lieb, 1973; Wang and Hioe, 1973), with a macroscopically populated field mode $\langle a \rangle$ and a macroscopic polarization $\langle S_x \rangle$ of the atoms. The observation of the Dicke phase transition employing a direct dipole transition was hindered due to the limited realizable dipole coupling strengths. However, it was theoretically proposed to make use of Raman transitions between different electronic ground states, allowing the critical coupling in a rotating frame of the driven-dissipative Dicke model to be reached (Dimer *et al.*, 2007).

Neglecting atomic collisional interactions and the dispersive shift of the cavity, the self-organization phase transition (see Sec. IV.G.2) can be mapped to the superradiant quantum phase transition of the Dicke model (Baumann *et al.*, 2010; Nagy *et al.*, 2010). Exploiting the quantized atomic motion, the two-mode ansatz $\Psi = \psi_0 c_0 + \psi_1 c_1$ for the atomic wave function can be inserted into the Hamiltonian (10). Here c_0 and c_1 are bosonic mode operators annihilating a particle in the flat BEC mode ψ_0 , respectively, in the excited motional mode $\psi_1 \propto \psi_0 \cos(kx) \cos(ky)$. Introducing the collective spin operators $S_+ = S_-^\dagger = c_1^\dagger c_0$ and $S_z = (c_1^\dagger c_1 - c_0^\dagger c_0)/2$, one arrives at the Dicke Hamiltonian

$$H/\hbar = -\Delta_c a^\dagger a + \omega_0 S_z + \frac{\Lambda}{\sqrt{N}} (a^\dagger + a)(S_+ + S_-), \quad (14)$$

with a bare energy of the motional excited state $\hbar\omega_0$ and a coupling strength $\Lambda = \eta\sqrt{N}/2$. Compared to the original Dicke model, the mode frequency ω has been mapped to $-\Delta_c$ in the rotating frame of the pump field. The observation of the onset of self-organization in the transversally pumped BEC constitutes the first realization of the Dicke phase transition (Baumann *et al.*, 2010). The phase diagram of the self-ordering phase transition is shown in Fig. 5 together with the well-matching theoretical prediction for the open Dicke model phase transition.

It is instructive to rewrite the long-range interaction (13) in terms of center-of-mass and relative coordinates. Focusing for simplicity on the 1D case results in

$$\begin{aligned} \mathcal{V}_{\text{lr}}(x, x') &= \mathcal{V} \cos(kx) \cos(kx') \\ &= \frac{\mathcal{V}}{2} [\cos(2kx_{\text{c.m.}}) + \cos(kx_{\text{rel}})], \end{aligned} \quad (15)$$

with $x_{\text{c.m.}} = (x + x')/2$ and $x_{\text{rel}} = x - x'$. The term $\cos(2kx_{\text{c.m.}})$ originates from the cavity standing-wave mode structure and breaks continuous translational invariance, pinning the center of mass of the system at the phase transition onto the underlying mode structure with periodicity $\lambda/2$. More interesting is the term $\cos(kx_{\text{rel}})$, which leads to the tendency of atoms to separate by a multiple of the wavelength λ . Owing to the different periodicities of the two terms, a parity symmetry is broken at the self-ordering phase transition. The interaction term capturing the relative coordinate allows this system to be mapped to the Hamiltonian mean-field model (Ruffo, 1994; Antoni and Ruffo, 1995; Dauxois, Latora *et al.*, 2002; Campa *et al.*, 2014; Schütz and Morigi, 2014). This model is a paradigmatic model of the statistical mechanics of nonadditive long-range systems. Employing this mapping, it was possible to show that the transition to spatial

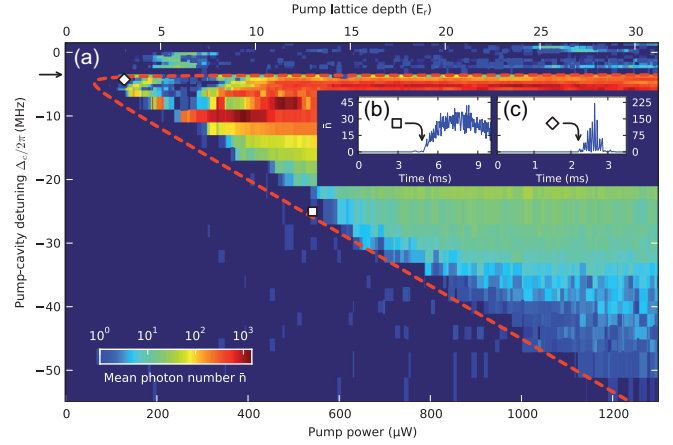


FIG. 5. Dicke model phase diagram. (a) The power of the transverse pump is increased over 10 ms for different values of the pump-cavity detuning Δ_c . The recorded mean intracavity photon number is displayed (intensity scale) as a function of pump power (and the corresponding pump lattice depth) and pump-cavity detuning Δ_c . A sharp phase boundary is observed over a wide range of values; this boundary is in good agreement with a theoretical mean-field model (dashed curve). The dispersively shifted cavity resonance for the nonorganized atom cloud is marked by the arrow on the vertical axis. (b),(c) Typical traces showing the intracavity photon number for different pump-cavity detunings, as indicated by the symbols. From Baumann *et al.*, 2010.

self-organization is a second-order phase transition of the same universality class as ferromagnetism, whose salient properties can be revealed by detecting the photons emitted by the cavity (Keller, Jager, and Morigi, 2017).

4. Lattice models with cavity-mediated long-range interactions

Ultracold atoms loaded into optical lattices are an unprecedented resource for the quantum simulation of condensed matter systems such as the Hubbard model (Lewenstein *et al.*, 2007; Bloch, Dalibard, and Zwerger, 2008). A prominent example is the experimental realization of the superfluid-to-Mott-insulator quantum phase transition (Greiner *et al.*, 2002) caused by the competition of kinetic and interaction energy. However, since the dominant interaction in quantum gases is the collisional interaction, simulating models with long-range interactions poses a challenge. Adding cavity-mediated long-range interactions to this setting thus opens the path to access long-range interacting, extended Hubbard models. If this additional energy scale competes with the other two, the phase diagram will feature, besides the superfluid and the Mott insulating phases, a density-modulated superfluid phase (the lattice supersolid) and a density-modulated insulating phase (the charge-density wave). Theoretical predictions discussed the resulting phases and phase diagrams in the case of commensurate and incommensurate lattices (Larson *et al.*, 2008; Fernández-Vidal *et al.*, 2010; Habibian *et al.*, 2013; Li, He, and Hofstetter, 2013; Bakhtiari *et al.*, 2015; Caballero-Benitez and Mekhov, 2015; Chen, Yu, and Zhai, 2016; Dogra *et al.*, 2016; Himbert *et al.*, 2019; Lin *et al.*, 2019).

The system is captured in a wide parameter range by the following extended Bose-Hubbard model:

$$H = -t \sum_{\langle e,o \rangle} (b_e^\dagger b_o + \text{H.c.}) + \frac{U_s}{2} \sum_{i \in e,o} n_i (n_i - 1) - \frac{U_l}{V} \left(\sum_e n_e - \sum_o n_o \right)^2 - \sum_{i \in e,o} \mu_i n_i. \quad (16)$$

In Eq. (16) e and o refer to the even or odd lattice sites, b_i is the bosonic annihilation operator at site i , $n_i = b_i^\dagger b_i$ counts the number of atoms on site i , V is the total number of lattice sites, and μ_i is the local chemical potential that depends on the external trapping potential. The first term captures the tunneling between neighboring sites at rate t . It supports superfluidity in the system since it favors delocalization of the atoms within each 2D layer. In contrast, the second term represents the on-site interaction with strength U_s and leads to a minimization of the energy if the atoms are localized on the individual lattice sites, favoring a balanced population of even and odd sites. The third term describes the effective global-range interactions of strength U_l , mediated by the cavity, and favors an imbalance between even and odd sites. The last term leads to an inhomogeneous distribution due to the trapping potential.

Self-organization in a cavity typically results in a 2D structuring of the atomic medium. If the cloud is additionally confined in a lattice along the third direction, it can be brought into an insulating, density-modulated regime (Klinger, Keßler, Bakhtiari *et al.*, 2015). An experimental scheme to implement a setting that in addition features the aforementioned superfluid-to-Mott-insulator phase transition, and thus also a transition between nonmodulated and modulated insulating phases, is shown in Fig. 6(a) (Landig *et al.*, 2016). A BEC is sliced into 2D systems that are subsequently exposed to a 2D optical lattice formed from one on-axis beam pumping the cavity and a standing-wave lattice perpendicular to the cavity. The latter simultaneously acts as a transverse pump field inducing cavity-mediated global-range interactions in the atomic system. The combined control over the lattice depth V_{2D} and the detuning Δ_c allows one to independently tune the ratios of collisional short-range interaction U_s , tunneling t , and global-range interaction U_l . In the experiment one observes absorption images of the atomic cloud after ballistic expansion, indicating whether the atomic system is insulating or superfluid and the field leaking from the cavity, signifying a homogeneous or a density-modulated system. Their combination allows the phase diagram to be determined, as shown in Fig. 6(b), which features the aforementioned phases.

Of special interest in the context of the global-range interaction is the first-order phase transition between the nonmodulated Mott insulating and the density-modulated charge-density wave phase. A system with only short-range interactions supports the formation of domain walls due to additivity. The reduction in energy scales with the volume of the domain, while the energy cost for the domain wall scales with its surface area. Fluctuations creating a domain wall thus grow and lead to a decay of the metastable state

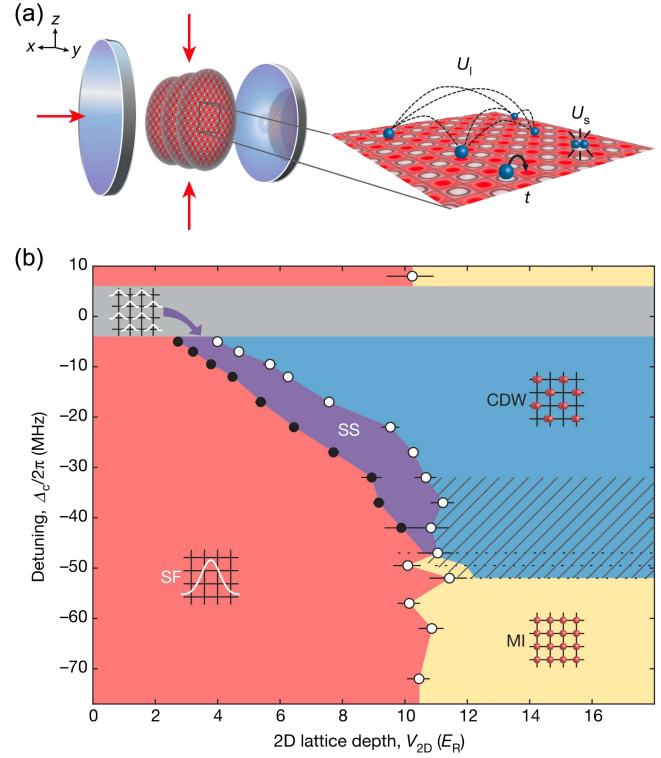


FIG. 6. Lattice models with cavity-mediated long-range interactions. (a) Left image: experimental scheme. A stack of 2D systems along the y axis is exposed to a 2D optical lattice in the x - z plane (red arrows). Right image: illustration of the three competing energy scales, tunneling t , short-range collisional interactions U_s , and global-range, cavity-mediated interactions U_l . (b) Measured phase diagram as a function of detuning Δ_c between pump field and cavity and 2D lattice depth V_{2D} , featuring superfluid (SF), lattice supersolid (SS), charge-density wave (CDW), and Mott insulating (MI) phases. From Landig *et al.*, 2016.

(Dauxois, Latora *et al.*, 2002). This is different in a global-range interacting system, where nonadditivity makes domain formation energetically costly: the energy of a domain wall here is proportional to the system size and not to the surface area. Accordingly, long-range interactions can stabilize metastable phases, whose lifetime then scales with system size and diverges in the thermodynamic limit (Antoni and Ruffo, 1995; Mukamel, Ruffo, and Schreiber, 2005; Campa, Dauxois, and Ruffo, 2009; Levin *et al.*, 2014; Defenu, 2021).

Quenching the system between these two insulating phases by changing the strength U_l of the global-range interaction leads to hysteresis and metastability, which has been observed in the cavity field measuring the imbalance between even and odd sites (Hruby *et al.*, 2018). The quench eventually triggers a switching process that results in a rearranged atomic distribution and self-consistent potential. The timescale during which this process takes place is intrinsically determined by the many-body dynamics of the gas and is continuously monitored in the experiment. The Mott insulator, in which the system is initially prepared, forms a wedding-cake structure consisting of an insulating bulk surrounded by superfluid shells at the surface. Such an inhomogeneous finite-size system can exhibit a first-order phase transition of the bulk

material (the Mott insulator) that is triggered by a second-order phase transition that took place previously on the system's surface (Lipowsky and Speth, 1983; Lipowsky, 1987), where the superfluid atoms possess higher mobility than in the insulating bulk (Hung *et al.*, 2010). Ground-state phases and quantum relaxation have been calculated for a 1D lattice in the thermodynamic limit (Blaß *et al.*, 2018).

C. Dipolar and Rydberg systems

The study of modulated and incommensurate phases arising from the competition between short-range attractive interactions and long-range repulsive ones has been a long-standing topic in condensed matter physics (Fisher, Pynn, and Skjeltorp, 1984; Blinc and Levanyuk, 1986). Several theoretical investigations focused on simplified models, where the competition was limited to finite-range interaction terms (Brazovskii, 1975; Swift and Hohenberg, 1977; Fisher and Selke, 1980). However, the natural occurrence of modulated phases is due mostly to the repulsive interaction decaying as a power law of the usual form $1/r^\alpha$. The most relevant examples include dipolar ($\alpha = 3$) and Coulomb ($\alpha = 1$) interactions.

In the framework of condensed matter experiments, dipolar interactions are known to produce modulated structures in a monolayer of polar molecules (Andelman, Broçhard, and Joanny, 1987), block copolymers (Bates and Fredrickson, 1990), ferrofluids (Cowley and Rosensweig, 1967; Dickstein *et al.*, 1993), superconducting plates (Faber, 1958), and thin ferromagnetic films (Saratz *et al.*, 2010). On the other hand, long-range Coulomb interactions are typical of low-dimensional electron systems, but experimental results are limited in this case. Evidences of stripe order have been found in 2D electron liquids (Borzi *et al.*, 2007), quantum Hall states (Lilly *et al.*, 1999; Pan *et al.*, 1999), and doped Mott insulators (Kivelson, Fradkin, and Emery, 1998). In this perspective, the appearance of stripe order is believed to be an ingredient in high-temperature superconductivity (Tranquada *et al.*, 1997; Parker *et al.*, 2010).

The strong relation between traditional investigations in solid-state systems and cold atomic platforms has emerged since the long-range nature of the forces between the atoms has begun to be exploited in experiments. Rydberg gases have been used to observe and study spatially ordered structures (Schauß *et al.*, 2012, 2015) and correlated transport (Schempp *et al.*, 2015). Dipolar spin-exchange interactions with lattice-confined polar molecules were observed as well (Yan *et al.*, 2013). Furthermore, dipolar atoms (Lu, Burdick, and Lev, 2012; Park, Will, and Zwierlein, 2015) can open a new window into the physics of competing long-range and short-range interactions (Natale *et al.*, 2019), clearing the path for the comprehension of modulated phases in strongly interacting quantum systems, as well as to higher-spin physics dynamics (de Paz *et al.*, 2013; Lepoutre *et al.*, 2019; Gabardos *et al.*, 2020; Patscheider *et al.*, 2020).

In the following we review basic notions on dipole-dipole interactions and dipolar gases, as needed for the following presentation. We then move to Rydberg atoms, focusing on their interactions and the mapping of their effective Hamiltonians on spin systems.

1. Dipolar interactions and dipolar gases

In the context of ultracold atoms, several platforms have been used to study the effect of electric and magnetic dipole-dipole interactions. A typical example is provided by electric dipole moments using heteronuclear molecules (Carr *et al.*, 2009; Moses *et al.*, 2017) or Rydberg atoms in an electric field (Saffman, Walker, and Mølmer, 2010). We remind that, due to rotational symmetry, there is no permanent electric dipole moment in an atom or in a molecule in its nondegenerate rotational ground state. However, when an external electric field couples to the electric dipole moment operator, an electric dipole moment may be induced. A permanent electric dipole moment in homonuclear molecules can be obtained with a ground-state atom bound to a second atom electronically excited to a high-lying Rydberg state (Li *et al.*, 2011). Another active area of research is provided by the manipulation of heteronuclear molecules, where an electric field mixes two rotational states within the electronic molecular ground state. In this way, one can generate ultracold molecular systems with a large electric dipole moment. Recent progress in this direction includes the creation of an ultracold gas of triatomic Na-K molecules from an atomic-diatom molecule mixture (Yang *et al.*, 2022) and the magneto-optical trapping of calcium monohydroxide polyatomic molecules (Vilas *et al.*, 2022). At variance, neutral atoms can have permanent magnetic dipole moments even at zero fields, and the effect of magnetic dipole interactions can be studied under full rotational symmetry at arbitrarily small magnetic fields.

In general, for two particles denoted by 1 and 2, with dipole moments along the unit vectors \mathbf{e}_1 and \mathbf{e}_2 and having a relative position is \mathbf{r} , the energy due to their dipole-dipole interaction reads

$$U_{dd} = \frac{C_{dd} (\mathbf{e}_1 \cdot \mathbf{e}_2) R^2 - (\mathbf{e}_1 \cdot \mathbf{R})(\mathbf{e}_2 \cdot \mathbf{r})}{4\pi R^5}. \quad (17)$$

The coupling constant C_{dd} is $\mu_0 \mu^2$ for particles having a permanent magnetic dipole moment μ (μ_0 is the permeability of vacuum) and d^2/ϵ_0 for particles having a permanent electric dipole moment d (ϵ_0 is the permittivity of vacuum) (Weber *et al.*, 2017). A relevant character of the dipolar interaction is its anisotropy. In fact, the dipole-dipole interaction has the angular symmetry of the Legendre polynomial of second order $P_2(\cos \theta)$, i.e., the d wave.

Dipolar gases, particularly dipolar Bose-Einstein condensates, have been studied (Lahaye *et al.*, 2009; Trefzger *et al.*, 2011; Baranov *et al.*, 2012). The presence on the nonlocal interaction $\propto 1/r^3$ and its anisotropy give rise to a series of interesting properties that have been theoretically and experimentally investigated. At the mean-field level, a non-local Gross-Pitaevskii equation describes the static ground-state properties, as well as the dynamical effects, such as the excitation spectrum, and the hydrodynamic behavior. Solitons, vortices, and the formation of patterns have intensively been studied [see the review by Lahaye *et al.* (2009)], as has the role of dipolar interactions in spinor Bose-Einstein condensates (Kawaguchi and Ueda, 2012; Ueda, 2017). The energy scale associated with dipolar interactions in alkali atoms is relatively small, in the hertz range. On the contrary,

highly magnetic atoms, such as Cr, Er, and Dy, display dipole moments of six, seven, and ten Bohr magnetons, respectively (Chomaz *et al.*, 2022). It is customary to define the length as

$$a_{dd} \equiv \frac{C_{dd}m}{12\pi\hbar^2}. \quad (18)$$

Equation (18) plays the role of a dipolar length, giving a measure of the absolute strength of the dipole-dipole interaction. The ratio $\varepsilon_{dd} \equiv a_{dd}/a$ of the dipolar length over the s -wave scattering length a may also be introduced in order to compare the relative strength of the dipolar and contact interactions. Thus, ε_{dd} often determines the physical properties of the system. The possibility of having a large dipole moment allows the exploration of regimes induced by the $1/r^3$ tail of the interaction (Chomaz *et al.*, 2022).

See the reviews by Lahaye *et al.* (2009), Trefzger *et al.* (2011), Baranov *et al.* (2012), Böttcher *et al.* (2020), and Chomaz *et al.* (2022) for further details and references on dipolar gases, and Carr *et al.* (2009), Gadway and Yan (2016), Bohn, Rey, and Ye (2017), Moses *et al.* (2017), Matsuda *et al.* (2020), Valtolina *et al.* (2020), and Bause *et al.* (2021) for details on polar molecules. We comment upon dipolar gases and polar molecules later in the text when discussing phenomena where the nonlocal, possibly long-range (depending on the dimension d) tail of the interactions $1/r^3$ plays a crucial role. In the remaining part of this section, the focus is centered on Rydberg atoms due to their recent applications for the simulation of spin systems with long-range and nonlocal interactions, which are the focus of this review.

2. Interactions between Rydberg atoms

In this discussion, we review the main mechanisms leading to the simulation of paradigmatic long-range spin Hamiltonians with Rydberg atoms in the frozen motion limit. When one restricts to alkali atoms and denotes by \mathbf{d}_i , $i = 1, 2$, the electric dipole moments, the dominant interaction term in the large r limit is the dipole-dipole interaction (17),

$$U_{dd} = \frac{1}{4\pi\epsilon_0} \frac{\mathbf{d}_1 \cdot \mathbf{d}_2 - 3(\mathbf{d}_1 \cdot \mathbf{n})(\mathbf{d}_2 \cdot \mathbf{n})}{R^3}, \quad (19)$$

with $\mathbf{n} = \mathbf{r}/r$. Representing as $|\alpha\rangle$ and E_α the single eigenstates and eigenenergies of each atom, one can compute in perturbation theory the effect of the perturbation given by Eq. (19). The unperturbed eigenenergies of the two-atom states are given by $E_{\alpha,\beta} = E_\alpha + E_\beta$, where for simplicity the greek letter α describes the set of quantum numbers (n, l, j, m_j) . Depending on the states involved, the relative energies, and the dipole-dipole interaction strength, one identifies one of two main regimes: the van der Waals regime or the resonant dipole-dipole regime. To illustrate the main difference between the two, we assume that two atoms in the state $|\alpha\beta\rangle$ are coupled to a single two-atom state $|\gamma\delta\rangle$; see Fig. 7(a). The reduced Hamiltonian in this two-state basis then takes the form

$$H_{\text{red}} = \begin{pmatrix} 0 & \tilde{C}_3/R^3 \\ \tilde{C}_3/R^3 & -\Delta_F \end{pmatrix}, \quad (20)$$

where $\Delta_F = E_\gamma + E_\delta - E_\alpha - E_\beta$ is the Förster defect, \tilde{C}_3 is an effective strength of the dipole-dipole interaction, and R is the distance between the two atoms. The eigenvalues of H_{red} are then $\Delta E = -\Delta_F/2 \pm \sqrt{\Delta_F^2/4 + 4(\tilde{C}_3/R^3)^2}$. The van der Waals regime is recovered if $\tilde{C}_3/R^3 \ll \Delta_F$. The state $|\alpha\beta\rangle$ is then only weakly admixed to $|\gamma\delta\rangle$. Its energy is perturbed to $\Delta E \approx (1/\Delta_F)(\tilde{C}_3/R^3)^2 \equiv \tilde{C}_6/R^6$. One obtains the scaling of the van der Waals coefficient with the principal quantum number n as $\tilde{C}_6 \propto n^{11}$, as verified experimentally in several cases (Béguin *et al.*, 2013; Weber *et al.*, 2017). More generally, to properly estimate the van der Waals coefficient, one has to formally include the contribution of all nonresonant states, employing second-order perturbation theory to compute the two-atom energy shift as

$$\Delta E_{\alpha\alpha} = \sum_{\beta,\gamma} \frac{|\langle\alpha\alpha|U_{dd}|\beta\gamma\rangle|^2}{E_{\alpha\alpha} - E_{\beta\gamma}}, \quad (21)$$

where the sum extends to all the states that are dipole coupled to $|\alpha\rangle$.

In the case where the $|\alpha\beta\rangle$ is resonant with $|\gamma\delta\rangle$, i.e., $E_{\alpha\beta} \approx E_{\gamma\delta}$, or, equivalently, $\Delta_F \ll \tilde{C}_3/R^3$, the two eigenvalues of H_{red} become $E_\pm \approx \pm C_3/R^3$, and the corresponding eigenstates are $|\pm\rangle = (|\alpha\beta\rangle \pm |\beta\alpha\rangle)/\sqrt{2}$. This is equivalent to a resonant flip-flop interaction $|\alpha\beta\rangle\langle\gamma\delta| + \text{H.c.}$ In this case the interaction energy scales as $1/R^3$ regardless of the distance between the two atoms (the Förster resonance). In the case of Rb it is easy to achieve resonance with weak electric fields (Ravets *et al.*, 2014). The resonant dipole-dipole interaction is also naturally realized for two atoms in two dipole-coupled Rydberg states. Moreover, this interaction is anisotropic, varying as $V(\theta) = 1 - 3\cos^2(\theta)$, with θ the angle between the internuclear axis and the quantization axis.

A central concept, essential for both many-body physics and quantum technology, is the Rydberg blockade (Jaksch *et al.*, 2000; Lukin *et al.*, 2001; Gaetan *et al.*, 2009; Urban *et al.*, 2009; Isenhower *et al.*, 2010; Wilk *et al.*, 2010), where the excitation of two or more atoms to a Rydberg state is prevented due to the interaction (Browaeys and Lahaye, 2020; Morgado and Whitlock, 2020). The blockade concept is illustrated in Fig. 7(b). The strong interactions between atoms excited to a Rydberg state can be exploited to suppress the simultaneous excitation of two atoms and to generate entangled states. Consider a resonant laser field that coherently couples the ground state $|g\rangle$ to a given Rydberg state $|r\rangle$ with a Rabi frequency Ω . In the case of two atoms separated by a distance R , the doubly excited state $|rr\rangle$ is shifted in energy by the quantity C_6/R^6 due to the van der Waals interaction, with C_6 the interaction coefficient (all the other pair states have energy nearly independent of R). Assuming that the condition $\hbar\Omega \ll C_6/R^6$ is fulfilled, that is, $R \ll R_b = (C_6/\hbar\Omega)^{1/6}$ (blockade radius), then, starting at the ground state $|gg\rangle$, the system performs collective Rabi oscillations with the state $|\psi\rangle = (|rg\rangle + |gr\rangle)/\sqrt{2}$. These considerations can be extended to an ensemble of N atoms, all included within a blockade volume. In this case, at most one Rydberg excitation is possible, inducing collective Rabi oscillations

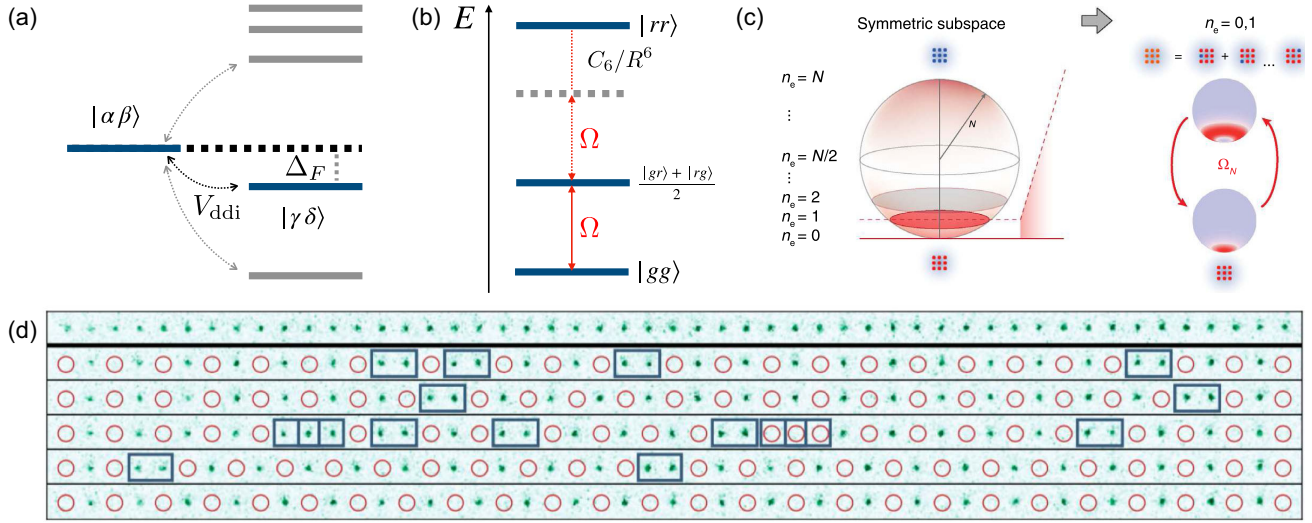


FIG. 7. Long-range interactions in systems of Rydberg atoms for many-body dynamics. (a) Illustration of the interaction between pairs of atoms excited to Rydberg states. Shown are the relevant dipole-coupled pair states labeled by quantum numbers α, β, \dots with the Förster defect Δ_F relative to the pair states $|\alpha\beta\rangle$ and $|\gamma\delta\rangle$. (b) Principle of the Rydberg blockade. For two nearby atoms, the van der Waals interaction $\propto C_6/R^6$ (R is the interatomic distance) shifts the doubly excited state $|rr\rangle$ preventing the double excitation of the atomic pair when $R < R_b = (C_6/\hbar\Omega)^{1/6}$. (c) Illustration of a superatom from the collective blockaded lattice of N atoms. Shown is a Bloch sphere with its basis states (labeled by excitation numbers n_e) and coupled states highlighted [south pole ($n_e = 0$) and singly excited state ($n_e = 1$), represented by the shaded (red) plane]. The small pictograms above and below the sphere depict the lattice system with atoms in the ground (below, in red) and Rydberg states (above, in blue). The dashed (red) line indicates an enlargement into the subspace spanned by the lowest two states. The Husimi distribution of these states and their enhanced coupling Ω_N is shown in the center. Adapted from [Zeicher *et al.*, 2015](#). (d) The first row displays the experimental image of the initial state of a Rydberg atom array. The following rows represent the atom array after a slow sweep across the phase transition, showing larger average sizes of correlated domains for the slower sweep. The green spots (open circles) represent atoms in the ground (Rydberg) state. The blue rectangles mark the position of domain walls. Courtesy of A. Omran.

with an enhanced frequency $\Omega_{\text{coll}} = \sqrt{N}\Omega$, leading to the so-called superatom picture, which is illustrated in Fig. 7(c). The system dynamics is confined to the symmetric subspace of zero excitations ($n_r = 0$) and one excitation ($n_r = 1$), whose bases are the Fock states $|0\rangle = |g_1, \dots, g_N\rangle$ and the entangled W state $|1\rangle = (1/\sqrt{N})\sum_{i=1}^N |g_1, \dots, r_i, \dots, g_N\rangle$, where g_i and r_i label the i th atom in the ground or Rydberg state ([Zeicher *et al.*, 2015](#)).

An important objective is to implement interacting many-body systems combining atomic motion with tunable long-range interaction via Rydberg atoms. The main experimental challenge is to bridge the mismatch in energy and timescales between the Rydberg excitation and the dynamics of the ground-state atoms. A possible solution is the so-called Rydberg dressing, where ground-state atoms are coupled off resonantly to Rydberg states, leading to effectively weaker interactions with lower decay rates ([Henkel, Nath, and Pohl, 2010](#); [Johnson and Rolston, 2010](#); [Pupillo *et al.*, 2010](#); [Balewski *et al.*, 2014](#); [Macrì and Pohl, 2014](#); [Jau *et al.*, 2016](#)). The main difficulty with this approach is that decay and loss processes of Rydberg atoms have to be controlled on timescales that are much longer than they are for near-resonant experiments, and more exotic loss processes become relevant ([Zeicher *et al.*, 2016, 2017](#); [Guardado-Sanchez *et al.*, 2021](#)). Rydberg dressing also allows one to impose local constraints, which are at the heart of the implementation of models related to gauge theories, like the quantum spin ice ([Glaetzle *et al.*, 2014](#)). Other predictions include cluster Luttinger liquids

in 1D, supersolid, and glassy phases; see Sec. IV.E for more details. It might also be possible to implement a universal quantum simulator or quantum annealer based on Rydberg dressing ([Lechner, Hauke, and Zoller, 2015](#); [Glaetzle *et al.*, 2017](#)).

3. Mapping to spin models

The two-atom picture described in Sec. II.C.2 can be extended to the many-body case. Including the coupling of single-atom states to an external coherent laser drive, one obtains in the rotating frame of the laser the Ising Hamiltonian ([Schauß *et al.*, 2012, 2015](#); [Labuhn *et al.*, 2016](#))

$$H_{\text{Ising}} = \frac{\hbar\Omega}{2} \sum_i \sigma_x^i - \sum_i \hbar\Delta n_i + \sum_{i<j} \frac{C_6}{R_{ij}^6} n_i n_j, \quad (22)$$

where $n_i = |r\rangle_i \langle r| = (1 + \sigma_z^i)/2$ is the projector to the excited state $|r\rangle$ and Δ is the single-atom detuning from the Rydberg state $|r\rangle$. Discussions with references on the simulation of quantum Ising models in a transverse field were given by [Schauss \(2018\)](#) and [Morgado and Whitlock \(2020\)](#). See [Lewenstein *et al.* \(2007\)](#) and [Trefzger *et al.* \(2011\)](#) for references on effective interacting lattice models obtained for dipolar gases in optical lattices at low energy.

The realization of the Ising Hamiltonian in Rydberg atom quantum simulators led to the observation of many interesting effects, from the Kibble-Zurek mechanism and its related

critical dynamics [see Fig. 7(d)] (Keesling *et al.*, 2019) to antiferromagnetic phases (Guardado-Sanchez *et al.*, 2018; Lienhard *et al.*, 2018; Scholl *et al.*, 2020; Ebadi *et al.*, 2021), quantum spin liquids (Samajdar *et al.*, 2021; Semeghini *et al.*, 2021; Verresen, Lukin, and Vishwanath, 2021), and the quantum critical dynamics of a 2D Ising quantum phase transition (Ebadi *et al.*, 2021). The trapping and manipulation of Rydberg atoms in optical tweezers with defect-free configurations has played a major role in this perspective (Barredo *et al.*, 2016; Endres *et al.*, 2016; Anderegg *et al.*, 2019; Covey *et al.*, 2019; Ohl de Mello *et al.*, 2019; Bohrdt *et al.*, 2020; Y. Wang *et al.*, 2020; Festa *et al.*, 2021; Schymik *et al.*, 2021).

Rydberg dressing provides an alternative way to implement quantum Ising models with important implications beyond quantum simulation. Two internal ground states are used to encode spin-up and spin-down states in the dressing protocol. Coherent many-body dynamics of Ising quantum magnets built up by Rydberg dressing are experimentally studied both in an optical lattice and in an atomic ensemble. An illustration of the Ising dynamics in a finite-range model is presented in Fig. 8, where we show the trajectories of the collective spin from Borish *et al.* (2020). An important application of this Hamiltonian is to study the Loschmidt echo protocol applied to the LMG one-axis twisting model for quantum metrology purposes (Gil *et al.*, 2014), for instance, for the preparation of non-Gaussian states that can be detected via the quantum Fisher information (Macrì, Smerzi, and Pezzè, 2016; Borish *et al.*, 2020). Rydberg dressing of atoms in optical tweezers can also be employed for the realization of programmable quantum sensors based on variational quantum algorithms, which are capable of producing entangled states on demand for precision metrology (Kaubruegger *et al.*, 2019). This investigation is not limited to Rydberg atoms, as it also extends naturally to ion platforms (Davis, Bentsen, and Schleier-Smith, 2016; Morong *et al.*, 2021).

A special case of the quantum Ising model arises when $a_{\text{latt}} < R_c < 2a_{\text{latt}}$, with a_{latt} the lattice spacing (nearest-neighbor blockade) and $V_{ij} \approx 0$ for everything beyond nearest neighbors. This situation was experimentally realized in a 1D chain of Rydberg atoms by Bernien *et al.* (2017) and Bluvstein *et al.* (2021). In this case one can derive an effective Hamiltonian for the low-energy subspace, which amounts to neglecting configurations with two adjacent excitations. In one dimension the resulting Hamiltonian takes the form of a PXP model

$$H = \sum_i \frac{\Omega_i}{2} P_{i-1} \sigma_x^i P_i, \quad (23)$$

where $P_i = |g\rangle\langle g|$ is the projector onto the ground state.

Resonant dipole-dipole interactions between Rydberg atoms are at the basis of several proposals to simulate the quantum dynamics of many-body spin systems. As an example, it is possible to see that a system containing two dipole-coupled Rydberg states can be mapped to a spin-1/2 XY model; see the review by Wu *et al.* (2021) and references therein. Coherent excitation transfer between two types of Rydberg states of different atoms has been observed in a

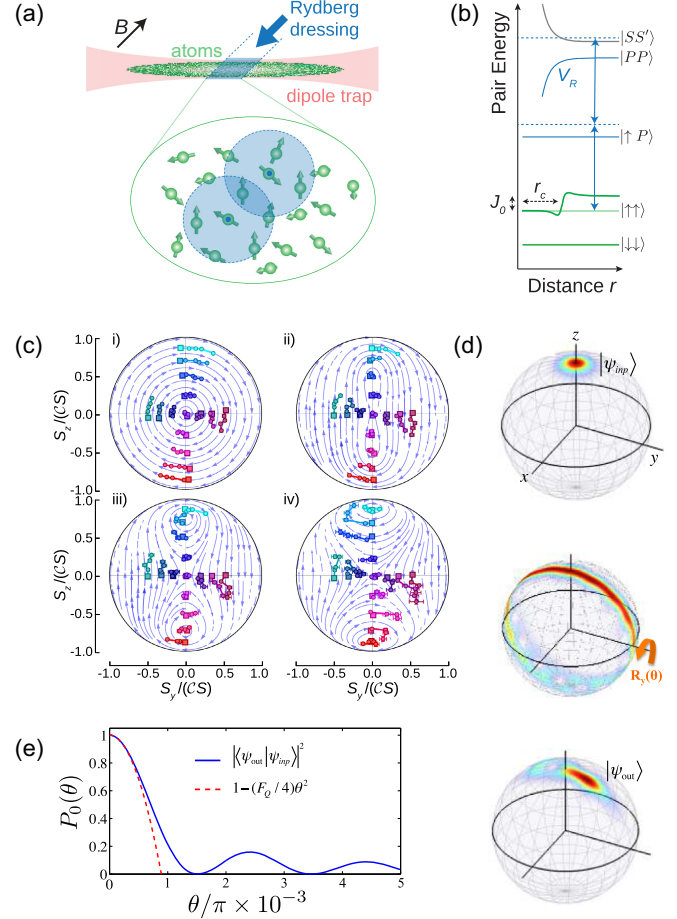


FIG. 8. Finite-range interactions in spin systems: dynamics and applications. (a) An experimental setup and Rydberg dressing scheme for a cloud of Cs atoms is held in an optical dipole trap and locally illuminated with 319 nm light to generate Ising interactions of a characteristic range r_c and strength J_0 . The quantization axis is set by a 1 G magnetic field B . (b) Energy level diagrams for a pair of atoms. (c) Transverse-field Ising dynamics. Trajectories for initial states $|\theta, \phi\rangle$ (square data points) and up to four Floquet cycles were obtained with dressing parameters $(\Omega, \Delta) = 2\pi \times (2.8, 25)$ MHz. (i)–(iv) $\Lambda_{\text{eff}} = 0, 1.2(2), 1.8(3), 2.7(4)$, respectively. The blue flow lines show mean-field theory for best fit $\Lambda = 0, 1.1, 1.5, 2.2$; see the main text. (a)–(c) Adapted from Borish *et al.*, 2020. (d) Loschmidt echo protocol applied to the LMG one-axis twisting model, with a snapshot of the Husimi distribution. Top image: a spin-polarized state is prepared at the north pole of the Bloch sphere. Center image: the interaction is switched on for a time t_1 (transformation U_1). The state is then rotated of an angle θ [$R_y(\theta)$]. Bottom image: the interaction is switched on again for a time t_2 (transformation U_2) such that $U_1 U_2 = 1$. In these plots $\theta/\pi = 0.01$ and $\tau/\pi = 0.05$. (e) Probability $P_0(\theta)$ (solid line) as a function of phase shift and as a function of θ for $\tau/\pi = 0.05$. The dashed line is the second-order expansion involving the quantum Fisher information F_Q . Here $N = 101$. (d),(e) Adapted from Macrì, Smerzi, and Pezzè, 2016.

three-atom system (Barredo *et al.*, 2015). The resulting long-range XY interactions give rise to many-body relaxation (Piñeiro Orioli *et al.*, 2018).

Given the well-known mapping between the XY model and hard-core bosons (Friedberg, Lee, and Ren, 1993), it is

possible to provide an experimental realization of the bosonic Su-Schrieffer-Heeger model (Su, Schrieffer, and Heeger, 1979) and its symmetry-protected topological order with a single-particle edge state (de Léséleuc *et al.*, 2019; Lienhard *et al.*, 2020); see also Kanungo *et al.* (2021). Proposals to observe topological bands (Peter *et al.*, 2015) and topologically protected edge states (Weber *et al.*, 2018) have been presented. Moreover, a realization of a density-dependent Peierls phase in a spin-orbit-coupled Rydberg system was recently demonstrated (Lienhard *et al.*, 2020).

We finally mention that with Rydberg systems one could implement digital simulation techniques (Georgescu, Ashhab, and Nori, 2014). The total unitary evolution operator $U(t)$ is decomposed into discrete unitary gates (Weimer *et al.*, 2010, 2011), and one can study a broad class of dynamical regimes of spin systems, such as nonequilibrium phase transitions and nonunitary conditional interactions in quantum cellular automata (Lesanovsky, Macieszczak, and Garrahan, 2019; Gillman, Carollo, and Lesanovsky, 2020; Wintermantel *et al.*, 2020). Kinetically constrained Rydberg spin systems in which a chain of several traps has each loaded with a single Rydberg atom and coupled with the bosonic operators expressing the deviation from the trap centers, also referred to as facilitated Rydberg lattices, have also been studied (Mazza, Schmidt, and Lesanovsky, 2020).

A promising further line of research is provided by Rydberg ions both for quantum simulation purposes (Müller *et al.*, 2008; Gambetta *et al.*, 2020) and for the realization of fast quantum gates for quantum information processing (Müller *et al.*, 2008; Mokhberi *et al.*, 2020). Two-dimensional ion crystals for quantum simulations of spin-spin interactions using interactions of Rydberg excited ions were proposed by Nath *et al.* (2015) to emulate topological quantum spin liquids using the spin-spin interactions between ions in hexagonal plaquettes in a 2D ion crystal. The role of a Rydberg ion is to modify the phonon mode spectrum in order to realize the constrained dynamics of the Balents-Fisher-Girvin model on the kagome lattice. There the effective spin-spin interaction for the hexagonal plaquette can be written as an extended XXZ model

$$H_{\sigma\sigma} = \sum_{i<j} J_{ij}^z \sigma_i^z \sigma_j^z + \sum_{i<j} J_{ij}^{\pm} (\sigma_i^x \sigma_j^x + \sigma_i^y \sigma_j^y). \quad (24)$$

Long-range XXZ Hamiltonians with tunable anisotropies can be Floquet engineered using resonant dipole-dipole interactions between Rydberg atoms and a periodic external microwave field coupling the internal spin states (Geier *et al.*, 2021; Scholl *et al.*, 2021).

Note that in a realistic Rydberg atom system coherent driving offered by external fields often competes with dissipation induced by coupling with the environment. Such a controllable driven-dissipative system with strong and non-local Rydberg-Rydberg interactions can be used to simulate many-body phenomena distinct from their fully coherent counterparts. Evolution of such an open many-body system is often governed by the master equation $\partial_t \rho = -i[H, \rho] + L\rho$, where ρ is the state of the system, H is the system Hamiltonian, and L is the Liouvillian superoperator (Gardiner and Zoller, 2004; Benatti and Floreanini, 2005;

Manzano, 2020). Correspondingly, several aspects of driven-dissipative dynamics in Rydberg systems and dissipative Rydberg media were addressed (Lesanovsky and Garrahan, 2013; Lee, Cho, and Choi, 2015; Goldschmidt *et al.*, 2016; Levi, Gutiérrez, and Lesanovsky, 2016; Letscher *et al.*, 2017; Lee *et al.*, 2019; Torlai *et al.*, 2019; Bienias *et al.*, 2020; Pistorius, Kazemi, and Weimer, 2020; Lourenço *et al.*, 2021).

III. THERMAL CRITICAL BEHAVIOR

Phase transitions are among the most noteworthy phenomena occurring in many-body systems. Among various kinds of phase transitions, continuous phase transitions are particularly interesting since they are tightly bound with the concept of universality. Thanks to the universality phenomenon, the same formalism can be applied to phase transitions occurring both at a finite temperature and at $T = 0$. The latter are usually denoted as quantum phase transitions (Sachdev, 1999). The intense efforts of the scientific community have paid their rewards, and the critical properties of several physical systems have been characterized (Pelissetto and Vicari, 2002).

Usually, universality is defined as the insensitivity of the critical scaling behavior of thermodynamic functions with respect to variations of certain microscopic details of the system under study, such as the lattice configurations or the precise shape of the couplings. This definition alone cannot be considered rigorous unless one specifies all the possible adjustments of the microscopic features that preserve universality. In the following, we reserve the adjective “universal” for all those phenomena that may be quantitatively described by a suitable continuous formulation. Therefore, in our language the concept of universality is strictly tied to the existence of a continuous field theory formulation, which, albeit ignoring the microscopic details of the lattice description, can produce an exact estimate for the universal quantities.

The quantum critical behavior of local models in dimension d at $T = 0$ can often be related to their critical scaling at finite temperature T , but in a dimension $d + 1$ (Sondhi *et al.*, 1997; Sachdev, 1999), with a typical example being the nearest-neighbor quantum Ising model in a transverse field (at $T = 0$) and the short-range classical Ising model at finite temperature (Mussardo, 2009). The situation changes for long-range models, and for this reason we review in this section the basic properties of equilibrium critical long-range systems at finite temperature and compare them in Sec. IV to the corresponding properties at zero temperature.

The prototypical playground for the study of universal properties at finite temperature are the classical $O(\mathcal{N})$ spin systems, whose Hamiltonian reads

$$H = -\frac{1}{2} \sum_{i \neq j} J_{ij} \mathbf{S}_i \cdot \mathbf{S}_j, \quad (25)$$

where \mathbf{S}_i is an \mathcal{N} -component spin vector with unit modulus, $J_{ij} > 0$ are ferromagnetic translational invariant couplings and the indices i and j run over all sites on any d -dimensional regular lattice of V sites. The usual terminology is that $\mathcal{N} = 1$ is the Ising model, $\mathcal{N} = 2$ is the XY model, $\mathcal{N} = 3$ is the Heisenberg model, and $\mathcal{N} \rightarrow \infty$ is the spherical model (Stanley, 1968). It is well known (Mussardo, 2009;

Nishimori and Ortiz, 2015) that for $\mathcal{N} \geq 1$ and $d > 2$ the Hamiltonian in Eq. (25) and fast enough decaying couplings (i.e., in the short-range limit) presents a finite-temperature phase transition between a low-temperature state $T < T_c$ with finite magnetization $m = |\langle \sum_i \mathbf{S}_i \rangle|/N \neq 0$ and a high-temperature phase with $m = 0$. For $\mathcal{N} = 1$, the phase transition also occurs for $d = 2$ (Mussardo, 2009; Nishimori and Ortiz, 2015).

Close to the critical point the thermodynamic quantities display power-law behavior as a function of the reduced temperature $\tau \equiv (T - T_c)/T_c$, with universal critical exponents that depend only on the symmetry index \mathcal{N} and the dimension d of the system. These critical exponents coincide with the ones of the $O(\mathcal{N})$ -symmetric field theory with the action

$$S[\boldsymbol{\varphi}] = \int d^d x \{ \partial_\nu \varphi_i \partial_\nu \varphi_i + \mu |\boldsymbol{\varphi}|^2 + g |\boldsymbol{\varphi}|^4 \}, \quad (26)$$

where $\boldsymbol{\varphi}$ is an \mathcal{N} -component vector with an unconstrained modulus, the lattice summation has been replaced by a real-space integration, $\nu = 1, \dots, d$ runs over the spatial dimensions, $i = 1, \dots, \mathcal{N}$ refers to the different components, the quadratic coupling controls the distance from the critical point ($\mu \propto \tau$), the value of the constant coupling is $g > 0$, and the summation over repeated indices is intended.

An extensive amount of theoretical investigations has been performed on the critical properties of $O(\mathcal{N})$ -symmetric models, in both their continuous and lattice formulations, reaching an unmatched accuracy in the determination of universal properties with a fair degree of consistency in the entire dimension range $2 \leq d \leq 4$ (Holovatch and Shpot, 1992; Kleinert, 2001; Pelissetto and Vicari, 2002; Codello, Defenu, and D'Odorico, 2015; Cappelli, Maffi, and Okuda, 2019). Numerical simulations, which are limited to integer-dimensional cases $d \in \mathbb{N}$, are mostly consistent with theoretical investigations (Pelissetto and Vicari, 2002), while the recently emerging conformal bootstrap results confirmed and extended the existing picture (Poland, Rychkov, and Vichi, 2019).

A. The weak long-range regime

Having introduced the formalism and notation for universality problems, we can start with the case of interest of long-range $O(\mathcal{N})$ spin systems, i.e., the Hamiltonian in Eq. (25) with $J_{ij} = J/r_{ij}^{d+\sigma}$, where r_{ij} is the distance between sites i and j , a coupling constant $J > 0$, and a positive decay exponent $d + \sigma \geq 0$. The Fourier transform of the matrix J_{ij} produces a long-wavelength mean-field propagator of the form $G_{\text{mf}} \sim J_\sigma q^\sigma + J_2 q^2$, setting the mean-field threshold for the relevance of long-range interactions to $\sigma_{\text{mf}}^* = 2$ (Fisher, Ma, and Nickel, 1972).

The renormalization group (RG) approach (Wegner and Houghton, 1973; Polchinski, 1984) can provide a comprehensive picture for the universal properties of long-range $O(\mathcal{N})$ models. In the so-called functional RG (FRG) one writes an, in principle, exact equation for the flow of the effective average action Γ_k of the model and then resort to

various approximation schemes (Wetterich, 1993; Berges, Tetradis, and Wetterich, 2002; Delamotte, 2012). The Γ_k is obtained by the introduction of a momentum space regulator $R_k(q)$, which cuts off the infrared divergences caused by slow modes $q \ll k$, while the high-momentum model $q \gg k$ is left almost untouched. The problem of weak long-range interactions in the continuous space could be then represented by the scale-dependent action

$$\Gamma_k[\boldsymbol{\varphi}] = \int d^d x \{ Z_k \partial_\nu^{\sigma/2} \varphi_i \partial_\nu^{\sigma/2} \varphi_i + U_k(\rho) \}, \quad (27)$$

where $\rho = (1/2)\varphi_i \varphi_i$ and the index $i = 1, \dots, \mathcal{N}$ is summed over as in Eq. (26).

The ansatz in Eq. (27) is already sufficient to qualitatively clarify the influence of long-range interactions on the universal properties. Indeed, the difference between the bare action (26) and the effective action (27) is limited to the presence of the fractional derivative $\partial_\mu^{\sigma/2}$ into the kinetic term instead of the traditional ∇^2 term. The definition of the fractional derivative in the infinite volume limit (Pozrikidis, 2016; Kwaśnicki, 2017) leads to the straightforward result in which its Fourier transform yields a fractional momentum term q^σ . The renormalization of the anomalous kinetic term q^σ is parametrized in Eq. (27) by a running wave-function renormalization Z_k , as is customarily done in the short-range case (Dupuis *et al.*, 2020).

The actual subtlety of the weak long-range universality resides in the competition between the analytic momentum term q^2 and the anomalous one q^σ arising due to the long-range interaction. This effect cannot be properly reproduced by the ansatz in Eq. (27), which includes only the most relevant momentum term at the canonical level in the low-energy behavior of long-range $O(\mathcal{N})$ models. Yet, Eq. (27) is revealed to be a useful approximation to recover and extend the mean-field description of the problem at least in the limit $\sigma \ll 2$, where the nonanalytic momentum term is the leading one.

Close to the transition, the correlation length of the system, which controls the spatial extent of the correlations $\langle \varphi(x)\varphi(0) \rangle \approx \exp(|x|/\xi)/x^{d-2}$, diverges as $\xi \propto \tau^{-\nu}$. Thus, the diverging critical fluctuations produce an anomalous scaling of the correlation functions via the presence of a finite anomalous dimension η . The standard definition used for short-range models (Nishimori and Ortiz, 2015) is

$$\langle \varphi(x)\varphi(0) \rangle \approx \frac{1}{|x|^{d-2+\eta}}. \quad (28)$$

Conventionally, we refer to a correlated universality when $\eta \neq 0$ and anomalous scaling appears. If one refers to the definition (28) of the decay of correlation functions in short-range systems, then the anomalous dimension of the long-range model is already finite at the mean-field level, giving $\eta_{\text{lr}} = 2 - \sigma$, due to the contributions of the power-law couplings to the scaling of the correlations (here and in the following the subscripts lr and sr stand for long- and short-range, respectively). However, to have a proper account of

correlation effects, it is convenient to redefine the anomalous dimension η_{lr} of the long-range $O(\mathcal{N})$ models as follows:

$$\eta_{\text{lr}}(d, \sigma) \equiv 2 - \sigma + \delta\eta, \quad (29)$$

with respect to the canonical dimension of the long-range terms, which is in agreement with the definition in the classic paper by Fisher, Ma, and Nickel (1972).

Therefore, the low-momentum scaling of the critical propagator becomes $G(q)^{-1} \approx q^{\sigma - \delta\eta}$. Within the RG formalism the correction $\delta\eta$ is expected to appear as a divergence of the wave-function renormalization, which signals the rise of a modified scaling. Yet, the β function of the wave-function renormalization for the fractional momentum term identically vanishes ($k\partial_k Z_k = 0$) for any d and σ , at least in the approximation parametrized by Eq. (27). Therefore, the correlated correction for long-range interactions vanishes,

$$\delta\eta = 0. \quad (30)$$

This result was first obtained by J. Sak in 1973 (Sak, 1973). The flow of the effective potential remains the only nontrivial RG evolution for the ansatz in Eq. (27).

Like the wave-function flow, the RG evolution of the effective potential $U_k(\rho)$ has been obtained following the traditional derivative expansion approach of the FRG (Delamotte, 2012) by introducing a suitable regulator function $R_k(q) = Z_k(k^\sigma - q^\sigma)\theta(k^\sigma - q^\sigma)$. The resulting β function for the effective potential reads

$$\begin{aligned} \partial_t \bar{U}_k &= -d\bar{U}_k(\bar{\rho}) + (d - \sigma)\bar{\rho}\bar{U}'_k(\bar{\rho}) + \frac{\sigma}{2}c_d(N - 1)\frac{1}{1 + \bar{U}'_k(\bar{\rho})} \\ &+ \frac{\sigma}{2}c_d\frac{1}{1 + \bar{U}'_k(\bar{\rho}) + 2\bar{\rho}\bar{U}''_k(\bar{\rho})}, \end{aligned} \quad (31)$$

with $c_d^{-1} = (4\pi)^{d/2}\Gamma(d/2 + 1)$. As usual in RG calculations, we set $t = \log(k/\Lambda_{\text{UV}})$ as the RG time, with Λ_{UV} the ultraviolet scale, typically $\sim 1/a_{\text{latt}}$. In Eq. (31) rescaled units are also used: $\bar{\rho} = Z_k k^{\sigma-d}\rho$ and $U_k(\bar{\rho}) = k^{-d}U_k(\rho)$.

1. Competing momentum contributions

The determination of the threshold decay exponent σ_* represents one of the most interesting questions in the study of weak long-range universality. Its value is the result of a subtle interplay between different momentum terms in the critical propagator and of their contribution to the universal behavior. In particular, the question concerns the renormalization of the long-range p^σ term and its effect on the p^2 one.

The first answer to this question was given by Fisher, Ma, and Nickel (1972), who took a second-order ε -expansion approach. This analysis suggested that the mean-field result $\eta = 2 - \sigma$ holds at all orders in perturbation theory with respect to the parameter $\varepsilon = 2\sigma - d$, a result later extended by Honkonen (1990). The conclusion of this study implied a discontinuity of the anomalous dimension η as a function of the parameter σ when σ reaches $\sigma_* = 2$, the mean-field prediction for σ_* (Fisher, Ma, and Nickel, 1972). The discontinuity issue was later solved with the inclusion of

both nonanalytic p^σ and analytic p^2 terms in the propagator; see Sak (1973), which confirmed the result $\eta = 2 - \sigma$ but found a different threshold value

$$\sigma_* = 2 - \eta_{\text{sr}}.$$

Most Monte Carlo (MC) investigations featuring specific algorithms for long-range interactions (Luijten and Blöte, 1997; Fukui and Todo, 2009; Gori *et al.*, 2017) appear to be in agreement with Sak's scenario ($\sigma_* = 2 - \eta$) (Luijten and Blöte, 2002; Angelini, Parisi, and Ricci-Tersenghi, 2014; Gori *et al.*, 2017; Horita, Suwa, and Todo, 2017). Nevertheless, in recent times several different theoretical pictures have been compatible with the $\sigma_* = 2$ result (Suzuki, 1973; Yamazaki, 1977; van Enter, 1982; Picco, 2012; Blanchard, Picco, and Rajabpour, 2013; Grassberger, 2013). Recently conformal bootstrap results (Behan *et al.*, 2017) confirmed Sak's scenario and, albeit not giving numerical estimates for the long-range critical exponents, furnished a rigorous framework for its understanding. A detailed study of RG fixed points in a model of symplectic fermions with a nonlocal long-range kinetic term was reported by Giuliani, Mastropietro, and Rychkov (2021).

In the framework of the FRG approach, the absence of the analytic term in Eq. (27) makes the aforementioned approximation unsuitable to properly investigate the $\sigma \simeq \sigma_*$ regime, where the momentum term interplay is crucial. A more complete parametrization that accounts for the leading and first subleading term in the expansion of the mean-field propagator was introduced by Defenu, Trombettoni, and Codello (2015).

The flow equations obtained by Defenu, Trombettoni, and Codello (2015) yield the following picture: when a fixed point can emerge for nonvanishing long-range coupling $J_\sigma \neq 0$, this implies that $\eta = 2 - \sigma$. Therefore, the fixed point value for the long-range coupling J_σ^* has to be such that the short-range momentum term in the propagator is renormalized with $\eta = 2 - \sigma$. This solution is possible only for $d/2 < \sigma < 2 - \eta_{\text{sr}}$, which is consistent with Sak's scenario, where $\eta = 2 - \sigma$. Therefore, while at the short-range fixed point the long-range coupling vanishes ($J_\sigma = 0$), with the long-range one the short-range momentum term does not vanish, but its scaling dimension is increased to match that of the long-range terms. This complex structure demonstrates that the effective dimension approach described for the long-range spherical model by Joyce (1966) (i.e., that the critical properties of a long-range system are the same as those of the corresponding short-range model, but in a higher dimension) apparently does not hold in the interacting case, as the critical propagator of the long-range universality class features a multiple power-law structure, already noticed in MC simulations (Angelini, Parisi, and Ricci-Tersenghi, 2014), that is absent in the short-range case; see also the discussions by Defenu, Trombettoni, and Codello (2015) and Defenu, Trombettoni, and Ruffo (2016, 2017).

The final summary for the universality picture for weak long-range ferromagnetic interactions is the following:

- For $\sigma \leq d/2$ the mean-field approximation correctly describes the universal behavior.

- For σ greater than the threshold value $\sigma_* = 2 - \eta_{\text{sr}}$ the model has the same critical exponents as the short-range model (the local, short-range model is strictly defined as the limit $\sigma \rightarrow \infty$).
- For $d/2 < \sigma \leq \sigma_*$ the system exhibits peculiar long-range critical exponents, which may be approximated by those of the short-range model in the effective fractional dimension⁴ $d_{\text{eff}} = (2 - \eta_{\text{sr}})d/\sigma$.

These results, albeit obtained in the approximated framework of the derivative expansion [see Defenu, Trombettoni, and Codello (2015)], also appear to hold for the full theory and it is fair to say that the result $\eta = 2 - \sigma$ has now been confirmed with multiple techniques (Defenu, Trombettoni, and Codello, 2015; Behan *et al.*, 2017; Gori *et al.*, 2017; Horita, Suwa, and Todo, 2017). In the FRG context, the validity of Sak's scenario has also been confirmed for long-range disordered systems (Balog, Tarjus, and Tissier, 2014).

The approximate nature of the effective dimension approach described by Defenu, Trombettoni, and Codello (2015) will not hinder its adoption to compute numerical estimates for the critical exponents. Indeed, the actual correction, rising from analytical contributions to the critical propagator, appears to be rather small, and the application of the effective dimension approach produced rather accurate theoretical benchmarks for MC data, in both the long-range Ising and percolation models; see Fig. 9.

2. Berezinskii-Kosterlitz-Thouless scaling

For short-range interacting models with continuous symmetry, the occurrence of spontaneous symmetry breaking (SSB) in $d = 2$ is forbidden by the Mermin-Wagner theorem (Mermin and Wagner, 1966; Hohenberg, 1967). Yet, the inclusion of long-range interactions with $0 < \sigma < \sigma_*$ modifies the scaling dimension of operators, also allowing SSB in low dimensions. The effect of such altered scaling is summarized by the effective dimension approach, which consists in the possibility for a long-range interacting system in d dimensions to reproduce, at least approximately, the scaling of any d_{eff} -dimensional short-range system with $d_{\text{eff}} \in [d, \infty]$.

Given these considerations, it is not difficult to generalize the results of the Mermin-Wagner theorem to long-range interactions (Bruno, 2001), leading to the vanishing of the inverse correlation length exponent in the $\sigma \rightarrow 2$ limit for $\mathcal{N} \geq 2$; see Fig. 10. For $d = \mathcal{N} = \sigma = 2$ the traditional picture for short-range models is recovered and the Berezinskii-Kosterlitz-Thouless (BKT) scenario occurs (Kosterlitz and Thouless, 1973; Kosterlitz, 1974; José, 2013).

BKT scaling is a characteristic of two-dimensional systems ranging from condensed matter (Nelson and Kosterlitz, 1977; Yong *et al.*, 2013) and cold atoms (Hadzibabic *et al.*, 2006; Murthy *et al.*, 2015) to network theory (Dorogovtsev, Goltsev, and Mendes, 2008) and biology (Nisoli and Bishop, 2014). Its prototypical realization is certainly the XY model, where its properties have been well characterized (Gupta *et al.*, 1988; Gupta and Baillie, 1992; Hasenbusch, Marcu, and Pinn, 1992)

⁴At the mean-field threshold the anomalous dimension vanishes ($\eta_{\text{sr}} = 0$) and, posing d_{eff} equal to the upper critical dimension ($d_{\text{eff}} = 4$), one obtains the mean-field threshold $\sigma_{\text{mf}} = d/2$.

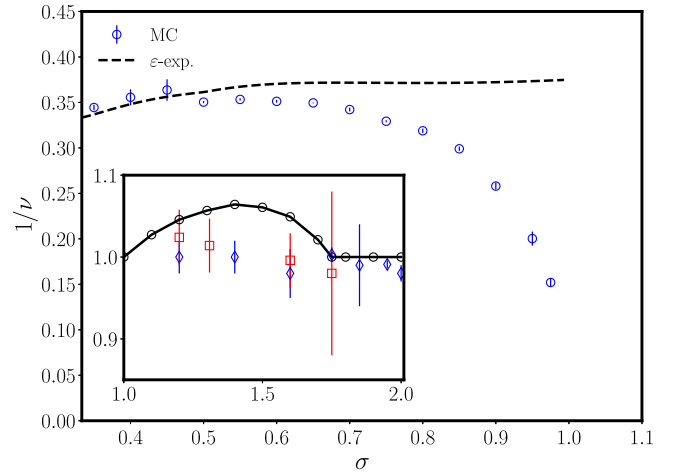


FIG. 9. Inverse correlation length exponent of long-range interactions. The results obtained from MC simulations for 1D long-range percolation are compared to the results of the effective dimension approach. The MC data of Gori *et al.* (2017) (empty blue circles) are compared to the results obtained using an effective dimension and the ϵ -expansion result (black dashed line) for the short-range model (Gracey, 2015). The low accuracy of the analytical result in the $\sigma \rightarrow 1$ limit is due to the appearance of BKT scaling (Cardy, 1981), which cannot be captured by the ϵ expansion. Inset: MC simulations for the long-range Ising model in $d = 2$ given by Luijten and Blöte (1997) and Angelini, Parisi, and Ricci-Tersenghi (2014) (blue diamonds and red squares, respectively). The black circles were obtained by mapping the conformal bootstrap results for the short-range critical exponents (El-Showk *et al.*, 2014) via the effective dimension approach described by Defenu, Trombettoni, and Codello (2015). The axis labels of the inset coincide with main axis labels.

and its relation to topological excitations first discovered (Kosterlitz, 2017).

Yet, the first theoretical indications of this topological phase transition occurred in long-range interacting classical systems (Thouless, 1969). In particular, the Coulomb gas problem and

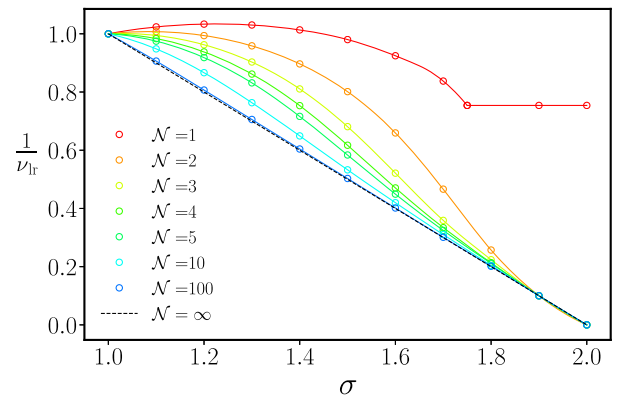


FIG. 10. Classical correlation length exponent. The correlation length exponent $1/\nu_r$ is given as a function of σ in $d = 2$ for several values of \mathcal{N} (from top, $\mathcal{N} = 1, 2, 3, 4, 5, 10, 100$). The discrepancy between the $\mathcal{N} = 1$ and the $\mathcal{N} \geq 2$ cases is in agreement with the expectations of the Mermin-Wagner theorem. The black dashed line is the analytical result obtained for the spherical model $\mathcal{N} = \infty$ (Joyce, 1966). Adapted from Defenu, Trombettoni, and Codello, 2015, where the FRG calculation of the critical exponent ν_r was discussed.

the Ising model with $d = \sigma = 1$ were known to display an infinite-order transition akin to the BKT mechanism before its traditional formulation (Anderson and Yuval, 1969; Anderson, Yuval, and Hamann, 1970). This fact is not surprising, since for $d = \sigma = 1$ the scaling dimension of the operators is consistent with that of the short-range interactions in $d = 2$. Understanding in detail the difference between the number of degrees of freedom in the traditional short-range BKT scaling with $d = \mathcal{N} = 2$ and the long-range one occurring for $d = \mathcal{N} = \sigma = 1$ is a more complicated and possibly open task, but it may be related to the irrelevance of amplitude fluctuations in $d = 2$ (Defenu *et al.*, 2017; Jakubczyk and Metzner, 2017; Krieg and Kopietz, 2017). Note that long-range BKT scaling occurring in $d = \sigma = 1$ occurs not only in the Ising model but also in long-range percolation and Potts models (Cardy, 1981; Gori *et al.*, 2017).

Despite this long-lasting relation between BKT scaling and long-range interactions, the influence of power-law couplings on topological scaling has been the subject of a limited amount of research thus far. Indeed, the applicability of the aforementioned threshold value $\sigma_* = 2 - \eta_{\text{sr}}$ to BKT scaling seems questionable since the anomalous dimension of two-point correlations in $d = \mathcal{N} = 2$ originates not from critical fluctuations but from long-wavelength phase fluctuations, which disrupt the zero-temperature magnetization. Long-range interactions with $\sigma < 2$ can be mathematically proven to stabilize spontaneous magnetization at finite temperature in the 2D XY model (Kunz and Pfister, 1976), thus implicitly suggesting that $\sigma_* = 2$. On the other hand, early results concerning the XY model on diluted Lévy graphs (Berganza and Leuzzi, 2013), which has been conjectured to lie in the same universality class of the long-range XY model, appeared to be consistent with $\sigma_* = 7/4$. However, these results have been challenged (Cescatti *et al.*, 2019). Moreover, self-consistent harmonic approximation results give an upper bound for σ_* equal to 2 (Giachetti *et al.*, 2021b). No MC results for the 2D XY model with nondisordered power-law long-range couplings around $\sigma = 2$ are available, to our knowledge.⁵

Extending the RG approach first employed by Kosterlitz (1974), Giachetti *et al.* (2021a) proposed a scenario of the complex phase diagram of the $d = 2$ long-range XY model, which features a novel transition between a low-temperature magnetized state ($T < T_*$) and an intermediate temperature state with topological scaling ($T_* < T < T_c$) that disappears at higher temperatures ($T > T_c$). This unexpected transition occurs only for $2 - 1/4 = 7/4 < \sigma < 2$, while for $\sigma \geq 2$ one has only two phases separated by a BKT transition, as in the short-range 2D XY model. These results were also applied to XXZ chains by Giachetti, Trombettoni *et al.* (2022), whose results are in agreement with those of Maghrebi, Gong, and Gorshkov (2017), as further discussed in Sec. IV.C.

Thus, the introduction of long-range interaction patterns in systems with $U(1)$ symmetry in $d = 2$ generates exotic critical features, which have no counterpart in the traditional universality classification (Raju *et al.*, 2019). This is not surprising, since the interplay between $U(1)$ systems and complex interaction patterns is known to generate peculiar critical

behavior as in the anisotropic 3D XY model (Shenoy and Chattopadhyay, 1995), coupled XY planes (Bighin *et al.*, 2019), 2D systems with anisotropic dipolar interactions (Maier and Schwabl, 2004; Vasiliev *et al.*, 2014) or four-body interactions (Antenucci, Ibáñez Berganza, and Leuzzi, 2015), and high-dimensional systems with Lifshitz criticality (Jacobs and Savit, 1983; Defenu, Trombettoni, and Zappalà, 2021).

B. Strong long-range regime

1. Ensemble inequivalence

The traditional universality problem concerns the numerical characterization of universal quantities in the strongly correlated regime, where long-range collective correlations are relevant and mean-field approximations, as well as other perturbative techniques, cannot in general be trusted. Such questions have no actual application to the case of long-range interactions with $\sigma < 0$, i.e., $\alpha < d$, since the divergent interaction strength stabilizes the mean-field solution of the problem and the Gaussian theory also reproduces the universal features at the critical point.

Nevertheless, several interesting effects arise due to strong long-range interactions in the thermodynamic behavior of statistical mechanics models. These effects may be loosely regarded as universal since they appear regardless of the particular model considered, as well as regardless of the introduction of any finite-range couplings, and they may be often characterized starting with a continuous description (Antoniazzi *et al.*, 2007; Bachelard *et al.*, 2011).

At equilibrium, the most striking feature of systems in the strong long-range regime is probably ensemble inequivalence, i.e., the appearance of substantial differences in the phase diagram of strong long-range systems depending on the application of the microcanonical or the canonical thermodynamic descriptions (Barré, Mukamel, and Ruffo, 2001). This property has been extensively revised in several review articles and books on the physics of classical long-range systems (Dauxois, Ruffo *et al.*, 2002; Campa, Dauxois, and Ruffo, 2009; Campa *et al.*, 2014) and there is no need to discuss it further here. For the following discussion, we simply mention the existence of two diverse issues of ensemble inequivalence.

The first example of ensemble inequivalence is found in systems with long-range attractive or antiferromagnetic interactions, which feature a two-phase coexistence state. These coexistence states are usually connected with a “dip” or a “convex intruder” in an otherwise concave entropy, possibly leading to a negative specific heat. The phase boundary associated with such coexistence states carries an infinite entropy cost that makes them unstable in the canonical ensemble. On the other hand, in the microcanonical description such entropy cost is not relevant, and these equilibrium states may be realized by tuning the energy (Lynden-Bell, 1999; Ispolatov and Cohen, 2001; Dauxois, Latora *et al.*, 2002). The same phenomenon is observed on sparse random graphs, where the condition of a negligible surface in the thermodynamic limit is violated (Barré and Gonçalves, 2007).

The second example of ensemble inequivalence is conventionally found in long-range systems with a two-parameter-dependent free energy $S(\varepsilon, \lambda)$, which present a line of

⁵See also the recent results of Sbierski *et al.* (2023).

second-order critical points along a line $\varepsilon_c(\lambda)$, terminating at a tricritical point at λ_c . The location of this tricritical point, as well as the structure of the first-order lines beyond it, depends on the considered thermodynamic ensemble. In particular, the microcanonical description as a function of the temperature $1/T = \partial S/\partial \varepsilon$ does not match the standard canonical description, as it should for short-range interacting systems (Barré, Mukamel, and Ruffo, 2001).

Note that the convex intruder causing the first case of ensemble inequivalence is not exclusive of long-range interacting systems, but it is also present in short-range systems with finite sizes, where the boundary contribution is comparable to the one from the finite bulk (Ispolatov and Cohen, 2001). This feature is then omitted in the thermodynamic limit in short-range systems, while it remains in strong long-range ones.

2. Violation of hyperscaling

Apart from ensemble inequivalence, the relevance of boundaries in the scaling theory of strong long-range systems produces several anomalies that influence the understanding of their critical behavior. In particular, we comment on the usual finite-size scaling theory, which relates the thermodynamic critical exponent of any quantity, for instance, the susceptibility

$$\chi \propto |T - T_c|^{-\gamma} \quad (32)$$

with its finite-size correction (Cardy, 1996)

$$\chi_N \propto N^{\gamma/\nu}, \quad (33)$$

where the subscript N indicates the corresponding quantity in a system of size N . In long-range systems, the correspondence between thermodynamic exponents and finite-size scaling ones is not obtained via the correlation length exponent ν , but rather via an exponent $\nu_* = \nu_{\text{mf}} d_{\text{uc}}$, where ν_{mf} and d_{uc} are, respectively, the mean-field correlation length exponent and the upper critical dimension of the corresponding short-range system (Botet, Jullien, and Pfeuty, 1982).

This modification of finite-size scaling theory has been related to the violation of hyperscaling and, more generally, to a nontrivial power-law scaling of the correlation length ξ with the system size N (Flores-Sola *et al.*, 2015), leading to several anomalous differences between the actual finite-size scaling of strong long-range systems and the mean-field solution (Colonna-Romano, Gould, and Klein, 2014). These observations are not peculiar to strong long-range systems but have also been found in the study of critical phenomena in short-range systems above the upper critical dimension (Binder, 1985; Luijten and Blöte, 1996; Flores-Sola *et al.*, 2016).

C. Competing nonlocal systems

Modulated phases resulting from the competition of interactions at different length scales are ubiquitous in nature (Seul and Andelman, 1995) and also display universal scaling close to their critical points. Despite this ubiquity, a comprehensive description of their universal behavior has not yet emerged and their understanding is apparently behind that of the homogeneous phase transition. A convenient effective action

for modulated phases was introduced by Brazovskii (1975); it reads

$$S[\varphi] = \frac{1}{2} \int \frac{d^d q}{(2\pi)^d} \vec{\varphi}(q) \left(\lambda + \frac{(q - q_0)^2}{m} \right) \vec{\varphi}(q) + u \int d^d x \frac{|\vec{\varphi}(x)|^4}{4!}, \quad (34)$$

where $\varphi(q)$ is the Fourier transform of $\varphi(x)$, which is an \mathcal{N} -component vector field, $q = |\vec{q}|$ is the momentum amplitude, and q_0 is a constant given by the nature of competing interactions. In writing Eq. (34) we assumed that the long-range tails of the interactions are not relevant ($\alpha > \alpha_*$).

The system described by the Hamiltonian (34) represents a different paradigm with respect to the ordinary \mathcal{N} -vector models. Indeed, the Hamiltonian (34) for $\lambda < 0$ supports a condensate with any of the finite wave vectors occurring on the $(d-1)$ -dimensional sphere $|\vec{q}| = q_0$. Therefore, the condensed phase of the model is somehow “doubly” symmetry broken since the model not only chooses the $i = 1$ component of the field in which it condenses but also must make a single choice for the wave vector $\vec{q} = \vec{q}_0$ out of the infinite set of equivalent order parameters with $|\vec{q}| = q_0$. The diversity in the symmetry-breaking procedure is also reflected in different phase space for fluctuations since the d -dimensional phase space around the $|\vec{q}| = q_0$ surface is anisotropic, with fluctuations parallel to the surface that are exactly degenerate and fluctuations away from it that are only nearly degenerate. This discussion should have clarified that the Brazovskii model in Eq. (34) does not belong to any of the usual universality classes of isotropic models and presents its own set of universal properties as a function of the parameters \mathcal{N} and d .

Interesting applications of the physics described by the Brazovskii model occur in two-dimensional or highly anisotropic systems, such as quantum Hall platforms (Fradkin and Kivelson, 1999), high T_c superconductors (Kivelson, Fradkin, and Emery, 1998; Kivelson *et al.*, 2003), and ultrathin magnetic films (Kashuba and Pokrovsky, 1993; Vaterlaus *et al.*, 2000; Saratz *et al.*, 2010). Nevertheless, the first efforts to apply the momentum shell renormalization group theory (Wilson and Kogut, 1974) to the Hamiltonian (34) with $d = 2$, resulting in the impossibility of constructing a reliable perturbative picture (Hohenberg and Swift, 1995). Applying the RG approach described by Shankar (1994) for fermionic systems, Hohenberg and Swift (1995) found that momentum-dependent corrections to the interacting coupling u are relevant and that no weak coupling expansion is possible in the treatment of modulated phases. Nevertheless, a symmetry analysis of these relevant corrections suggests the appearance of a second-order nematic-isotropic transition (Barci and Stariolo, 2007). Similar difficulties have been encountered by more modern treatments (Shiwa, 2006), and the description of systems belonging to the Brazovskii universality has been confined to mean-field theory (Barci and Stariolo, 2007; Barci, Ribeiro, and Stariolo, 2013; Capati *et al.*, 2015), scaling arguments (Barci and Stariolo, 2009; Portmann *et al.*, 2010; Barci and Stariolo, 2011; Mendoza-Coto and Stariolo, 2012), and numerical simulations (Cannas *et al.*, 2006; Poderoso, Arenzon, and Levin, 2011).

Recently the study of the nematic-isotropic transitions in the Brazovskii model has been extended beyond the analytic momentum paradigm in Eq. (34) to include long-range repulsive interactions of the form $1/r^{\alpha'}$, with particular focus on the Coulomb ($\alpha' = 1$) and dipolar ($\alpha' = 3$) cases (Mendoza-Coto, Stariolo, and Nicolao, 2015). Note particularly that, within the effective field theory approach of Mendoza-Coto, Stariolo, and Nicolao (2015), it is possible to show the exact correspondence between the universality of the nematic-isotropic transition and that of homogeneous rotor models at finite temperature with decay exponent $\alpha = \alpha' + 2$ (Mendoza-Coto, Barci, and Stariolo, 2017). Therefore, for modulated phases with $d = 2$, the relevant regime for long-range interactions is rigidly shifted in such a way that any power-law decay $\alpha' > 2$ is always irrelevant, while for $\alpha' < 2$ the interaction energy also remains finite in the absence of any rescaling due to the modulation pattern of the order parameter.

Within this framework, the scalar φ^4 theory with competing long-range and short-range interactions lies in the same universality class as the long-range ferromagnetic $O(2)$ model with $\sigma = \alpha'$ described in Sec. III.A (Mendoza-Coto, Stariolo, and Nicolao, 2015). Therefore, for $\alpha' > 2$ the isotropic nematic transition displays in $d = 2$ BKT scaling, as in the short-range XY model, while for $\alpha' < 2$ actual orientational order occurs. Given this relation, one would expect, based on the work of Giachetti, Trombettoni *et al.* (2022), that for $\alpha' \in [1.75, 2]$ the same phenomenology as described in Sec. III.A.2 will occur.

IV. QUANTUM CRITICAL BEHAVIOR

Our discussion of zero-temperature criticality starts with the observation that field theory approaches allow the universal behavior at a $T = 0$ quantum critical point to be related to that of the corresponding $T \neq 0$ classical phase transition in dimension $d + z$, where z is the dynamical critical exponent (Sachdev, 1999). This correspondence is exact for local, continuous $O(\mathcal{N})$ field theories with $z = 1$ and it can also be proven for the one-dimensional lattice Ising model in a transverse field (Mussardo, 2009; Dutta *et al.*, 2015). Thus, it is natural to connect, whenever possible, the universal behavior in the quantum regime to that of finite-temperature phase transitions for long-range models. In the following, we divide our presentation according to the nature of the variables at hand.

A. Quantum rotor models

Given the correspondence between quantum and classical universalities, $O(\mathcal{N})$ field theories also constitute a paradigmatic model for quantum critical behavior. However, unlike in the classical case they generally do not describe the universality of ferromagnetic quantum spin systems, since quantum spins possess $SU(\mathcal{N})$ rather than $O(\mathcal{N})$ symmetry. Nevertheless, the low-energy behavior of quantum $O(\mathcal{N})$ models describes the physics of several quantum models, such as the quantum Ising model $\mathcal{N} = 1$, superfluid systems $\mathcal{N} = 2$, and antiferromagnetic quantum Heisenberg spin systems, which correspond to $\mathcal{N} = 3$ (Sachdev, 1999).

In this context, a convenient lattice representation of quantum $O(\mathcal{N})$ field theories is provided by quantum rotor models, whose Hamiltonian reads

$$H_R = -\sum_{ij} \frac{J_{ij}}{2} \hat{\mathbf{n}}_i \cdot \hat{\mathbf{n}}_j + \frac{\lambda}{2} \sum_i \hat{\mathcal{L}}_i^2, \quad (35)$$

where $\hat{\mathbf{n}}_i$ are n -component unit length vector operators ($\hat{\mathbf{n}}_i^2 = 1$), λ is a real constant, and \mathcal{L} is the invariant operator formed from the asymmetric rotor space angular momentum tensor (Sachdev, 1999). As previously done, we focus on power-law decaying ferromagnetic couplings $J_{ij} = J/r_{ij}^{d+\sigma}$, with $J > 0$.

In the short-range limit ($\sigma \rightarrow \infty$) the continuum formulation of quantum $O(\mathcal{N})$ rotor models would exactly correspond to a $(d + 1)$ -dimensional $O(\mathcal{N})$ field theory, with the extra dimension representing the temporal propagation of quantum fluctuations. However, in the long-range regime the field theory action is anisotropic as the spatial coordinates feature a leading nonanalytic momentum term, at least for $\sigma < \sigma_*$. Following the same FRG approach as in Sec. III.A, one can introduce the following ansatz for the effective action of an $O(\mathcal{N})$ quantum rotor model:

$$\Gamma_k = \int d\tau \int d^d x \{ K_k \partial_\tau \varphi_i \partial_\tau \varphi_i - Z_k \varphi_i \Delta^{\sigma/2} \varphi - Z_{2,k} \varphi_i \Delta \varphi + U_k(\rho) \}, \quad (36)$$

where Δ is the spatial Laplacian in d dimensions, τ is the ‘‘Trotter’’ or imaginary time direction, $\varphi_i(x)$ is the i th component ($i \in \{1, \dots, n\}$) of the system, and $\rho \equiv \sum \varphi_i^2/2$ is the system order parameter. In Eq. (36) the summation over repeated indices is again intended.

Remember that the ansatz in Eq. (36) for the effective action, albeit sufficient to characterize the physics of long-range rotor models, only approximately represents the exact critical action of correlated models. Indeed, it contains only two kinetic terms in the d spatial directions, as necessary to represent the competition between long-range and short-range contributions to the critical propagator, but does not contain momentum-dependent corrections to the theory vertices (Dupuis *et al.*, 2020). As expected, the time direction τ does not contain any fractional derivative, so one may obtain a nonunity value for the dynamical critical exponent z defined by the scaling of the dispersion relation $\omega \propto q^z$.

1. Effective dimension approach

The characterization of the critical properties of the action in Eq. (36) proceeds in analogy with the case of classical anisotropic systems (Defenu, Trombettoni, and Ruffo, 2016), but it leads to a far more interesting picture. Scaling analysis allows the universal properties of long-range quantum rotor models in d dimensions to be approximately related to those of their classical short-range correspondents in an effective dimension as

$$d_{\text{eff}} = \frac{2(d+z)}{\sigma}, \quad (37)$$

where d and z are, respectively, the dimension and the dynamical critical exponent of the long-range model under study. For $\sigma < 2$ it is found that $z = \sigma/2$ (Defenu, Trombettoni, and Ruffo, 2017). Inserting this value of z into Eq. (37) and imposing $d_{\text{eff}} = 4$ one then obtains $\sigma_{\text{mf}} = 2d/3$, which is to be compared to the classical result $\sigma_{\text{mf}} = d/2$. For $d = 1$ one has $\sigma_{\text{mf}} = 2/3$.

The anisotropy between the time and the spatial direction in the long-range model is already apparent in the mean-field estimations for the critical exponents (Dutta and Bhattacharjee, 2001; Monthus, 2015)

$$\eta = 2 - \sigma, \quad (38)$$

$$z = \sigma/2, \quad (39)$$

$$\nu = 1/\sigma. \quad (40)$$

Upon inserting the result in Eq. (39) into the effective dimension relation in Eq. (37), one obtains the mean-field expression $d_{\text{eff}} = 2d/\sigma + 1$, which proves that the effective dimension of quantum rotor models is increased by 1 with respect to the classical case, as occurs for traditional short-range systems.

The correspondence between quantum and classical $O(\mathcal{N})$ models based on the effective dimension approach in Eq. (37) exactly applies to quadratic models in general (Vojta, 1996) and is expected to be close to the upper critical dimension. Thus, we can employ the effective dimension approach to construct the phase diagram displayed in Fig. 11. Indeed, the upper critical dimension result d_{uc} can be derived using the condition $d \geq 4$, so

$$d_{\text{uc}} = \frac{3}{2}\sigma, \quad (41)$$

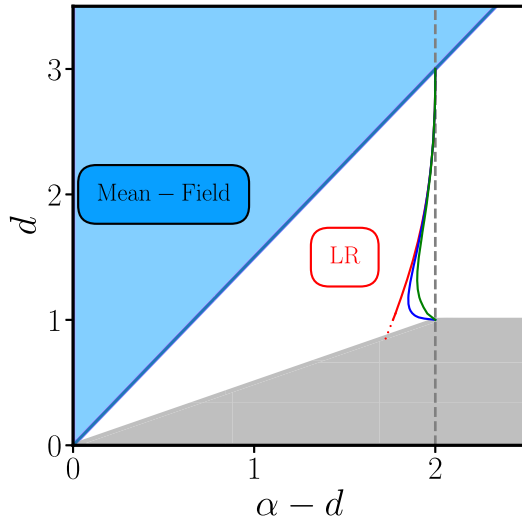


FIG. 11. Phase diagram of long-range quantum rotors models in the plane d, σ . The universal behavior features the mean-field critical exponents in Eqs. (38), (39), and (40) in the cyan shaded region (upper left corner), while the universal properties are associated with an interacting Wilson-Fisher point in the white region. The red, blue, and green lines represent the boundary between long-range and short-range universality ($\mathcal{N} = 1, 2, 3$ from left to right, respectively). Finally, the gray shaded region (lower right corner) displays no phase transition at all.

as also follows from standard scaling arguments (Dutta and Bhattacharjee, 2001). Correspondingly, the lower critical dimension d_{lc} for continuous symmetries $\mathcal{N} \geq 2$ follows from the condition $d_{\text{eff}} \leq 2$, which yields

$$d_{\text{lc}} = \frac{\sigma}{2}. \quad (42)$$

We emphasize once again that Eq. (42) is valid only for continuous symmetries $\mathcal{N} \geq 2$. As a result, correlated universality is observed in the region $2 \leq d_{\text{eff}} < 4$, i.e., the cyan shaded region in Fig. 11. Therefore, the critical exponents do not coincide with the mean-field result, and we need to take the effective potential in Eq. (36) into account.

2. Beyond mean-field critical exponents

The study of the action in Eq. (36) evidences two regimes, as the same mechanism is found for the transition between the long-range and the short-range universality that occurs at $\sigma_* = 2 - \eta_{\text{sr}}$, as in the classical case. For $\sigma > \sigma_*$ the effective action of quantum rotor models is isotropic and analytic in the momentum sector, and its flow equations are identical to the ones in the classical $d + 1$ case (Codello, Defenu, and D'Odorico, 2015). For $\sigma < \sigma_*$, however, the anisotropy between spatial and imaginary time dimensions produces the following novel flow equations for the effective potential and the wave-function renormalization K_k :

$$\begin{aligned} \partial_t \bar{U}_k &= (d+z)\bar{U}_k(\bar{\rho}) - (d+z-\sigma)\bar{\rho}\bar{U}'_k(\bar{\rho}) \\ &\quad - \frac{\sigma}{2}(N-1)\frac{1-\eta_\tau z/(3\sigma+2d)}{1+\bar{U}'_k(\bar{\rho})} \\ &\quad - \frac{\sigma}{2}\frac{1-\eta_\tau z/(3\sigma+2d)}{1+\bar{U}'_k(\bar{\rho})+2\bar{\rho}\bar{U}''_k(\bar{\rho})}, \end{aligned} \quad (43)$$

$$-\frac{\partial_t K_k}{K_k} = \eta_\tau = \frac{f(\bar{\rho}_0, \bar{U}^{(2)}(\bar{\rho}_0))(3\sigma+2d)}{d+(3\sigma+d)[1+f(\bar{\rho}_0, \bar{U}^{(2)}(\bar{\rho}_0))]} \quad (44)$$

In the derivation of Eqs. (43) and (44), analytic terms in the spatial direction are discarded (Defenu, Trombettoni, and Ruffo, 2017) setting $Z_{2,k} = 0$ in Eq. (36), as their contributions to the RG running of other quantities remain small up to $\sigma \simeq \sigma_*$; see the discussion in Sec. III.A.1.

The numerical study of quantum long-range $O(\mathcal{N})$ models appears to be more extensive in the literature than the classical case. Numerical simulations for both the quantum long-range Ising and $O(2)$ rotor models have been performed, yielding numerical curves for both critical exponents z and ν while also confirming the mean-field result $\eta = 2 - \sigma$ in the correlated regime (Sperstad, Stiansen, and Sudbø, 2012). Figure 12 compares the numerical estimates obtained with the flow equations (43) and (44) using the solution approach described by Codello, Defenu, and D'Odorico (2015) and Defenu, Trombettoni, and Codello (2015) along with the results from the MC simulations of Sperstad, Stiansen, and Sudbø (2012).

In Fig. 12 (upper panel) the dynamical critical exponent z is reported as a function of σ in $d = 1$. These numerical results

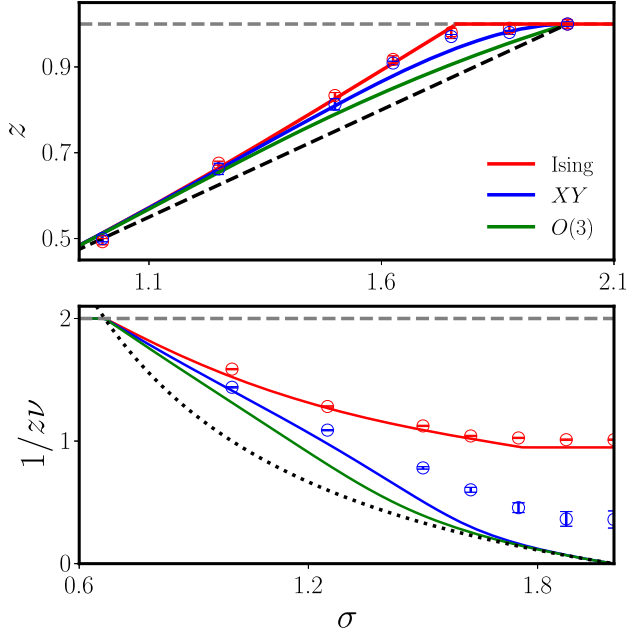


FIG. 12. Universal properties of long-range quantum rotor models. Upper panel: estimates for the dynamical critical exponent $z = \sigma/(2 - \eta_r)$ obtained using the fixed point solution of the evolution equations (43) and (44) in the cases $\mathcal{N} = 1, 2, 3$ in red, blue, and green (from top to bottom), respectively. Lower panel: inverse correlation length exponents $\mathcal{N} = 1, 2, 3$, progressing from top to bottom. The MC simulations of Sperstad, Stiansen, and Sudbø (2012) are shown as empty circles in the $\mathcal{N} = 1, 2$ cases top (red) and bottom (blue) lines, respectively. In both panels the upper gray dashed lines represent the mean-field results, while the dashed lower black lines represent the spherical model results ($\mathcal{N} = \infty$).

have been obtained solving Eqs. (43) and (44) at the fixed points and studying their stability matrix accordingly, as described by Codello, Defenu, and D’Odorico (2015) and Defenu, Trombettoni, and Codello (2015). The mean-field region $\sigma < 2/3$ is not shown, as it is exactly described by the analytical estimates in Eqs. (38)–(40). Numerical results for $\sigma < 1/2$ deviating from the mean-field expectation have not been reported (Fey and Schmidt, 2016). The dynamical critical exponents of the transverse-field Ising model with long-range power-law interaction in the weak long-range regime were derived by Maghrebi, Gong, and Gorshkov (2017) up to two-loop order within the renormalization group theory. Recent quantum Monte Carlo (QMC) simulations have shown substantial agreement with the behaviors displayed in Fig. 12 (Kozioł *et al.*, 2021). Note that recent simulations have also targeted the finite-temperature transition at $\alpha < d$ (Gonzalez-Lazo *et al.*, 2021) and the two-dimensional case (Fey, Kapfer, and Schmidt, 2019; Kozioł *et al.*, 2019). Nonlocal dissipation can act on Ising lattices molding the universality class of their critical points (Marino, 2021) and can potentially be realized and characterized in cavity experiments (Seetharam *et al.*, 2021).

Out of the mean-field region, correlation effects tend to increase the value of the dynamical critical exponent, increasing the gap with the analytic prediction in Eq. (39). This effect is mitigated for continuous symmetries $\mathcal{N} \geq 2$ due to the

vanishing of the anomalous dimension at the short-range threshold $\sigma_* = 2$. Accordingly, the agreement between the FRG curves and the numerical MC results (the red solid line and circles in Fig. 12) remains consistent in the entire σ range. On the other hand, the $\mathcal{N} = 2$ case displays poorer overall consistency, due mostly to the inaccuracy of the MC estimates. Indeed, while the effective action parametrization in Eq. (36) proved unable to properly describe the continuous BKT line (Gräter and Wetterich, 1995), it consistently reproduces the scaling of critical exponents in the BKT limit (Codello, Defenu, and D’Odorico, 2015).⁶

The lower accuracy found for the $\mathcal{N} = 2$ case is confirmed by the comparison of the MC simulation for the correlation length estimates to the FRG curve (the blue circles and line in Fig. 12). Indeed, the MC data provide a finite correlation length exponent in the limit $\sigma \rightarrow 2$ for the O(2) model, in contradiction to rigorous analytical predictions from the $d_{\text{eff}} - 2$ expansion (Brézin and Zinn-Justin, 1976). On the contrary, the FRG curve correctly reproduces the expected feature, as it did in the classical case; see Fig. 10. Therefore, the flow equations (43) and (44) yield all the qualitative features and reach quantitative accuracy for all values d , σ , and N in the phase diagram of quantum long-range O(\mathcal{N}) models, producing good accuracy with exact numerical simulations. The difficulties in the FRG characterization of the BKT transition (Gräter and Wetterich, 1995; Jakubczyk, Dupuis, and Delamotte, 2014; Jakubczyk and Metzner, 2017) appear not to be problematic in this case, as MC simulations are plagued by severe finite-size effects as well. Recent numerical results on the long-range XY model were reported by Adelhardt *et al.* (2020).

A notable fact is that the MC points in Fig. 12 appear to also provide $\sigma_* = 2 - \eta_{\text{sr}}$, with $\eta = 1/4$, for $\mathcal{N} = 2$, without any apparent distinction between the $\mathcal{N} = 1$ and 2 cases. As mentioned, this is in stark contradiction to the picture furnished by FRG, which suggests that $\sigma_* = 2$ identically for all continuous symmetries. The correct picture is most likely in between, as suggested by the analysis presented in Sec. III.A.2.

B. Kitaev chain

The introduction of long-range couplings in Fermi systems produces radically different results with respect to the bosonic case. The Kitaev chain (Kitaev, 2001) emerged as one of the most studied playgrounds in which effects of long-range terms have been investigated. In the fermionic context we first consider the generalized Kac-normalized (Kac, Uhlenbeck, and Hemmer, 1963) long-range Kitaev chain (Maity, Bhattacharya, and Dutta, 2020). Its Hamiltonian reads

$$H = - \sum_{j=1}^N \sum_{r=1}^R \left(J_r c_j^\dagger c_{j+r} + \Delta_r c_j^\dagger c_{j+r}^\dagger + \text{H.c.} \right) - h \sum_{j=1}^N \left(1 - 2c_j^\dagger c_j \right), \quad (45)$$

⁶Note that the power-law scaling of BKT correlations originates from phase correlations and does not contradict the vanishing of the anomalous dimension defined according to Eq. (44) (Defenu *et al.*, 2017).

where

$$J_r = t \frac{d_r^{-\alpha}}{\mathcal{N}_\alpha}, \quad \Delta_r = g \frac{d_r^{-\beta}}{\mathcal{N}_\beta} \quad (46)$$

are the hopping and pairing profiles, respectively, with hopping $t > 0$ and normalization satisfying one of the two relations

$$\mathcal{N}_x = \begin{cases} \sum_{r=1}^R d_r^{-x}, & \text{Kac rescaling,} \\ 1, & \text{otherwise,} \end{cases} \quad (47)$$

where R denotes the range of the interactions; d_r is the distance between the sites i and $i + r$; $x \equiv \alpha, \beta$ refers to the power-law exponents; h is the chemical-potential strength; and c_j and c_j^\dagger are the fermionic annihilation and creation operators, which obey the canonical anticommutation relations $\{c_l, c_j^\dagger\} = \delta_{l,j}$ and $\{c_l, c_j\} = 0$. In Eq. (47) we allowed the possibility of either implementing Kac rescaling or leaving the couplings unscaled, as in the literature both conventions are employed.

The definition of distance depends on the choice of the boundary conditions. Thus, a ring structure, i.e., closed boundary conditions, leads to the definition $d_r = \min(r, L - r)$, while open boundary conditions simply produce $d_r = r$. Conventionally, (anti)periodic boundary conditions allow the straightforward analytical solution of the problem in the short-range limit. Yet, long-range couplings extending over the entire chain length lead to the cancellation of the hopping (pairing) operators for antiperiodic (periodic) boundary conditions due to the anticommutation relations (Alecce and Dell'Anna, 2017). This issue justifies the introduction of a finite interaction range R into the Hamiltonian in Eq. (45).

In the following we mainly discuss the ring convention with $d_r = \min(r, L - r)$ and fix $R = L/2 - 1$, where L is the number of sites in the ring chain. This choice allows us to deal with ring boundary conditions but still obtain a nontrivial thermodynamic limit $L \rightarrow \infty$, where the couplings display infinite-range tails. One can thus introduce the Fourier transform

$$c_j = \frac{1}{\sqrt{L}} \sum_k^{\text{B.z.}} c_k e^{ikj}, \quad (48)$$

where the sum is over the first Brillouin zone. On a finite ring the values of the momenta have to be chosen in order to comply with periodic ($k = 2\pi n/L$) or antiperiodic ($k = [2\pi(n + 1/2)]/L$) boundary conditions. The Hamiltonian in momentum space reads

$$H = \sum_k^{\text{B.z.}} [(c_k^\dagger c_k - c_{-k}^\dagger c_{-k})(h - J_k) + (c_k^\dagger c_{-k}^\dagger - c_k c_{-k})\Delta_k], \quad (49)$$

where the momentum space couplings have been obtained by Fourier transforming J_r and Δ_r :

$$J_k = \frac{t}{\mathcal{N}_\alpha} \sum_{r=1}^R \frac{\cos(kr)}{r^\alpha}, \quad (50)$$

$$\Delta_k = \frac{g}{\mathcal{N}_\beta} \sum_{r=1}^R \frac{\sin(kr)}{r^\beta}. \quad (51)$$

The Hamiltonian (49) is quadratic and can be explicitly diagonalized via a Bogoliubov transformation

$$c_k = i \sin \frac{\theta_k}{2} \gamma_k + \cos \frac{\theta_k}{2} \gamma_{-k}^\dagger, \quad (52)$$

where γ_k and γ_k^\dagger are fermionic operators that, respectively, annihilate and create Bogoliubov quasiparticles. They obey the conventional anticommutation relations $\{\gamma_k, \gamma_p^\dagger\} = \delta_{k,p}$ and $\{\gamma_k, \gamma_p\} = 0$. The proper choice for the momentum-dependent angle θ_k in order to diagonalize the Hamiltonian (49) reads

$$\theta_k = \arctan \frac{\Delta_k}{h - J_k}, \quad (53)$$

which leads to the diagonal Hamiltonian

$$H = \sum_k^{\text{B.z.}} \omega_k (\gamma_k^\dagger \gamma_k - \gamma_{-k} \gamma_{-k}^\dagger) \quad (54)$$

with the quasiparticle spectrum

$$\omega_k = \sqrt{(h - J_k)^2 + \Delta_k^2}. \quad (55)$$

In the thermodynamic limit $L \rightarrow \infty$, the short-range model ($\alpha, \beta \rightarrow \infty$) features the familiar relations $J_k = t \cos(k)$ and $\Delta_k = g \sin(k)$. Accordingly, the minimal gap occurs at $k = 0, \pi$, depending on the sign of h , and vanishes as the chemical potential approaches the critical values $h \rightarrow \pm t$. The two short-range critical points $h = \pm t$ feature a soft mode at, respectively, $k = 0, \pi$, in correspondence to the appearance of ferromagnetic or antiferromagnetic order in the short-range Ising chain obtained using the Jordan-Wigner transformation (Fradkin, 2013). Yet, in terms of the fermionic operators of the Kitaev chain no local order is found, but the quantum critical points divide different topological phases, where only non-local string orders are found (Chitov, 2018).

Without loss of generality, we can then impose $t = g = 1$ from now on, fixing the location of the short-range critical point. Upon crossing the critical point, the system undergoes a quantum phase transition between a topologically trivial phase at $|h| > 1$ and one featuring a finite winding number

$$w = \frac{1}{2\pi} \oint d\theta_k, \quad (56)$$

where the integral has to be taken along the periodic Brillouin zone.

In terms of topological properties, the quantum phase transition occurs between the trivial phase $w = 0$ at $|h| > 1$ and the topologically nontrivial phase at $|h| < 1$. The existence of a nontrivial topological order in the bulk of the system is connected to the occurrence of zero-energy Majorana modes at the boundaries with the normal phase. In particular, such zero-energy Majorana modes are found at the edges of the finite chain with open boundaries (Kitaev, 2001).

The inclusion of interactions beyond the nearest-neighbor case modifies and extends this traditional picture.

Before continuing the discussion, we observe that the use of open boundary conditions allows one to predict that the edge modes are exponentially localized at the chain edges in the isotropic case when pairing and tunneling rates are equal, i.e., $\alpha = \beta$ (Jäger, Dell'Anna, and Morigi, 2020). Algebraic decay of the edge modes is found in the anisotropic case when either the exponent or the rates of tunneling and pairing are different. In the latter case, the smallest exponent causes the algebraic scaling of the tails, while at short distances the decay is exponential. For slow enough power-law decaying superconducting pairings, the massless Majorana modes at the edges pair into a massive non-local Dirac fermion localized at both edges of the chain called a topological massive Dirac fermion with fractional topological numbers (Viyuela *et al.*, 2016).

Note that signatures of Majorana edge modes have been studied in ferromagnetic atomic chains on top of superconducting leads (Nadj-Perge *et al.*, 2014). In this context, the realization of power-law decaying couplings via Ruderman-Kittel-Kasuya-Yosida interactions has been proposed (Klinovaja *et al.*, 2013). A weakening of the bulk-boundary correspondence in the presence of a long-range pairing with Aubry-André-Harper on-site modulation has been observed (Fraxanet *et al.*, 2021). For this model, a 2D Chern invariant can still be defined. However, in contrast to the short-range model, this topological invariant does not correspond to the number of edge mode crossings.

1. Finite-range couplings

As usual, finite-range interactions with $R < \infty$ in the thermodynamic limit cannot alter the universal critical scaling close to the quantum phase transition, but they may alter the topological phase diagram, leading to modifications in the number and properties of the edge modes. However, this is not the case if finite-range interactions appear only in the hopping or the pairing sector separately, i.e., $\beta \rightarrow \infty$ or $\alpha \rightarrow \infty$, respectively. There the phase diagram remains almost unaltered with respect to the short-range case, apart from a modification of the critical boundaries, which become anisotropic, with the $k = 0, \pi$ instabilities occurring at different values of $|h|$.

For generic values of α and β , the topological phase diagram also contains regions with $|w| > 1$, with a maximum value equal to the range of the interactions $|w|_{\max} = R$. The range of parameters in which w is maximum decreases with α , and the phase diagram of the standard Kitaev chain model is recovered in the $\alpha \rightarrow \infty$ limit independently of β . The winding number may also assume intermediate values between 1 and R with steps of 2 (Alecce and Dell'Anna, 2017).

The separation into even and odd numbers of Majorana modes depending on the range R is justified by the possibility for Majorana modes on the same edge to annihilate each other one by one per edge, according to the mechanism described by Alecce and Dell'Anna (2017). The topological phase with $|w| = 1$ instead persists for each interaction range $R \geq 1$

because the annihilation of a single Majorana pair requires overlap between the two wave functions that peaked at the opposite edges of the chain.

2. Infinite-range pairing

In general, the influence of long-range interactions on topology has also been investigated for infinite-range couplings in antiferromagnetic spin-1 chains where α_* for the survival of the topological phase depends on the frustrated or unfrustrated nature of the long-range terms, i.e., $\alpha \simeq 0$ or 3 (Gong, Maghrebi, Hu, Foss-Feig *et al.*, 2016; Gong, Maghrebi, Hu, Wall *et al.*, 2016). Moreover, the interplay between topology and long-range connectivity generates a wide range of peculiar phenomena, including novel quantum phases (Gong, Maghrebi, Hu, Foss-Feig *et al.*, 2016), modifications of the area law (Gong *et al.*, 2017), and breaking of the Lieb-Robinson theorem (Maghrebi *et al.*, 2016).

The first studies of the long-range Kitaev chain focused on the case of infinite-range long-range couplings $R \propto L$ only in the pairing sector (Vodola *et al.*, 2014), leading to the thermodynamic limit expressions

$$J_k = \cos(kr), \quad (57)$$

$$\Delta_k = \frac{1}{\mathcal{N}_\beta} \sum_{r=1}^{\infty} \frac{\sin(kr)}{r^\beta} = \frac{\text{Im}[\text{Li}_\beta(e^{ik})]}{2\zeta(\beta)}, \quad (58)$$

where the case $\mathcal{N}_\beta = 1$ is discussed first. In the absence of Kac rescaling, the critical line at $h = -1$ appearing in the short-range models persists independently of β , while the one at $h = 1$ disappears as soon as $\beta < 1$. Notably some references discuss the persistence of the $h = -1$ critical line below $\alpha = 1$ (Lepori *et al.*, 2016; Lepori and Dell'Anna, 2017). Subsequent work clarified that the ground-state energy of the system

$$e_{\infty, \beta} = \int_{-\pi}^{\pi} \omega_k dk \quad (59)$$

remains finite for all β and h due to the fermionic nature of the model and at variance with the classical case. Yet, the zero-momentum spectrum diverges ($\lim_{k \rightarrow 0} \omega_k \rightarrow \infty$) for $\beta < 1$, leading to the disappearance of the quantum critical point at $h = 1$, which could be made stable by the introduction of Kac rescaling, as in the classical case; see Eq. (47). This entire picture is in loose agreement with the discussion in Sec. III.C, where we have shown that for modulated phases, characterized by instability at finite momentum, no internal energy divergence is detected for a decay exponent $\alpha < d$, while ferromagnetic models with homogeneous order need Kac rescaling.

Therefore, the divergence in $k = 0$ is the cause for the disappearance of the $h = 1$ quantum critical point for $\alpha < 1$. At the same time, at every finite α divergences in some k derivatives for ω_k occur both at $k = 0$ and at $k = \pi$ (Vodola *et al.*, 2014; Lepori *et al.*, 2016), giving rise to interesting effects in the correlation decay and the dynamics (Lepori,

Trombettoni, and Vodola, 2017). In particular, these divergencies generate several novel features in the equilibrium behavior of the Kitaev chain. They may be summarized by the following main effects:

- Hybrid decay of static correlations with an intermediate-range exponential part and power-law tails (Lepori, Trombettoni, and Vodola, 2017), which can be connected to the existence of a Lieb-Robinson bound peculiar to long-range systems (Foss-Feig *et al.*, 2015; Van Regemortel, Sels, and Wouters, 2016; Hernández-Santana *et al.*, 2017).
- A breakdown of conformal invariance for $\beta < 2$ has been found (Lepori *et al.*, 2016). Nevertheless, the scaling of the von Neumann entropy fulfills the area law up to $\alpha = 1$ as in the short-range limit ($\beta \rightarrow \infty$) (Eisert, Cramer, and Plenio, 2010). At the critical point, the central charge defined by the logarithmic correction to the von Neumann entropy remains $c = 1/2$ as in the short-range limit as well (Lepori *et al.*, 2016).
- Below the threshold $\beta = 1$, logarithmic corrections to the area law have been found out of criticality, modeled by

$$S(\ell) = \frac{c_{\text{eff}}}{6} \log(\ell), \quad (60)$$

where ℓ is the size of the bipartition (Vodola *et al.*, 2014, 2016). Notably this correction, which is identical to that of short-range systems at criticality (Calabrese and Cardy, 2004; Holzhey, Larsen, and Wilczek, 1994), has also been found in the Ising model (Koffel, Lewenstein, and Tagliacozzo, 2012).

- Again below $\beta = 1$, the topological phase at $\mu < 1$, the Majorana edge modes, which remained well separated in the short-range limit, hybridize and produce a massive Dirac mode, effectively lifting the ground-state degeneracy present for $\beta > 1$. This mechanism is analogous to that occurring in the short-range limit at finite size (Kitaev, 2001). An explicit proof of this fact was given by Patrick, Neupert, and Pachos (2017) for $\alpha = \beta = 0$.

All of these features are also found in the general case $\alpha, \beta < \infty$, almost independently of the value of α (Vodola *et al.*, 2016; Alecce and Dell'Anna, 2017; Lepori and Dell'Anna, 2017; Solfanelli *et al.*, 2023), and they can be straightforwardly reproduced using a continuous effective field theory description (Lepori *et al.*, 2016). Therefore, all the aforementioned properties can be classified as universal, according to our previous definition. Note that the peculiar nature of the long-range Kitaev chain at $\beta < 1$ is signaled by a noninteger value of the winding number defined in Eq. (56), which in principle is not admissible. This effect points toward a general breakdown of the traditional theory for topological phases in short-range systems (Schnyder *et al.*, 2008; Kitaev, 2009), leading to modifications in the bulk-edge correspondence (Lepori and Dell'Anna, 2017).

3. The $\alpha = \beta$ case and its relation to the long-range Ising model

The topological features of the $\alpha < \infty$ case are not substantially different from the $\alpha \rightarrow \infty$ case, as it is the paring term in Eq. (45) that induces the topological behavior. Yet, the

presence of long-range hopping substantially alters both the critical and dynamical properties of the long-range Kitaev chain. Before discussing such properties, it is convenient to discuss the case $\alpha = \beta$, which is strongly tied to the case of $1/2$ spins. In this perspective, it is convenient to first introduce the long-range Ising model Hamiltonian

$$H = -\sum_{l < j} J_{lj} \sigma_l^x \sigma_j^x - h \sum_j \sigma_j^z, \quad (61)$$

where $\sigma_j^{\{x,y,z\}}$ are the Pauli matrices on site j , h is the transverse-field strength, and J_r , with $r = |l - j|$, is the spin coupling profile with power-law scaling ($\propto 1/r^\alpha$, $\alpha \geq 0$). As usual, in the limit $\alpha \rightarrow \infty$ one recovers the short-range Ising model, which is integrable and can be exactly solved with a Jordan-Wigner transformation (Fradkin, 2013). Another interesting limit is reached for $\alpha \rightarrow 0$, where the Hamiltonian (61) represents the LMG model (Glick, Lipkin, and Meshkov, 1965; Lipkin, Meshkov, and Glick, 1965; Meshkov, Glick, and Lipkin, 1965). In this limit, the flat infinite-range interaction leads to permutation symmetry and allows one to employ the Dicke basis (Nussenzweig, 1973), which scales linearly with the system size and yields a tractable description of the system that is amenable via exact diagonalization.

The equilibrium phase diagram of the Hamiltonian (61) and its universal properties have been discussed in Sec. IV.A in the case $\mathcal{N} = d = 1$. In summary, the system displays a finite-temperature phase transition for $\alpha < 2$ (Dyson, 1969; Thouless, 1969; Dutta and Bhattacharjee, 2001) within the same universality class of the classical long-range Ising model (Defenu, Trombettoni, and Codello, 2015). In the limit $T \rightarrow 0$, the system displays a quantum critical point at finite h , whose universal properties depend on the value of σ according to Fig. 11 (Defenu, Trombettoni, and Ruffo, 2017). In the nearest-neighbor limit $\alpha \rightarrow \infty$ the universal behavior exactly corresponds to that of the Kitaev chain with $\alpha = \beta > 2$ as a consequence of the Jordan-Wigner mapping.

Therefore, one expects a qualitative understanding of the Hamiltonian (61) to result from the mapping of the spin operators $\sigma_j^{\{x,y,z\}}$ onto fermions (Jaschke *et al.*, 2017; Vanderstraeten *et al.*, 2018)

$$\sigma_j^z = 1 - 2c_j^\dagger c_j, \quad (62)$$

$$\sigma_j^y = -i \left[\prod_{m=1}^{j-1} (1 - 2c_m^\dagger c_m) \right] (c_j - c_j^\dagger), \quad (63)$$

$$\sigma_j^x = - \left[\prod_{m=1}^{j-1} (1 - 2c_m^\dagger c_m) \right] (c_j + c_j^\dagger), \quad (64)$$

where the fermionic annihilation and creation operators are represented, respectively, by c_j and c_j^\dagger and, according to the canonical anticommutation relations, one has $\{c_l, c_j\} = 0$ and $\{c_l, c_j^\dagger\} = \delta_{l,j}$. Note that the Jordan-Wigner transformation is highly nonlocal and, despite preserving the excitation spectrum of the system, yields radically different eigenstates and

topological properties; for a discussion of this topic, see Greiter, Schnells, and Thomale (2014) and references therein.

The fermionic Hamiltonian for the long-range Ising model reads

$$H = -\sum_{l < j} J_{|l-j|} (c_l^\dagger - c_l) \left[\prod_{n=l+1}^{j-1} (1 - 2c_n^\dagger c_n) \right] (c_j^\dagger + c_j) - h \sum_j (1 - 2c_j^\dagger c_j). \quad (65)$$

An exact solution of the Hamiltonian (65) is not possible due to the inclusion of increasingly longer fermionic strings. To introduce a treatable model, valid close to the fully paramagnetic limit, one can employ the following approximation (Jaschke *et al.*, 2017):

$$\prod_{n=l+1}^{j-1} (1 - 2c_n^\dagger c_n) = 1 \quad (66)$$

for every $j \geq l + 2$ and neglect all the nonquadratic string operators on the first line of Eq. (65). The resulting Hamiltonian reads

$$H = -\sum_{l < j} J_{|l-j|} (c_l^\dagger c_j + c_l^\dagger c_j^\dagger - c_l c_j - c_l c_j^\dagger) - h \sum_j (1 - 2c_j^\dagger c_j), \quad (67)$$

which corresponds to the Hamiltonian (45) in the infinite-range limit $R \rightarrow \infty$ with identical hopping and pairing functions, i.e., $g = t$ and $\alpha = \beta$.

In the nearest-neighbor limit, the fermions in the Hamiltonian (67) can be interpreted as domain walls in the spin language. Consistently, long-range interactions introduce an effective nonquadratic coupling between such domain walls, which we have discarded in Eq. (66) (Fradkin, 2013). Since the relevance of the quartic terms of the Hamiltonian (65) crucially depends on the interaction range, it is not surprising that Eq. (66) alters the universal properties of the model, and the Hamiltonian (67) thus does not lie in the same universality class as the long-range Ising model for $\sigma = \alpha - 1 < 2$. The difficulty to reproduce the universal properties of the long-range Ising model at small α with the purely fermionic Hamiltonian can also be understood via an effective dimension argument.

According to Eq. (37), the long-range Ising model displays the effective dimension $d_{\text{eff}} = 1$ for $\alpha > 3$, and therefore it is not surprising that the universal properties of the fermionic theory in Eq. (67) correspond to those of the interacting theory described by Eq. (36). Conversely, for $\alpha < 5/3$ the effective dimension becomes large ($d_{\text{eff}} > 4$), and the universal features of the effective action in Eq. (36) are exactly captured by the mean-field approximation, which features bosonic excitations and cannot be reduced to the purely fermionic theory in Eq. (67). In the intermediate range ($5/3 < \alpha < 3$) the low-energy excitations possess a hybrid

fermionic-bosonic character that cannot be captured by the purely fermionic Hamiltonian (67).

4. The general $\alpha \neq \beta$ case

In Sec. IV.B.3, we discussed the relation between the universal properties of the Ising model and those of the Kitaev chain with $\alpha = \beta$ and $t = g$. Now we explicitly derive the critical exponents of the Kitaev chain in the general case with $R \propto L$ and

$$J_k = \frac{1}{\zeta(\alpha)} \sum_{r=1}^{\infty} \frac{\cos(kr)}{r^\alpha} = \frac{\text{Re}[\text{Li}_\alpha(e^{ik})]}{2\zeta(\alpha)}, \quad (68)$$

$$\Delta_k = \frac{1}{\zeta(\beta)} \sum_{r=1}^{\infty} \frac{\sin(kr)}{r^\beta} = \frac{\text{Im}[\text{Li}_\beta(e^{ik})]}{2\zeta(\beta)}, \quad (69)$$

which are the momentum range couplings determining the single-particle spectrum in Eq. (55). In analogy with the nearest-neighbor case, the long-range Kitaev chain features two quantum critical points, corresponding to the softening of the $k = 0$ or $k = \pi$ modes. When the Kac-normalized expressions in Eqs. (68) and (69) are employed, the location of the ‘‘homogeneous’’ critical point is fixed at $h_c^h = 1$, regardless of the choice of α or β . Conversely, the $k = \pi$ instability occurs at the α -dependent critical point $h_c^a = 1 - 2^\alpha$. The definition of critical exponents is given by the scaling of the excitation spectrum close to each of these quantum critical points,

$$\lim_{h \rightarrow h_c^a} \omega_k \approx |h - h_c^a|^\nu, \quad k = 0, \pi, \quad (70)$$

$$\lim_{k \rightarrow 0, \pi} \omega_k \approx k^z, \quad h = h_c^c. \quad (71)$$

As in the case of rotor models (see Sec. IV.A), the two exponents z and ν are sufficient to characterize the entire critical scaling.

Following the definitions in Eqs. (70), it is straightforward to verify that $\lim_{k \rightarrow 0} \Delta_k = 0$ and that the critical exponent combination is $z\nu = 1$ for each of the two quantum critical points, regardless of the values of α and β . Determination of the dynamical scaling exponent z close to the h_c^h quantum critical point requires the following expansions of the Fourier couplings close to $k = 0$:

$$J_k = 1 + \sin(\alpha\pi/2) \frac{\Gamma(1-\alpha)}{\zeta(\alpha)} k^{\alpha-1} - \frac{\zeta(\alpha-2)}{2\zeta(\alpha)} k^2 + O(k^3) \quad \text{if } \alpha < 3, \quad (72)$$

$$J_k = 1 + \frac{2 \log(k) - 3}{4\zeta(3)} k^2 + O(k^3) \quad \text{if } \alpha = 3, \quad (73)$$

$$J_k = 1 - \frac{\zeta(\alpha-2)}{2\zeta(\alpha)} k^2 + O(k^{\alpha-1}) \quad \text{if } \alpha > 3, \quad (74)$$

and

$$\Delta_k = \cos(\beta\pi/2) \frac{\Gamma(1-\beta)}{\zeta(\beta)} k^{\beta-1} + \frac{\zeta(\beta-1)}{\zeta(\beta)} k + O(k^3) \quad \text{if } \beta < 2, \quad (75)$$

$$\Delta_k = \frac{6[1 - \log(k)]}{\pi^2} k + O(k^3) \quad \text{if } \beta = 2, \quad (76)$$

$$\Delta_k = \frac{\zeta(\beta-1)}{\zeta(\beta)} k + O(k^{\beta-1}) \quad \text{if } \beta > 2. \quad (77)$$

Apart from their relevance to the present case, Eqs. (72)–(77) display a typical example of anomalous terms in the excitation spectrum generated by long-range interactions. A close inspection of Eqs. (72)–(77) leads to the following result for the equilibrium dynamical critical exponent:

$$z = \begin{cases} \phi - 1 & \text{if } \phi < 2, \\ 1 & \text{if } \phi > 2, \end{cases} \quad (78)$$

where $\phi = \min(\alpha, \beta)$. According to the result in Eq. (78) the relevant region for long-range couplings in the long-range Kitaev chain radically differs from the case of the $O(\mathcal{N})$ rotor model described in Sec. IV.A. Indeed, long-range interactions in the Kitaev chain also remain irrelevant in the range $2 < \alpha, \beta < 3$, while long-range couplings in rotor models would be relevant in the entire $\alpha < 3$ region. Yet, even if long-range hopping couplings with $2 < \alpha < 3$ do not alter the critical behavior, they still introduce relevant momentum terms in the hopping sector. This discrepancy yields further evidence that the approximation in Eq. (66) crucially alters the universal behavior at small α and β .

For the forthcoming discussion, it is crucial to notice that long-range interactions with different power-law exponents $\alpha \neq \beta$ modify the influence of the hopping and pairing term on the critical scaling. Indeed, while for short-range interactions the dynamical critical scaling exponents are determined by the low-momentum terms in the pairing coupling, for relevant long-range interactions with $\alpha < \beta$ it is the scaling of the hopping coupling that determines z . A similar scenario may also occur for finite-range competing interactions and it is known to cause peculiar dynamical features (Deng, Ortiz, and Viola, 2009; Defenu *et al.*, 2019; Divakaran *et al.*, 2009), which is discussed in Sec. V.C.1.

In summary, this section has delineated the equilibrium critical properties of quadratic fermionic systems, with a power-law decaying coupling of different decay rates. Yet, the same characterization cannot be provided in the case of fermionic systems with long-range nonquadratic interactions, such as

$$H = \sum_{\langle ij \rangle, s} (c_{i,s}^\dagger c_{j,s} + \text{H.c.}) + \sum_{i \neq j} V_{ij} n_i n_j, \quad (79)$$

where the $c_{i,s}^\dagger$ operator and its conjugate create and annihilate a fermion with spin s on the i th site of the lattice, while n_i represents the total density operator on the same site.

Our understanding of the influence of long-range density-density interactions on the critical behavior of Fermi systems is still relatively incomplete. One notable counterexample is the 1D case, where mapping of fermionic systems onto bosonic or spin degrees of freedom is possible.

In particular, the ground state of continuous 1D fermions interacting via unscreened Coulomb repulsion was characterized by bosonization techniques, finding metallic features and a classical Wigner-crystal phase with slow-decaying charge correlations (Schulz, 1993; Wang, Millis, and Das Sarma, 2001). Numerical confirmation of this theoretical picture has been provided by density matrix renormalization group (DMRG) (Fano *et al.*, 1999) and variational MC methods (Casula, Sorella, and Senatore, 2006; Astrakharchik and Girardeau, 2011; Lee and Drummond, 2011). The corresponding lattice systems with commensurate filling have been numerically shown to display an insulating ground state, still of Wigner-crystal character, in contradiction with the bosonization picture in the continuum (Poilblanc *et al.*, 1997; Capponi, Poilblanc, and Giamarchi, 2000).

C. XXZ models

The Hamiltonian of the long-range XXZ spin chain reads

$$H = \sum_{i>j} J_{ij} (-\sigma_i^x \sigma_j^x - \sigma_i^y \sigma_j^y + \sigma_i^z \sigma_j^z), \quad (80)$$

where $J_{ij} \approx r_{ij}^{-\alpha}$ refers to the usual long-range couplings. Notice that in Eq. (80) all the couplings x - x , y - y , and z - z directions actually corresponds to having hard-core bosons with long-range density-density interactions; see Sec. IV.D for more details.

Conventionally, the solution in the $\alpha \rightarrow \infty$ limit is obtained through (Abelian) bosonization, showing that the universal properties of the spin Hamiltonian (80) are exactly described by the effective action of the quantum sine-Gordon model, which also describes the universality of $O(2)$ quantum rotors (Sachdev, 1999; Giamarchi, 2004; Fradkin, 2013).

However, such a mapping is not possible in the presence of long-range couplings. Nevertheless, one can split the Hamiltonian into long-range and short-range contributions and then consider the long-range couplings only as a perturbation of the short-range action (Maghrebi, Gong, and Gorshkov, 2017); see also Bermudez *et al.* (2017). As a result, one can consider the low-energy action

$$S[\theta] = \frac{K}{2\pi u} \int d\tau dx \{ (\partial_\tau \theta)^2 + u^2 (\partial_x \theta)^2 \} - g \int d\tau \int dx dy \frac{\cos[\theta(\tau, x) - \theta(\tau, y)]}{|x - y|^\alpha}, \quad (81)$$

where K is the so-called Luttinger parameter, u is a velocity scale, and g is proportional to the strength of the long-range interactions.

The final picture obtained for the critical behavior of the action in Eq. (81) is analogous to that discussed for the 2D XY classical case at finite temperature. In fact, one can define the

shifted decay exponent $\sigma = \alpha - d = \alpha - 1$ and derive the flow equations

$$\begin{aligned} \frac{dy_k}{dt} &= -(2 - 4K)y_k, \\ \frac{d\tilde{g}_k}{dt} &= -\left(2 - \sigma - \frac{1}{2K}\right)\tilde{g}_k, \end{aligned} \quad (82)$$

where y_k is the fugacity of topological excitations and \tilde{g}_k is the dimensionless long-range coupling; see the discussion in Sec. III.A.2. The phase diagram resulting from Eqs. (82) follows in close analogy the one obtained in the classical case; see Sec. III.A.2 and [Giachetti, Trombettoni *et al.* \(2022\)](#).

As long as $\sigma > 2$, long-range interactions are irrelevant and the system displays universal BKT scaling. Conversely, for $\sigma < 2$ a new phase emerges at large enough K , where the long-range RG coupling \tilde{g} grows indefinitely. As a consequence, a finite order parameter appears in the x - y plane $\langle \sigma^+ \rangle \neq 0$ and the system undergoes spontaneous symmetry breaking. Evidence of this quasicorder to true-order transition was found in a numerical DMRG calculation. Indeed, computing the effective central charge of the model, [Maghrebi, Gong, and Gorshkov \(2017\)](#) were able to show that this quantity changes from $c_{\text{eff}} = c = 1$, which is typical of the isotropic short-range sine-Gordon model ([Mussardo, 2009](#)), to $c_{\text{eff}} > 1$ at $\sigma < 2$. This change in the effective central charge is compatible with the appearance of a new phase with broken Lorentzian symmetry ([Maghrebi, Gong, and Gorshkov, 2017](#)). Correspondingly, the dynamical critical exponents deviate from unity and acquire the expected value for anisotropic long-range field theories $z = \sigma/2$. Including the renormalization of the Luttinger parameter does not alter the aforementioned picture. The half-chain entanglement entropy scaling features an anomalous $\propto \log(L)$ contribution in the ordered phase caused by the Goldstone mode ([Frérot, Naldesi, and Roscilde, 2017](#)).

Making a characterization of the long-distance correlation functions, [Maghrebi, Gong, and Gorshkov \(2017\)](#) showed that the ordered phase displays a finite correlation length ξ that diverges exponentially as the critical point with the quasicordered phase is reached. This exponential divergence is reminiscent of the behavior of the correlation length at the BKT transition ([Fradkin, 2013](#)).

D. Hard-core bosons in one dimension

In the section on the Kitaev chain, we discussed the possibility of also recovering the homogeneous critical point of the Kitaev chain for $\alpha, \beta < 1$ by explicitly introducing Kac rescaling, which is at variance with existing studies ([Vodola *et al.*, 2014](#)). In this section, we review results on this matter by explicitly showing that implementing (or not implementing) the Kac rescaling may significantly alter the equilibrium phase diagram of a long-range interacting quantum model.

Restricting our analysis to the one-dimensional case, we can relate the findings discussed in Sec. IV.C to the study of hard-core bosons with arbitrary power-law interactions. The Hamiltonian under consideration reads

$$H = -t \sum_{i=1}^L (c_i^\dagger c_{i+1} + \text{H.c.}) + \sum_{i>j} V_{ij}^{(\alpha)} n_i n_j, \quad (83)$$

with the power-law decaying potential including Kac rescaling

$$V_{|i-j|}^{(\alpha)} = \frac{1}{\mathcal{N}_\alpha} \frac{V}{d_{i-j}^\alpha} V > 0. \quad (84)$$

As in the Kitaev chain study presented in Sec. IV.B, owing to the quantum nature of the system one can choose to implement or not implement Kac rescaling according to the physical situation; see Eq. (47). DRMg simulations have been performed on the Hamiltonian (83) to characterize the phase of the system. In particular, from the energy of the N particles ground state $E_0(n)$ one can define the single-particle gap

$$\Delta(n) = E_0(n+1) + E_0(n-1) - 2E_0(n), \quad (85)$$

which displays radically different behaviors, depending on the implementation (or nonimplementation) of the Kac rescaling, as the numerical results reported in Fig. 13 indicate.

In particular, the numerical simulations in the absence of Kac rescaling predict a finite single-particle gap in the thermodynamic limit, which is consistent with an insulating phase for all values of the interaction coupling V of the potential in Eq. (84). This scenario has been first evidenced by [Capponi, Poilblanc, and Giamarchi \(2000\)](#) for $\alpha = 1$ and then confirmed, in the general α case, by the simulations presented by [Botzung *et al.* \(2021\)](#). Conversely, the implementation of

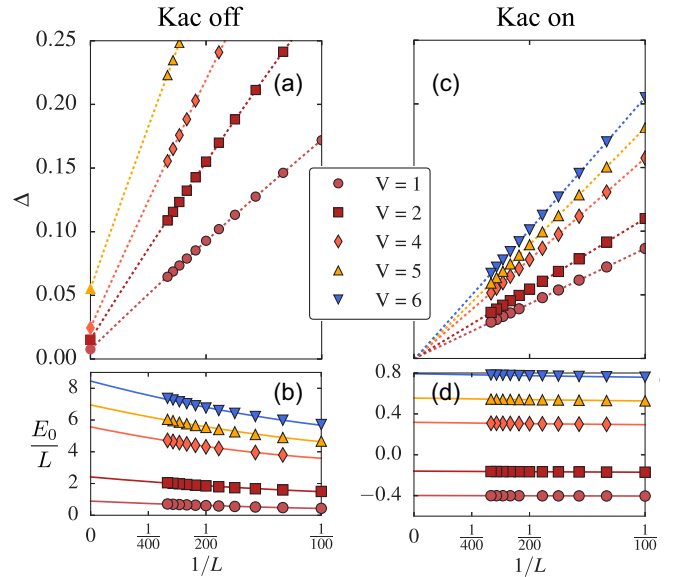


FIG. 13. Comparison of Kac-on and Kac-off finite-size scalings for hard-core bosons. The scaling of the boson single-particle energy, as defined in Eq. (85), is displayed as a function of the system size. The results have been obtained via a DRMg computation at half filling $\langle n_i \rangle = 0.5$ for $\alpha = 1$ and different interaction strengths V (in units of the hopping energy t). The difference between the Kac scaled or unscaled scenario is evident, as in the first case the single-particle energy always vanishes in the thermodynamic limit, while in the second case the system remains gapped up to the thermodynamic limit. Adapted from [Botzung *et al.*, 2021](#).

Kac rescaling induces metallic behavior in the entire range $0 \leq \alpha < 1$, regardless of the interaction coupling $V > 0$. This proves that the restoration of extensive interaction energy significantly alters the phase diagram of the Hamiltonian (83).

Theoretical understanding of the discrepancy between the scaled and unscaled theories can be obtained via the Luttinger-liquid theory (Giamarchi, 2004), which reduces the universal behavior of the Hamiltonian (83) to that of the continuous action

$$H_{LL} = \frac{u}{2\pi} \int dx \left\{ K(\pi\Pi)^2 + \frac{(\partial_x\varphi)^2}{K} - \frac{g}{\pi} \cos(4\varphi) \right\}, \quad (86)$$

where the parameters u and K depend on the Fermi velocity v_F and wave vector k_F according to

$$uK = v_F, \quad (87)$$

$$\frac{u}{K} = v_F + \frac{1}{\pi} \sum_{r=1}^L V_r^{(\alpha)} [1 - \cos(k_F r)]. \quad (88)$$

It is straightforward to show that the universal physics of the Luttinger-liquid Hamiltonian (86) is the same as that of the sine-Gordon model (Malard, 2013), featuring an infinite-order transition between a line of free fixed points with power-law bosonic correlations $\langle a_i^\dagger a_j \rangle = |i - j|^{-1/2K}$ and a massive phase with exponential correlations. Therefore, the free field theory phase corresponds to the metallic phase of the Hamiltonian (83). One can show that g is given by

$$g = \sum_{r=1}^L V_r^{(\alpha)} \cos(2k_F r) \quad (89)$$

and that the metallic phase breaks down beyond the critical coupling strength K_c , which at half filling corresponds to $K_c = 1/2$ when multiple umklapp processes are neglected. In the nearest-neighbor limit $\alpha \rightarrow \infty$ this scenario describes the metal-insulator transition appearing at $V_c = 2t$. This transition lies in the BKT universality, and the breakdown of the metallic phase is akin to vortex proliferation in the physics of the 2D XY model.

For $\alpha > 1$ the introduction of Kac rescaling does not influence the physics and the picture does not change, apart from obvious changes in the value of the critical interaction strength. On the other hand, the aforementioned universal picture is broken as soon as $\alpha = 1$ since, in the absence of Kac rescaling, the first term in the summation of Eq. (88) diverges in the thermodynamic limit $\sum_r V_r^1 \sim \log(L)$, leading to a vanishing K coupling. At the same time, the interaction coupling remains finite due to the alternating sign in Eq. (89), and therefore the system lingers in the insulating phase, as verified with numerical computations (Capponi, Poilblanc, and Giamarchi, 2000; Botzung *et al.*, 2021).

The situation is reversed by the introduction of Kac rescaling, which imposes convergence on the first summation of Eq. (88), regardless of the α value, while it makes the interaction coupling vanish identically. It does not come as a surprise, then, that the Kac scaled systems always lie in the

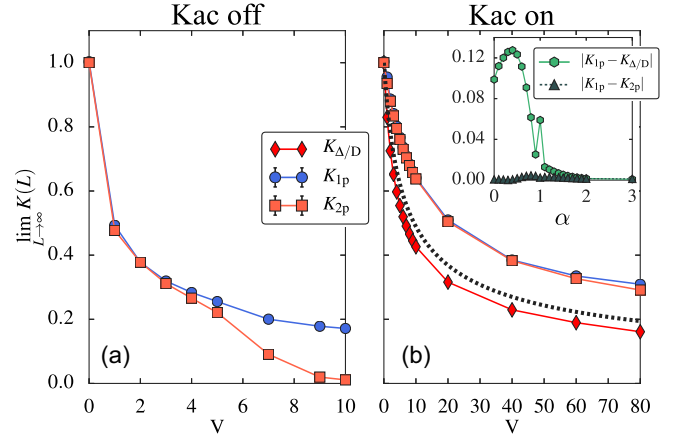


FIG. 14. Luttinger parameter. Thermodynamic limit extrapolation of the Luttinger parameter K given as a function of the long-range interaction strength V at half filling in the case $\alpha = 0.5$ (the same scenario has been obtained for several α values in the range $0 < \alpha < 1$). The three different definitions for the Luttinger parameter have been compared in both the (a) Kac unscaled and (b) Kac scaled cases (Botzung *et al.*, 2021). As a function of α , given a fixed value of the interaction [$V = 1.5$ in the inset of (b)], there is no discrepancy between the Luttinger parameter obtained using a correlation function $K_{1p} = K_{2p}$, confirming the metallic character of the system. Still the conventional Luttinger-liquid theory is not obeyed since the Luttinger parameter does not fit the gap scaling K_{Δ} . As seen in the inset of (b), the traditional Luttinger-liquid picture is recovered for $\alpha > 1$.

metallic phase. While the Luttinger-liquid theory can reproduce the metallic (insulator) character in the presence (absence) of Kac's rescaling, the actual features of the phase in both cases are not completely consistent with the continuous theory prediction. Indeed, the comparison between the numerical values for the K coupling obtained by the single-particle correlation functions (K_{1p}), the structure factor (K_{2p}), and the finite-size scaling of the gap ($K_{\Delta} = \partial\Delta/\partial L^{-1}$) (Kohn, 1964) do not match each other and especially do not match the prediction of Luttinger-liquid theory in the Kac rescaled case; see Fig. 14. Therefore, both the metallic and insulating phases at $\alpha < 1$ fail to obey Luttinger-liquid theory (Botzung *et al.*, 2021). Note that this picture does not apply to the flat interaction case $\alpha = 0$, which is analytically solvable and can be treated separately (Botzung *et al.*, 2021).

E. Soft-core interactions

In this section, we discuss the case of nonlocal interactions while also addressing cases of competing interactions relevant for some of the previously introduced physical systems. Given the rich variety of physical behaviors in these systems, we do not attempt to cover all the phenomena. Rather, after an introduction we focus on two main classes of applications: the clustering phenomena induced by typical nonlocal interactions and the structural phase transitions occurring in mesoscopic long-range interactions.

The phase structure of ensembles of particles interacting via nonlocal potentials diverging at the origin has been

extensively studied in the last few decades both in the classical and more recently in the quantum regime (Likos, 2001). A major problem concerns the study of freezing transitions and the respective crystal structure, which depends on the steepness of the potential, the dimensionality, and the details of the external trapping. At the classical level, power-law diverging potentials of the form $V(r) = \varepsilon(\sigma/r)^\alpha$, where $\varepsilon > 0$ is an energy scale, σ has the dimension of a length, and r is the interparticle distance, result in the formation of a crystalline state at arbitrarily high temperatures. Moreover, one can show that to ensure the stability against explosion (infinite thermodynamic observables, such as the energy per particle or pressure) one has to impose $\alpha > d$ (Weeks, 1981), with d the system dimensionality, i.e., to be in the weak long-range or short-range regime. If this condition is violated, i.e., $\alpha \leq d$, a neutralizing background could be introduced to stabilize one-component systems such as the one-component plasma (Baus and Hansen, 1980). Both Kac rescaling and the introduction of a neutralizing background can be used to perform calculations and regularize physical quantities, but note that, while Kac rescaling preserves the functional power-law form of the interactions, a neutralizing background may introduce screening effects for charged systems. The study of quantum systems with density-density power-law interactions without an intrinsic length scale provides a quantum counterpart of these results holding for classical systems, and it was subsequently investigated (Büchler *et al.*, 2007; Dalmonte, Pupillo, and Zoller, 2010; Pupillo *et al.*, 2010).

Another interesting class of interactions is the one that does not diverge at the origin; i.e., it is bounded. In soft-matter physics, these soft-core potentials arise as effective interactions between the centers of mass of soft, flexible macromolecules such as polymer chains, dendrimers, polyelectrolytes, etc. Indeed, the centers of mass of two macromolecules can coincide without violation of the excluded volume conditions, hence bringing about a bounded interaction (Likos *et al.*, 2007). A relevant consequence of the removal of the on-site divergence is the possibility of overlapping particles, which under certain conditions can lead to clustering. A rigorous criterion holding for a fluid at sufficiently high densities states that a nonattractive and bounded pair potential should satisfy the following requirements: (i) it is bounded, (ii) it is positive definite, (iii) it decays fast enough to zero at large separations that it is integrable and its Fourier transform exists, and (iv) it is free of attractive parts, i.e., it does not display clustering. Otherwise, if the Fourier transform of the pair potential has a negative value for a finite momentum k_m , then the system can freeze into clustered crystals with multiple occupied sites with an intercluster distance $\propto 1/k_m$ (Likos *et al.*, 2001). An intuitive way to understand such a criterion is via the high-density limit of the structure factor $S(k)$ of a fluid, which is a measure of the susceptibility of the system to a spontaneous spatial modulation having wave number k . Within the framework of the fluctuation-dissipation theorem, $S(k)$ appears to be a proportionality factor between a weak external potential of wave number k and the associated linear density response. Employing the Ornstein-Zernike relation (Chaikin and Lubensky, 1995; Hansen and McDonald, 2013), one finds that in the high-density limit the structure factor is given by

$$S(\mathbf{k}) = \frac{1}{1 + \rho\beta V(\mathbf{k})}, \quad (90)$$

where $V(\mathbf{k})$ is the Fourier transform of the potential and ρ is the system density. Hence, a structure factor with a high peak at some wave number k_m is a signal of an incipient transition of the fluid to a spatially modulated system, i.e., a crystal. Recently Mendoza-Coto, Cenci *et al.* (2021) presented a sufficient criterion for the emergence of cluster phases with low filling (up to two particles per cluster) in an ensemble of interacting classical particles with generic (also diverging at the origin) repulsive two-body interactions in the classical zero-temperature limit valid at intermediate densities. The basis of the criterion is a zero-temperature comparison of the energy imbalance between the single-particle lattice and the first cluster-crystal configuration at small density obtained by the use of the Fourier transform of a regularized version of the potential. It determines the relevant characteristics of the interaction potential that make the energy of a two-particle cluster-crystal become smaller than that of a simple triangular lattice in two dimensions. See also Díaz-Méndez *et al.* (2017) for an application to the formation of a vortex glass in clean systems of thin films of “type-1.5” superconductors.

In the quantum regime, it is possible to provide a connection between the emergence of a structural transition to the structure factor $S(k)$ via an analysis of the spectrum of elementary excitation through the Feynman-Bijl relation (Feynman, 1954) $S(\mathbf{k}) = \hbar^2 k^2 / 2m\varepsilon(\mathbf{k})$, where $\varepsilon(\mathbf{k})$ is the energy of excitations at momentum \mathbf{k} . A peak at finite momentum \mathbf{k} of $S(\mathbf{k})$ is associated with the presence of a roton minimum in the spectrum $\varepsilon(\mathbf{k})$. Eventually upon softening of the roton minimum the system enters the roton instability. This connection has been realized in experiments; see O’Dell *et al.* (2000), O’Dell, Giovanazzi, and Kurizki (2003), Santos, Shlyapnikov, and Lewenstein (2003), Mottl *et al.* (2012), Chomaz *et al.* (2018), and Hertkorn *et al.* (2021).

Dilute quantum gases can feature long-range interactions if the constituent particles have (i) a strong magnetic dipole moment, (ii) a strong permanent electric dipole moment as in polar molecules, or (iii) an induced electric dipole moment as in Rydberg atoms or cavity-mediated systems. Specifically, quantum gases of atoms with strong magnetic dipole moments have been extensively employed as an experimental platform to detect the relation between the microscopic long-range interactions and the low-energy excitation spectra (Bismut *et al.*, 2012) and to study crystallization in a quantum many-body setting (Lahaye *et al.*, 2009; Trefzger *et al.*, 2011; Baranov *et al.*, 2012; Böttcher *et al.*, 2020). The interplay among the collisional contact interactions, the magnetic dipolar interaction, and repulsive quantum fluctuations (Lima and Pelster, 2011) can give rise to the stabilization of droplets (Chomaz *et al.*, 2016) or the formation of a supersolid phase if the droplets share phase coherence in the ground state (Tanzi, Lucioni *et al.*, 2019; Böttcher *et al.*, 2021; Norcia *et al.*, 2021; Sohmen *et al.*, 2021; Tanzi *et al.*, 2021), or to a rich set of patterns out of equilibrium (Parker *et al.*, 2009). An interesting case is provided by doubly dipolar systems, magnetic and electric, which may display dimensional cross-over in the droplet phase, in the absence of an external

confinement potential (Mishra, Santos, and Nath, 2020). For sufficiently strong interactions dipolar systems display a roton instability that triggers the phase transition to a dipolar supersolid and arrays of isolated quantum droplets (Baillie *et al.*, 2016; Baillie and Blakie, 2018) or filaments in three dimensions (Cinti *et al.*, 2017). A similar phenomenology of self-organized ground-state density modulations was predicted for a BEC illuminated by a single, circularly polarized laser beam in the weak saturation limit by Giovanazzi, O’Dell, and Kurizki (2002). The appearance of a structural transition via a softening of the roton minimum has also been extensively studied in the context of Rydberg-dressed systems where an intrinsic soft-core potential can be engineered via laser coupling to highly excited electronic states. In the following we focus on results both in the continuum and on a lattice, leading to pattern formation in the presence of soft-core pairwise interactions.

1. Quantum phases

We start by considering a system of N bosons interacting via two-body soft-core potentials of the type

$$V(r) = \frac{V_0}{r^\alpha + R_c^\alpha}, \quad (91)$$

where R_c is a characteristic length of the pair potential. While the considered interaction does not straightforwardly occur in natural crystals, it can be designed in ultracold atom experiments. As commented in Sec. II.C soft-core interactions of the type described by Eq. (91) can be realized with Rydberg-dressed atoms where $\alpha = 6$, for which the Hamiltonian provides a prototype system for addressing the general physical picture. In general, this interaction approaches a constant value V_0/R^α as the interparticle distance r decreases below the soft-core distance R_c and drops to zero for $r \gg R_c$. The limiting case $\alpha \rightarrow \infty$ yields the soft-disk model (Pomeau and Rica, 1994), while $\alpha = 3$ and 6 correspond to soft-core dipole-dipole (Cinti *et al.*, 2010) and van der Waals interactions (Henkel, Nath, and Pohl, 2010; Henkel *et al.*, 2012) that can be realized with ultracold atoms (Maucher *et al.*, 2011) or polar molecules (Büchler *et al.*, 2007; Micheli *et al.*, 2007).

The mean-field analysis of the structure factor suggests the occurrence of spontaneous symmetry breaking at zero temperature in the form of a cluster-crystal phase that occurs at sufficiently high densities. According to dimensional analysis, this phase should remain stable in dimensions $d > 1$. Moreover, owing to the bosonic symmetry of this single-component system, in a certain parameter interval of the phase diagram one might expect the system to display both crystalline and superfluid properties, i.e., the simultaneous breaking of continuous translational and global gauge symmetry, a supersolid state. The first mention of such a state goes back to Gross (1957), who presented a theory for a density-modulated superfluid emerging from a mean-field model for solid helium. A microscopic picture of supersolidity was proposed by Andreev, Lifshitz, and Chester (ALC) (Andreev and Lifshitz, 1969) and is based on the following two key assumptions: (i) that the ground state of a bosonic crystal

contains defects such as vacancies and interstitials and (ii) that these defects can delocalize, thereby giving rise to superfluidity. For a review on the subject and the debate on the observation of this phase in solid helium, see Boninsegni and Prokof’ev (2012). For a more recent discussion of the observation of supersolid phases in dipolar systems in both quasi-one-dimensional and quasi-two-dimensional setups, see the review by Böttcher *et al.* (2021).

Soft-core potentials for hard-core bosons or spinless fermions on 1D lattice systems described by the Hamiltonian

$$H = -t \sum_{\langle i,j \rangle} b_i^\dagger b_j + V \sum_{i < j; r_{ij} < r_c} n_i n_j, \quad (92)$$

where b_i (b_i^\dagger) are hard-core bosonic annihilation (creation) operators localized on site i and $n_i = b_i^\dagger b_i$ is the density in i , lead to correlated quantum liquid phases that do not fall into the conventional Luttinger-liquid paradigm. Characteristic features of these anomalous cluster Luttinger liquids (CLLs) include a deformation of the critical surface in momentum space and are evident in correlation functions such as momentum distributions and structure factors (Mattioli *et al.*, 2013; Dalmonte *et al.*, 2015) using DMRG and bosonization techniques. Recently the spinful Fermi-Hubbard model with both on-site interactions and soft-core (density-density) interactions was investigated (Botzung *et al.*, 2019), generalizing the Fermi-Hubbard model with a soft-core radius equal to a lattice site studied by Nakamura (2000). It displays different types of CLLs and a nontrivial supersymmetric critical line. The continuum version of this model was studied by Rossotti *et al.* (2017), which showed evidence of the CLLs via exact quantum Monte Carlo simulations. The phase diagram of one-dimensional soft-core bosons is shown in Fig. 15(a), together with the excitation spectrum in Fig. 15(b). The acoustic mode of the CLL phase [Figs. 15(a) and 15(b)] is gapless at $q = q_c$, corresponding to k_F at this density. Above the transition line, located (with $t = 1$) at $U = U_c = 18$ [Fig. 15(b), left panel], this lowest excitation turns into the rotonic mode [Fig. 15(b), center and right panels]. A weaker secondary mode also appears in the strongly correlated liquid phase, in the form of a secondary roton. This secondary excitation in the Luttinger-liquid phase can be linked to incipient cluster formation due to particles being preferentially localized close to either the left or the right neighbor. The gap of both such Luttinger-liquid excitations and the anharmonic optical modes of the CLL phase vanish at the transition.

In the higher-dimensional case in the continuum, a good description is provided by a mean-field treatment (Pomeau and Rica, 1994; Henkel, Nath, and Pohl, 2010; Macrì *et al.*, 2013), which is justified by the application of the first Born approximation to the two-body scattering problem for the interaction potential in Eq. (91) (Cinti *et al.*, 2014). In mean-field theory the system dynamics is described by a nonlocal Gross-Pitaevskii equation (GPE) that reads

$$i\partial_t \psi(\mathbf{r}, t) = \left(-\frac{\nabla^2}{2} + \gamma \int d\mathbf{r}' U(\mathbf{r} - \mathbf{r}') |\psi(\mathbf{r}', t)|^2 \right) \psi(\mathbf{r}, t), \quad (93)$$

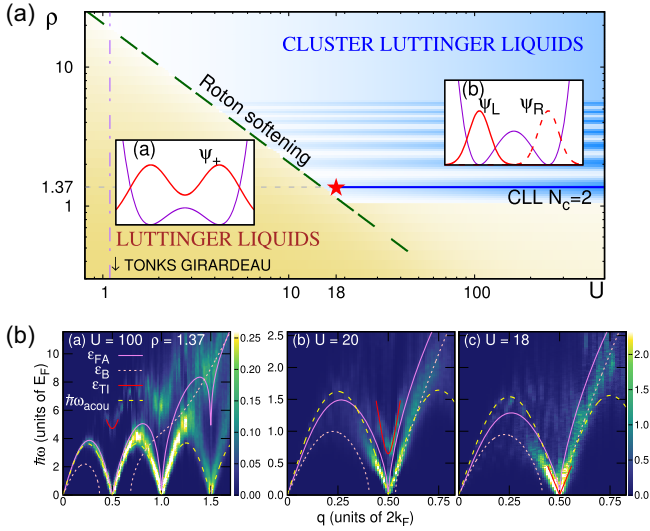


FIG. 15. Zero-temperature phase diagram of one-dimensional soft-core bosons in the continuum and their excitation spectrum. (a) Phase diagram of one-dimensional soft-core bosons (log-log scale). A star marks the critical point between the Luttinger-liquid and CLL phases for densities commensurate with two-particle clusters. The long-dashed line corresponds to the softening of the Bogoliubov roton. (b) Spectra at $\rho = 1.37$ with decreasing U , compared to Feynman (ϵ_{FA} , thin solid lines) and Bogoliubov approximations (ϵ_B , dotted lines), and the harmonic chain acoustic mode ω_{acou} (dashed lines). At $q \approx q_c$, the secondary mode is fitted by the transverse Ising spectrum ϵ_{TI} (thick solid). Adapted from [Rossotti *et al.*, 2017](#).

where $\mathbf{r} \rightarrow \mathbf{r}/R_c$, $U(\mathbf{r}) = U_0/(1+r^6)$, and $\gamma = mnU_0/(\hbar^2 R_c^2)$ is a dimensionless interaction strength that determines the ground-state properties and the excitation dynamics. Equation (93) has been reported in reduced density units, which are employed hereafter. The energy can be derived from the GPE energy functional

$$H[\psi_0] = \int d\mathbf{r} \frac{1}{2} |\nabla \psi_0|^2 + \frac{\gamma}{2} \int d\mathbf{r} d\mathbf{r}' |\psi_0(\mathbf{r})|^2 U(\mathbf{r}-\mathbf{r}') |\psi_0(\mathbf{r}')|^2. \quad (94)$$

To numerically determine the location of the transition from a uniform to a modulated ground state, one can first expand the wave function $\psi_0(\mathbf{r})$ in Fourier series as

$$\psi_0(\mathbf{r}) = \sum_{\mathbf{Q}} C_{\mathbf{Q}} e^{i\mathbf{Q}\cdot\mathbf{r}}, \quad (95)$$

where $\mathbf{Q} = n\mathbf{b}_1 + m\mathbf{b}_2$, n and m are integers, and $\mathbf{b}_1 = (2\pi/a)(1, -1/\sqrt{3})$ and $\mathbf{b}_2 = (2\pi/a)(0, 2/\sqrt{3})$ are the reciprocal lattice basis vectors of a triangular lattice in two dimensions. One can then substitute Eq. (95) into Eq. (93) and iteratively solve the nonlinear equations for $C_{\mathbf{Q}}$ until convergence is reached ([Kunimi and Kato, 2012](#)). This procedure allows the optimal lattice spacing, the chemical potential, and the coefficients $C_{\mathbf{Q}}$ to be determined. One finds that for low interaction strengths ($\gamma \lesssim 28$) the ground state of the system is in a uniform superfluid phase. Upon increasing the interaction at $\gamma \approx 28$ one crosses a first-order phase transition to a cluster

supersolid phase characterized by a finite superfluid fraction and broken translational invariance where particles arrange in clusters (each cluster contains an average number of particles according to the density) in a triangular geometry. For even larger interactions ($\gamma \gtrsim 38$) the ground state preserves triangular symmetry but superfluidity vanishes, resulting in an uncorrelated cluster crystal.

The validity of the previously mentioned mean-field theory is limited to the regime of high densities, where the depletion of the condensate remains small in a wide range of interaction strengths. At lower densities, one has to resort to *ab initio* methods to deal with the development of nontrivial correlations. Numerical results were obtained from path-integral Monte Carlo (PIMC) simulations ([Ceperley, 1995](#)) based on the continuous-space worm algorithm ([Boninsegni, Prokof'ev, and Svistunov, 2006](#)) to determine the equilibrium properties of the system in the canonical ensemble, that is, at a fixed temperature T and a fixed particle number (of the order of a few hundred). The properties of the system ground state are obtained by extrapolating observables, such as the total energy, superfluid fraction, and pair correlations to the zero-temperature limit.

In Fig. 16(a) the zero-temperature phase diagram of two-dimensional soft-core bosons in continuum space is presented. At small densities $R_c^2 \rho \leq 0.5$ one finds two phases: a superfluid and an insulating triangular crystal composed of singly occupied sites, that is, where the number of lattice sites N_s equals the particle number N . A distinctive consequence of the soft-core interaction is that the energy cost for forming close particle pairs is bound by V_0 . This fact potentially enables the formation of crystalline phases with $N > N_s$ above a critical density where doubly occupied lattice sites become energetically favorable on increasing the lattice constant.

The most interesting behavior takes place around the superfluid-solid quantum phase transition at $N/N_s = 2$. Starting with the insulating solid with doubly occupied lattice sites, removing a small number of particles does not cause structural changes of the ground state but rather creates a small fraction $f_{def} = (2N_s - N)/N_s > 0$ of zero-point crystal defects in the form of singly occupied sites. These defects delocalize and give rise to a finite superfluid fraction, which is in agreement with the ALC scenario. Note that the coexistence of a cluster crystalline structure, breaking translational symmetry in equilibrium, and of particle diffusion is explained here by a thermally activated hopping mechanism, where particles delocalize without altering the underlying cluster crystalline matrix ([Díaz-Méndez *et al.*, 2015](#)).

The extension of this picture to the lattice case is obtained by considering the 2D extended Bose-Hubbard model in the presence of both finite-range soft-core interactions and a hardcore constraint. On the square lattice, this model already displays interesting behavior ([Pupillo *et al.*, 2008](#); [Masella *et al.*, 2019](#)). For intermediate interaction strengths $4 \leq V/t \leq 4.45$ the stripes can turn into a superfluid, thus leading to a self-assembled array of quasi-one-dimensional superfluids. These bosonic superstripes turn into an isotropic supersolid with decreasing interaction strength. Notice that the mechanism for stripe formation is based on cluster self-assembling that differs from recently proposed mechanisms for dipolar

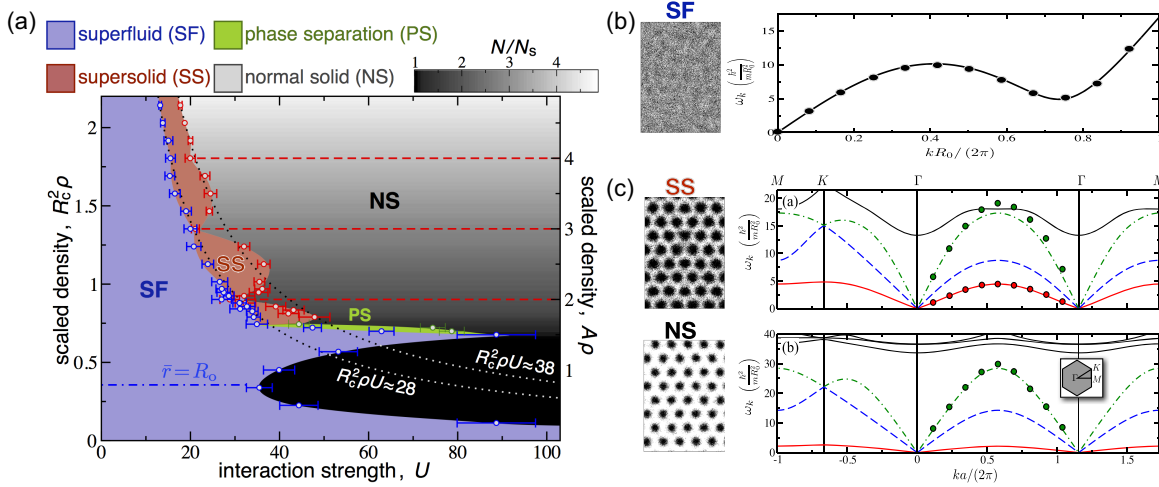


FIG. 16. Two-dimensional soft-core bosons in the continuum and their excitation spectrum. (a) The phase diagram displays the emergence of SF and normal solid (NS) and SS phases for the varying interaction strength U and density ρ . The density on the left y axis was scaled by the soft-core radius R_c . The right axis gives the density in units of the inverse area $A = \sqrt{3}(1.6R_c)^2/2$ of the unit cell of the high-density solid phase, corresponding to the lattice site occupation N/N_s for a given number of particles and lattice sites N and N_s , respectively. For $A\rho \gtrsim 1.5$, the gray region labeled as NS corresponds to a cluster crystal with $N/N_s > 1$, as indicated by the gray scale. The horizontal dashed lines refer to the integer filling. Supersolid phases with different occupation numbers are found between two hyperbolas defined by $R_c^2 \rho U = \text{const}$ (dotted lines). At high densities ($A\rho \gtrsim 3.5$) they can be understood in terms of density-modulated superfluids. In contrast, superfluidity within the low-density supersolid lobes emerges from delocalized zero-point defects according to the ALC scenario. Adapted from Cinti *et al.*, 2014. (b) Left panel: PIMC snapshot illustrating the particle density profile in the SF phase. Right panel: excitation spectrum in the superfluid phase at $\gamma = 11.86$ compared to the PIMC data (circles) of Saccani, Moroni, and Boninsegni (2012). (c) Left panel: PIMC snapshot illustrating the particle density profile in the SS and NS phases. Right panel: mean-field spectra (solid, dashed, and dash-dotted lines) at $\gamma = 16.93$ (top) and $\gamma = 30.62$ (bottom) numerically computed along the three symmetry directions of the Brillouin zone (see the inset of the bottom panel). The symbols represent the PIMC data of Saccani, Moroni, and Boninsegni (2012) for longitudinal excitations computed along the direction Γ - M - Γ in the first two Brillouin zones. (b),(c) Adapted from Macrì *et al.*, 2013.

magnetic atoms (Böttcher *et al.*, 2021), spin-orbit-coupled BECs (Li *et al.*, 2017), or BECs with cavity-mediated interactions (Léonard, Morales, Zupancic, Esslinger, and Donner, 2017). A two-component version of this model in the square lattice was proposed by Li *et al.* (2018). Among the several phases of the model, one can observe that the components that interact via a soft-core potential can induce a supersolid phase in the other component. The out-of-equilibrium dynamics following a temperature quench to values well below the hopping amplitude ($T/t \ll 1$) shows that together with classical solid phases and supersolids (for $3.8 \leq V/t \leq 4.2$) a normal glass is observed (for $V/t > 5.5$) without any remnant superfluidity (Angelone *et al.*, 2020). One observes that in a triangular lattice the same system after a temperature quench displays a superglass and a normal glass phase (Angelone, Mezzacapo, and Pupillo, 2016). At a high enough temperature, the glass and superglass turn into a floating stripe solid and a supersolid, respectively. Similar models of systems with nonlocal interactions diverging at the origin leading to glassy phases were recently investigated in the context of type-1.5 superconductors (W. Wang *et al.*, 2020), where the particles are pointlike vortices in the presence of external disorder. The phase diagram of rotating Rydberg-dressed atoms in magnetic traps was studied by Burrello, Lesanovsky, and Trombettoni (2020), who showed, using the Lindemann criterion, that there is an optimal value of the dressing parameters minimizing the

ratio between the filling factor of the system and its critical value to enter the Hall regime.

The three-dimensional soft-core model was originally investigated by Henkel, Nath, and Pohl (2010) and Ancilotto, Rossi, and Toigo (2013) in the repulsive case and by Maucher *et al.* (2011) in the attractive one within a mean-field approach based on the solution of the 3D GPE of Eq. (93). In the repulsive isotropic case, the ground-state phase diagram displays a transition from a superfluid phase at low density and interactions to a fcc supersolid at intermediate densities that is induced by a roton instability similar to the 2D case. For attractive interactions, one can prove the existence of bright soliton self-bound macroscopic states that are stabilized purely by the competition of kinetic and negative mean-field energies.

2. Elementary excitations

The elementary excitations in the mean-field approximation are found by expanding the GPE energy functional around the solution $\psi_0(\mathbf{r})$, thereby obtaining the so-called Bogoliubov-de Gennes equations (Macrì *et al.*, 2013; Macrì, Saccani, and Cinti, 2014). Denoting the change in $\psi(\mathbf{r}, t)$ by $\delta\psi(\mathbf{r}, t) = e^{-i\mu t}[u(\mathbf{r})e^{-i\omega t} - v^*(\mathbf{r})e^{i\omega t}]$ and substituting this expression into the GPE (93), one finds a set of two coupled linear differential equations for the Bogoliubov amplitudes $u(\mathbf{r})$ and $v(\mathbf{r})$. The solution of the Bogoliubov-de Gennes equations in the uniform superfluid phase is analytical,

$$\epsilon_q = \sqrt{\frac{q^2}{2} \left(\frac{q^2}{2} + 2\gamma U_q \right)}, \quad (96)$$

and depends only on the modulus of the excitation vector \mathbf{q} . In Eq. (96) U_q is the Fourier transform of the potential. Equation (96) can be extended to the case of multibody interactions (Laghi, Macrì, and Trombettoni, 2017). The spectrum is linear for small momenta and the slope defines the sound velocity of the system; for sufficiently large γ (the specific value depends on the shape of the interaction) one recovers the usual roton-maxon spectrum that is common in other physical systems with nonlocal interactions as ultracold dipolar systems or superfluid ^4He . In nonuniform phases, one has to rely on a numerical solution of the Bogoliubov equations. One can use a Fourier expansion of the Bogoliubov amplitudes followed by diagonalization of the corresponding equations. The results presented in Figs. 16(b) and 16(c) are obtained using a grid-based solution in real space for the lowest excitation bands and for \mathbf{q} vectors lying in the first Brillouin zone (Macrì *et al.*, 2013) for a soft-shoulder potential. Figure 16 shows the excitation energies along the three symmetry axes of the Brillouin zone corresponding to the underlying triangular lattice. We find three gapless bands, i.e., three Goldstone modes, reflecting the symmetries that are broken in the supersolid phase (Watanabe and Murayama, 2012, 2013). In addition to the superfluid band due to the breaking of global gauge symmetry, two bands correspond to longitudinal and transverse phonon excitations of the two-dimensional lattice. Even in the insulating phase, Bogoliubov–de Gennes equations yield excellent agreement for the longitudinal phonon mode with quantum Monte Carlo calculations based on the method of genetic inversion, which allows the calculation of the Laplace transform $F(k, \tau) = \int d\omega e^{-\tau\omega} S(k, \omega)$ of the dynamic structure factor (Saccani, Moroni, and Boninsegni, 2012). However, this technique is unable to describe the breakdown of global superfluidity. This indicates that each droplet maintains a high condensate fraction despite the apparent lack of global phase coherence between the crystalline ordered droplets. Proper identification of each band can be made by computing local fluctuations on top of the mean-field solution $\psi_0(r)$. One can distinguish the transverse band from the direction of the fluctuations, which is orthogonal to the perturbing vector k . The contribution of this band to phase fluctuations is strongly suppressed. The first and third bands both contribute to density and phase fluctuations with different weights. The first band is mostly responsible for phase, whereas the third band is mainly responsible for density fluctuations. Therefore, the lower band can be associated with the superfluid response of the system, whereas the other two bands can be associated with the classical collective excitations of the crystal. The results for a Rydberg-dressed potential of Eq. (91) were reported by Macrì, Saccani, and Cinti (2014). They compared the modes obtained by the solution of the Bogoliubov–de Gennes equations to quantum Monte Carlo calculations with the inclusion of the transverse excitation band. Good agreement between the two techniques has been obtained for all three excitation bands. We comment that the calculation and the measurement of the excitation spectra also received significant attention in the context of

dipolar systems, in both trapped superfluid and droplet phases (Baillie, Wilson, and Blakie, 2017; Petter *et al.*, 2019), and in supersolids (Tanzi, Rocuzzo *et al.*, 2019; Petter *et al.*, 2020) in both ground states and excited states (such as in vortices) (Cidrim *et al.*, 2018; Lee *et al.*, 2018; Rocuzzo *et al.*, 2020).

F. Structural transitions in mesoscopic long-range systems

The physics of structural transitions in power-law potentials has been closely studied in prototypical mesoscopic systems of ions and dipolar systems thanks to its close connection to experimental realizations. The simplest one-dimensional case of a chain of singly charged particles confined by a harmonic potential exhibits a sudden transition to a zigzag configuration when the radial potential reaches a critical value, depending on the particle number (Blumel *et al.*, 1988; Birkl, Kassner, and Walther, 1992). For charged particles interacting via the Coulomb potential ($\alpha = 1$), this structural change is a phase transition of second order whose order parameter is the crystal displacement from the chain axis (Schiffer, 1993; Morigi and Fishman, 2004; Piacente *et al.*, 2004; Fishman *et al.*, 2008), as was also experimentally observed (Enzer *et al.*, 2000; Kaufmann *et al.*, 2012). In the quantum limit the universality of the transition lies in the same class as the ferromagnetic Ising chain in a transverse field (Porras and Cirac, 2004; Friedenauer *et al.*, 2008; Shimshoni, Morigi, and Fishman, 2011). The zigzag transition also appears in strongly interacting one-dimensional electrons systems, i.e., quantum wires, whose Wigner-crystal phase corresponds to a splitting of the Fermi gas into two chains (Meyer, Matveev, and Larkin, 2007). The zigzag transition has also been related to the Peierls instability that occurs in antiferromagnetic spin chains coupled to phonon modes (Bermudez and Plenio, 2012).

As the range of the interactions decreases to $\alpha > 2$, the nature of the transition is radically modified due to the coupling between transverse and axial vibrations (Cartarius, Morigi, and Minguzzi, 2014), which leads to a weakly first-order transition in analogy with the case of ferromagnetic transitions in the presence of phonon excitations (Larkin and Pikin, 1969; Imry, 1974). This is particularly relevant to the study of self-organized phases in polar systems (Góral, Santos, and Lewenstein, 2002; Astrakharchik *et al.*, 2007; Büchler *et al.*, 2007). In the case of purely dipolar interactions, detailed QMC calculations at zero temperature investigated the fluid-solid transition (Moroni and Boninsegni, 2014), ruling out the microemulsion scenario for any physical realization of this system, given the exceedingly large predicted size of the bubbles. In higher dimensions crystals of repulsively interacting ions in planar traps form hexagonal lattices and undergo an instability toward a multilayer structure as the transverse trap frequency is reduced. The new structure is composed of three planes, with separation increasing continuously from zero. Mapping to a six-state clock model can be performed, implying that fluctuations split the buckling instability into two thermal transitions, accompanied by the appearance of an intermediate critical phase. A BKT phase is predicted when interfacing the disordered and the ordered phase (Podolsky, 2016).

Another important case is the generalization to the case of multiscale potentials, which was recently studied in the quantum regimes by Cinti and Macrì (2019), Abreu, Cinti, and Macrì (2020), and Pupillo, Zihlerl, and Cinti (2020), which, for specific configurations of the pairwise potential, can support quasicrystalline phases or stripe phases. The corresponding criteria to realize structural phases in these more complex potentials have been investigated (Mendoza-Coto and Stariolo, 2012; Mendoza-Coto, Stariolo, and Nicolao, 2015; Mendoza-Coto, Barci, and Stariolo, 2017; Mendoza-Coto, Nicolao, and Díaz-Méndez, 2019; Mendoza-Coto, Turcati *et al.*, 2021).

Finally, we comment on the presence of smectic, nematic, and hexatic phases in quantum systems with competing non-local interactions, which presents several analogies to the case of classical liquid-crystal systems (Abanov *et al.*, 1995). This parallel, which derives from the similarity between the anisotropic nature of the stripe order and the elongated shape of liquid-crystal molecules, allows the application of traditional results from liquid-crystal systems (de Gennes and Prost, 1993; Chaikin and Lubensky, 1995) to predict the qualitative, and to some extent also quantitative, phase behavior of many systems with modulated order parameters.

In the context of dipolar Fermi gases theory has thus far been ahead of experiments, with several preliminary theoretical calculations predicting exotic scenarios, such as p -wave superfluid (Bruun and Taylor, 2008), supersolid (Lu *et al.*, 2015), hexatic (Bruun and Nelson, 2014; Lechner, Büchler, and Zoller, 2014), and Wigner-crystal phases (Matveeva and Giorgini, 2014). In these systems stripe formation (in the form of charge-density waves) and nematic phases should also occur with features analogous to the ones present in low-temperature long-range solid-state systems.

G. Flat interactions

Systems with flat interactions ($\alpha = 0$) constitute a unique setup in the realm of long-range interactions since they often allow exact analytical solutions of their thermodynamic and critical properties, at least at large scales. Yet, several of their qualitative features exactly reproduce the more complex physics of general strong long-range systems with $0 < \alpha < d$. This role makes such systems worthy of a special focus, and in this section we consider examples of fully connected quantum systems.

1. Lipkin-Meshkov-Glick model

The LMG, one of the most well-known examples of strong long-range interacting model in the quantum realm, was first introduced as a simple test for the validity of perturbative techniques in many-body theories (Glick, Lipkin, and Meshkov, 1965; Lipkin, Meshkov, and Glick, 1965; Meshkov, Glick, and Lipkin, 1965). Subsequently the model was applied to investigating many-body systems, which has allowed for descriptions in terms of mean-field interactions, such as coupled BECs (Cirac *et al.*, 1998) and BCS systems (Dusuel and Vidal, 2005b). The LMG Hamiltonian describes N spin-1/2-coupled flat ferromagnetic interactions of strength J/N as

$$H_{\text{LMG}} = -\frac{J}{N} \sum_{i < j} (\sigma_i^x \sigma_j^x + \gamma \sigma_i^y \sigma_j^y) - h \sum_j \sigma_j^z, \quad (97)$$

where γ is the anisotropy parameter. At $\gamma = 0$, the former Hamiltonian corresponds to the fully connected quantum Ising model in a transverse field.

The key property of any flat interaction problem is the possibility to rephrase it in terms of the collective variable, which is the linear combination of all the microscopic variables. Indeed, in our case one can introduce the collective spin $S_\mu = \sum_{i=1}^N \sigma_i^\mu / 2$, where $\mu \in \{x, y, z\}$. In terms of the new variables Eq. (97) reads

$$H_{\text{LMG}} = -\frac{2J}{N} (S_x^2 + \gamma S_y^2) - 2h S_z + \frac{J}{2} (1 + \gamma), \quad (98)$$

which describes a single self-coupled N -component spin immersed in a magnetic field. The Hamiltonian H_{LMG} preserves both the total spin and the total magnetization values

$$[H_{\text{LMG}}, \mathbf{S}^2] = 0, \quad [H_{\text{LMG}}, S_z] = 0, \quad (99)$$

where $\mathbf{S}^2 = S_x^2 + S_y^2 + S_z^2$. The highly symmetric nature of this model also makes it particularly amenable to numerical techniques, making it a prominent test bed for novel algorithms (Albash and Lidar, 2018; Bapst and Semerjian, 2012). Moreover, it has been used to demonstrate several generic properties of quantum critical points, such as finite-size (Botet, Jullien, and Pfeuty, 1982) and entanglement scaling (Amico *et al.*, 2008; Wichterich, Vidal, and Bose, 2010).

Currently the LMG model is also subject to renewed interest due to its relation with the well-known Dicke model, which is often used to describe driven-dissipative experimental setups, such as the cavity QED experiments outlined in Sec. II.B. Its Hamiltonian contains spin-1/2 operators coupled to the cavity electromagnetic field. In analogy with the long-range Ising model, the Dicke model displays a phase transition between a disordered ground state with $\langle \sigma_x \rangle = \langle a^\dagger a \rangle = 0$ and a superradiant one with polarized spins and a finite photon density inside the cavity $\langle a^\dagger a \rangle \neq 0$ (Dicke, 1954). At equilibrium, it can be rigorously proven that the Hamiltonian of the Dicke and LMG models are equivalent in the thermodynamic limit and then produce the same critical behavior (Gibberd, 1974; Brankov, Zagrebnov, and Tonchev, 1975).

The contribution of quantum fluctuations to the thermodynamic observables is washed away in the large size limit $N \rightarrow \infty$ and the total spin \mathbf{S} effectively becomes classical (Bapst and Semerjian, 2012; Chayes *et al.*, 2008). Therefore, the control parameter for quantum fluctuations in the LMG model is $1/N$, which plays the same role of \hbar in more traditional single-body problems. In the following, we restrict to $h > 1$, as the spectrum of the model is symmetric under inversion $h \rightarrow -h$, and to ferromagnetic interactions $J > 0$. A discussion on the physics of the antiferromagnetic problem $J < 0$ and its relation to the supersymmetric formalism was given by Vidal, Mosseri, and Dukelsky (2004). For ferromagnetic interactions $J > 0$, the ground state always belongs to the maximum spin $S = N/2$ subsector of the Hilbert space.

Apart from the fully isotropic limit $\gamma = 1$, the LMG Hamiltonian cannot be analytically solved (Botet and Jullien, 1983). Nevertheless, the LMG Hamiltonian is integrable and can be solved via an algebraic Bethe ansatz (Pan and Draayer, 1999) or by mapping it to the Richardson-Gaudin Hamiltonian (Dukelsky, Pittel, and Sierra, 2004). Here we follow a simpler route and employ the $1/N$ expansion. We first characterize the critical behavior employing the mean-field approximation using the noninteracting variational ansatz obtained via the external product of the single spin states

$$|\psi_l\rangle = \cos\left(\frac{\theta_l}{2}\right)e^{-i\varphi_l/2}|\uparrow\rangle + \sin\left(\frac{\theta_l}{2}\right)e^{i\varphi_l/2}|\downarrow\rangle. \quad (100)$$

Since the system is translationally invariant, we can assume that $(\theta_l, \varphi_l) = (\theta, \varphi) \forall l$, corresponding to the spin expectation values

$$\mathbf{S} = \frac{N}{2}(\sin\theta\cos\varphi, \sin\theta\sin\varphi, \cos\theta), \quad (101)$$

which coincide with the classical spin value. Owing to the inversion symmetry of the model $S_x \rightarrow -S_x$, one can select $\varphi = 0$ and $J = 1$ without loss of generality. From the energy minimization within the mean-field ansatz, one obtains the explicit expression

$$\theta = \begin{cases} 0 & \text{if } h \geq 1, \\ \arccos(h) & \text{if } 0 \leq h \leq 1 \end{cases} \quad (102)$$

for the angle θ . The semiclassical equations of motion for the total spin operators yield the system gap in the thermodynamic limit (Botet and Jullien, 1983)

$$\Delta = \begin{cases} 2\sqrt{(h-1)(h-\gamma)} & \text{if } h \geq 1, \\ 0 & \text{if } 0 \leq h \leq 1. \end{cases} \quad (103)$$

A close inspection of Eqs. (100)–(103) is all that one needs to comprehend the quantum phase transition in the LMG problem. At $h \geq 1$ only the solution $\varphi = \theta = 0$ exists, and the system is fully magnetized along the magnetic field direction $\langle S_z \rangle = 1$. As h decreases below $h_c = 1$, a two state appears with $\theta \neq 0$ and $\varphi = 0, \pi$ and the in-plane magnetization continuously increases in the interval $[0, 1]$, while the transverse magnetization vanishes only at $h = 0$. Accordingly, the gap Δ between the ground and the first excited state, which is finite at $h > 1$, smoothly vanishes as $h \rightarrow 1^+$ with scaling behavior characterized by the critical exponent $z\nu = 1/2$. Note that the mean-field scenario can be applied only to the thermodynamic limit, while it cannot capture finite-size fluctuations. Indeed, in the ordered phase $h < 1$ the system gap Δ cannot vanish at a finite size, since quantum fluctuations will lift the degeneracy and produce an exponentially vanishing gap $\Delta_N \propto \exp(-N)$ (Newman and Schulman, 1977).

To partially capture finite-size fluctuations, it is convenient to perform the Holstein-Primakoff expansion (Holstein and Primakoff, 1940) for the N -spin variable \mathbf{S} around the mean-field expectation value (Botet and Jullien, 1983; Dusuel and

Vidal, 2005a). One first rotates the total spin in order to align it with the mean-field magnetization, introducing the new variable $\bar{\mathbf{S}} = R(\theta)\mathbf{S}$, with the rotation matrix

$$R(\theta) = \begin{pmatrix} \cos\theta & 0 & \sin\theta \\ 0 & 1 & 0 \\ -\sin\theta & 0 & \cos\theta \end{pmatrix}, \quad (104)$$

where θ is given by Eq. (102). The realigned spin variables can then be expanded using the equivalence

$$\bar{S}_z = \frac{N}{2} - a^\dagger a, \quad (105)$$

$$\bar{S}_+ = \bar{S}_x + i\bar{S}_y = \sqrt{N}\left(1 - \frac{a^\dagger a}{N}\right)^{1/2} a, \quad (106)$$

$$\bar{S}_- = \bar{S}_x - i\bar{S}_y = \sqrt{N}a^\dagger\left(1 - \frac{a^\dagger a}{N}\right)^{1/2}, \quad (107)$$

where the boson operators $[a, a^\dagger] = 1$ have been introduced. This excitation characterizes a small depletion of the mean-field spin expectation due to the finite-size quantum fluctuations. At leading order in $1/N$ only quantum corrections up to order $1/N$ have to be retained, yielding a quadratic bosonic Hamiltonian that can subsequently be diagonalized using a Bogoliubov transformation $a \rightarrow b$ (Dusuel and Vidal, 2005a). The net result is

$$H_{\text{LMG}} = NE_0 + e_0 + \omega b^\dagger b + O\left(\frac{1}{N}\right), \quad (108)$$

such that we have reduced the many-body problem in Eq. (97) to an effective zero-dimensional one that is described by a single harmonic oscillator mode. This is the peculiarity of several fully connected systems: the actual spectrum in the thermodynamic limit is constituted not of a continuum dispersion relation, but rather of a single quantum mode whose contribution to the thermodynamic quantities is increasingly washed out as it approaches the thermodynamic limit.

The quantities appearing in Eq. (108) can easily be written in terms of the internal parameter and the average magnetization $m = 2\langle S_z \rangle/N$. The internal mean-field energy maintains the same form in both the symmetric and broken phases $E_0 = (-1 - 2hm + m^2)/2$, while the next-to-leading energy correction reads

$$e_0 = \begin{cases} -h + (1 + \gamma)/2 + \sqrt{(h-1)(h-\gamma)} & \text{for } h > 1, \\ -(1 - \gamma)/2 + \sqrt{(1-h^2)(1-\gamma)} & \text{for } h < 1, \end{cases} \quad (109)$$

and the dynamical gap

$$\omega = \begin{cases} 2\sqrt{(h-1)(h-\gamma)} & \text{for } h > 1, \\ \sqrt{(1-h^2)(1-\gamma)} & \text{for } h < 1. \end{cases} \quad (110)$$

Notice that ω is not the actual gap Δ of the system, at least not in the ordered phase, where the minimal gap occurs between the two classical ground states with different symmetry. It instead represents the minimal gap between two states connected by the Hamiltonian dynamics.

As expected, the dynamical gap in Eq. (110) vanishes approaching the transition with a dynamical critical exponent $z\nu = 1/2$, which is in agreement with the semiclassical prediction for the disordered phase; see Eq. (103). The exponent is symmetric on both sides of the transition and independent of the value of $\gamma \neq 1$, proving that the anisotropy plays no role in the universal behavior. The only exception is $\gamma = 1$, where the system acquires continuous rotation symmetry, giving rise to a gapless ordered phase and a critical exponent $z\nu = 1$; an analytical solution of the problem is available in this case (Dusuel and Vidal, 2005a).

The in-plane magnetization $\langle S_x \rangle / N \propto \sqrt{1 - h^2}$ is consistent with a critical exponent $\beta = 1/2$. Similar arguments can be used to show that all the thermodynamic critical exponents, i.e., those associated with global thermodynamic quantities, are in agreement with mean-field theory. The question becomes more complex, however, if we consider the scaling of spatial-dependent quantities such as the correlation length. Conventionally, the critical exponent ν is associated with the scaling of the correlation length ξ at a quantum critical point $\xi \propto \lambda^{-\nu}$, where λ is the control parameter. This critical exponent is particularly important since it relates to the thermodynamic singularities of any critical quantity, with its finite-size scaling close to the transition (Fisher, 1967; Fisher and Barber, 1972). However, in a strong long-range system, and particularly in a fully connected one, no concept of length, or especially of correlation length, exists.

However, even in the absence of any definition of length, it is possible to define a correlation number that diverges close to the critical point $N_c \propto |h - 1|^{\nu_*}$. In general, this correlation number will be proportional to the correlation volume $N_c \propto \xi^d$ and, assuming that the scaling has to remain the same for all systems in the mean-field regime, one obtains the estimate

$$\nu_* = d_{uc}\nu. \quad (111)$$

The quantity d_{uc} represents the upper critical dimension of the corresponding nearest-neighbor model (Botet, Jullien, and Pfeuty, 1982). Since the LMG Hamiltonian (97) corresponds to that of the quantum Ising model in a transverse field with $d_{uc} = 3$, the correlation number exponents read $\nu_* = 3/2$.

This scaling theory, which was introduced by Botet, Jullien, and Pfeuty (1982), provides the exact value for the finite-size scaling of the dynamical gap ω_N , which can be obtained by incorporating higher-order $1/N$ corrections into Eq. (110) via the continuous unitary transformation approach, yielding $\omega_N \approx N^{-1/3}$ (Dusuel and Vidal, 2004, 2005a), which is in perfect agreement with the generalized finite-size scaling theory $\omega_N \approx N^{-z\nu/\nu_*}$. Despite this apparent simplicity, it has been shown that for large enough anisotropy parameters the spectrum of the LMG model may not converge to the prediction of Eq. (108), due to the influence of two competing semiclassical trajectories (Ribeiro, Vidal, and Mosseri, 2007).

More generally the convergence to the “simple” thermodynamic limit solution in fully connected models has been shown to present several anomalous features (Colonna-Romano, Gould, and Klein, 2014). In particular, it has been shown that the actual picture for the finite-size scaling of many-body systems above the upper critical dimension d_{uc} is actually more complicated than that depicted by Botet, Jullien, and Pfeuty (1982) since the zero and fluctuation modes present different scaling behaviors, and therefore different quantities may display different finite-size corrections depending on the dominating contribution to that quantity (Flores-Sola *et al.*, 2016).

2. Self-organization phase transition in cavity QED

The LMG model can effectively be realized using cavity QED platforms, whose self-organization transition can be described by a pure fully connected spin Hamiltonian upon elimination of the cavity field in Eq. (14). There the cavity-mediated long-range interaction [Eq. (13)] favors for $\mathcal{V} < 0$ a density modulation of the quantum gas and induces density correlations with a spatial periodicity λ along the pump and cavity directions. These density correlations are the collective elementary excitations of the system with energy $\hbar\omega_s$ and correspond to the creation and annihilation of correlated pairs of atoms in the momentum mode $|\mathbf{p}_1\rangle$. However, the kinetic energy term in Eqs. (10) stabilizes the gas against this modulation.

Only if the long-range interaction becomes sufficiently strong can the gain in potential energy overcome the cost in kinetic energy, and the system undergoes a quantum phase transition to a self-ordered state (Nagy, Szirmai, and Domokos, 2008; Piazza, Strack, and Zwerger, 2013). At this point, the energy $\hbar\omega_s$ of the collective excitation has softened such that the mode $|\mathbf{p}_1\rangle$ can be macroscopically populated without energetic cost. The atomic density acquires a checkerboard modulation that efficiently scatters photons into the resonator, and the atoms can further lower their energy in the emerging optical interference lattice potential.

A few years after self-organization of a thermal gas coupled to an optical cavity had been observed (Black, Chan, and Vuletić, 2003), the phase transition to a self-ordered state of a bosonic quantum gas coupled to a cavity was realized (Baumann *et al.*, 2010). While for a thermal gas the threshold is set by thermal density fluctuations, for a quantum gas the critical point scales with the recoil energy. A BEC of 10^5 ^{87}Rb atoms is harmonically trapped at the location of a single mode of a high-finesse optical cavity. The transverse pump power is linearly increased over tens of milliseconds. The experimental signature for self-ordering of a BEC, where the motion is quantized, is twofold as shown in Fig. 17: The cavity photon occupation rises abruptly when the critical interaction is reached, as can be observed via the light field leaking from the cavity. In addition, the momentum state distribution, as observed from absorption images after ballistic expansion, changes from occupying only the zero-momentum state $|\mathbf{p}_0\rangle$ below the critical point to a superposition of the momentum states $|\mathbf{p}_0\rangle$ and $|\mathbf{p}_1\rangle$ above the critical point. In real space, this momentum state occupation corresponds to a checkerboard order of the atomic density. When the transverse pump power

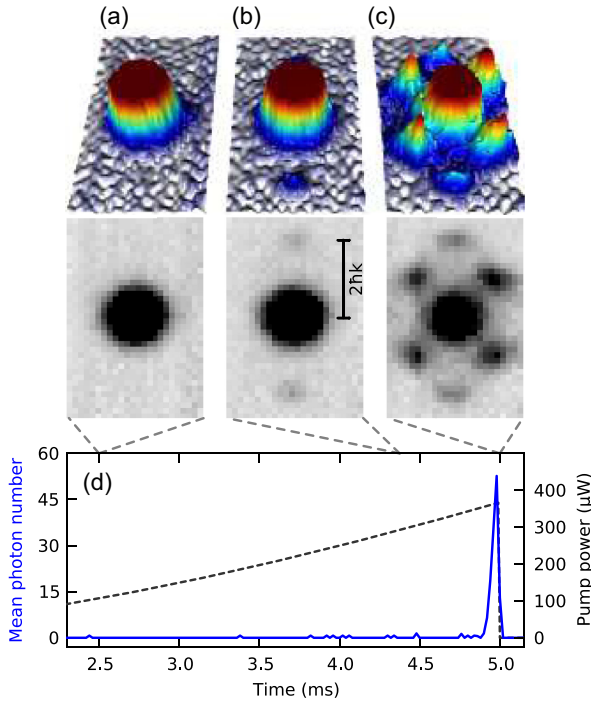


FIG. 17. Signatures of atomic self-organization in an optical cavity. (a) The transverse pump power (dashed line) is gradually increased while the mean intracavity photon number (solid line) is monitored. After the sudden release of the atomic cloud and its subsequent ballistic expansion, absorption images are made for pump powers corresponding to transverse pump lattice depths of (b) $2.6E_r$, (c) $7.0E_r$, and (d) $8.8E_r$. (d) Self-organization is manifested by an abrupt buildup of the cavity field accompanied by the formation of momentum components at $(p_x, p_y) = (\pm\hbar k, \pm\hbar k)$. The weak momentum components at $(0, \pm 2\hbar k)$ result from loading the atoms into the one-dimensional standing-wave potential of the transverse pump laser. From [Baumann *et al.*, 2010](#).

is ramped down again, the normal phase with an empty cavity and macroscopic occupation of only the single momentum state $|\mathbf{p}_0\rangle$ is recovered. As discussed in Sec. II.B.3, the self-organization phase transition can be mapped to the Dicke phase transition.

The mode softening preceding the phase transition ([Horak and Ritsch, 2001](#); [Nagy, Szirmai, and Domokos, 2008](#); [Öztop, Müstecaplıoğlu, and Türeci, 2013](#)) has been studied using a variant of Bragg spectroscopy ([Mottl *et al.*, 2012](#)). The cavity is seeded with a weak coherent field at a variable detuning with respect to the transverse pump frequency. If the detuning matches the soft mode frequency ω_s , energy and momentum conservation are fulfilled and the momentum mode $|\mathbf{p}_1\rangle$ becomes macroscopically occupied by the probing process. At the same time, photons from the transverse pump are scattered into the cavity. The measured mode frequency ω_s as a function of transverse pump power is displayed in Fig. 18. For the case of negative long-range interaction $\mathcal{V} < 0$, a clear mode softening toward the critical point of the self-organization phase transition is observed. In contrast, a positive long-range interaction $\mathcal{V} > 0$ is leading to a mode hardening without any phase transition.

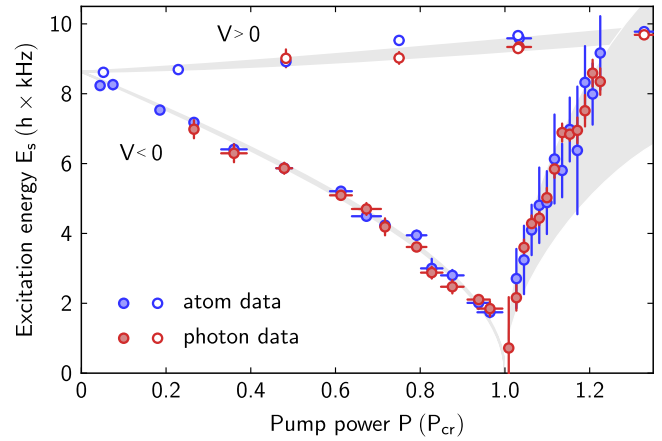


FIG. 18. Excitation spectrum across the self-organization phase transition. The measured resonance frequencies $E_s = \hbar\omega_s$, which were obtained from atomic and photonic signals, are shown in blue and red, respectively, for positive (open circles) and negative interaction strengths (solid circles) \mathcal{V} . Gray shading indicates the theoretical prediction, including experimental uncertainties. From [Mottl *et al.*, 2012](#).

Also in the case of a sideband-resolving cavity $\kappa < \omega_s$, a self-organization phase transition takes place. However, owing to the increased photon lifetime, the intracavity field acquires a retardation with respect to the atomic evolution, and the effective cavity-mediated atom-atom interaction can no longer be captured in the simple form of Eq. (13) ([Klinger, Keßler, Bakhtiari *et al.*, 2015](#)). In this case, it is more appropriate to use the coupled equation of motion. As we discuss in Sec. V.C.4, the sideband resolved regime allows one to study quench experiments that can be interpreted with a Kibble-Zurek model.

The long-range interaction can be engineered to act on more than the atomic density. By exploiting the atomic vector polarizability or Raman schemes coupling different atomic ground states, an effective long-range interaction acting on the pseudospin can be realized ([Camacho-Guardian, Paredes, and Caballero-Benítez, 2017](#); [Kroeze *et al.*, 2018](#); [Landini *et al.*, 2018](#)).

3. Discrete and continuous symmetry breaking

The Dicke Hamiltonian (14) is invariant under the parity transformation $(a, S_{\pm}) \rightarrow (-a, -S_{\pm})$. Accordingly, at the phase transition to the self-organized phase a discrete \mathbf{Z}_2 symmetry is broken, where the atomic density localizes on either the even or odd sites of the emerging checkerboard lattice and the cavity light field phase locks to either 0 or π with respect to the pump field phase. Site-resolving real-space imaging of the atomic system has not yet been achieved. However, this discrete symmetry breaking has been observed in the phase of the light field leaking from the cavity using a phase-sensitive heterodyne detection system ([Baumann *et al.*, 2011](#)).

The discrete nature of this symmetry breaking is dictated by the boundary conditions of the single cavity mode. The symmetry can, however, be enhanced to a continuous $U(1)$ symmetry, as had been originally discussed for highly

degenerate multimode cavities (Gopalakrishnan, Lev, and Goldbart, 2009). In addition, the self-organization of a transversely driven BEC in the combined fields of two degenerate single-mode cavities crossing under an angle of 60° allows an approximate continuous $U(1)$ symmetry to be engineered, as was demonstrated experimentally (Léonard, Morales, Zupancic, Esslinger, and Donner, 2017). Photons from the pump field were scattered into both cavities, and the atoms self-organized in the resulting interference potential. This system is invariant with respect to redistributing photons between the two modes, where the interference lattice potential breaks a continuous spatial symmetry depending on the relative photon occupation of the two cavities. The unique real-time access to the light field leaking from the optical cavities allowed one to identify the fundamental collective excitations of the underlying $U(1)$ symmetry as a phase and an amplitude mode (Léonard, Morales, Zupancic, Donner, and Esslinger, 2017). The continuous symmetry can be reduced to a $\mathbf{Z}_2 \otimes \mathbf{Z}_2$ symmetry if atom-mediated scattering between the two cavities is present (Lang, Piazza, and Zwerger, 2017; Morales *et al.*, 2018). Extending the scheme to multiple crossing cavities, higher symmetries such as a continuous $SO(3)$ rotational symmetry might also be realizable (Chiacchio and Nunnenkamp, 2018). Furthermore, a continuous symmetry can be broken if two counterpropagating modes of a ring cavity are instead employed, as was proposed for a transversally driven BEC (Mivehvar *et al.*, 2018), and realized for a BEC coupled to a ring cavity where two longitudinal modes were simultaneously driven. This configuration can be regarded as the minimal model of a supersolid state of matter (Schuster *et al.*, 2020), which was discussed in Sec. IV.E.

4. Criticality of the self-ordering phase transition

The critical behavior of the single-mode self-organization phase transition corresponds to that of the open Dicke model, falling into the universality class of the mean-field classical Ising model (Emary and Brandes, 2003; Nagy *et al.*, 2010; Kirton *et al.*, 2019). The constant flow of energy from the pump laser to the cavity leakage causes additional fluctuations of the cavity field and, accordingly, larger density fluctuations. The cavity dissipation thus makes the system leave its ground state and irreversibly evolve into a nonequilibrium steady state. The global-range interaction instead turns the phase transition into a quantum bifurcation in a zero-dimensional system, such that there is no notion of a divergent correlation length. However, one can investigate the critical exponent of the fluctuations of the order parameter. While a mean-field exponent of $1/2$ is expected in the closed system (see the discussion in Sec. IV.G.1), the prediction for the open system is 1, as given by the vanishing of the imaginary part of the spectrum at the critical point (Nagy, Szirmai, and Domokos, 2011; Öztop *et al.*, 2012). The open system thus effectively behaves thermally. Note that the actual steady state of the system might not be reached in experiments, since close to the critical point the quasinormal modes vanish, leading to a critical slowdown. An analysis going beyond the mapping to the open Dicke model and also considering a finite temperature of the quantum gas produces an interesting picture of the interplay between the self-organizing phase transition and

Bose-Einstein condensation (Piazza, Strack, and Zwerger, 2013; Piazza and Strack, 2014).

Monitoring the light field leaking from the cavity during self-organization gives real-time access to the order parameter of the phase transition; see Eq. (11). This allows one to not only measure the mean density modulation of the atomic cloud but also detect the fluctuations of the system (Brennecke *et al.*, 2013). Heterodyne detection of the light field provides the low-energy spectrum of the system, which can be directly converted into the dynamical structure factor of the gas at the wave vector of self-organization (Landig *et al.*, 2015); see Figs. 19(a)–19(d). The observed spectrum features a carrier at zero frequency with respect to the pump laser frequency and sidebands at positive and negative frequencies. The sidebands are signatures of density fluctuations, indicating either the creation or the annihilation of quasiparticles. Approaching the critical pump power P_{cr} , the mode softening is visible in the vanishing sideband frequency. At the critical point, a strong coherent field emerges at the carrier frequency, indicating the buildup of a static coherent density modulation. The amplitude of the carrier and the integrated sidebands converted into density modulation and density fluctuations, respectively, is displayed in Fig. 19(f). While the density modulation changes by more than 4 orders of magnitude, the density fluctuations diverge toward the critical point. From these data, critical exponents of 0.7(1) and 1.1(1) for the fluctuations of the order parameter can be extracted on the normal and self-organized sides, respectively. The sideband asymmetry visible in Figs. 19(b)–19(d) can be used not only to determine the occupation of the quasiparticle mode but also to extract the irreversible entropy production rate (Brunelli *et al.*, 2018) when the system crosses the phase transition.

V. DYNAMICAL CRITICAL BEHAVIOR

In this section, we review the multifaceted aspects of dynamical regimes in quantum long-range systems, emphasizing as much as possible universal behaviors. Given the vast amount of literature on the subject, we have arranged the material by presenting first a discussion of metastability, a hallmark of long-range systems, followed by a presentation of results on the Lieb-Robinson bound, the Kibble-Zurek mechanism, dynamical phase transitions, and confinement in quantum long-range systems. Miscellaneous material is presented in Sec. V.F.

A. Metastability and diverging equilibration times

Diverging equilibration times in the thermodynamic limit are a well-known characteristic of long-range interacting systems. Recently the absence of equilibration of strong long-range quantum systems has been directly linked to their peculiar single-particle spectrum, which leads to a violation of Boltzmann's H theorem and the appearance of finite Poincaré recurrence times in the thermodynamic limit (Defenu, 2021). These observations are in agreement with the aforementioned properties (see Sec. I.B), which are common to thermodynamically large long-range systems and finite local ones, such as the impossibility to fully disregard boundary over bulk phenomena (Barré and Gonçalves, 2007; Latella *et al.*, 2015),

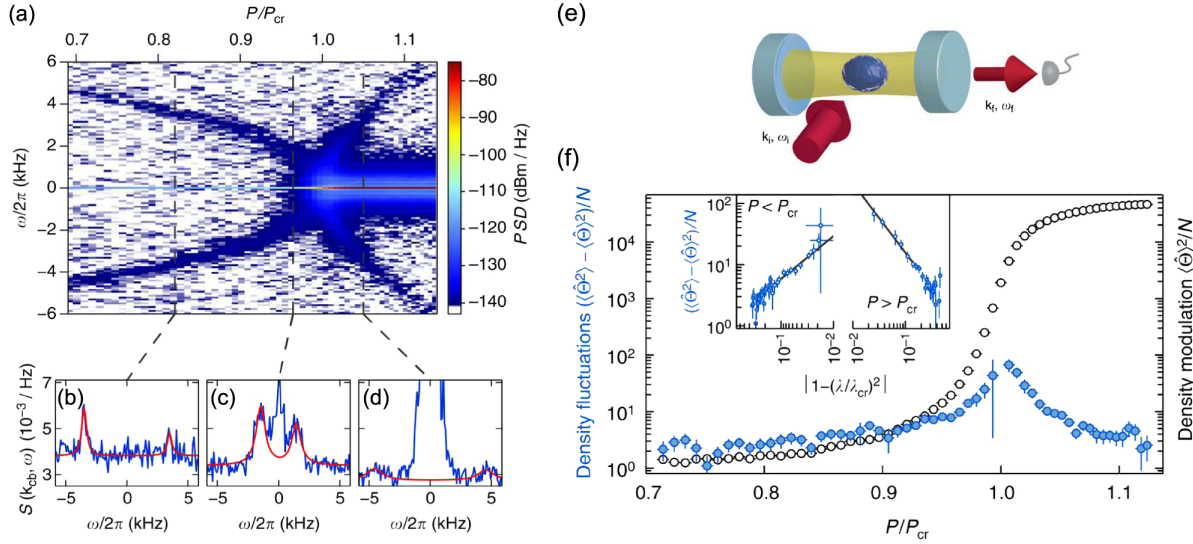


FIG. 19. Critical behavior of the self-organizing phase transition. (a) Power spectral density (PSD) of the light field leaking out of the cavity shown as a function of frequency shift ω with respect to the pump laser frequency and the relative transverse pump power P/P_{cr} . Two sidebands are visible, corresponding to the incoherent creation ($\omega < 0$) and annihilation ($\omega > 0$) of quasiparticles. The energy of these quasiparticles vanishes toward the critical point. At the phase transition, a strong coherent field at the pump frequency appears ($\omega = 0$). (b)–(d) Normalized dynamic structure factor for three different values of P/P_{cr} [see the dashed lines in (a)]. While the positions and widths of the sidebands give direct access to the energy and lifetime of the quasiparticles, the sideband asymmetry can be used to determine the occupation of the quasiparticle mode. (e) Sketch of the measurement setup. The atoms coupled to the cavity mode are illuminated by the transverse pump field at frequency ω_i , while the frequency emitted from the cavity is ω_f . A heterodyne detection system gives access to the PSD shown as a function of $\omega = \omega_i - \omega_f$ in (a). (f) The data can be used to extract the divergent density fluctuations and the emerging density modulation. Inset: Density fluctuations shown on a double logarithmic scale, which allows the critical exponents of 0.7(1) and 1.1(1) to be determined on the normal and self-organized sides, respectively. From Landig *et al.*, 2015.

the existence of concave entropy regions (Ispolatov and Cohen, 2001), or the presence of a macroscopic energy gap between the ground state and the first excited state (Gupta, Campa, and Ruffo, 2012a, 2012b).

The key point is that the spin-wave spectrum of the systems does not become continuous in the thermodynamic limit, as the eigenvalues of a long-range coupling matrix can be shown to remain discrete even in the infinite component limit, forming a pure point spectrum (Last, 1996) similar to the one appearing in strongly disordered systems (Thouless, 1972; Fröhlich and Spencer, 1983; Simon, Taylor, and Wolff, 1985; Scardicchio and Thiery, 2017). A discussion of the spectral discreteness of long-range couplings in the thermodynamic limit was presented by Defenu (2021) and employed to justify the observation of diverging equilibration times in a long-range Ising model, quenched across its quantum critical point (Kastner, 2011).

The first evidence of QSSs in quantum systems has been described in the prototypical example of the long-range Ising chain; see Eq. (61). The QSSs have been shown to appear for quenches starting well inside the paramagnetic phase in the $h \rightarrow +\infty$ limit and terminating in deep in the ferromagnetic phase at $h = 0$. The system is then prepared in the transversally polarized ground state and evolved according to the classical ferromagnetic Hamiltonian in the absence of a transverse field. It follows that the expectation of the global operator $m_z = \langle \sum_i \sigma_i^z \rangle / N$ with the Hamiltonian (61) evolves from the initial value $\lim_{t \rightarrow 0} m_z = 1$ to the equilibrium expectation $\lim_{t \rightarrow \infty} m_z = 0$ if the system actually equilibrates; see Fig. 20(a). These observations may be extended to any

choice of the initial and final magnetic fields h_i and h_f using the Kitaev chain representation of the Ising model given in Eq. (66); see the discussion in Sec. IV.B.3.

Recall that for $1 < \alpha < 3$ the correspondence between the fermion and spin Hamiltonians in, respectively, Eqs. (61) and (66) is not exact. Yet, the existence of the quantum critical points is preserved and the equilibration scenario for the two systems is analogous (Essler, Evangelisti, and Fagotti, 2012; Van Regemortel, Sels, and Wouters, 2016). The analogy between the transition of the Ising and Kitaev chain was discussed in Sec. IV.B.3 and by Jaschke *et al.* (2017) and Defenu, Enss, and Halimeh (2019). Within the Kitaev chain perspective, the critical point at $h = h_c = 1$ is signaled by the property $\lim_{k \rightarrow 0^\pm} \theta_k = \pm\pi/2$, where the critical Bogoliubov quasiparticles are constituted by an equal superposition of electrons and holes ($|u_{k=0}| = |v_{k=0}| = 1/\sqrt{2}$). This phenomenon is often interpreted as a Dirac mode resulting from the superposition of two Majorana edge states (Fradkin, 2013).

In the strong long-range regime ($0 < \alpha < 1$) and in the presence of the Kac rescaling a full characterization of the quantum phase transition in the Kitaev chain has not yet been attempted. Indeed, no clear continuum limit can emerge for this regime in the thermodynamic limit due to the spectral discreteness evidenced by Defenu (2021). Nevertheless, the existence of the quantum critical point can also be inferred in the strong long-range regime by analyzing the $k \rightarrow 0$ limit of the Bogoliubov angles.

The equilibration of a weak long-range Kitaev chain after a sudden quench of the chemical potential h is summarized in

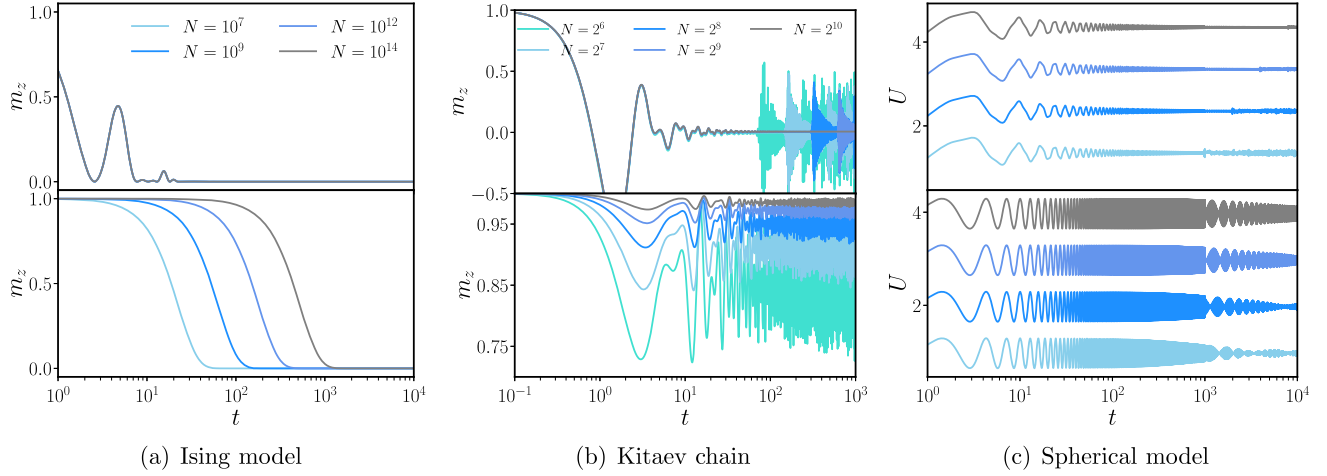


FIG. 20. Evidence of QSSs in the long-range Ising chain, the Kitaev chain, and the one-dimensional spherical model, from left to right, respectively. In each panel the top subpanel displays the case of weak long-range interactions $\alpha > 1$, where roughly the same equilibration properties of the nearest-neighbor case are found. Conversely, the bottom subpanels show the case of strong long-range interactions $\alpha < d$, where dynamical fluctuations survive in the $t \rightarrow \infty$ limit. (a) Transverse magnetization of the long-range Ising model [see the Hamiltonian (61)] after a quench from the fully paramagnetic state at $h \rightarrow \infty$ deep into the ordered phase at $h \rightarrow 0$. While the observable expectation equilibrates at long times for $\alpha = 2.0$ (top subpanel), it persists in its initial value for increasingly long times as the system size increases for $\alpha = 0.5$ (bottom subpanel); see the discussion given by Kastner (2011). A similar signature is noticed in the case of the Hamiltonian (67), i.e., the Kitaev chain representation of the Ising model, where the dynamics can be exactly solved for any global quench across the phase boundary. (b) Evolution of the spatial and quantum average of the σ_z in Eq. (62) for a long-range Kitaev chain with $\alpha \gtrsim 12$ (top subpanel) and $\alpha = 0.4$ (bottom subpanel for $h_i \gg 1$ to $h_f = 0.4$). (c) Lack of equilibration also appears for noncritical quenches, as shown for the potential energy U of a quantum spherical model with long-range interactions. Dynamical fluctuations reduce as size increases for decay rates $\alpha > 1$; see the upper subpanel, where the $\alpha \gtrsim 12$ case is shown for increasing system sizes $N \in [2^9, 2^{10}, 2^{11}, 2^{12}]$ from bottom to top. Conversely, dynamical fluctuations tend to increase for $\alpha < 1$, as shown in the lower subpanel for $\alpha = 0.2$, again displayed from bottom to top; see Defenu (2021).

the upper subpanel of Fig. 20(b). The initial state of the system is the ground state at $h = h_i \gg 1$, deep in the normal phase, where $m_z \approx 1$. This initial state is evolved according to the ferromagnetic Hamiltonian with $h = h_f < 1$. The explicit description of the quench dynamics solution was given by Defenu, Enss, and Halimeh (2019). Note that in the language of Fermi quasiparticles the magnetization reads

$$m_z = 1 - \frac{2}{N} \sum_i \langle c_i^\dagger c_i \rangle. \quad (112)$$

From the long-time dynamics of the observable in Eq. (112), it is evident that the equilibration in the weak long-range Kitaev chain [see the upper panel in Fig. 20(b)] mimics the case of the long-range Ising model with $\alpha = 2$ [see the upper panel in Fig. 20(a)]. The initial value of the observable rapidly equilibrates to a long-time expectation that becomes time independent in the long-time limit. In other words, any observable $A(t)$ relaxes to equilibrium if it approaches its Cesaro's average

$$\bar{A} = \lim_{T \rightarrow \infty} \langle A \rangle_T, \quad (113)$$

with

$$\langle \dots \rangle_T = \frac{1}{T} \int_0^T \dots dt.$$

Moreover, the dynamical fluctuations, which are quantified by the parameter

$$Q_A(T) = \langle |A(t) - \bar{A}|^2 \rangle_T, \quad (114)$$

must disappear in the long-time limit

$$\lim_{T \rightarrow \infty} Q_A(T) \approx 0. \quad (115)$$

Equation (115) is the conventional way to define equilibration in closed quantum systems (Reimann, 2008; Linden *et al.*, 2009; Short, 2011; de Oliveira *et al.*, 2018).

For $\alpha > d$ the result $\lim_{T \rightarrow \infty} Q_{m_z}(T) = 0$ can be exactly proven for most quadratic models as well as for the Ising model for sudden quenches from $h_i = +\infty$ to $h_f = 0$ thanks to the Riemann-Lebesgue lemma (Hughes-Hallett *et al.*, 2008). In other words, equilibration occurs in these systems as the Poincaré recurrence times diverge for $N \rightarrow \infty$. This phenomenon is evident in the numerical computation of the m_z expectation value for both the Ising and the Kitaev chain with $\alpha > 1$; see the upper panels in Figs. 20(a) and 20(b).

This picture is radically altered in the $\alpha < 1$ case; see the bottom panels in Fig. 20(b). Indeed, the dynamical evolution of the observable m_z persists near its initial value for longer times as the system size is increased, which is in agreement with the $\tau_{\text{eq}} \propto N^\beta$ expectation coming from classical systems (Campa, Dauxois, and Ruffo, 2009). The $\beta = 1/2$ scaling observed in the long-range Ising model appears to be related

with the scaling of Poincaré recurrence time due to the discrete spectrum of long-range systems (Kastner, 2011; Defenu, 2021). Note also that the scaling of timescales in long-range systems is influenced by the Kac rescaling, and that these observations may be altered by modifying the regularization procedures (Bachelard and Kastner, 2013).

While the phenomenologies of the Kitaev and Ising models are analogous, the quantitative features of the dynamical evolution display some peculiar differences. In particular, in the long-range Ising model, no oscillatory fluctuations are present, while they occur in the Kitaev chain. These differences are probably due to the differing quench boundaries between the two models. Despite these details, it is evident that the curves in the lower panels of Figs. 20(a) and 20(b) will both yield $\lim_{T,N \rightarrow \infty} Q_{m_z}(T) \neq 0$.

The appearance of the QSSs has often been connected to the scaling of equilibration times of critical observables such as the magnetization (Antoni and Ruffo, 1995; Mukamel, Ruffo, and Schreiber, 2005; Campa, Dauxois, and Ruffo, 2009). However, signatures of persistent time fluctuations in classical systems have also been found in generic thermodynamic observables, as for the evolution of internal energy in systems of particles with attractive power-law pair interactions (Gabrielli, Joyce, and Marcos, 2010). The same picture can also describe many-body quantum systems. Indeed, persistent dynamical fluctuations are also observed for noncritical quantities or quenches, as occurs for the internal energy of the spherical model; see Fig. 20(c).

B. Lieb-Robinson bound

An understanding of the maximum speed at which information propagates in many-body systems allows one to put tight bounds on fundamental questions, such as how fast a quantum system can thermalize (Calabrese and Cardy, 2006) or how much quantum information can be transmitted through a quantum channel (Bose, 2007). In short-range interacting systems the Lieb-Robinson bound predicts a constant

maximal velocity that confines the information to a linear effective light cone (Lieb and Robinson, 1972). Long-range interactions substantially alter this picture since the traditional definition of group velocity does not apply to their case. Accordingly, the spreading of correlations, information, or entanglement speeds up dramatically, leading to a wide range of exotic dynamical properties, which may be exploited for fast information transmission, improved quantum state preparation, and similar applications. Thus, it is not surprising that a large body of theory work has emerged in recent years in order to find tighter propagation bounds for different values of the power-law exponent α (Hastings and Koma, 2006; Lashkari *et al.*, 2013; Eisert *et al.*, 2013; Hauke and Tagliacozzo, 2013; Hazzard *et al.*, 2013; Schachenmayer *et al.*, 2013; Gong *et al.*, 2014; Hazzard *et al.*, 2014; Foss-Feig *et al.*, 2015; Rajabpour and Sotiriadis, 2015; Storch, van den Worm, and Kastner, 2015; Matsuta, Koma, and Nakamura, 2017; Chen and Lucas, 2019; Sweke, Eisert, and Kastner, 2019; Tran, Ehrenberg *et al.*, 2019; Tran, Guo *et al.*, 2019; Else *et al.*, 2020; Guo *et al.*, 2020; Hermes *et al.*, 2020; Kuwahara and Saito, 2020; Tran *et al.*, 2020).

Most of the current understanding of correlations and entanglement spreading in the presence of long-range interactions was based on prototypical systems. In those systems, the synergy between analytical and numerical investigations has been particularly fruitful (Hauke and Tagliacozzo, 2013; Schachenmayer *et al.*, 2013; Hazzard *et al.*, 2014; Nezhadhighi and Rajabpour, 2014; Rajabpour and Sotiriadis, 2015; Schachenmayer, Pikovski, and Rey, 2015a, 2015b). The general understanding of propagation in long-range systems is summarized in Fig. 21. This qualitative picture applies almost regardless of the particular model, the quantity, and the decay range α .

In analogy with other universal results in the short-range regime, entanglement scaling in long-range models with $\alpha \gg 3$ reproduces the well-known light-cone shape observed for local systems (Lieb and Robinson, 1972); see Fig. 21, right panel. For intermediate values of α (see the center panel

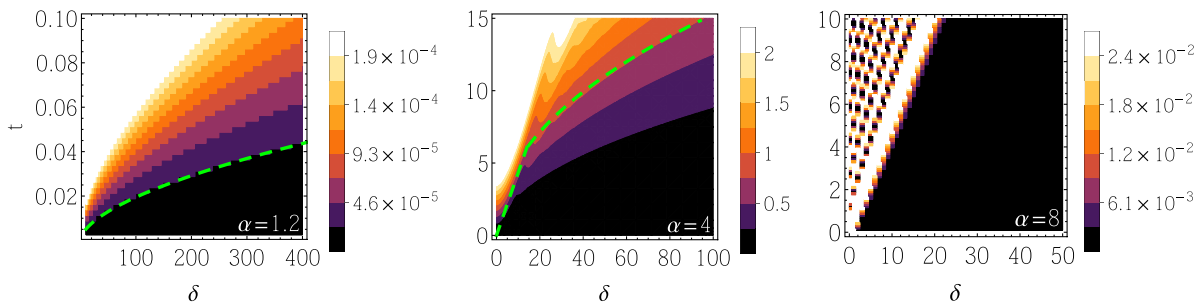


FIG. 21. Different models and physical quantities are shown in the different panels, but the overall picture remains the same. Left panel: detection probability for a signal sent through a quantum channel between two sites at distance δ shown for the long-range Ising chain (Eisert *et al.*, 2013). The green dashed line displays the power law $\delta \propto t^{1.7}$. Center panel: connected correlation functions between two sites at distance δ in a long-range field theory; see the effective action in Eq. (36) with $d = 1$ and $\alpha = 4$ (Rajabpour and Sotiriadis, 2015). The short-distance spreading resembles the conventional light cone observed with local interactions, while for larger distances long-range effects appear, and power-law scaling is observed. The green dashed curve is a guide for the eye. Right panel: mutual information between two lattice sites at distance δ in the Kitaev chain described by the Hamiltonian (49) with vanishing pairing and long-range hopping ($\alpha = 8$). The decay rate is large enough that only the light cone is observed. From Storch, van den Worm, and Kastner, 2015.

in Fig. 21) cone-light propagation is observed at short distances, while correlations between distant sites are heavily influenced by the presence of the long-range terms. Multispeed prethermalization for lattice spin models with long-range interactions in the regime $d < \alpha < d + 2$ was studied by Frérot, Naldesi, and Roscilde (2018). The behavior of correlations at intermediate decay is akin to the one found in the critical behavior of the long-range Kitaev chain in Sec. IV.B.4, where long-range hopping amplitudes with $2 < \alpha < 3$ do not modify the universal scaling behavior, but they alter the overall shape of excitations. However, in the Kitaev chain long-range hopping influences the subcritical behavior only for $\alpha < 3$, while the light-cone bending is also observed for $\alpha = 4$ (Rajabpour and Sotiriadis, 2015), as discussed by Storch, van den Worm, and Kastner (2015).

Finally, at smaller α (Fig. 21, left panel) the universal scaling is altered by long-range interactions and, accordingly, the correlations propagate faster than any possible group velocity, thereby disrupting the linear light-cone shape.

Analytical insight into information propagation in long-range system may also be achieved by general Lieb-Robinson-type bounds. A first contribution in this direction was given by Hastings and Koma (2006), yielding for $\alpha > d$

$$\| [O_A(t), O_B(0)] \| \leq C \| O_A \| \| O_B \| \frac{|A||B|(e^{v|t|} - 1)}{[d_{A,B} + 1]^\alpha}. \quad (116)$$

The regions A and B are a disjunct subset of the d -dimensional lattice. The generic operator expectations O_A and O_B receive contributions only from Hilbert-space states whose support lies in the spatial regions A and B , respectively. In Eq. (116) $\| \cdot \|$ denotes the operator norm and $d_{A,B}$ is the distance between the regions A and B . The importance of Eq. (116) derives from its generality since it applies to a wide range of observables, while it is straightforwardly extended also to other nonlocal quantities, such as the equal time correlators (Bravyi, Hastings, and Verstraete, 2006; Nachtergaele, Ogata, and Sims, 2006). In its regime of validity $\alpha > d$, the bound in Eq. (116) qualitatively reproduces the shape in the left panel of Fig. 21. However, the wave-front propagation obtained using Eq. (116) is logarithmic rather than power law and thus does not faithfully describe larger α values. Further insight into this problem was obtained by Gong *et al.* (2014), where a more general bound was derived that was capable of reproducing both the Lieb-Robinson result in the local limit ($\alpha \rightarrow \infty$) and Eq. (116). Even this general bound appears not to be tight on the entire α range but rather to be more accurate at large α .

The extension of the previous picture to the strong long-range regime needs to account for the influence of diverging long-range interactions with $\alpha < d$ on the systems timescales. In analogy with the equilibration rate of QSSs (see Sec. V.A), the fastest propagation scale in strong long-range systems is found to vanish as a power law approaching the thermodynamic limit $\tau_{\text{fastest}} \propto N^{-q}$ with $q > 0$ (Bachelard and Kastner, 2013). Accordingly, signal propagation becomes increasingly fast as the system approaches the thermodynamic limit and hinders the traditional formulation of the Lieb-Robinson bound. To circumvent such complications it is convenient

to introduce a rescaled time $\tau = tN^q$. In terms of this ‘‘proper’’ time variable, the bound for $\alpha < d$ takes the same form as in the weak long-range regime, but with τ in spite of t on the rhs of Eq. (116) (Storch, van den Worm, and Kastner, 2015).

The aforementioned results for $\alpha < d$ produce the shortest signaling time t_{ss} between the edges of a system of size N to scale as $t_{\text{ss}} \gtrsim N^{2\alpha/d-2} \log N$, which leads to the possibility of a vanishing time for transmitting information between linearly distant sites of a strong long-range system. However, such fast signals have never been observed or described; instead, a size-independent signaling time was evidenced in several situations (Eisert *et al.*, 2013; Hauke and Tagliacozzo, 2013; Eldredge *et al.*, 2017). Moreover, for specific initial states strong long-range interactions may be inconsequential to signal propagation due to the so-called shielding effect (Santos, Borgonovi, and Celardo, 2016).

Focusing on quadratic Hamiltonians a much tighter bound $t_{\text{ss}} \gtrsim N^{\alpha/d-1/2}$ can be obtained, which is saturated for $\alpha < d/2$ by the quantum state transfer protocol described by Guo *et al.* (2020). They also provided a stricter bound for general interacting spin systems. Note that the Lieb-Robinson bound can also be used to predict the velocity of quantum information scrambling, whose importance lies at the edge between high-energy and condensed matter physics (Sekino and Susskind, 2008; Maldacena, Shenker, and Stanford, 2016; Gärtner *et al.*, 2017; Bentsen, Gu, and Lucas, 2019). In this context, the role of long-range interactions is particularly relevant due to their inclusion in most quantum mechanical models of black holes, possibly making these systems the fastest information scramblers in nature (Lashkari *et al.*, 2013).

Despite the fast propagation and scrambling of correlations due to long-range interactions, the growth of entanglement entropy after a sudden quench is strongly reduced. In particular, in the strong long-range regime ($\alpha < d$) it can become as slow as the logarithmic regime, even in the absence of disorder (Schachenmayer *et al.*, 2013; Buyskikh *et al.*, 2016; Pappalardi *et al.*, 2018). This peculiar phenomenon is connected with a suppression of the quasiparticle contribution to the von Neumann entanglement entropy, which is known to be governed by collective spin excitations related to spin squeezing (Sørensen and Mølmer, 2001; Tóth *et al.*, 2007; Pezzé and Smerzi, 2009). Extending to the dynamical case the bosonization procedure outlined in Sec. IV.G.1 (Rückriegel, Kreisel, and Kopietz, 2012; Lerose, Žunkovič, Marino *et al.*, 2019) made it possible to show that the rate of divergence of semiclassical trajectories governs the transient growth of entanglement. This provides a transparent and quantitative relationship between entanglement propagation measures (such as entropy, quantum Fisher information, and spin squeezing) and chaos quantifiers (such as Lyapunov exponents and out-of-time-order correlations) in the semiclassical regime (Lerose and Pappalardi, 2020a, 2020b). Fast entanglement growth is recovered only at criticality, corresponding to an unstable separatrix terminating onto a saddle point in phase space. Similarly, when the classical dynamics is chaotic (such as for kicked or multispecies models), the growth is fast, with a rate related to Lyapunov exponents. In addition, long-but-finite-range interactions open up a finite layer of instability

with fast entanglement growth due to the presence of a chaotic dynamical phase (Lerose *et al.*, 2018; Lerose, Žunkovič, Marino *et al.*, 2019). Correlation spreading with van der Waals interactions and the presence of positional disorder in two dimensions were investigated by Menu and Roscilde (2020). Multifractality and localization of spin-wave excitations above a ferromagnetic ground state are observed. In addition, the spreading of entanglement and correlations starting with a factorized state exhibits anomalous diffusion with a variable dynamical exponent.

1. Experimental observation

The propagation of correlations and the violation of the local Lieb-Robinson bound have been observed in trapped-ion quantum simulators for $0.6 \lesssim \alpha \lesssim 1.2$ (Jurcevic *et al.*, 2014; Richerme *et al.*, 2014). Jurcevic *et al.* (2014) studied the dynamics following either a global or a local quench of a long-range XY Hamiltonian; see Eq. (9). The experimental system consists of a 15 ion chain, prepared in a product state where only the central spin is flipped with respect to the rest of the system. In this system the global magnetization $S_z = \sum_i \sigma_i^z$ is a conserved quantity; therefore, the excitation can be described as a magnon quasiparticle that propagates from the center throughout the system. After the local quench, Jurcevic *et al.* (2014) observed that for $\alpha < 1$ the light cone calculated considering only the nearest-neighbor couplings did not capture the dynamics of the system well; see Figs. 22(a)–22(c).

Richerme *et al.* (2014) performed a global quench under both Ising [Eq. (6)] and XY [Eq. (9)] Hamiltonians, measuring the evolution of the connected two-body correlations

$$C_{1,1+r}(t) = \langle \sigma_1^z(t) \sigma_{1+r}^z(t) \rangle - \langle \sigma_1^z(t) \rangle \langle \sigma_{1+r}^z(t) \rangle.$$

The light-cone boundary is extracted by measuring the time it takes a correlation of fixed amplitude ($C_{i,j} \sim 0.1 C_{i,j}^{\max}$, where $C_{i,j}^{\max}$ is the largest connected correlation between two ions) to travel an ion-ion separation distance r . For strongly long-range interactions ($\alpha < 1$), an accelerating information transfer is observed through the chain. This fast propagation of correlations is explained by the direct long-range coupling between distant spins. The increased propagation velocities quickly surpass the Lieb-Robinson velocity for a system with equivalent nearest-neighbor-only interactions: $v = 12eJ_{\max}$, where e is Euler's number and J_{\max} is the maximum Ising coupling strength for a given spin-spin coupling matrix.

C. Kibble-Zurek mechanism

The correlation length of a quantum system diverges approaching its quantum critical points, while the dynamical gap vanishes. As a result, the dynamical scaling of the observables when the system is driven across the transition is reminiscent of the thermodynamic scaling at equilibrium. Yet, for this scaling to be displayed the drive has to be slow enough that the dynamical evolution occurs in the vicinity of the equilibrium critical point.

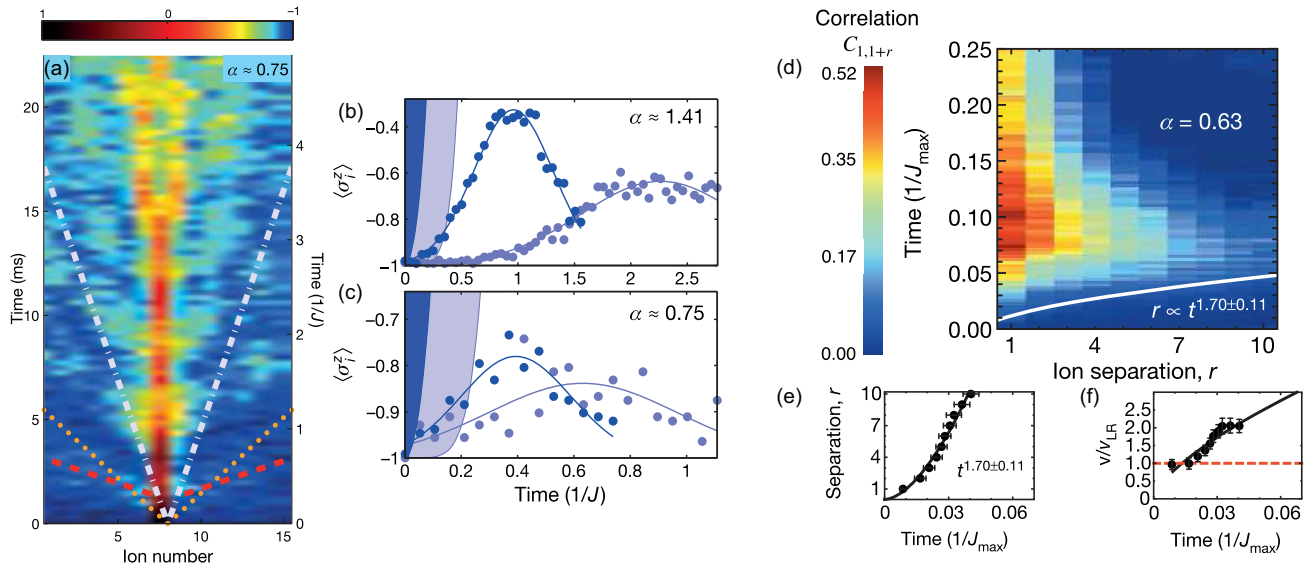


FIG. 22. Propagation of quantum information in long-range trapped-ion systems. (a) Single-site magnetization $\langle \sigma_i^z(t) \rangle$ as a function of time, following a quantum quench of the long-range XY Hamiltonian (9), with the central eighth ion initially flipped. The dashed red lines are fits to the observed magnon arrival times [bottom of (b)]; dot-dashed white lines, light cone for averaged nearest-neighbor interactions; orange dots, after renormalization by the algebraic tail. The white lines are in clear disagreement with the red lines. (b),(c) Gaussian fits to magnon arrival time [the red lines in (a)] for ions 6 (dark blue on the left) and 13 (light blue on the right) with $\alpha \approx 1.41$ (top) and $\alpha \approx 0.75$ (bottom). A nearest-neighbor Lieb-Robinson bound captures most of the signal (shaded region) in the $\alpha \approx 1.41$ case and does not for $\alpha \approx 0.75$. Adapted from Jurcevic *et al.*, 2014. (d) Spatial and time-dependent correlations following a global quench of a long-range Ising Hamiltonian (6) with $\alpha = 0.63$. (e) Correlation propagation velocity. (f) The curvature of the boundary shows an increasing propagation velocity, quickly exceeding the short-range Lieb-Robinson velocity bound v (red dashed line). The solid lines give a power-law fit to the data that depends slightly on the choice of fixed contour $C_{i,j}$. Adapted from Richerme *et al.*, 2014.

We now consider a critical system with an internal control parameter λ such that a quantum critical point occurs at $\lambda_c = 0$ ($\lambda = |T - T_c|/T_c$ for finite-temperature phase transitions). Conventionally, any slow enough drive of internal parameters $\lambda(t) = \delta t$ will only produce adiabatic corrections $\sim \delta^2$ to the observable expectations with respect to the equilibrium value, as can be deduced using simple thermodynamic arguments (Zwerverger, 2008). However, when crossing an equilibrium critical point, the traditional adiabatic picture breaks down and the residual energy (heat) generated by the drive displays nonanalytic behavior $E_{\text{res}} \approx \delta^\theta$ with $\theta < 2$ (Zurek, 1996). In most local systems such nonanalytic scaling emerges due to the formation of topological defects according to the Kibble-Zurek mechanism, as confirmed by several condensed matter experiments; see del Campo and Zurek (2014) for a review.

In the quantum realm, the simplest example of defect production is furnished by the Landau-Zener problem, which describes a two-level system driven through an avoided level crossing (Zener, 1932; Landau and Lifshitz, 1991; Damski, 2005), but actual Kibble-Zurek scaling is observed only in quantum many-body systems in the thermodynamic limit (Zurek, Dorner, and Zoller, 2005; Dziarmaga, 2010). The heuristic scaling argument at the basis of the Kibble-Zurek mechanism can be proven to exactly apply to the nearest-neighbor Ising model, i.e., the Hamiltonian (61) in the $\alpha \rightarrow \infty$ limit, since that problem can be mapped to an infinite ensemble of Landau-Zener transitions (Dziarmaga, 2005).

In a general system, the Kibble-Zurek argument relies on the so-called adiabatic-impulse approximation, where in the dynamical evolution of a system starting in its ordered ground state at $t = -\infty$ is assumed to adiabatically follow the drive until the so-called freezing time $-\hat{t}$. Beyond the “freezing” time the equilibration rate of the system becomes too small with respect to the drive velocity and the system state cannot follow the Hamiltonian modification as it is approaching the quantum critical point at $t = 0$. Therefore, the dynamics is assumed to remain frozen at all times $t > -\hat{t}$ up to the crossing of the quantum critical point (at $t = 0$) and after, until the equilibration rate of the system grows back and the “unfreezing” time \hat{t}' , where adiabaticity is restored, is reached.

Once the system has unfrozen, the state evolution will resume on the opposite side of the transition, where the Hamiltonian ground state is supposed to break the Hamiltonian symmetry. Thus, the dynamics will induce a transition between the symmetric and a symmetry-broken state. However, this transition will occur at a finite correlation length $\hat{\xi}$ since the process starts only at $t \geq \hat{t}' = \hat{t}$, at least for a symmetric transition. The dynamics has thus modified the character of the continuous phase transition, making it similar to a first-order one, and the system will likely form topological defects whose size would be roughly proportional to the finite correlation volume $\hat{\xi}^d$. Therefore, the total defect density scales according to $n_{\text{exc}} \approx \hat{\xi}^{-d}$.

During the adiabatic stage of the dynamics, the system observables acquire the equilibrium expectation of the instantaneous Hamiltonian, and so does the minimal gap of the system $\Delta(t) = \Delta(\lambda(t))$. A proper estimation of the drive strength on the system is $\dot{\Delta}/\Delta$, which has to be compared with the equilibration time Δ^{-1} , leading to the adiabatic condition

$$\dot{\Delta} \ll \Delta^2. \quad (117)$$

The freezing time \hat{t} is defined by the breakdown of the adiabatic condition $\dot{\Delta}(\hat{t}) \simeq \Delta(\hat{t})^2$. Applying the critical scaling of the minimal gap with λ , one obtains the scaling of the freezing time $\hat{t} \approx \delta^{-\nu/(1+\nu)}$ and, accordingly, the freezing length scaling $\hat{\xi} \approx \delta^{-\nu/(1+\nu)}$, which leads to the defect density expression

$$n_{\text{exc}} \approx \hat{\xi}^{-d} \approx \delta^{d\nu/(1+\nu)}. \quad (118)$$

The application of the traditional Kibble-Zurek picture is complicated by different effects, depending on the strong or weak nature of the long-range interactions. In the former case, the additional relevance of boundaries with respect to local systems produces clear difficulties in the definition of the topological defects. In the latter case, the presence of the competing scaling contributions discussed in Sec. IV.B.4 leads to novel scaling regimes that are not encompassed by the traditional Kibble-Zurek framework.

1. Kitaev chain

The appearance of multiple scaling contributions to the critical behavior of long-range quantum systems was exemplified in the study of the Kitaev chain in Sec. IV.B.4. In this section, we consider the effect of such multiple scalings on the universal dynamics.

The study of exactly solvable toy models is at the root of the current understanding of Kibble-Zurek scaling in general quantum systems. Indeed, the first studies of defect formation in quantum systems were pursued on the nearest-neighbor Ising model, where finite-size scaling arguments led to the prediction

$$n_{\text{exc}}^{\text{fss}} \approx \delta^{1/2z}, \quad (119)$$

which produces $n_{\text{exc}} \approx \sqrt{\delta}$, in agreement with the Kibble-Zurek prediction in Eq. (118), since $z = \nu = 1$ in this case (Zurek, Dorner, and Zoller, 2005). Soon after this seminal investigation, an exact solution to the universal slow dynamics of the Ising model has been provided by mapping it to an infinite sum of Landau-Zener problems, each representing the dynamics of a single fermionic quasiparticle excitation (Dziarmaga, 2005).

Indeed, the dynamical evolution of quadratic fermions can be described in terms of the Bogoliubov amplitudes via

$$i\hbar \frac{d}{dt} \begin{pmatrix} u_k \\ v_k \end{pmatrix} = \begin{pmatrix} \varepsilon_\alpha(k, t) & \Delta_\beta(k) \\ -\Delta_\beta(k) & \varepsilon_\alpha(k, t) \end{pmatrix} \begin{pmatrix} u_k \\ v_k \end{pmatrix}, \quad (120)$$

which generically represents an ensemble of two-level systems whose energy and coupling are given by the momentum space kinetic and pairing terms, respectively. Thus, the Kibble-Zurek dynamics of the Kitaev chain can be studied exactly and this solution is not limited to the nearest-neighbor case, which represents the Ising model, but it can be extended to any form of the long-range couplings.

Consider a slow variation of the chemical potential h in the Hamiltonian (45) with the usual slow drive form $h(t) = h_c + \delta t$, with the time spanning in the interval $t \in [-h_c/\delta, h_c/\delta]$. In the small δ limit, the system is adiabatically ramped from a point deep in the topological phase $h = 0$ across the quantum phase transition and up into the trivial phase $h = 2h_c$. In the following we focus on a ramp across the quantum phase transition occurring at $h_c = 1$.

Within this dynamical protocol the dynamical system in Eq. (120) reduces to the k -dependent Landau-Zener problem (Landau and Lifshitz, 1969; Damski, 2005). Thus, the excitation probability of each Bogoliubov quasiparticle can be computed according to the Landau-Zener formula

$$\langle \gamma_k^\dagger \gamma_k \rangle = n_{\text{exc}}(k) = \exp\left(-\frac{\pi}{\delta^2} \Delta_\beta(k)^2\right) + O(\delta^2 \Delta_\beta(k)^4). \quad (121)$$

Equation (121) explicitly reports only the leading term in the $k \rightarrow 0$ limit, which is the relevant one for the universal behavior. However, when one considers a slow quench in a finite time interval $t \in [-h_c/\delta, h_c/\delta]$, the discontinuity in the drive derivative at the borders of the interval induces δ^2 corrections to the excitations probability (Dziarmaga, 2010; Defenu *et al.*, 2019).

The excitation probability in Eq. (121) depends only on the pairing term in Hamiltonian (45), so the universal slow dynamics is fully determined by the low-momentum scaling of the pairing coupling. Accordingly, the excitation density can be obtained by integrating Eq. (121) over the Brillouin zone

$$\int n_{\text{exc}}(k) dk \approx \delta^{1/2z_\Delta}, \quad (122)$$

where we have defined z_Δ from the scaling of the pairing coupling $\lim_{k \rightarrow 0} \Delta_\beta(k) \approx k^{z_\Delta}$. The result in Eq. (122) has also been employed to prove the validity of the Kibble-Zurek

argument in Kitaev chains with long-range pairing terms (Dutta and Dutta, 2017) in addition to the purely local case (Dziarmaga, 2005).

Apart from the aforementioned results, which explicitly refer to quadratic Fermi systems, the application of adiabatic perturbation theory to slow quenches close to quantum critical points predicts the scaling of the defect density to agree with the Kibble-Zurek prediction $\theta = d\nu/(1+z\nu)$ (Polkovnikov, 2005). This prediction comes from the assumption that the scaling form of the critical propagator reproduces the equilibrium critical exponents. Since for 1D Fermi systems one has $z\nu = 1$, the perturbative argument yields $d\nu/(z\nu + 1) = 1/2z$, which is in agreement with the finite-size scaling argument in Eq. (119). However, it was realized long ago (Dziarmaga, 2010) that the correspondence between the exact scaling in Eq. (122) and the perturbative prediction is tied to the relevance of the pairing term with respect to the momentum term in the scaling of the quasiparticle gap; see Eq. (55).

As outlined in Sec. IV.B.4, the presence of long-range anisotropic couplings in 1D Fermi systems may produce equilibrium scaling exponents dominated by the kinetic term in the gap scaling [see Eq. (78)], unlike what occurs in short-range systems. Similarly, the introduction of nonlocal finite-range couplings in the Kitaev model has been known to produce a modified equilibrium scaling with a kinetic dominated dynamical critical exponent. The latter phenomenon is found only near multicritical points, where finite-range nonlocal couplings become relevant and are known to lead to a violation of the Kibble-Zurek result (Deng, Ortiz, and Viola, 2009; Divakaran *et al.*, 2009; Dziarmaga, 2010).

At variance, the anisotropic Kitaev model with weak long-range couplings in the $\alpha < \beta$ regime already displays the aforementioned kinetic dominated scaling at a second-order quantum critical point (Defenu *et al.*, 2019). In particular, its dynamical phase diagram, which is depicted in Fig. 23, contains four different regions. Two of them (the green and white regions in Fig. 23) fulfill the Kibble-Zurek prediction,

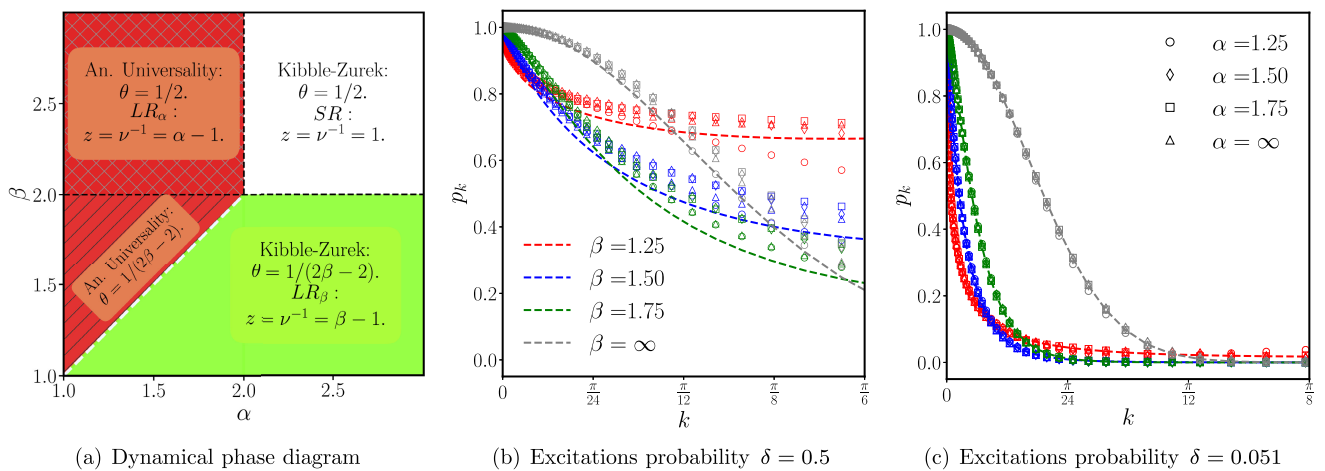


FIG. 23. Kibble-Zurek mechanism in long-range Kitaev chains. (a) Dynamical phase diagram reporting the universal slow-dynamics exponents of the anisotropic Kitaev chain in the (α, β) plane. (b),(c) Numerical analysis of Eq. (120) compared with the analytic formula in Eq. (121) for intermediate and small dynamical rates $\delta = 0.5, 0.05$. Each line represents a different value of $\beta = 1.25, 1.50, 1.75, \infty$, from bottom to top at small k . Different values of α are displayed with different symbols; see the legend in (c). Adapted from Defenu *et al.*, 2019.

with the nearest-neighbor universal exponents ($\theta = 1/2$ in the white region) and the pairing dominated critical exponents [$\theta = (2\beta - 2)^{-1}$ in the green region]. The conventional prediction $\theta = z\nu/(1 + z\nu)$ cannot be applied to the two red regions in Fig. 23, where $\alpha < \beta$, to the point that in the upper portion of the red region the nearest-neighbor prediction for the dynamics $\theta = 1/2$ remains valid deep in the regime where the equilibrium universal behavior is dominated by long-range interactions.

The absence of kinetic contributions to the critical dynamics holds only in the strict $\delta \rightarrow 0$ limit. Therefore, nonuniversal corrections still carry a sizable contribution to the defect density from the power law α as long as $\delta \lesssim 1$, as shown in Fig. 23(b), where a full numerical computation of the defect density for various points in the (α, β) plane (reported in different colors and shapes; see the legends in Fig. 23) is compared with the analytical prediction in Eq. (121) (dashed lines). These nonuniversal corrections are rapidly washed out in the slow drive limit; see Fig. 23(c), where the excitation probability at different α but with the same β collapse on each other.

Note that the agreement between the analytic prediction in Eq. (120) and the numerical result shown in Fig. 23(b) is limited by the δ^2 contributions to the excitation probability, which in turn are generated by the finite edge points of the present dynamical protocol. Actually, for a slow linear quench in the infinite interval $t \in [-\infty, \infty]$ the result in Eq. (120) will remain valid independently on the δ value.

In summary, several diverse predictions exist for the defect scaling after slow quenches in quantum many-body systems. In particular, the finite-size scaling argument in Eq. (119) and the traditional Kibble-Zurek result in Eq. (118) remain consistent with each other and with the exact solution for quadratic fermions as long as $z\nu = 1$. The last condition always holds for the fermionic system described in Sec. IV.B, but this is not the case for the interacting field theories described in Sec. IV.A, where the dynamical critical exponent $z\nu$ depends on the decay exponent; see Fig. 12. In particular, the mean-field approximation produces the result $z\nu = 1/2$ for rotor models, in agreement with the result observed in the LMG model, which represents the $\alpha = 0$ limit of such theories. In the following, we examine these extreme cases in detail and show how the Kibble-Zurek mechanism is modified by interactions in the strong long-range regime.

2. Lipkin-Meshkov-Glick model

In the following, the difficulty to reconcile the finite-size scaling prediction in Eq. (119) with the perturbative result $\theta = d\nu/(1 + z\nu)$ (Polkovnikov, 2005) is exemplified by a study of the flat interaction case $\alpha = 0$ such as that involving the LMG model, whose equilibrium behavior was described in Sec. IV.G. Apart from its prototypical role, the interest in the LMG model is motivated by the possibility to experimentally study slow dynamics in this system thanks to cold atoms in cavity experiments (Brennecke *et al.*, 2013), cold atoms in spin-1 ferromagnetic BECs (Saito, Kawaguchi, and Ueda, 2007; Anquez *et al.*, 2016; Hoang *et al.*, 2016; Xue, Yin, and You, 2018), and its relation to the BCS model (Dusuel and Vidal, 2005b).

The first numerical results on the scaling of the defect density after an adiabatic ramp crossing the quantum critical point of the LMG model could not be reproduced using the Kibble-Zurek formula in Eq. (118), but they displayed qualitative agreement with the finite-size scaling prediction in Eq. (119) (Caneva, Fazio, and Santoro, 2008). Yet, more intensive numerical studies unveiled a more complicated landscape where the adiabatic crossing of the equilibrium quantum critical point displays no actual Kibble-Zurek scaling, but rather a universal behavior as a function of the scaled variable $\Lambda = N\delta$ (Acevedo *et al.*, 2014), while nonanalytic corrections for the defect scaling were found for quenches up to the critical point (Hwang, Puebla, and Plenio, 2015).

This scenario can be safely reconstructed by the study of the effective critical theory depicted in Sec. IV.G.1. However, since the effective harmonic theory, which describes the fully connected problem at the order $1/N$, was obtained at equilibrium, it is first convenient to generalize the treatment to the dynamical case. Our goal is to consider the LMG problem with time-dependent coupling $h(t)$, with the system initially prepared at equilibrium at any initial time t_i and then manipulated across the quantum critical point. Thus, during the time evolution the average expectation value of the global spin will change as the order parameter is modified by the dynamics as soon as $h(t) < h_c$. As a consequence, the assumption of small quantum depletion of the classical equilibrium expectation $\langle S \rangle$, which is at the basis of the Holstein-Primakov expansion in Eqs. (105)–(107), is dynamically disrupted by the macroscopic change in the order parameter.

A simple solution to this difficulty is obtained by considering a time-dependent classical magnetization for the Holstein-Primakov expansion via the time-dependent spin-wave approximation introduced by Rückriegel, Kreisel, and Kopietz (2012). This solution strategy for the time-dependent, fully connected problem has already been employed to characterize the chaotic dynamical phase that emerges upon the inclusion of additional nearest-neighbor couplings on top of the LMG Hamiltonian (Lerose *et al.*, 2018; Lerose, Žunkovič, Marino *et al.*, 2019).

At the leading order $1/N$ this procedure effectively decouples the classical evolution of the order parameter from the quantum fluctuations. Ramping the magnetic field slowly across the critical point $h(t) = h_c - \delta t$ for $t \in [-1/\delta, 1/\delta]$ is equivalent to dynamically modifying the frequency of both the classical field and the quantum fluctuations according to the equilibrium equations (110) and (103). In principle, an accurate description of the ramp dynamics at finite δ would need the description of the backaction of the displacement of the classical observable from its equilibrium configuration into the dynamics of the quantum mode.

However, in the adiabatic limit $\delta \rightarrow 0$ we can employ the classical adiabatic theorem (Landau and Lifshitz, 1976) to conclude that the classical trajectory will remain close to the instantaneous solution $\theta(t) - \theta_{\text{eq}} \approx \delta^2$ and $\varphi(t) - \varphi_{\text{eq}} \approx \delta^2$, where the equilibrium contributions are $\varphi_{\text{eq}} = 0$ and θ_{eq} , as given in Eq. (102). Yet, based on the previous discussion the classical δ^2 correction is going to be superseded by that arising from quantum fluctuations. Indeed, quantum fluctuations in the LMG problem are effectively described by a single

harmonic mode adiabatically ramped across its fully degenerate quantum critical point.

None of the results on defect scaling presented at the beginning of Sec. V.C apply to this problem since the general result derived by dynamical perturbation theory does not apply to Bose quasiparticles (de Grandi and Polkovnikov, 2010). In fact, it was first noticed through asymptotic expansion that a quasistatic transformation of a harmonic oscillator with a linear time scaling of its frequency across the fully degenerate point $\omega(t)^2 \approx (\delta t)^2$ produces nonadiabatic corrections that do not vanish in the $\delta \rightarrow 0$ limit (Bachmann, Fraas, and Graf, 2017). This result does not directly apply to the LMG case, since for a linear scaling of the control parameter $\lambda(t) = h(t) - h_c = \delta t$ the dynamical frequency for the spin-wave model reads

$$\omega(t)^2 \approx \delta |t| \quad (123)$$

at leading order in the small-time δ expansion. Based on the conventional adiabatic argument $\dot{\omega}(t) \ll \omega(t)^2$, the faster the drive vanishes across the fully degenerate point, the stronger nonadiabatic effects are. Therefore, one may in principle expect the linear drive in Eq. (123) to be more adiabatic than the $\sim t^2$ case studied by Bachmann, Fraas, and Graf (2017) and to present a different nonadiabatic scaling.

In general, the characterization of slow dynamics for different kinds of excitations and dynamical scaling is relevant to the problem of long-range interactions. Indeed, we showed that the quantum long-range Ising model in Eq. (61) varies as a function of α from a critical point with Fermi quasiparticles ($\alpha > \alpha_*$) to a purely bosonic effective field theory [$\alpha < (5/3)d$]. In the first case ($\alpha > \alpha_*$), the validity of the Kibble-Zurek argument follows from the derivation of Dziarmaga (2005), which generally applies to critical systems with Fermi quasiparticles. In the intermediate case [$\alpha_* > \alpha > (5/3)d$] nonanalytic scaling $\sim \delta^\theta$ follow from the dynamical perturbation theory result of Polkovnikov (2005). However, this picture cannot be applied to Bose quasiparticles, whose large occupation numbers hinder the applicability of adiabatic perturbation theory (de Grandi and Polkovnikov, 2010).

Thus, the Kibble-Zurek scaling of mean-field systems, such as the LMG, whose excitation spectrum is described by free bosons, needs a tailored framework to be understood (Defenu *et al.*, 2018). In this perspective, one can consider a single dynamically driven Harmonic mode with a Hamiltonian

$$H(t) = \frac{1}{2}[p^2 + \omega(t)^2 x^2], \quad (124)$$

which faithfully describes the dynamics in Eq. (97), when adiabatic δ^2 corrections coming from the classical dynamics of the order parameter are neglected (Defenu *et al.*, 2018); see also Eq. (97).

For any time-dependent frequency a complete set of time-dependent states $\psi_n(x, t)$ can be constructed whose occupation is conserved by the dynamics (Lewis, 1967, 1968; Lewis and Riesenfeld, 1969). To determine the excitation density and the ground-state fidelity with respect to the instantaneous equilibrium solution of the problem, we define the adiabatic

basis $\psi_n^{\text{ad}}(x, t)$, which is obtained taking the conventional time-independent Harmonic oscillator eigenstates and replacing the constant frequency with the time-dependent one (Dabrowski and Dunne, 2016). Accordingly, one can expand the exact time-dependent state in terms of the adiabatic basis $\psi(x, t) = \sum c_n(t) \psi_n^{\text{ad}}(x, t)$, leading to the excitation density $n_{\text{exc}}(t) = \sum_{n \in 2\mathbb{N}} n |c_n|^2$, the adiabatic ground-state fidelity $f(t) = |c_0|^2$, and the residual heat $Q(t) = \omega(t) n_{\text{exc}}(t)$ expressions.

According to the behavior of these observables in the adiabatic limit $\delta \rightarrow 0$ the dynamical evolution described by Eq. (124) presents the following three regimes:

- (1) Perturbative regime ($Q \sim \delta^2$).
- (2) Kibble-Zurek regime ($Q \sim \delta^{2\nu/(1+\nu)}$, half ramp).
- (3) Nonadiabatic regime [$Q \sim O(1)$, full ramp].

Regime (1) occurs for a finite minimal frequency at the critical point $\lim_{t \rightarrow 0} \omega(t) = \omega_0 \neq 0$: there the adiabatic perturbation theory result produces the analytic δ^2 corrections predicted by dynamical perturbation theory. Regime (2) is realized in a dynamics terminating at the quantum critical point $\omega_0 = 0$, where nonanalytic corrections appear that are encompassed by the Kibble-Zurek argument. The actual crossing of the quantum critical point occurs only in regime (3) and the actual non-adiabatic regime is realized, leading to rate-independent corrections to the adiabatic observables, as seen in the following.

For a finite thermodynamic system, we expect the dynamical gap not to completely vanish at the critical point but to present a finite correction vanishing according to a finite-size scaling $\omega_0^2 \approx N^{-1/\nu_*}$, where $\nu_* = 3/2$ according to Eq. (111). After the scaling transformation discussed by Defenu *et al.* (2018), the residual scaled frequency therefore depends only on the parameter combination $\Lambda = N\delta$. Then, since the minimal scaled frequency reads $\tilde{\omega}^2(0) \approx \Lambda^{-2/3}$, it follows that the thermodynamic limit ($N \rightarrow \infty$) and the adiabatic one ($\delta \rightarrow 0$) do not commute. Rather, the same dynamical evolution for thermodynamical observables occurs for different sizes and drive rates as long as the combination Λ remains fixed. The universal behavior evidenced for this harmonic effective model faithfully reproduces exact numerical computations. Indeed, a comparison between the analytic and numerical analyses of the LMG model is shown in Fig. 24 proving that the ‘‘anomalous’’ scaling described by Acevedo *et al.* (2014) is perfectly justified by the effective model studied here and introduced by Defenu *et al.* (2018).

3. Structural transitions

Ion crystals and, in general, structural transitions occurring in nonlocal systems with competing interactions first triggered theoretical interest in the Kibble-Zurek scaling of nonhomogeneous systems (Zurek, 2009; Chiara *et al.*, 2010; del Campo *et al.*, 2010). In the presence of inhomogeneity, the critical point occurs at different moments in the different regions of the system, restoring adiabaticity for a dynamical transition where critical excitations propagate faster than the phase boundaries. An argument straightforward enough to justify the previous picture is found by generalizing the scaling theory outlined at the beginning of Sec. V.C in the nonhomogeneous case.

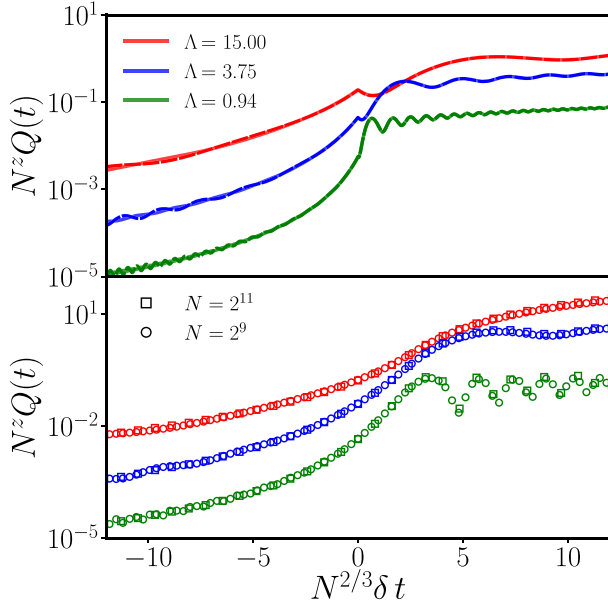


FIG. 24. Universal slow dynamics of the LMG model. Heat curves obtained via the effective model in Eq. (124) (upper panel) and via a full numerical solution of the time-dependent LMG model in Eq. (97) (lower panel) with a time-dependent coupling $J = h_c - \delta t$ performed by Acevedo *et al.* (2014). Each color represents a value of $\Lambda = N\delta = 15, 3.75, 0.94$, progressing from top to bottom, with $N = 2^9$ and $N = 2^{11}$ (dashed and solid lines in the upper panel). Both the heat and time variables were rescaled following the notation of Acevedo *et al.* (2014). As expected, the curves at different sizes but the same Λ collapse both in theory and in the exact simulations. Moreover, the similarity between the theoretical model and the numerics is noteworthy. Despite the fact that the model in Eq. (124) is simply an effective model that does not account for the mean-field energy shift, it captures quantitative features such as the initial smooth increase and the oscillations of the residual energy. The numerical data displayed in the lower panel are courtesy of Acevedo *et al.* (2014).

We consider a both spatial and time-dependent control parameter $\lambda(x, t)$ such that the critical front occurs at $\lambda(x, t) \approx 0$, while in general one has

$$\lambda(x, t) = \alpha(x - v_p t), \quad (125)$$

where $v_p > 0$ is the velocity of the phase front. Locally, the inhomogeneous control parameter in Eq. (125) resembles a homogeneous case with ramp rate $\delta = \alpha v_p$. Accordingly, all the locations of the systems where $\lambda(x, t) < 0$ already lie in the symmetry-broken phase, and they can then communicate the orientation of the order parameter across the phase boundary at $\lambda(x, t) \approx 0$ toward the symmetric regions of the system where $\lambda(x, t) > 0$. The maximal velocity \hat{v}_p at which this communication occurs can be found via the relation $\hat{v}_p = \hat{\xi}/\hat{t}$. As long as $v_p \gg \hat{v}_p$ inhomogeneity is not relevant, since the regions on the opposite side of the phase front are effectively decoupled. On the contrary, defect formation is suppressed for $v_p \ll \hat{v}_p$ due to the symmetry-broken regions of the system coordinating with the ones at $\lambda(x, t) > 0$.

Following the previous discussion, one can use the conventional scaling relations for the homogeneous Kibble-Zurek mechanism to obtain $\hat{v}_p \sim \delta^{(z-1)\nu/(z\nu+1)} \sim \alpha^{(z-1)\nu/(\nu+1)}$, which in turn leads to the “critical” ramp rate

$$\hat{\delta} \sim \alpha^{(z\nu+1)/(1+\nu)}. \quad (126)$$

At rates $\delta \gg \hat{\delta}$ the system effectively behaves homogeneously and the traditional results for the excitations density are retrieved. Conversely, in the slow drive limit $\delta \ll \hat{\delta}$ inhomogeneity becomes relevant and can alter the universal Kibble-Zurek scaling. Accordingly, in the homogeneous limit the critical rate vanishes $\lim_{\alpha \rightarrow 0} \hat{\delta} = 0$. Several examples of nonhomogeneous Kibble-Zurek mechanism can be found in the literature (Schaller, 2008; Zurek and Dorner, 2008; Collura and Karevski, 2010; Dziarmaga and Rams, 2010).

Thanks to their tunability (Lemmer *et al.*, 2015), trapped-ion platforms have played a crucial role in both the theoretical and experimental investigations of defects formation in the nonhomogeneous realm (Schneider, Porras, and Schaetz, 2012; Lemmer *et al.*, 2015). By adiabatically altering the trapping parameters, it is possible to drive the system across the structural transition that was outlined in Sec. IV.F (Baltrusch, Cormick, and Morigi, 2012). However, this procedure will naturally generate localized defects, which is in agreement with the Kibble-Zurek theory (Schneider, Porras, and Schaetz, 2012). A similar phenomenology is also expected for sudden quenches across the boundary of the structural transition (del Campo *et al.*, 2010; Landa *et al.*, 2010). Moreover, the dynamics of local defects in Coulomb crystals have been proposed to realize the Frenkel-Kontorova model (Pruttivarasin *et al.*, 2011; Cormick and Morigi, 2012).

The experimental exploration of the quantum dynamics and formation of kinks in Coulomb crystals (Pyka *et al.*, 2013; Ulm *et al.*, 2013) have shown good agreement with the theory expectation (Landa *et al.*, 2010), providing a flexible tool to investigate defect formation according to the inhomogeneous Kibble-Zurek mechanism (Chiara *et al.*, 2010; del Campo *et al.*, 2010).

4. Cavity systems

Quench experiments based on quantum gases in optical cavities (Baumann *et al.*, 2011; Klinder, Keßler, Wolke *et al.*, 2015) have also been interpreted within the framework of the Kibble-Zurek mechanism (Kibble, 1976; Zurek, 1985; del Campo and Zurek, 2014). The global character of the cavity-mediated interaction inhibits the formation of domains, and thus also of defects during the crossing of this second-order phase transition. However, remnants of the Kibble-Zurek mechanism can be found in hysteretic behavior and the symmetry breaking itself.

In the case of a retarded cavity-mediated interaction, i.e., where the cavity linewidth κ is comparable to the recoil frequency ω_r , pronounced dynamical hysteresis has been observed when the self-organization phase transition is crossed (Klinder, Keßler, Wolke *et al.*, 2015); see Fig. 25. The intracavity light field corresponding to the order parameter shows a hysteresis loop that encloses an area exhibiting a

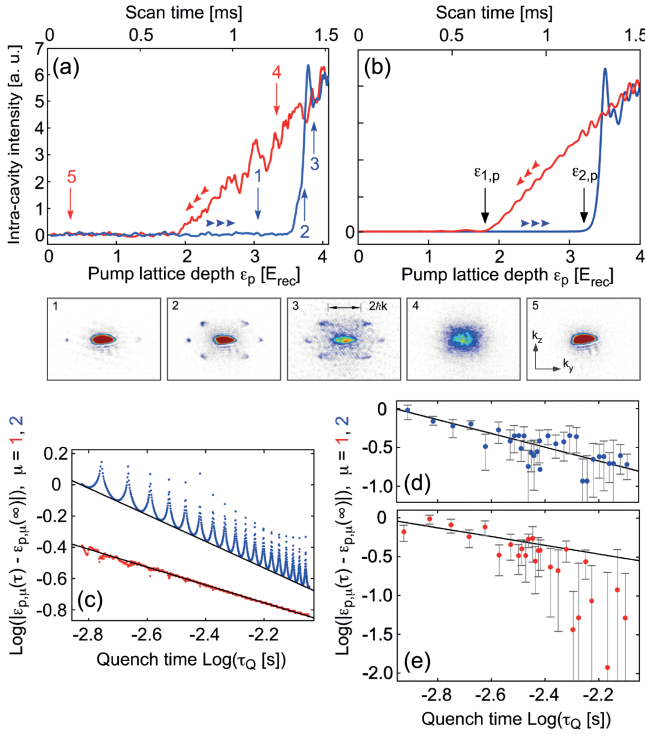


FIG. 25. Dynamical critical behavior at the self-organization phase transition. (a) Intra-cavity intensity while the transverse pump lattice depth ϵ_p is ramped up (blue) and down (red) in ramps of 1.5 ms each. Shown beneath the panel are momentum spectra (1)–(5), recorded at increasing times during the ϵ_p ramp, indicated by the numbered arrows in (a). (b) Mean-field calculation according to (a) neglecting collisional interactions and assuming an infinite system. The points $\epsilon_{p,1}$ and $\epsilon_{p,2}$ indicate the upper and lower critical lattice depths. (c) Mean-field calculations of $\epsilon_{p,1}$ and $\epsilon_{p,2}$ as a function of quench time, resulting in exponents of $(n_1, n_2) = (-0.57, 0.85)$ for power-law fits. (d), (e) Experimentally determined dependence of the upper and lower critical lattice depths on the quench time, together with solid lines reproducing the power-law dependences of (c). From Klinder, Keßler, Wolke *et al.*, 2015.

power-law dependence upon the duration of the quench across the phase transition. Real-time observation of the intra-cavity field thus allows one to identify at which coupling strength the system effectively freezes its dynamics, depending on the quench rate. A simple power-law model allows dynamical exponents $z\nu$ to be extracted. However, a deeper interpretation would require a comprehensive extension of the study of universality to driven-dissipative systems (Sieberer *et al.*, 2013; Klinder, Keßler, Wolke *et al.*, 2015). In particular, note that these experimental observations appear not to follow the theoretical predictions outlined in Sec. V.C.2 and by Acevedo *et al.* (2014) and Defenu *et al.* (2018) for isolated quantum systems.

In the limit of large cavity linewidth with respect to the atomic recoil frequency (Baumann *et al.*, 2011), the hysteresis loop is vanishing (Klinder, Keßler, Wolke *et al.*, 2015), but the effect of the quench rate can be observed in the discrete symmetry breaking described in Sec. IV.G.3. The finite size of the system naturally leads to a small symmetry-breaking field, thereby completely dominating the symmetry-breaking

process in the limit of adiabatically crossing the phase transition. However, for a finite quench rate, the approach to the phase transition can again be divided into a quasiadiabatic regime where the system follows the control parameter and an impulse regime where the system is effectively frozen. For increasing quench rates of the transverse pump power, the coupling strength separating these two regimes is decreasing, as captured by Zurek's equation (Zurek, Dorner, and Zoller, 2005) $|\dot{\zeta}/\zeta| = \Delta/\hbar$, with $\zeta = (\Lambda_c - \Lambda)/\Lambda_c$ describing the distance to the critical point (see also Sec. II.B.3) and the energy gap between the ground and first excited state $\Delta = \hbar\omega_0\sqrt{1 - \Lambda^2/\Lambda_c^2}$. Accordingly, in the experiments the symmetry breaking for large quench rates becomes dominated by quantum fluctuations and increasingly independent of the symmetry-breaking field. A quantitative agreement of the observations with the model was found (Baumann *et al.*, 2011).

D. Dynamical phase transitions

One of the most relevant scaling phenomena in the far-out-of-equilibrium realm is provided by dynamical phase transitions (Zvyagin, 2016; Mori *et al.*, 2018). In particular, after the sudden quench of a control parameter dynamical phase transitions may be classified into two main families. The first family displays a possibly local order parameter $A(t)$, whose long-time Cesaro's average \bar{A} , defined according to Eq. (113), characterizes different steady states (Eckstein and Kollar, 2008; Moeckel and Kehrein, 2008; Eckstein, Kollar, and Werner, 2009; Sciolla and Biroli, 2010; Halimeh *et al.*, 2017; Lang, Frank, and Halimeh, 2018). While this phenomenon is naturally observed for quenches across equilibrium symmetry-breaking transitions, diverse dynamical phases may also arise in quantum systems, which do not possess any finite-temperature phase transition. There, following a sudden quench, the order parameter $A(t)$ always equilibrates to its normal phase expectation in the long-time limit ($\bar{A} = 0$ for ferromagnetic systems), but the dynamical phase transition can be observed in a sudden change in the scaling approach to equilibrium (Altman and Auerbach, 2002; Barmettler *et al.*, 2009; Heyl, 2014; Lang, Frank, and Halimeh, 2018).

Experimental evidence of this first kind of dynamical transitions has been found in a linear chain of trapped $^{171}\text{Yb}^+$ ion spins stored in a Paul trap (Zhang, Pagano *et al.*, 2017). The system was initialized in the ferromagnetic product state $|\psi_0\rangle = |\downarrow\downarrow\downarrow\downarrow\cdots\downarrow\rangle_x$ and then evolved according to the long-range Ising Hamiltonian (61). The dynamical quantum phase transition occurs when the ratio $\hbar/J_0 \sim 1$, where J_0 is the strength of long-range interactions ($V_r \propto J_0/r^\alpha$) and the order parameter changes abruptly from ferromagnetic to paramagnetic order. The observation of the dynamical transition has been obtained by measuring the late time average of the two-body correlator defined as

$$C_2 = \frac{1}{N^2} \sum_{ij} \langle \sigma_i^x \sigma_j^x \rangle \quad (127)$$

after the quantum quench.

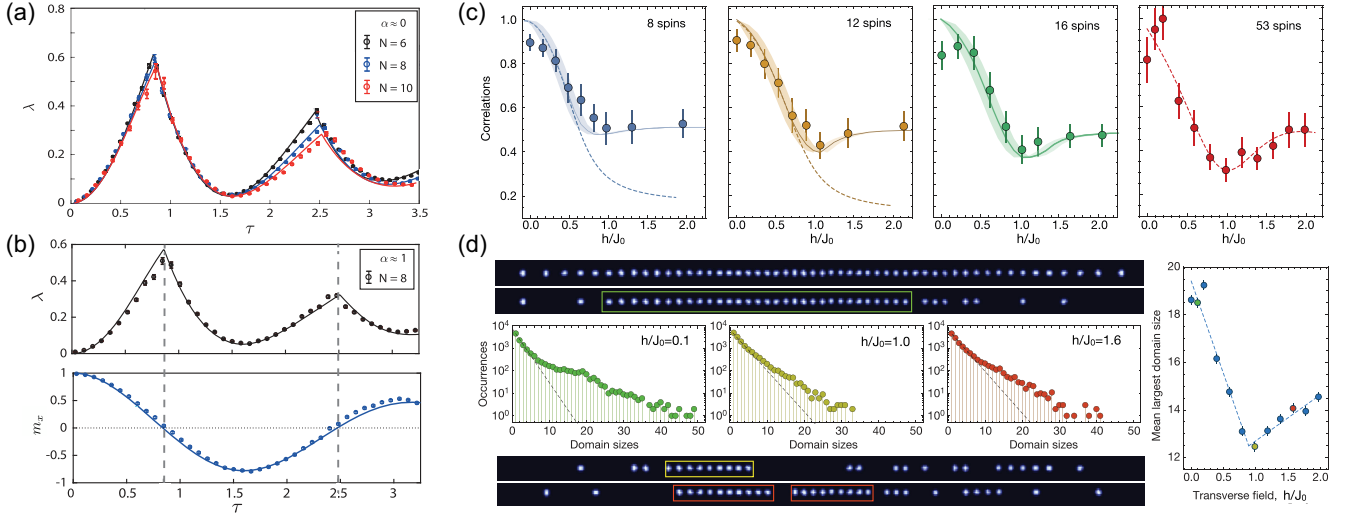


FIG. 26. (a),(b) Type-I and (c),(d) type-II dynamical phase transitions. (a) Measured rate function λ for three different system sizes at $h/J_0 \approx 2.38$, with $\tau = th$ the dimensionless time. The kinks in the evolution become sharper for larger N . Here the rate function is defined based on the return probability to the ground-state manifold, namely, $\lambda(t) = N^{-1} \log(P_{|\psi_0\rangle} + P_{|-\psi_0\rangle})$, where $|-\psi_0\rangle = |\uparrow\uparrow\uparrow\cdots\uparrow\rangle_x$. (b) Comparison between the rate function $\lambda(t)$ and the magnetization evolution $m_x(t)$. The inversion of the magnetization sign corresponds to the nonanalyticity of the rate function $\lambda(t)$. The solid lines are exact numerical predictions based on the experimental parameters ($h/J_0 = 2$). Adapted from [Jurcevic *et al.*, 2017](#). (c) Long-time averaged values of the two-body correlations C_2 for different numbers of spins in the chain. The solid lines are exact numerical solutions to the Schrödinger equation, and the shaded regions take into account uncertainties from experimental Stark shift calibration errors. The dashed lines for $N = 12, 16$ are calculations using a canonical (thermal) ensemble with an effective temperature corresponding to the initial energy density. (d) Domain statistics and reconstructed single-shot images of 53 spins. Top and bottom images: reconstructed images based on binary detection of the spin state. The top image shows a chain of 53 ions in bright spin states. The other three images show 53 ions in combinations of bright and dark spin states. Center panel: statistics of the sizes of domains for three different values of h/J_0 plotted on a logarithmic scale. The dashed lines are fits to the exponential functions that are expected for an infinite-temperature thermal state. Long tails of deviations are clearly visible and vary depending on h/J_0 . Right panel: mean of the largest domain sizes in every experimental shot. The dashed lines represent a piecewise linear fit used to extract the transition point. The green, yellow, and red data points correspond to the transverse fields shown in the domain statistics data in the center panel on the left. Adapted from [Zhang, Pagano *et al.*, 2017](#).

The measured late time correlator C_2 features a dip at the critical point that sharpens scaling up the system size N up to 53 $^{171}\text{Yb}^+$ qubits, as shown in Fig. 26(c). Additional evidence of the occurrence of the dynamical phase transition can also be observed in higher-order correlations, such as the distribution of domain sizes throughout the entire chain, as shown in Fig. 26(d). The occurrence of the dynamical phase transition is observed in the decreased probabilities of observing long strings of aligned ions at the critical point $h/J_0 \sim 1$. This is shown by measuring the mean largest domain size as a function of the transverse-field strength, for late times and repeated experimental shots, which feature a sharp transition at the critical point. Another recent experimental realization of dynamical phase transitions within the LMG model was reported by [Muniz *et al.* \(2020\)](#). The experiment was performed with large ensembles of ^{88}Sr atoms in an optical cavity where magnetic interactions can be accurately tuned ([Norcia *et al.*, 2018](#)) and reported the observation of distinct dynamical phases of matter in this system. A similar setup has also been proposed for the observation of dynamical phases of the BCS model in superconductivity as a function of system parameters and the prepared initial states ([Lewis-Swan *et al.*, 2021](#)).

The second family of dynamical phase transitions features periodic nonanalyticities in the Loschmidt return rate ([Heyl, Polkovnikov, and Kehrein, 2013](#)). It is convenient to define

the return probability to the initial state $|\psi_0\rangle$ after a quantum quench under the Hamiltonian H as $\mathcal{G}(t) = \langle\psi_0|e^{-iHt}|\psi_0\rangle$. This quantity exhibits nonanalyticities that are formally analogous to those of the partition function of the corresponding equilibrium system, which is defined as $Z = \text{Tr}(e^{-H/k_B T})$ ([Heyl, Polkovnikov, and Kehrein, 2013](#)). Along this analogy, the complex counterpart of the thermodynamic free-energy density $f = -N^{-1}k_B T \log(Z)$ is the rate function $\lambda(t) = -N^{-1} \log[\mathcal{G}(t)]$. In the thermodynamic limit, this quantity exhibits dynamical real-time nonanalyticities that play a role as the nonanalytic behavior analogous to the free-energy density of a thermodynamic system at equilibrium.

As a consequence of these statements, the nonanalyticities in the return rate signal the occurrence of dynamical quantum phase transitions at certain critical evolution times after the sudden quench. These phenomena have generated a high degree of interest from both the theoretical ([Heyl, 2018](#); [Mori *et al.*, 2018](#)) and experimental communities ([Jurcevic *et al.*, 2017](#); [Fläschner *et al.*, 2018](#)). The first theoretical description of dynamical phase transitions in return rates has been shown in the case of the nearest-neighbor transverse-field Ising chain. There nonanalytic cusps in the return rate could be observed only after a sudden quench across the equilibrium critical point. It was shown by several subsequent examples that dynamical crossing of an equilibrium phase boundary may not

produce the aforementioned cusps in the return rates, while sudden quenches within the same phase may produce the so-called type-II dynamical phase transitions (Andraschko and Sirker, 2014; Vajna and Dóra, 2014).

Therefore, the dynamical critical point for the appearance of type-II dynamical phase transitions does not need to coincide with the quantum critical point of the system at equilibrium. Further proof of this distinction comes from the strong dependence of the dynamical critical point on the initial state of the system (Halimeh *et al.*, 2017; Lang, Frank, and Halimeh, 2018). In this perspective, long-range interactions have been shown to produce several additional dynamical phases with respect to the simple nearest-neighbor case (Halimeh and Zauner-Stauber, 2017; Homrighausen *et al.*, 2017; Defenu, Enss, and Halimeh, 2019; Urich *et al.*, 2020). It is thus not surprising that the first observation of type-II dynamical phase transitions has been detected in a trapped-ion simulation of the long-range Ising Hamiltonian (61).

The simulation was performed with a linear chain of trapped $^{40}\text{Ca}^+$ ion spins (Jurcevic *et al.*, 2017). The system is prepared in the classical eigenstate, which minimizes the ferromagnetic interactions $|\psi_0\rangle = |\downarrow\downarrow\downarrow\cdots\downarrow\rangle_x$. A finite transverse field is suddenly switched on (quenched) such that the Hamiltonian (61) lies in $h > J_0$, with J_0 the average nearest-neighbor spin-spin coupling. Figure 26 displays the return rate λ , which exhibits clear nonanalyticities at the critical times t_c . As expected, the Loschmidt echo cusps also correspond to the zero crossings of the order parameter at the critical times t_c ; see Fig. 26(b).

The correspondence between the zero crossings of the order parameter and the cusps of the return rate $\lambda(t)$ is not the only relation between the two families of dynamical phase transitions. Indeed, the dynamical critical points for type-I and type-II transitions were shown to coincide (Halimeh *et al.*, 2017; Žunkovič *et al.*, 2018). More generally, the fundamental relations between thermodynamic equilibrium phases and their dynamical counterparts has been extensively explored not only in terms of order parameters (Ajisaka, Barra, and Žunkovič, 2014; Heyl, 2018; Žunkovič *et al.*, 2018; Titum *et al.*, 2019) but also with respect to scaling and universality (Heyl, 2015), discrete or continuous symmetry breaking (Žunkovič, Silva, and Fabrizio, 2016; Weidinger *et al.*, 2017; Huang, Banerjee, and Heyl, 2019), and the nature of the quasiparticles (Syed, Enss, and Defenu, 2021).

Free-fermionic systems, which are described by the Kitaev Hamiltonians studied in Sec. IV.B, played a prominent role in both the experimental and the theoretical study of dynamical phase transitions. Indeed, despite the absence of a local order parameter in the equilibrium topological phase transition of the Kitaev chain, dynamical phase transitions also occur in these models (Vajna and Dóra, 2015; Budich and Heyl, 2016; Bhattacharya and Dutta, 2017a, 2017b), where they have been experimentally observed (Fläschner *et al.*, 2018). The possibility of also analytically solving free-fermionic models in the presence of long-range hopping or pairing produced a comprehensive understanding of how additional dynamical phases can be influenced by corrections to scaling in the spectrum, as well as its relation to the results for the Ising model (Defenu, Enss, and Halimeh, 2019). Despite the

absence of any local order parameter in free Fermi systems, a relation exists between the occurrence of cusps in the Loschmidt echo and the zero crossings of the nonlocal string order parameter (Urich *et al.*, 2020).

Despite its close relation to the Kitaev chain (see Sec. IV.B.3), the long-range Ising model presents a more complex phenomenology with respect to the Kitaev chain. Indeed, the Ising model supports the appearance of domain-wall confinement due to long-range interactions (Liu *et al.*, 2019). These confined excitations behave like Stark-localized particles in an effective confining potential (Lerose *et al.*, 2020); see also Sec. V.E. This domain-wall coupling was found to be the reason for the appearance of anomalous cusps in quantum quenches at sufficiently small transverse-field strengths (Halimeh and Zauner-Stauber, 2017; Halimeh *et al.*, 2020), while the absence of quasiparticles coupling in the Kitaev chain disrupts the anomalous phase (Defenu, Enss, and Halimeh, 2019).

Critical quenches where the postquench Hamiltonian is critical are known to yield long-time universal scaling behavior following the mechanism of aging (Chiocchetta *et al.*, 2017). These kinds of phenomena are strongly influenced by long-range interactions, as studied by Halimeh and Maghrebi (2021). In particular, in the LMG model, depending on the type of quench, three behaviors where both the short-time dynamics and the stationary state at long times are effectively thermal, quantum, and genuinely nonequilibrium were identified. Each stationary state is characterized by distinct static and dynamical critical exponents (Titum and Maghrebi, 2020).

E. Confinement

As shown in Sec. V.B, long-range interactions can give rise to the fast spreading of correlations. However, while focusing on trapped-ion systems in this section we review a different regime in which long-range interactions allow the observation of confinement.

In general, spin models can be engineered to exhibit confinement of correlations and meson production. Kormos *et al.* (2017) studied the case of a global quench with the nearest-neighbor Ising Hamiltonian

$$H = -J \sum_i \sigma_i^x \sigma_{i+1}^x + h_z \sum_i \sigma_i^z + h_x \sum_i \sigma_i^x, \quad (128)$$

with both transverse field h_z and longitudinal field h_x . In this case, the dynamics produces confinement of quasiparticles and magnetization oscillations with frequencies related to the mass and energy differences between the bound states most involved in the dynamics. In this setting, the quasiparticle excitation is mapped to domain walls whose separation is energetically suppressed by the longitudinal field, which causes the appearance of a ladder of discrete meson states in the low-energy spectrum of the system (James, Konik, and Robinson, 2019). After a quantum quench in this system, both correlation spreading and energy flow (Mazza *et al.*, 2019) are suppressed, even if the system is nonintegrable and nondisordered.

A similar phenomenology can also be observed in long-range spin systems described by Hamiltonian (61), as theorized by Liu *et al.* (2019) for low-energy states and $\alpha < 3$

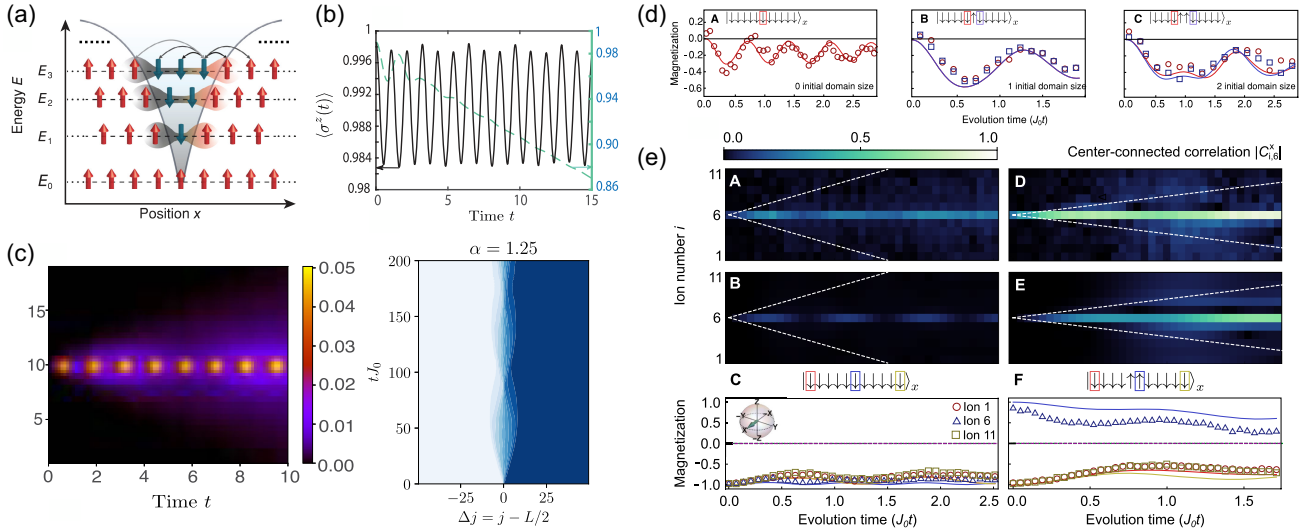


FIG. 27. Confinement in long-range spin systems. (a) Magnetic domain walls in Ising spin chains can experience an effective confining potential that increases with distance analogously to the strong nuclear force. This potential results in mesonlike domain-wall bound states (labeled E_1 to E_3) that influence the postquench dynamics. Adapted from Tan *et al.*, 2021. (b) Magnetization oscillation $\langle \sigma_z(t) \rangle$ (black line) vs time after quenching to $\alpha = 2.3$ and $B_z = 0.27J_0$ for $N = 20$. The dashed green lines show the magnetization for the transverse-field Ising model with nearest-neighbor interactions only. The numerical calculations were adapted from Liu *et al.* (2019). (c) Left panel: confinement of correlation in long-range systems for $\alpha = 2.3$ starting with the polarized state $|\downarrow\downarrow\cdots\downarrow\rangle$. Adapted from Liu *et al.*, 2019. Right panel: confinement of correlation in long-range systems for $\alpha = 1.25$ starting with the highly excited state $|\downarrow\downarrow\cdots\downarrow\uparrow\uparrow\cdots\uparrow\rangle$. Adapted from Leroše, Žunkovič, Silva, and Gambassi, 2019. (d) Magnetization oscillations ($\alpha \sim 1.1$) starting with low-energy product states to probe the first three meson masses. Adapted from Tan *et al.*, 2021. (e) Confinement dynamics at $B_z/J_0 \approx 0.75$, $L = 11$, $\alpha \sim 1.1$. Top row: absolute value of experimental center-connected correlations $|C_{i,6}^x(t)|$ averaged over 2000 experiments. Middle row: $|C_{i,6}^x(t)|$, calculated by solving the Schrödinger equation. The dashed white lines show correlation propagation bounds (light cones) in the limit $\alpha \rightarrow \infty$ (nearest-neighbor interactions). Bottom row: measured individual-spin magnetizations along their initialization axes $\langle \sigma_i^z(t) \rangle$ averaged over 2000 experiments. The symbols represent magnetization data, and the solid colored curves represent theoretical magnetizations calculated by solving the Schrödinger equation. Purple (green) dashed lines represent thermal expectation values extracted from a canonical (microcanonical) ensemble averaged over the three displayed spins. Adapted from Tan *et al.*, 2021.

[see Figs. 27(b) and 27(c)] and by Leroše, Žunkovič, Silva, and Gambassi (2019) for highly excited states with $\alpha < 2$ [see Fig. 27(d)]. The confining potential induced by the long-range tail of the interaction on the domain walls acts, to a first approximation, as an effective longitudinal field that constrains the evolution of the spin excitations; see Fig. 27(a). Therefore, in the regime in which the transverse field h_z is smaller than the spin-spin interaction J_0 , long-range interactions cause a phenomenology analogous to that found in the Hamiltonian (128): the presence of bound states results in magnetization oscillations and a slow spread of correlations.

Magnetization oscillations have been observed experimentally for a chain of up to 38 ions (Tan *et al.*, 2021), showing a mass scaling that is in agreement with theory in the low-energy part of the spectrum. Tan *et al.* (2021) used a smaller chain of 11 ions to probe the first few bound states by preparing different initial product states and measuring the magnetization $\langle \sigma_i^z(t) \rangle$ at the center of the chain (for zero initial domain walls) or next to the boundaries of the initial domain (for two initial domain walls). The initial states have been chosen to maximize the matrix elements of the magnetization between the prepared state i and the adjacent higher-energy bound state $i + 1$, allowing the energy gap between these two states to be extracted; see Fig. 27(d). Similarly, a slow spread of correlations has been observed by measuring two-body

correlations of the central spin with the rest of the system, resulting in a much slower correlation spread than in the nearest-neighbor Ising chain; see Fig. 27(e).

The possibility of engineering mesons in long-range interacting spin systems has sparked an increasing body of theoretical works on the existence of string breaking in a specific range of parameters (Verdel *et al.*, 2020) and meson collisions (Karpov *et al.*, 2020; Surace and Leroše, 2021).

F. Other dynamical phenomena

1. Many-body localization

Long-range interacting quantum systems have also been explored in different settings, including disordered fields or interactions or in a Floquet setting, where the system is subjected to a periodic drive. In the presence of disorder, long-range interacting quantum systems can exhibit many-body localization (MBL), where the system fails to thermalize at long times owing to the existence of an extensive set of quasilocals integrals of motion (Nandkishore and Huse, 2015; Abanin *et al.*, 2019). However, sufficiently long-range interactions can destroy many-body localization, as shown by Pino (2014) and Yao *et al.* (2014). In this perspective, as occurred for the XXZ model in Secs. IV.C and IV.D, it is important to differentiate between the case of long-range exchange couplings, i.e., hopping terms in the Hubbard model

representation, and long-range density-density interactions, i.e., Ising interactions in the spin formalism.

In particular, for long-range hopping terms, analytical arguments have been used to predict the boundary $\alpha < 3d/2$ (Burin, 2015a) as a condition for delocalization in long-range spin systems governed by an XY Hamiltonian, while in the case of long-range Ising interactions the boundary value has been found to be $\alpha_* = 2d$ (Burin, 2015b). Within this framework, the relaxation rates of local excitations in dipolar disordered systems were studied in two and three dimensions by Nandkishore and Gopalakrishnan (2021) as a function of frequency and temperature. In the case of a long-range spin exchange, Safavi-Naini *et al.* (2019) showed numerical evidence indicating that an XY model is delocalized for $\alpha < 1$ in one dimension, in contrast with the $\alpha_* = 1.5$ result of Burin (2015a). This other prediction might be due to how dominant finite-size effects are for system sizes that can be simulated exactly. In this respect, Maksymov and Burin (2020) studied the scaling with the size of the critical disorder for $\alpha < (3/2)d$. Nandkishore and Sondhi (2017) used bosonization arguments to show that MBL can arise in one-dimensional systems with $\sim r$ interactions and speculate that MBL can be observed in two-dimensional systems with $\log(r)$ interactions, and in three-dimensional systems with $1/r$ interactions. MBL has been predicted with a mean-field analysis (Roy and Logan, 2019) on the disordered XXZ model with different power-law exponents for $\beta < 1/2$ and $\beta < \alpha$, where α is the decay exponent long-range exchange couplings and β that of long-range Ising interactions. MBL has also been found numerically in all-to-all systems (Sierant *et al.*, 2019) and fermionic system with long-range hopping (Nag and Garg, 2019).

An important feature of MBL in the presence of long-range density-density interactions is algebraic localization of the quasilocal integrals of motion (LIOMs) that characterize the MBL phase (Pino, 2014; De Tomasi, 2019). Conversely, in short-range interacting systems LIOMs are exponentially localized and entanglement entropy grows logarithmically. However, since in MBL long-range systems LIOMs are algebraically localized, one would expect entanglement entropy to grow polynomially (Safavi-Naini *et al.*, 2019). In particular, Deng *et al.* (2020) showed that in a variety of models (the XY , XXZ , and extended Hubbard models) with power-law interactions there is a universal power-law growth of the entanglement entropy at the MBL transition. Experimental signatures of many-body localization in long-range systems, such as memory of the initial states (Smith *et al.*, 2016), confirmed numerically by Wu and Das Sarma (2016), and slow growth of the second-order Renyi entropy (Brydges *et al.*, 2019), have been observed in trapped-ion chains of up to 20 qubits.

More recently disorder-free, “stark” MBL (Schulz *et al.*, 2019; van Nieuwenburg, Baum, and Refael, 2019) has been predicted to be more resilient than “standard” MBL to long-range exchange couplings (Bhakuni and Sharma, 2020). This phenomenon was later connected to the Hilbert-space shattering caused by conservation laws (Khemani, Hermele, and Nandkishore, 2020; Moudgalya *et al.*, 2021). Signatures of this type of disorder-free MBL have been observed in a trapped-ion chain of up to 25 qubits with long-range

interactions decaying with $\alpha \sim 1.3$ and a strong effective magnetic field gradient (Morong *et al.*, 2021). As mentioned in Sec. II.A.1, a large magnetic field makes the Ising model an effective XY model with long-range exchange couplings, and in this case the LIOMs are given by the Wannier-Stark states. Conversely, in the case of long-range density-density interactions, one expects Hilbert-space fragmentation, which has also been studied in short-range interacting disordered spinless fermions (Bar Lev, Cohen, and Reichman, 2015; De Tomasi *et al.*, 2019). In particular, in Hubbard models with polar interactions and nearest-neighbor hoppings (Li, Deng, and Santos, 2021) the power-law tail plays a crucial role because it induces Hilbert-space shattering and MBL-like localization in the absence of any disorder, even for moderate ratios of the polar interactions versus hopping. This is not the case for models with both nearest-neighbor hopping and density-density interactions, where Hilbert-space fragmentation does not lead to disorder-free MBL (De Tomasi *et al.*, 2019).

2. Periodic drive

Quantum many-body systems with both disorder and interactions have recently been used to observe new phases of matter in periodically driven Floquet systems (Else, Bauer, and Nayak, 2016; Khemani *et al.*, 2016; von Keyserlingk, Khemani, and Sondhi, 2016; Yao and Nayak, 2018) in which discrete-time translational symmetry is spontaneously broken. The observation of time-crystalline behavior has been achieved in a periodically driven 1D trapped-ion chain with on-site static disorder (Zhang *et al.*, 2017) and a 3D disordered sample of nitrogen-vacancy (N-V) centers with a dipolar interaction (Choi *et al.*, 2017). However, it was later shown numerically (Khemani, Moessner, and Sondhi, 2019) that neither realization realizes a genuine discrete time crystal where MBL prevents the system from heating to infinite temperature, instead promoting a prethermal (trapped ions) and critical (N-V centers) time crystal. Recently genuine MBL time crystals have been realized in systems with disordered interactions in a system of nine ^{13}C nuclear spins coupled to a single N-V center (Randall *et al.*, 2021) and in the Google quantum computer (Mi *et al.*, 2022) using 20 superconducting qubits with fully programmable interactions. In the same spirit, quasiperiodic Floquet drives have been predicted (Friedman *et al.*, 2022) to realize an emergent dynamical symmetry-protected topological phase that was experimentally realized with ten atomic ions by Dumitrescu *et al.* (2022).

Long-range interactions play a special role in the case of prethermal discrete time crystals, where the temporal and spatial long-range order is exhibited only for low-energy initial states (Machado *et al.*, 2020). A prethermal discrete time crystal has been observed and characterized experimentally in a trapped-ion chain of up to 25 spins (Kyprianidis *et al.*, 2021). Limit cycles and time-crystalline behavior have also been predicted and experimentally observed in periodically driven many-body cavity QED systems (Cosme *et al.*, 2018; Keßler *et al.*, 2019, 2020; Georges *et al.*, 2021). In addition, even without providing a time-dependent external drive, many-body cavity QED systems can feature nonstationary periodically evolving states that emerge due to the competition between dissipative and coherent processes in

long-range interacting systems, as has been recently experimentally observed (Dogra *et al.*, 2019) and theoretically analyzed (Buča and Jaksch, 2019; Chiacchio and Nunnenkamp, 2019).

Time crystals and, in general, Floquet dynamics has also been found to be a source of dynamical phase transitions (Kosior and Sacha, 2018; Yang *et al.*, 2019). Indeed, novel dynamical transitions can be engineered by periodic driving. In the particular case of the long-range Ising model, the periodic drive can stabilize phases, called Kapitza phases, with magnetic ordering without an equilibrium counterpart (Lerose, Marino *et al.*, 2019). Moreover, in the study of the quantum Ising chain, long-range interactions have been shown to induce a large variety of different “higher-order” discrete time crystal phases, where the periodicity of the response is a multiple nT of the external drive period T (Collura *et al.*, 2021; Pizzi, Knolle, and Nunnenkamp, 2021; Giachetti, Solfanelli *et al.*, 2022). Note that a similar structure of the time crystal phases has also been predicted to occur in periodically driven BCS superconductors (Ojeda Collado *et al.*, 2021).

VI. CONCLUSION AND OUTLOOK

In this review, we have discussed the main AMO systems in which long-range interactions are naturally present, and we have also emphasized the fact that in many such systems the range of the interaction can be controlled and varied, giving rise to tunable values of α . This can be seen in the spirit of quantum simulations, where one has a high degree of control over the system and on its crucial properties.

We have discussed most of the quantum models that are currently possible to simulate, focusing, in particular, on lattice and spin models. A variety of spin models, such as quantum Ising, XX , and XXZ models (and their variants), with tunable long-range interactions can be implemented. These spin models alongside bosonic and fermionic models with long-range density-density interactions provide an ample arena of models in which the long rangedness of the interactions plays a key role. While substantial progress has been made in the simulations of quantum long-range lattice models, many more models have yet to find their way, such as bosonic and fermionic models with long-range hopping (a task presently hard to be implemented) and long-range multibody and multispin terms (Andrade *et al.*, 2021).

In experiments, the main challenges are centered on gaining more tunability of the spin-spin interactions through individual atom control. For example, trapped-ion systems are routinely used as quantum computing platforms (Bruzewicz *et al.*, 2019; Wright *et al.*, 2019; Pino *et al.*, 2021) where individual qubit control and detection are necessary ingredients to exploit the long-range connectivity of pairwise quantum logic gate operations. Leveraging the same technological advances, trapped-ion simulators are posed to explore a wider range of physical models where long-range interactions and high connectivity play crucial roles, ranging from high-energy physics (Martinez *et al.*, 2016; Muschik *et al.*, 2017) to spin-boson models (Gorman *et al.*, 2018; Safavi-Naini *et al.*, 2018) and quantum glasses (Rademaker and Abanin, 2020).

In addition, many-body cavity QED systems have demonstrated the first results on tuning the interaction range. In the next step, the resulting many-body phases, phase transitions, and associated phenomena including the Brazovskii transition, glassiness, or frustration have to be explored. Having these tunable-range interactions compete with short-range collisional interactions will allow strongly correlated regimes to be accessed and the rich universe of extended Hubbard models to be explored.

Long-range couplings induce a dispersion relation $\propto k^\sigma$ as opposed to the standard relation $\propto k^2$ in short-range systems. Given the nature of the dispersion relation in long-range systems, one can expect (and find in some cases with microscopic calculations) that the effective low-energy model features fractional derivatives (or fractional Laplacians) altering the scaling of the observables in the system. While this modified scaling is at least partially understood for $O(\mathcal{N})$ systems (Defenu *et al.*, 2020), its counterpart in interacting lattice systems remains to be thoroughly investigated (Lepori *et al.*, 2016; Iglói *et al.*, 2018; Ferraretto and Salasnich, 2019; Botzung *et al.*, 2021).

Relevant nonanalytic momentum terms in quantum long-range models induce an universal behavior that effectively corresponds to that of a classical model in the fractional $d + z$ dimension, with $z < 1$ (Defenu, Trombettoni, and Ruffo, 2017). For this reason, the spatial dimensionality does not appear to play as crucial a role in long-range systems as it does in the local case, since long-range couplings alter the spectral dimension of the bare theory (Leuzzi *et al.*, 2008; Millán *et al.*, 2021). A similar effect may also be expected in the strong long-range regime, where the spectral dimension is not defined, but the spectral properties are still expected to rule the universal behavior both at and out of equilibrium. Nevertheless, the connection between those spectral properties and universal aspects of celebrated phenomena such as ensemble inequivalence, negative specific heats, and quasistationary states largely remain to be explored and exploited (Kastner, 2010; Defenu, 2021).

Several recent results not fully established in the long-range literature have not been discussed in details. The choice of topics has been motivated by the goal to advocate for the inclusion of long-range physics, and quantum long-range systems, particularly in university-taught courses. The inexhaustive list of topics we did not discuss includes the well established interplay between long-range couplings and disorder (Kotliar, Anderson, and Stein, 1983; Leuzzi *et al.*, 2008; Katzgraber, Larson, and Young, 2009), recently studied in the context of long-range interactions (Millán *et al.*, 2021). In addition, the presence of long-range correlated noise in quantum computing devices (Aharonov, Kitaev, and Preskill, 2006) has been reconsidered in the context of studies on long-range systems (Biella *et al.*, 2013; Chávez *et al.*, 2019; Seetharam *et al.*, 2022). Finally, examples of quantum circuits, where long-range couplings or disorder generates a peculiar scaling of entanglement (Block *et al.*, 2022; Minato *et al.*, 2022; Xu, 2022), promising to induce further excitement on applications of long-range interactions, were not substantially covered in our review. Nevertheless, a careful reading of the literature shows that the information provided

in this review should put the interested reader in a position to fully understand the phenomena typically discussed in such recent areas of research.

The analysis of the different systems presented in this review ultimately shows that long-range interactions provide an ingredient that we can control and use for different purposes. On the one hand, they can be exploited to control the stationary states and the thermalization properties. On the other hand, they may affect the phase diagram and the universality properties. Additionally, they can be a resource in the quantum control of the system, providing a useful knob to control the dynamics and the implementation of quantum information tasks, where they can be used to improve the efficiency of control gates and the unitary dynamics needed to modify in the desired way the quantum state of the system.

Long-range properties can also be exploited in typical quantum simulation contexts, as highlighted in the simulation of dynamical gauge field theory with AMO systems (Bañuls *et al.*, 2020; Davoudi *et al.*, 2020; Davoudi, Linke, and Pagano, 2021), where suitably tailored long-range interactions can be used to simulate the effect of dynamical gauge fields. Similarly, they can play a role in the study of quantum devices and the thermodynamic aspects of quantum registers.

The study of the possible uses of long-range interactions in quantum simulators and devices is only at the beginning and will benefit from (and motivate in turn) progress in systems in which the long-range nature of the interactions can be controlled, as in the mode control of interactions with trapped ions. Several systems in which long-range interactions may play a crucial role remain to be fully investigated, such as ultracold fermionic gases. We envision a significant interplay between the study of new equilibrium phases and dynamical regimes in quantum long-range systems and their focused embodiment in quantum devices and simulators. We hope that this review triggers such combined studies to fully exploit the richness of quantum long-range systems.

ACKNOWLEDGMENTS

We thank all our colleagues within the long-range community, who engaged us in many fruitful interactions and discussions over the years. In particular, we acknowledge useful correspondence on the content of this review with O. L. Acevedo, A. Lerose, G. Morigi, and L. Quiroga. We acknowledge A. Daley, L. Dell’Anna, Z.-X. Gong, J. A. S. Lourenço, M. Maghrebi, G. Morigi, D. Mukamel, R. Nandkishore, D. O’Dell, G. Pupillo, A. M. Rey, L. Santos, J. Schachenmayer, and P. Schauss for their valuable feedback and careful reading of the manuscript. N. D. acknowledges funding from the Swiss National Science Foundation (SNF) project “Out-of-equilibrium dynamics of long-range quantum matter (out-dream)” (Project No. 200021_207537) and the Deutsche Forschungsgemeinschaft (DFG, German Research Foundation) under Germany’s Excellence Strategy Grant No. EXC2181/1-390900948 (the Heidelberg STRUCTURES Excellence Cluster). T. D. acknowledges funding from the SNF NCCR QSIT program and the project “Cavity-assisted pattern recognition” (Project No. IZBRZ2 186312), funding from EU Horizon 2020: ITN grant ColOpt (Project No. 721465), and funding from the Swiss State Secretariat for Education,

Research and Innovation (SERI). T. M. acknowledges CNPq for support through Bolsa de produtividade em Pesquisa Grant No. 311079/2015-6 and the Serrapilheira Institute (Grant No. Serra-1812-27802). A. T. and S. R. acknowledge support from the MISTI Global Seed Fund’s MIT-FVG Collaboration Grants “NV centers for the test of the quantum Jarzynski equality (NVQJE)” and “Non-equilibrium thermodynamics of dissipative quantum systems.” G. P. acknowledges support from the NSF CAREER grant (Grant No. PHY-2144910), the Army Research Office (Grant No. W911NF22C0012), the Army Research Laboratory (Grant No. W911QX21C0031), Welch Foundation Grant No. C-2154, and the Office of Naval Research (Grants No. N00014-20-1-2695 and No. N00014-12-1-2665) and the Office of Naval Research Young Investigator Program (Grant No. N00014-22-1-2282). the G. P. acknowledges that this material is based upon work supported by the U.S. Department of Energy, Office of Science, Office of Nuclear Physics under Award No. DE-SC0021143 and Early Career Award No. DE-SC0023806. S. R. acknowledges funding from the MIUR PRIN 2017 project “Coarse-grained description for non-equilibrium systems and transport phenomena (CO-NEST)” (Grant No. 201798CZL).

Note added.—Recent experimental efforts have witnessed the occurrence of continuous symmetry breaking in two-dimensional systems with long-range interactions (Feng *et al.*, 2022; Chen *et al.*, 2023).

REFERENCES

- Abanin, D. A., E. Altman, I. Bloch, and M. Serbyn, 2019, *Rev. Mod. Phys.* **91**, 021001.
- Abanov, A., V. Kalatsky, V. L. Pokrovsky, and W. M. Saslow, 1995, *Phys. Rev. B* **51**, 1023.
- Abreu, B., F. Cinti, and T. Macrì, 2020, *arXiv:2009.10203*.
- Acevedo, O. L., L. Quiroga, F. J. Rodríguez, and N. F. Johnson, 2014, *Phys. Rev. Lett.* **112**, 030403.
- Adelhardt, P., J. A. Koziol, A. Schellenberger, and K. P. Schmidt, 2020, *Phys. Rev. B* **102**, 174424.
- Aharonov, D., A. Kitaev, and J. Preskill, 2006, *Phys. Rev. Lett.* **96**, 050504.
- Ajisaka, S., F. Barra, and B. Žunkovič, 2014, *New J. Phys.* **16**, 033028.
- Albash, T., and D. A. Lidar, 2018, *Rev. Mod. Phys.* **90**, 015002.
- Alecce, A., and L. Dell’Anna, 2017, *Phys. Rev. B* **95**, 195160.
- Altman, E., and A. Auerbach, 2002, *Phys. Rev. Lett.* **89**, 250404.
- Amico, L., R. Fazio, A. Osterloh, and V. Vedral, 2008, *Rev. Mod. Phys.* **80**, 517.
- Ancilotto, F., M. Rossi, and F. Toigo, 2013, *Phys. Rev. A* **88**, 033618.
- Andelman, D., F. Broçhard, and J.-F. Joanny, 1987, *J. Chem. Phys.* **86**, 3673.
- Anderegg, L., L. W. Cheuk, Y. Bao, S. Burchesky, W. Ketterle, K.-K. Ni, and J. M. Doyle, 2019, *Science* **365**, 1156.
- Anderson, P. W., and G. Yuval, 1969, *Phys. Rev. Lett.* **23**, 89.
- Anderson, P. W., G. Yuval, and D. R. Hamann, 1970, *Phys. Rev. B* **1**, 4464.
- Andrade, B., Z. Davoudi, T. Graß, M. Hafezi, G. Pagano, and A. Seif, 2021, *arXiv:2108.01022*.
- Andraschko, F., and J. Sirker, 2014, *Phys. Rev. B* **89**, 125120.
- Andreev, A. F., and I. M. Lifshitz, 1969, *Sov. Phys. JETP* **29**, 1107.

- Angelini, M. C., G. Parisi, and F. Ricci-Tersenghi, 2014, *Phys. Rev. E* **89**, 062120.
- Angelone, A., F. Mezzacapo, and G. Pupillo, 2016, *Phys. Rev. Lett.* **116**, 135303.
- Angelone, A., T. Ying, F. Mezzacapo, G. Masella, M. Dalmonte, and G. Pupillo, 2020, *Phys. Rev. A* **101**, 063603.
- Anquez, M., B. A. Robbins, H. M. Bharath, M. Boguslawski, T. M. Hoang, and M. S. Chapman, 2016, *Phys. Rev. Lett.* **116**, 155301.
- Antenucci, F., M. Ibáñez Berganza, and L. Leuzzi, 2015, *Phys. Rev. B* **92**, 014204.
- Antoni, M., and S. Ruffo, 1995, *Phys. Rev. E* **52**, 2361.
- Antoniazzi, A., F. Califano, D. Fanelli, and S. Ruffo, 2007, *Phys. Rev. Lett.* **98**, 150602.
- Astrakharchik, G. E., J. Boronat, I. L. Kurbakov, and Y. E. Lozovik, 2007, *Phys. Rev. Lett.* **98**, 060405.
- Astrakharchik, G. E., and M. D. Girardeau, 2011, *Phys. Rev. B* **83**, 153303.
- Bachelard, R., T. Dauxois, G. De Ninno, S. Ruffo, and F. Staniscia, 2011, *Phys. Rev. E* **83**, 061132.
- Bachelard, R., and M. Kastner, 2013, *Phys. Rev. Lett.* **110**, 170603.
- Bachmann, S., M. Fraas, and G. M. Graf, 2017, *Ann. Inst. Henri Poincaré* **18**, 1755.
- Baillie, D., and P. B. Blakie, 2018, *Phys. Rev. Lett.* **121**, 195301.
- Baillie, D., R. M. Wilson, R. N. Bisset, and P. B. Blakie, 2016, *Phys. Rev. A* **94**, 021602.
- Baillie, D., R. M. Wilson, and P. B. Blakie, 2017, *Phys. Rev. Lett.* **119**, 255302.
- Bakhtiari, M. R., A. Hemmerich, H. Ritsch, and M. Thorwart, 2015, *Phys. Rev. Lett.* **114**, 123601.
- Balewski, J. B., A. T. Krupp, A. Gaj, S. Hofferberth, R. Löw, and T. Pfau, 2014, *New J. Phys.* **16**, 063012.
- Balog, I., G. Tarjus, and M. Tissier, 2014, *J. Stat. Mech.* P10017.
- Baltrusch, J. D., C. Cormick, and G. Morigi, 2012, *Phys. Rev. A* **86**, 032104.
- Bañuls, M. C., *et al.*, 2020, *Eur. Phys. J. D* **74**, 165.
- Bapst, V., and G. Semerjian, 2012, *J. Stat. Mech.* P06007.
- Baranov, M. A., M. Dalmonte, G. Pupillo, and P. Zoller, 2012, *Chem. Rev.* **112**, 5012.
- Barci, D. G., L. Ribeiro, and D. A. Stariolo, 2013, *Phys. Rev. E* **87**, 062119.
- Barci, D. G., and D. A. Stariolo, 2007, *Phys. Rev. Lett.* **98**, 200604.
- Barci, D. G., and D. A. Stariolo, 2009, *Phys. Rev. B* **79**, 075437.
- Barci, D. G., and D. A. Stariolo, 2011, *Phys. Rev. B* **84**, 094439.
- Bar Lev, Y., G. Cohen, and D. R. Reichman, 2015, *Phys. Rev. Lett.* **114**, 100601.
- Barmettler, P., M. Punk, V. Gritsev, E. Demler, and E. Altman, 2009, *Phys. Rev. Lett.* **102**, 130603.
- Barré, J., and B. Gonçalves, 2007, *Physica (Amsterdam)* **386A**, 212.
- Barré, J., D. Mukamel, and S. Ruffo, 2001, *Phys. Rev. Lett.* **87**, 030601.
- Barredo, D., S. de Léséleuc, V. Lienhard, T. Lahaye, and A. Browaeys, 2016, *Science* **354**, 1021.
- Barredo, D., H. Labuhn, S. Ravets, T. Lahaye, A. Browaeys, and C. S. Adams, 2015, *Phys. Rev. Lett.* **114**, 113002.
- Bates, F. S., and G. H. Fredrickson, 1990, *Annu. Rev. Phys. Chem.* **41**, 525.
- Baumann, K., C. Guerlin, F. Brennecke, and T. Esslinger, 2010, *Nature (London)* **464**, 1301.
- Baumann, K., R. Mottl, F. Brennecke, and T. Esslinger, 2011, *Phys. Rev. Lett.* **107**, 140402.
- Baus, M., and J.-P. Hansen, 1980, *Phys. Rep.* **59**, 1.
- Bause, R., A. Kamijo, X.-Y. Chen, M. Duda, A. Schindewolf, I. Bloch, and X.-Y. Luo, 2021, *arXiv:2106.10089*.
- Béguin, L., A. Vernier, R. Chicireanu, T. Lahaye, and A. Browaeys, 2013, *Phys. Rev. Lett.* **110**, 263201.
- Behan, C., L. Rastelli, S. Rychkov, and B. Zan, 2017, *Phys. Rev. Lett.* **118**, 241601.
- Benatti, F., and R. Floreanini, 2005, *Int. J. Mod. Phys. A* **19**, 3063.
- Bentsen, G., Y. Gu, and A. Lucas, 2019, *Proc. Natl. Acad. Sci. U.S.A.* **116**, 6689.
- Bentsen, G., T. Hashizume, A. S. Buyskikh, E. J. Davis, A. J. Daley, S. S. Gubser, and M. Schleier-Smith, 2019, *Phys. Rev. Lett.* **123**, 130601.
- Berganza, M. I., and L. Leuzzi, 2013, *Phys. Rev. B* **88**, 144104.
- Berges, J., N. Tetradis, and C. Wetterich, 2002, *Phys. Rep.* **363**, 223.
- Bermudez, A., and M. B. Plenio, 2012, *Phys. Rev. Lett.* **109**, 010501.
- Bermudez, A., L. Tagliacozzo, G. Sierra, and P. Richerme, 2017, *Phys. Rev. B* **95**, 024431.
- Bernien, H., *et al.*, 2017, *Nature (London)* **551**, 579.
- Bhakuni, D. S., and A. Sharma, 2020, *Phys. Rev. B* **102**, 085133.
- Bhattacharya, U., and A. Dutta, 2017a, *Phys. Rev. B* **96**, 014302.
- Bhattacharya, U., and A. Dutta, 2017b, *Phys. Rev. B* **95**, 184307.
- Biella, A., F. Borgonovi, R. Kaiser, and G. L. Celardo, 2013, *Europhys. Lett.* **103**, 57009.
- Bienias, P., *et al.*, 2020, *Phys. Rev. Res.* **2**, 033049.
- Bighin, G., N. Defenu, I. Nándori, L. Salasnich, and A. Trombettoni, 2019, *Phys. Rev. Lett.* **123**, 100601.
- Binder, K., 1985, *Z. Phys. B* **61**, 13.
- Birkl, G., S. Kassner, and H. Walther, 1992, *Nature (London)* **357**, 310.
- Bismut, G., B. Laburthe-Tolra, E. Maréchal, P. Pedri, O. Gorceix, and L. Vernac, 2012, *Phys. Rev. Lett.* **109**, 155302.
- Black, A. T., H. W. Chan, and V. Vuletić, 2003, *Phys. Rev. Lett.* **91**, 203001.
- Blanchard, T., M. Picco, and M. A. Rajabpour, 2013, *Europhys. Lett.* **101**, 56003.
- Blaß, B., H. Rieger, G. Roósz, and F. Iglói, 2018, *Phys. Rev. Lett.* **121**, 095301.
- Blatt, R., and C. F. Roos, 2012, *Nat. Phys.* **8**, 277.
- Blatt, R., and D. Wineland, 2008, *Nature (London)* **453**, 1008.
- Blinic, R., and A. P. Levanyuk, 1986, *Incommensurate Phases in Dielectrics*, Modern Problems in Condensed Matter Sciences Vol. 14 (North-Holland, Amsterdam).
- Bloch, I., J. Dalibard, and W. Zwerger, 2008, *Rev. Mod. Phys.* **80**, 885.
- Block, M., Y. Bao, S. Choi, E. Altman, and N. Y. Yao, 2022, *Phys. Rev. Lett.* **128**, 010604.
- Bluemel, R., J. M. Chen, E. Peik, W. Quint, and W. Schleich, 1988, *Nature (London)* **334**, 309.
- Bluvstein, D., *et al.*, 2021, *Science* **371**, 1355.
- Bohn, J. L., A. M. Rey, and J. Ye, 2017, *Science* **357**, 1002.
- Bohrdt, A., A. Omran, E. Demler, S. Gazit, and F. Grusdt, 2020, *Phys. Rev. Lett.* **124**, 073601.
- Boninsegni, M., N. Prokof'ev, and B. Svistunov, 2006, *Phys. Rev. Lett.* **96**, 070601.
- Boninsegni, M., and N. V. Prokof'ev, 2012, *Rev. Mod. Phys.* **84**, 759.
- Borish, V., O. Marković, J. A. Hines, S. V. Rajagopal, and M. Schleier-Smith, 2020, *Phys. Rev. Lett.* **124**, 063601.
- Borzi, R. A., S. A. Grigera, J. Farrell, R. S. Perry, S. J. S. Lister, S. L. Lee, D. A. Tennant, Y. Maeno, and A. P. Mackenzie, 2007, *Science* **315**, 214.
- Bose, S., 2007, *Contemp. Phys.* **48**, 13.
- Botet, R., and R. Jullien, 1983, *Phys. Rev. B* **28**, 3955.
- Botet, R., R. Jullien, and P. Pfeuty, 1982, *Phys. Rev. Lett.* **49**, 478.
- Böttcher, F., J.-N. Schmidt, J. Hertkorn, K. S. H. Ng, S. D. Graham, M. Guo, T. Langen, and T. Pfau, 2020, *arXiv:2007.06391*.

- Böttcher, F., J.-N. Schmidt, J. Hertkorn, K. S. H. Ng, S. D. Graham, M. Guo, T. Langen, and T. Pfau, 2021, *Rep. Prog. Phys.* **84**, 012403.
- Botzung, T., D. Hagenmüller, G. Masella, J. Dubail, N. Defenu, A. Trombettoni, and G. Pupillo, 2021, *Phys. Rev. B* **103**, 155139.
- Botzung, T., G. Pupillo, P. Simon, R. Citro, and E. Ercolessi, 2019, [arXiv:1909.12168](https://arxiv.org/abs/1909.12168).
- Brankov, I. G., V. A. Zagrebnov, and I. S. Tonchev, 1975, *Theor. Math. Phys.* **22**, 13.
- Bravyi, S., M. B. Hastings, and F. Verstraete, 2006, *Phys. Rev. Lett.* **97**, 050401.
- Brazovskii, S. A., 1975, *Zh. Eksp. Teor. Fiz.* **68**, 175, <http://cds.cern.ch/record/478680?ln=it>.
- Brennecke, F., R. Mottl, K. Baumann, R. Landig, T. Donner, and T. Esslinger, 2013, *Proc. Natl. Acad. Sci. U.S.A.* **110**, 11763.
- Brézin, E., and J. Zinn-Justin, 1976, *Phys. Rev. Lett.* **36**, 691.
- Britton, J. W., B. C. Sawyer, A. C. Keith, C. C. J. Wang, J. K. Freericks, H. Uys, M. J. Biercuk, and J. J. Bollinger, 2012, *Nature (London)* **484**, 489.
- Browaeys, A., and T. Lahaye, 2020, *Nat. Phys.* **16**, 132.
- Brown, L. S., and G. Gabrielse, 1986, *Rev. Mod. Phys.* **58**, 233.
- Brunelli, M., *et al.*, 2018, *Phys. Rev. Lett.* **121**, 160604.
- Bruno, P., 2001, *Phys. Rev. Lett.* **87**, 137203.
- Bruno, G. M., and D. R. Nelson, 2014, *Phys. Rev. B* **89**, 094112.
- Bruun, G. M., and E. Taylor, 2008, *Phys. Rev. Lett.* **101**, 245301.
- Bruzewicz, C. D., J. Chiaverini, R. McConnell, and J. M. Sage, 2019, *Appl. Phys. Rev.* **6**, 021314.
- Brydges, T., A. Elben, P. Jurcevic, B. Vermersch, C. Maier, B. P. Lanyon, P. Zoller, R. Blatt, and C. F. Roos, 2019, *Science* **364**, 260.
- Buča, B., and D. Jaksch, 2019, *Phys. Rev. Lett.* **123**, 260401.
- Büchler, H. P., E. Demler, M. Lukin, A. Micheli, N. Prokof'ev, G. Pupillo, and P. Zoller, 2007, *Phys. Rev. Lett.* **98**, 060404.
- Budich, J. C., and M. Heyl, 2016, *Phys. Rev. B* **93**, 085416.
- Burin, A. L., 2015a, *Phys. Rev. B* **92**, 104428.
- Burin, A. L., 2015b, *Phys. Rev. B* **91**, 094202.
- Burrello, M., I. Lesanovsky, and A. Trombettoni, 2020, *Phys. Rev. Res.* **2**, 023290.
- Bustingorry, S., E. Jagla, and J. Lorenzana, 2005, *Acta Mater.* **53**, 5183.
- Buyskikh, A. S., M. Fagotti, J. Schachenmayer, F. Essler, and A. J. Daley, 2016, *Phys. Rev. A* **93**, 053620.
- Caballero-Benitez, S. F., and I. B. Mekhov, 2015, *Phys. Rev. Lett.* **115**, 243604.
- Calabrese, P., and J. Cardy, 2004, *J. Stat. Mech.* P06002.
- Calabrese, P., and J. Cardy, 2006, *Phys. Rev. Lett.* **96**, 136801.
- Camacho-Guardian, A., R. Paredes, and S. F. Caballero-Benítez, 2017, *Phys. Rev. A* **96**, 051602.
- Campa, A., T. Dauxois, D. Fanelli, and S. Ruffo, 2014, *Physics of Long-Range Interacting Systems* (Oxford University Press, New York).
- Campa, A., T. Dauxois, and S. Ruffo, 2009, *Phys. Rep.* **480**, 57.
- Caneva, T., R. Fazio, and G. E. Santoro, 2008, *Phys. Rev. B* **78**, 104426.
- Cannas, S. A., M. F. Michelon, D. A. Stariolo, and F. A. Tamarit, 2006, *Phys. Rev. B* **73**, 184425.
- Capati, M., S. Caprara, C. di Castro, M. Grilli, G. Seibold, and J. Lorenzana, 2015, *Nat. Commun.* **6**, 7691.
- Cappelli, A., L. Maffi, and S. Okuda, 2019, *J. High Energy Phys.* **01**, 161.
- Capponi, S., D. Poilblanc, and T. Giamarchi, 2000, *Phys. Rev. B* **61**, 13410.
- Cardy, J., 1996, *Scaling and Renormalization in Statistical Physics*, Cambridge Lecture Notes in Physics (Cambridge University Press, Cambridge, England).
- Cardy, J. L., 1981, *J. Phys. A* **14**, 1407.
- Carr, L. D., D. DeMille, R. V. Krems, and J. Ye, 2009, *New J. Phys.* **11**, 055049.
- Cartarius, F., G. Morigi, and A. Minguzzi, 2014, *Phys. Rev. A* **90**, 053601.
- Casula, M., S. Sorella, and G. Senatore, 2006, *Phys. Rev. B* **74**, 245427.
- Ceperley, D. M., 1995, *Rev. Mod. Phys.* **67**, 279.
- Cescatti, F., M. Ibáñez-Berganza, A. Vezzani, and R. Burioni, 2019, *Phys. Rev. B* **100**, 054203.
- Chaikin, P. M., and T. C. Lubensky, 1995, *Principles of Condensed Matter Physics*, 1st ed. (Cambridge University Press, Cambridge, England).
- Chávez, N. C., F. Mattiotti, J. A. Méndez-Bermúdez, F. Borgonovi, and G. L. Celardo, 2019, *Eur. Phys. J. B* **92**, 144.
- Chayes, L., N. Crawford, D. Ioffe, and A. Levit, 2008, *J. Stat. Phys.* **133**, 131.
- Chen, C., *et al.*, 2023, *Nature (London)* **616**, 691.
- Chen, C.-F., and A. Lucas, 2019, *Phys. Rev. Lett.* **123**, 250605.
- Chen, Y., Z. Yu, and H. Zhai, 2016, *Phys. Rev. A* **93**, 041601.
- Chiacchio, E. I. R., and A. Nunnenkamp, 2018, *Phys. Rev. A* **98**, 023617.
- Chiacchio, E. I. R., and A. Nunnenkamp, 2019, *Phys. Rev. Lett.* **122**, 193605.
- Chiara, G. D., A. del Campo, G. Morigi, M. B. Plenio, and A. Retzker, 2010, *New J. Phys.* **12**, 115003.
- Chiocchetta, A., A. Gambassi, S. Diehl, and J. Marino, 2017, *Phys. Rev. Lett.* **118**, 135701.
- Chitov, G. Y., 2018, *Phys. Rev. B* **97**, 085131.
- Choi, S., *et al.*, 2017, *Nature (London)* **543**, 221.
- Chomaz, L., S. Baier, D. Petter, M. J. Mark, F. Wächtler, L. Santos, and F. Ferlaino, 2016, *Phys. Rev. X* **6**, 041039.
- Chomaz, L., I. Ferrier-Barbut, F. Ferlaino, B. Laburthe-Tolra, B. L. Lev, and T. Pfau, 2022, [arXiv:2201.02672](https://arxiv.org/abs/2201.02672).
- Chomaz, L., R. M. W. van Bijnen, D. Petter, G. Faraoni, S. Baier, J. H. Becher, M. J. Mark, F. Wächtler, L. Santos, and F. Ferlaino, 2018, *Nat. Phys.* **14**, 442.
- Christensen, J. E., D. Hucul, W. C. Campbell, and E. R. Hudson, 2020, *npj Quantum Inf.* **6**, 35.
- Cidrim, A., F. E. A. dos Santos, E. A. L. Henn, and T. Macrì, 2018, *Phys. Rev. A* **98**, 023618.
- Cinti, F., A. Cappellaro, L. Salasnich, and T. Macrì, 2017, *Phys. Rev. Lett.* **119**, 215302.
- Cinti, F., P. Jain, M. Boninsegni, A. Micheli, P. Zoller, and G. Pupillo, 2010, *Phys. Rev. Lett.* **105**, 135301.
- Cinti, F., and T. Macrì, 2019, *Condens. Matter* **4**, 93.
- Cinti, F., T. Macrì, W. Lechner, G. Pupillo, and T. Pohl, 2014, *Nat. Commun.* **5**, 3235.
- Cirac, J. I., M. Lewenstein, K. Mølmer, and P. Zoller, 1998, *Phys. Rev. A* **57**, 1208.
- Codello, A., N. Defenu, and G. D'Odorico, 2015, *Phys. Rev. D* **91**, 105003.
- Collura, M., A. De Luca, D. Rossini, and A. Lerose, 2021, [arXiv:2110.14705](https://arxiv.org/abs/2110.14705).
- Collura, M., and D. Karevski, 2010, *Phys. Rev. Lett.* **104**, 200601.
- Colonna-Romano, L., H. Gould, and W. Klein, 2014, *Phys. Rev. E* **90**, 042111.
- Cormick, C., and G. Morigi, 2012, *Phys. Rev. Lett.* **109**, 053003.
- Cosme, J. G., C. Georges, A. Hemmerich, and L. Mathey, 2018, *Phys. Rev. Lett.* **121**, 153001.
- Covey, J. P., I. S. Madjarov, A. Cooper, and M. Endres, 2019, *Phys. Rev. Lett.* **122**, 173201.
- Cowley, M. D., and R. E. Rosensweig, 1967, *J. Fluid Mech.* **30**, 671.

- Cross, M. C., and P. C. Hohenberg, 1993, *Rev. Mod. Phys.* **65**, 851.
- Dabrowski, R., and G. V. Dunne, 2016, *Phys. Rev. D* **94**, 065005.
- Dalmonte, M., W. Lechner, Z. Cai, M. Mattioli, A. M. Läuchli, and G. Pupillo, 2015, *Phys. Rev. B* **92**, 045106.
- Dalmonte, M., G. Pupillo, and P. Zoller, 2010, *Phys. Rev. Lett.* **105**, 140401.
- Damski, B., 2005, *Phys. Rev. Lett.* **95**, 035701.
- Dauxois, T., V. Latora, A. Rapisarda, S. Ruffo, and A. Torcini, 2002, in *Dynamics and Thermodynamics of Systems with Long-Range Interactions*, Lecture Notes in Physics Vol. 602, edited by T. Dauxois, S. Ruffo, E. Arimondo, and M. Wilkens (Springer, Berlin).
- Dauxois, T., S. Ruffo, E. Arimondo, and M. Wilkens, 2002, Eds., *Dynamics and Thermodynamics of Systems with Long-Range Interactions*, Lecture Notes in Physics Vol. 602 (Springer-Verlag, Berlin).
- Davis, E., G. Bentsen, and M. Schleier-Smith, 2016, *Phys. Rev. Lett.* **116**, 053601.
- Davis, E. J., G. Bentsen, L. Homeier, T. Li, and M. H. Schleier-Smith, 2019, *Phys. Rev. Lett.* **122**, 010405.
- Davis, E. J., A. Periwal, E. S. Cooper, G. Bentsen, S. J. Evered, K. Van Kirk, and M. H. Schleier-Smith, 2020, *Phys. Rev. Lett.* **125**, 060402.
- Davoudi, Z., M. Hafezi, C. Monroe, G. Pagano, A. Seif, and A. Shaw, 2020, *Phys. Rev. Res.* **2**, 023015.
- Davoudi, Z., N. M. Linke, and G. Pagano, 2021, arXiv:2104.09346.
- Defenu, N., 2021, *Proc. Natl. Acad. Sci. U.S.A.* **118**, e2101785118.
- Defenu, N., A. Codello, S. Ruffo, and A. Trombettoni, 2020, *J. Phys. A* **53**, 143001.
- Defenu, N., T. Enss, and J. C. Halimeh, 2019, *Phys. Rev. B* **100**, 014434.
- Defenu, N., T. Enss, M. Kastner, and G. Morigi, 2018, *Phys. Rev. Lett.* **121**, 240403.
- Defenu, N., G. Morigi, L. Dell'Anna, and T. Enss, 2019, *Phys. Rev. B* **100**, 184306.
- Defenu, N., A. Trombettoni, and A. Codello, 2015, *Phys. Rev. E* **92**, 052113.
- Defenu, N., A. Trombettoni, I. Nándori, and T. Enss, 2017, *Phys. Rev. B* **96**, 174505.
- Defenu, N., A. Trombettoni, and S. Ruffo, 2016, *Phys. Rev. B* **94**, 224411.
- Defenu, N., A. Trombettoni, and S. Ruffo, 2017, *Phys. Rev. B* **96**, 104432.
- Defenu, N., A. Trombettoni, and D. Zappalà, 2021, *Nucl. Phys. B* **964**, 115295.
- de Gennes, P. G., and J. Prost, 1993, *The Physics of Liquid Crystals*, 2nd ed., International Series of Monographs on Physics Vol. 83 (Clarendon Press, Oxford).
- de Grandi, C., and A. Polkovnikov, 2010, in *Quantum Quenching, Annealing and Computation*, Lecture Notes in Physics Vol. 802, edited by A. K. Chandra, A. Das, and B. K. Chakrabarti (Springer, Berlin), pp. 75–114.
- Dehmelt, H. G., 1968, *Adv. At. Mol. Phys.* **3**, 53.
- Delamotte, B., 2012, in *Order, Disorder and Criticality*, Vol. 3, edited by Y. Holovatch (World Scientific, Singapore), pp. 1–77.
- del Campo, A., and W. H. Zurek, 2014, *Int. J. Mod. Phys. A* **29**, 1430018.
- del Campo, A., G. De Chiara, G. Morigi, M. B. Plenio, and A. Retzker, 2010, *Phys. Rev. Lett.* **105**, 075701.
- de Léséleuc, S., V. Lienhard, P. Scholl, D. Barredo, S. Weber, N. Lang, H. P. Büchler, T. Lahaye, and A. Browaeys, 2019, *Science* **365**, 775.
- Deng, S., G. Ortiz, and L. Viola, 2009, *Phys. Rev. B* **80**, 241109.
- Deng, X., G. Masella, G. Pupillo, and L. Santos, 2020, *Phys. Rev. Lett.* **125**, 010401.
- de Oliveira, T. R., C. Charalambous, D. Jonathan, M. Lewenstein, and A. Riera, 2018, *New J. Phys.* **20**, 033032.
- de Paz, A., A. Sharma, A. Chotia, E. Maréchal, J. H. Huckans, P. Pedri, L. Santos, O. Gorceix, L. Vernac, and B. Laburthe-Tolra, 2013, *Phys. Rev. Lett.* **111**, 185305.
- De Tomasi, G., 2019, *Phys. Rev. B* **99**, 054204.
- De Tomasi, G., D. Hetterich, P. Sala, and F. Pollmann, 2019, *Phys. Rev. B* **100**, 214313.
- Díaz-Méndez, R., F. Mezzacapo, F. Cinti, W. Lechner, and G. Pupillo, 2015, *Phys. Rev. E* **92**, 052307.
- Díaz-Méndez, R., F. Mezzacapo, W. Lechner, F. Cinti, E. Babaev, and G. Pupillo, 2017, *Phys. Rev. Lett.* **118**, 067001.
- Dicke, R. H., 1954, *Phys. Rev.* **93**, 99.
- Dickstein, A. J., S. Erramilli, R. E. Goldstein, D. P. Jackson, and S. A. Langer, 1993, *Science* **261**, 1012.
- Dimer, F., B. Estienne, A. S. Parkins, and H. J. Carmichael, 2007, *Phys. Rev. A* **75**, 013804.
- Divakaran, U., V. Mukherjee, A. Dutta, and D. Sen, 2009, *J. Stat. Mech.* P02007.
- Dogra, N., F. Brennecke, S. D. Huber, and T. Donner, 2016, *Phys. Rev. A* **94**, 023632.
- Dogra, N., M. Landini, K. Kroeger, L. Hruby, T. Donner, and T. Esslinger, 2019, *Science* **366**, 1496.
- Dorogovtsev, S. N., A. V. Goltsev, and J. F. F. Mendes, 2008, *Rev. Mod. Phys.* **80**, 1275.
- Douglas, J. S., H. Habibian, C. L. Hung, A. V. Gorshkov, H. J. Kimble, and D. E. Chang, 2015, *Nat. Photonics* **9**, 326.
- Dubin, D. H. E., and T. M. O'Neil, 1999, *Rev. Mod. Phys.* **71**, 87.
- Dukelsky, J., S. Pittel, and G. Sierra, 2004, *Rev. Mod. Phys.* **76**, 643.
- Dumitrescu, P. T., J. Bohnet, J. Gaebler, A. Hankin, D. Hayes, A. Kumar, B. Neyenhuis, R. Vasseur, and A. C. Potter, 2022, *Nature (London)* **607**, 463.
- Dupuis, N., L. Canet, A. Eichhorn, W. Metzner, J. M. Pawłowski, M. Tissier, and N. Wschebor, 2020, arXiv:2006.04853.
- Dusuel, S., and J. Vidal, 2004, *Phys. Rev. Lett.* **93**, 237204.
- Dusuel, S., and J. Vidal, 2005a, *Phys. Rev. B* **71**, 224420.
- Dusuel, S., and J. Vidal, 2005b, *Phys. Rev. A* **71**, 060304.
- Dutta, A., G. Aeppli, B. K. Chakrabarti, U. Divakaran, T. F. Rosenbaum, and D. Sen, 2015, *Quantum Phase Transitions in Transverse Field Spin Models: From Statistical Physics to Quantum Information* (Cambridge University Press, Cambridge, England).
- Dutta, A., and J. K. Bhattacharjee, 2001, *Phys. Rev. B* **64**, 184106.
- Dutta, A., and A. Dutta, 2017, *Phys. Rev. B* **96**, 125113.
- Dyson, F. J., 1969, *Commun. Math. Phys.* **12**, 91.
- Dziarmaga, J., 2005, *Phys. Rev. Lett.* **95**, 245701.
- Dziarmaga, J., 2010, *Adv. Phys.* **59**, 1063.
- Dziarmaga, J., and M. M. Rams, 2010, *New J. Phys.* **12**, 055007.
- Ebadi, S., *et al.*, 2021, *Nature (London)* **595**, 227.
- Eckstein, M., and M. Kollar, 2008, *Phys. Rev. Lett.* **100**, 120404.
- Eckstein, M., M. Kollar, and P. Werner, 2009, *Phys. Rev. Lett.* **103**, 056403.
- Eisert, J., M. Cramer, and M. B. Plenio, 2010, *Rev. Mod. Phys.* **82**, 277.
- Eisert, J., M. Van Den Worm, S. R. Manmana, and M. Kastner, 2013, *Phys. Rev. Lett.* **111**, 260401.
- Eldredge, Z., Z.-X. Gong, J. T. Young, A. H. Moosavian, M. Foss-Feig, and A. V. Gorshkov, 2017, *Phys. Rev. Lett.* **119**, 170503.
- Else, D. V., B. Bauer, and C. Nayak, 2016, *Phys. Rev. Lett.* **117**, 090402.
- Else, D. V., F. Machado, C. Nayak, and N. Y. Yao, 2020, *Phys. Rev. A* **101**, 022333.

- El-Showk, S., M. Paulos, D. Poland, S. Rychkov, D. Simmons-Duffin, and A. Vichi, 2014, *Phys. Rev. Lett.* **112**, 141601.
- Emary, C., and T. Brandes, 2003, *Phys. Rev. E* **67**, 066203.
- Endres, M., H. Bernien, A. Keesling, H. Levine, E. R. Anschuetz, A. Krajenbrink, C. Senko, V. Vuletic, M. Greiner, and M. D. Lukin, 2016, *Science* **354**, 1024.
- Enzer, D. G., *et al.*, 2000, *Phys. Rev. Lett.* **85**, 2466.
- Essler, F. H. L., S. Evangelisti, and M. Fagotti, 2012, *Phys. Rev. Lett.* **109**, 247206.
- Faber, T. E., 1958, *Proc. R. Soc. A* **248**, 460.
- Fano, G., F. Ortolani, A. Parola, and L. Ziosi, 1999, *Phys. Rev. B* **60**, 15654.
- Feng, L., O. Katz, C. Haack, M. Maghrebi, A. V. Gorshkov, Z. Gong, M. Cetina, and C. Monroe, 2022, [arXiv:2211.01275](https://arxiv.org/abs/2211.01275).
- Feng, L., W. L. Tan, A. De, A. Menon, A. Chu, G. Pagano, and C. Monroe, 2020, *Phys. Rev. Lett.* **125**, 053001.
- Fernández-Vidal, S., G. De Chiara, J. Larson, and G. Morigi, 2010, *Phys. Rev. A* **81**, 043407.
- Ferraretto, M., and L. Salasnich, 2019, *Phys. Rev. A* **99**, 013618.
- Festa, L., N. Lorenz, L.-M. Steinert, Z. Chen, P. Osterholz, R. Eberhard, and C. Gross, 2021, [arXiv:2103.14383](https://arxiv.org/abs/2103.14383).
- Fey, S., S. C. Kapfer, and K. P. Schmidt, 2019, *Phys. Rev. Lett.* **122**, 017203.
- Fey, S., and K. P. Schmidt, 2016, *Phys. Rev. B* **94**, 075156.
- Feynman, R. P., 1954, *Phys. Rev.* **94**, 262.
- Fisher, M. E., 1967, *Rep. Prog. Phys.* **30**, 615.
- Fisher, M. E., and M. N. Barber, 1972, *Phys. Rev. Lett.* **28**, 1516.
- Fisher, M. E., S.-k. Ma, and B. G. Nickel, 1972, *Phys. Rev. Lett.* **29**, 917.
- Fisher, M. E., R. Pynn, and A. Skjeltorp, 1984, in *Multicritical Phenomena*, 1st ed., edited by R. Pynn and A. Skjeltorp, NATO Advanced Science Institutes, Series B, Vol. 106 (Springer, New York).
- Fisher, M. E., and W. Selke, 1980, *Phys. Rev. Lett.* **44**, 1502.
- Fishman, S., G. De Chiara, T. Calarco, and G. Morigi, 2008, *Phys. Rev. B* **77**, 064111.
- Fläschner, N., D. Vogel, M. Tarnowski, B. S. Rem, D. S. Lühmann, M. Heyl, J. C. Budich, L. Mathey, K. Sengstock, and C. Weitenberg, 2018, *Nat. Phys.* **14**, 265.
- Flores-Sola, E., B. Berche, R. Kenna, and M. Weigel, 2016, *Phys. Rev. Lett.* **116**, 115701.
- Flores-Sola, E. J., B. Berche, R. Kenna, and M. Weigel, 2015, *Eur. Phys. J. B* **88**, 28.
- Foss-Feig, M., Z.-X. Gong, C. W. Clark, and A. V. Gorshkov, 2015, *Phys. Rev. Lett.* **114**, 157201.
- Fradkin, E., 2013, *Field Theories of Condensed Matter Physics*, 2nd ed. (Cambridge University Press, Cambridge, England).
- Fradkin, E., and S. A. Kivelson, 1999, *Phys. Rev. B* **59**, 8065.
- Fraxanet, J., U. Bhattacharya, T. Grass, D. Rakshit, M. Lewenstein, and A. Dauphin, 2021, *Phys. Rev. Res.* **3**, 013148.
- Frérot, I., P. Naldesi, and T. Roscilde, 2017, *Phys. Rev. B* **95**, 245111.
- Frérot, I., P. Naldesi, and T. Roscilde, 2018, *Phys. Rev. Lett.* **120**, 050401.
- Friedberg, R., T. Lee, and H. Ren, 1993, *Ann. Phys. (N.Y.)* **228**, 52.
- Friedenauer, A., H. Schmitz, J. T. Glueckert, D. Porras, and T. Schaetz, 2008, *Nat. Phys.* **4**, 757.
- Friedman, A. J., B. Ware, R. Vasseur, and A. C. Potter, 2022, *Phys. Rev. B* **105**, 115117.
- Fröhlich, J., and T. Spencer, 1983, *Commun. Math. Phys.* **88**, 151.
- Fukui, K., and S. Todo, 2009, *J. Comput. Phys.* **228**, 2629.
- Gabardos, L., B. Zhu, S. Lepoutre, A. M. Rey, B. Laburthe-Tolra, and L. Vernac, 2020, *Phys. Rev. Lett.* **125**, 143401.
- Gabrielli, A., M. Joyce, and B. Marcos, 2010, *Phys. Rev. Lett.* **105**, 210602.
- Gadway, B., and B. Yan, 2016, *J. Phys. B* **49**, 152002.
- Gaetan, A., Y. Miroshnychenko, T. Wilk, A. Chotia, M. Viteau, D. Comparat, P. Pillet, A. Browaeys, and P. Grangier, 2009, *Nat. Phys.* **5**, 115.
- Gambetta, F. M., C. Zhang, M. Hennrich, I. Lesanovsky, and W. Li, 2020, *Phys. Rev. Lett.* **125**, 133602.
- Gardiner, C., and P. Zoller, 2004, *Quantum Noise: A Handbook of Markovian and Non-Markovian Quantum Stochastic Methods with Applications to Quantum Optics* (Springer-Verlag, Berlin).
- Gärtner, M., J. G. Bohnet, A. Safavi-Naini, M. L. Wall, J. J. Bollinger, and A. M. Rey, 2017, *Nat. Phys.* **13**, 781.
- Geier, S., N. Thaicharoen, C. Hainaut, T. Franz, A. Salzinger, A. Tebben, D. Grimshandl, G. Zürn, and M. Weidemüller, 2021, [arXiv:2105.01597](https://arxiv.org/abs/2105.01597).
- Georges, C., J. G. Cosme, H. Keßler, L. Mathey, and A. Hemmerich, 2021, *New J. Phys.* **23**, 023003.
- Georgescu, I. M., S. Ashhab, and F. Nori, 2014, *Rev. Mod. Phys.* **86**, 153.
- Giachetti, G., N. Defenu, S. Ruffo, and A. Trombettoni, 2021a, *Phys. Rev. Lett.* **127**, 156801.
- Giachetti, G., N. Defenu, S. Ruffo, and A. Trombettoni, 2021b, *Europhys. Lett.* **133**, 57004.
- Giachetti, G., A. Solfanelli, L. Correale, and N. Defenu, 2022, [arXiv:2203.16562](https://arxiv.org/abs/2203.16562).
- Giachetti, G., A. Trombettoni, S. Ruffo, and N. Defenu, 2022, *Phys. Rev. B* **106**, 014106.
- Giamarchi, T., 2004, *Quantum Physics in One Dimension*, International Series of Monographs on Physics Vol. 121 (Oxford University Press, New York).
- Gibberd, R. W., 1974, *Aust. J. Phys.* **27**, 241.
- Gil, L. I. R., R. Mukherjee, E. M. Bridge, M. P. A. Jones, and T. Pohl, 2014, *Phys. Rev. Lett.* **112**, 103601.
- Gillman, E., F. Carollo, and I. Lesanovsky, 2020, *Phys. Rev. Lett.* **125**, 100403.
- Giovanazzi, S., D. O'Dell, and G. Kurizki, 2002, *Phys. Rev. Lett.* **88**, 130402.
- Giuliani, A., V. Mastropietro, and S. Rychkov, 2021, *J. High Energy Phys.* **01**, 26.
- Glaetzle, A. W., M. Dalmonte, R. Nath, I. Rousochatzakis, R. Moessner, and P. Zoller, 2014, *Phys. Rev. X* **4**, 041037.
- Glaetzle, A. W., R. M. W. van Bijnen, P. Zoller, and W. Lechner, 2017, *Nat. Commun.* **8**, 15813.
- Glick, A. J., H. J. Lipkin, and N. Meshkov, 1965, *Nucl. Phys.* **62**, 211.
- Goldschmidt, E. A., T. Boulier, R. C. Brown, S. B. Koller, J. T. Young, A. V. Gorshkov, S. L. Rolston, and J. V. Porto, 2016, *Phys. Rev. Lett.* **116**, 113001.
- Gong, Z. X., M. F. Maghrebi, A. Hu, M. Foss-Feig, P. Richerme, C. Monroe, and A. V. Gorshkov, 2016, *Phys. Rev. B* **93**, 205115.
- Gong, Z.-X., M. Foss-Feig, F. G. S. L. Brandão, and A. V. Gorshkov, 2017, *Phys. Rev. Lett.* **119**, 050501.
- Gong, Z.-X., M. Foss-Feig, S. Michalakis, and A. V. Gorshkov, 2014, *Phys. Rev. Lett.* **113**, 030602.
- Gong, Z.-X., M. F. Maghrebi, A. Hu, M. L. Wall, M. Foss-Feig, and A. V. Gorshkov, 2016, *Phys. Rev. B* **93**, 041102(R).
- Gonzalez-Lazo, E., M. Heyl, M. Dalmonte, and A. Angelone, 2021, [arXiv:2104.15070](https://arxiv.org/abs/2104.15070).
- Gopalakrishnan, S., B. L. Lev, and P. M. Goldbart, 2009, *Nat. Phys.* **5**, 845.
- Gopalakrishnan, S., B. L. Lev, and P. M. Goldbart, 2010, *Phys. Rev. A* **82**, 043612.

- Gopalakrishnan, S., B. L. Lev, and P. M. Goldbart, 2011, *Phys. Rev. Lett.* **107**, 277201.
- Góral, K., L. Santos, and M. Lewenstein, 2002, *Phys. Rev. Lett.* **88**, 170406.
- Gori, G., M. Michelangeli, N. Defenu, and A. Trombettoni, 2017, *Phys. Rev. E* **96**, 012108.
- Gorman, D. J., B. Hemmerling, E. Megidish, S. A. Moeller, P. Schindler, M. Sarovar, and H. Haeflner, 2018, *Phys. Rev. X* **8**, 011038.
- Gracey, J. A., 2015, *Phys. Rev. D* **92**, 025012.
- Grassberger, P., 2013, *J. Stat. Phys.* **153**, 289.
- Gräter, M., and C. Wetterich, 1995, *Phys. Rev. Lett.* **75**, 378.
- Greer, A. L., 2000, *Nature (London)* **404**, 134.
- Greiner, M., O. Mandel, T. Esslinger, T. W. Hänsch, and I. Bloch, 2002, *Nature (London)* **415**, 39.
- Greiter, M., V. Schnells, and R. Thomale, 2014, *Ann. Phys. (Amsterdam)* **351**, 1026.
- Gross, E. P., 1957, *Phys. Rev.* **106**, 161.
- Guardado-Sanchez, E., P. T. Brown, D. Mitra, T. Devakul, D. A. Huse, P. Schauf, and W. S. Bakr, 2018, *Phys. Rev. X* **8**, 021069.
- Guardado-Sanchez, E., B. M. Spar, P. Schauss, R. Belyansky, J. T. Young, P. Bienias, A. V. Gorshkov, T. Iadecola, and W. S. Bakr, 2021, *Phys. Rev. X* **11**, 021036.
- Gubser, S. S., J. Knaute, S. Parikh, A. Samberg, and P. Witaszczyk, 2017, *Commun. Math. Phys.* **352**, 1019.
- Guo, A. Y., M. C. Tran, A. M. Childs, A. V. Gorshkov, and Z.-X. Gong, 2020, *Phys. Rev. A* **102**, 010401.
- Guo, Y., V. D. Vaidya, R. M. Kroeze, R. A. Lunney, B. L. Lev, and J. Keeling, 2019, *Phys. Rev. A* **99**, 053818.
- Gupta, R., and C. F. Baillie, 1992, *Phys. Rev. B* **45**, 2883.
- Gupta, R., J. DeLapp, G. G. Batrouni, G. C. Fox, C. F. Baillie, and J. Apostolakis, 1988, *Phys. Rev. Lett.* **61**, 1996.
- Gupta, S., A. Campa, and S. Ruffo, 2012a, *Phys. Rev. E* **86**, 061130.
- Gupta, S., M. Potters, and S. Ruffo, 2012b, *Phys. Rev. E* **85**, 066201.
- Gyongyosi, L., and S. Imre, 2019, *Comput. Sci. Rev.* **31**, 51.
- Habibian, H., A. Winter, S. Paganelli, H. Rieger, and G. Morigi, 2013, *Phys. Rev. Lett.* **110**, 075304.
- Hadzibabic, Z., P. Krüger, M. Cheneau, B. Battelier, and J. Dalibard, 2006, *Nature (London)* **441**, 1118.
- Halimeh, J. C., and M. F. Maghrebi, 2021, *Phys. Rev. E* **103**, 052142.
- Halimeh, J. C., M. Van Damme, V. Zauner-Stauber, and L. Vanderstraeten, 2020, *Phys. Rev. Res.* **2**, 033111.
- Halimeh, J. C., and V. Zauner-Stauber, 2017, *Phys. Rev. B* **96**, 134427.
- Halimeh, J. C., V. Zauner-Stauber, I. P. McCulloch, I. de Vega, U. Schollwöck, and M. Kastner, 2017, *Phys. Rev. B* **95**, 024302.
- Hansen, J.-P., and I. R. McDonald, 2013, *Theory of Simple Liquids: With Applications to Soft Matter*, 4th ed. (Academic Press, New York).
- Happer, W., 1972, *Rev. Mod. Phys.* **44**, 169.
- Harty, T., D. Allcock, C. Ballance, L. Guidoni, H. Janacek, N. Linke, D. Stacey, and D. Lucas, 2014, *Phys. Rev. Lett.* **113**, 220501.
- Harty, T. P., M. A. Sepiol, D. T. C. Allcock, C. J. Ballance, J. E. Tarlton, and D. M. Lucas, 2016, *Phys. Rev. Lett.* **117**, 140501.
- Hasenbusch, M., M. Marcu, and K. Pinn, 1992, *Nucl. Phys. B, Proc. Suppl.* **26**, 598.
- Hastings, M. B., and T. Koma, 2006, *Commun. Math. Phys.* **265**, 781.
- Hauke, P., and L. Tagliacozzo, 2013, *Phys. Rev. Lett.* **111**, 207202.
- Hazzard, K. R. A., S. R. Manmana, M. Foss-Feig, and A. M. Rey, 2013, *Phys. Rev. Lett.* **110**, 075301.
- Hazzard, K. R. A., M. van den Worm, M. Foss-Feig, S. R. Manmana, E. G. Dalla Torre, T. Pfau, M. Kastner, and A. M. Rey, 2014, *Phys. Rev. A* **90**, 063622.
- Henkel, N., F. Cinti, P. Jain, G. Pupillo, and T. Pohl, 2012, *Phys. Rev. Lett.* **108**, 265301.
- Henkel, N., R. Nath, and T. Pohl, 2010, *Phys. Rev. Lett.* **104**, 195302.
- Hepp, K., and E. H. Lieb, 1973, *Ann. Phys. (N.Y.)* **76**, 360.
- Hermes, S., T. J. G. Apollaro, S. Paganelli, and T. Macrì, 2020, *Phys. Rev. A* **101**, 053607.
- Hernández-Santana, S., C. Gogolin, J. I. Cirac, and A. Acín, 2017, *Phys. Rev. Lett.* **119**, 110601.
- Hertkorn, J., *et al.*, 2021, *Phys. Rev. X* **11**, 011037.
- Heyl, M., 2014, *Phys. Rev. Lett.* **113**, 205701.
- Heyl, M., 2015, *Phys. Rev. Lett.* **115**, 140602.
- Heyl, M., 2018, *Rep. Prog. Phys.* **81**, 054001.
- Heyl, M., A. Polkovnikov, and S. Kehrein, 2013, *Phys. Rev. Lett.* **110**, 135704.
- Himbert, L., C. Cormick, R. Kraus, S. Sharma, and G. Morigi, 2019, *Phys. Rev. A* **99**, 043633.
- Hoang, T. M., H. M. Bharath, M. J. Boguslawski, M. Anquez, B. A. Robbins, and M. S. Chapman, 2016, *Proc. Natl. Acad. Sci. U.S.A.* **113**, 9475.
- Hohenberg, P. C., 1967, *Phys. Rev.* **158**, 383.
- Hohenberg, P. C., and J. B. Swift, 1995, *Phys. Rev. E* **52**, 1828.
- Holovatch, Y., and M. Shpot, 1992, *J. Stat. Phys.* **66**, 867.
- Holstein, T., and H. Primakoff, 1940, *Phys. Rev.* **58**, 1098.
- Holzhey, C., F. Larsen, and F. Wilczek, 1994, *Nucl. Phys.* **B424**, 443.
- Homrighausen, I., N. O. Abeling, V. Zauner-Stauber, and J. C. Halimeh, 2017, *Phys. Rev. B* **96**, 104436.
- Honkonen, J., 1990, *J. Phys. A* **23**, 825.
- Horak, P., and H. Ritsch, 2001, *Phys. Rev. A* **63**, 023603.
- Horita, T., H. Suwa, and S. Todo, 2017, *Phys. Rev. E* **95**, 012143.
- Hruby, L., N. Dogra, M. Landini, T. Donner, and T. Esslinger, 2018, *Proc. Natl. Acad. Sci. U.S.A.* **115**, 3279.
- Huang, Y.-P., D. Banerjee, and M. Heyl, 2019, *Phys. Rev. Lett.* **122**, 250401.
- Hughes-Hallett, D., *et al.*, 2008, *Calculus: Single Variable*, 5th ed. (Wiley, New York).
- Hung, C.-L., A. González-Tudela, J. I. Cirac, and H. J. Kimble, 2016, *Proc. Natl. Acad. Sci. U.S.A.* **113**, E4946.
- Hung, C.-L., X. Zhang, N. Gemelke, and C. Chin, 2010, *Phys. Rev. Lett.* **104**, 160403.
- Hwang, M. J., R. Puebla, and M. B. Plenio, 2015, *Phys. Rev. Lett.* **115**, 180404.
- Iglói, F., B. Blaß, G. Roósz, and H. Rieger, 2018, *Phys. Rev. B* **98**, 184415.
- Imry, Y., 1974, *Phys. Rev. Lett.* **33**, 1304.
- Isenhower, L., E. Urban, X. L. Zhang, A. T. Gill, T. Henage, T. A. Johnson, T. G. Walker, and M. Saffman, 2010, *Phys. Rev. Lett.* **104**, 010503.
- Ising, E., 1925, *Z. Phys.* **31**, 253.
- Islam, R., C. Senko, W. C. Campbell, S. Korenblit, J. Smith, A. Lee, E. E. Edwards, C. C. J. Wang, J. K. Freericks, and C. Monroe, 2013, *Science* **340**, 583.
- Ispolatov, I., and E. G. D. Cohen, 2001, *Physica (Amsterdam)* **295A**, 475.
- Jacobs, L., and R. Savit, 1983, *Ann. N.Y. Acad. Sci.* **410**, 281.
- Jäger, S. B., L. Dell'Anna, and G. Morigi, 2020, *Phys. Rev. B* **102**, 035152.
- Jaksch, D., J. I. Cirac, P. Zoller, S. L. Rolston, R. Côté, and M. D. Lukin, 2000, *Phys. Rev. Lett.* **85**, 2208.
- Jakubczyk, P., N. Dupuis, and B. Delamotte, 2014, *Phys. Rev. E* **90**, 062105.
- Jakubczyk, P., and W. Metzner, 2017, *Phys. Rev. B* **95**, 085113.
- James, A. J. A., R. M. Konik, and N. J. Robinson, 2019, *Phys. Rev. Lett.* **122**, 130603.

- Jaschke, D., K. Maeda, J. D. Whalen, M. L. Wall, and L. D. Carr, 2017, *New J. Phys.* **19**, 033032.
- Jau, Y. Y., A. M. Hankin, T. Keating, I. H. Deutsch, and G. W. Biedermann, 2016, *Nat. Phys.* **12**, 71.
- Johnson, J. E., and S. L. Rolston, 2010, *Phys. Rev. A* **82**, 033412.
- Jordan, E., K. A. Gilmore, A. Shankar, A. Safavi-Naini, J. G. Bohnet, M. J. Holland, and J. J. Bollinger, 2019, *Phys. Rev. Lett.* **122**, 053603.
- José, J. V., 2013, Ed., *40 Years of Berezinskii-Kosterlitz-Thouless Theory* (World Scientific, Singapore).
- Joyce, G. S., 1966, *Phys. Rev.* **146**, 349.
- Jozsa, R., and N. Linden, 2003, *Proc. R. Soc. A* **459**, 2011.
- Jurcevic, P., B. P. Lanyon, P. Hauke, C. Hempel, P. Zoller, R. Blatt, and C. F. Roos, 2014, *Nature (London)* **511**, 202.
- Jurcevic, P., H. Shen, P. Hauke, C. Maier, T. Brydges, C. Hempel, B. P. Lanyon, M. Heyl, R. Blatt, and C. F. Roos, 2017, *Phys. Rev. Lett.* **119**, 080501.
- Kac, M., G. E. Uhlenbeck, and P. C. Hemmer, 1963, *J. Math. Phys. (N.Y.)* **4**, 216.
- Kanungo, S. K., J. D. Whalen, Y. Lu, M. Yuan, S. Dasgupta, F. B. Dunning, K. R. A. Hazzard, and T. C. Killian, 2021, [arXiv:2101.02871](https://arxiv.org/abs/2101.02871).
- Karpov, P. I., G. Y. Zhu, M. P. Heller, and M. Heyl, 2020, [arXiv:2011.11624](https://arxiv.org/abs/2011.11624).
- Kashuba, A., and V. L. Pokrovsky, 1993, *Phys. Rev. Lett.* **70**, 3155.
- Kastner, M., 2010, *Phys. Rev. Lett.* **104**, 240403.
- Kastner, M., 2011, *Phys. Rev. Lett.* **106**, 130601.
- Katzgraber, H. G., D. Larson, and A. P. Young, 2009, *Phys. Rev. Lett.* **102**, 177205.
- Kaubruegger, R., P. Silvi, C. Kokail, R. van Bijnen, A. M. Rey, J. Ye, A. M. Kaufman, and P. Zoller, 2019, *Phys. Rev. Lett.* **123**, 260505.
- Kaufmann, H., S. Ulm, G. Jacob, U. Poschinger, H. Landa, A. Retzker, M. B. Plenio, and F. Schmidt-Kaler, 2012, *Phys. Rev. Lett.* **109**, 263003.
- Kawaguchi, Y., and M. Ueda, 2012, *Phys. Rep.* **520**, 253.
- Keesling, A., *et al.*, 2019, *Nature (London)* **568**, 207.
- Keller, T., S. B. Jager, and G. Morigi, 2017, *J. Stat. Mech.* 064002.
- Keßler, H., J. G. Cosme, M. Hemmerling, L. Mathey, and A. Hemmerich, 2019, *Phys. Rev. A* **99**, 053605.
- Keßler, H., P. Kongkhambut, C. Georges, L. Mathey, J. G. Cosme, and A. Hemmerich, 2020, [arXiv:2012.08885](https://arxiv.org/abs/2012.08885).
- Khemani, V., M. Hermele, and R. Nandkishore, 2020, *Phys. Rev. B* **101**, 174204.
- Khemani, V., A. Lazarides, R. Moessner, and S. L. Sondhi, 2016, *Phys. Rev. Lett.* **116**, 250401.
- Khemani, V., R. Moessner, and S. L. Sondhi, 2019, [arXiv:1910.10745](https://arxiv.org/abs/1910.10745).
- Kibble, T. W. B., 1976, *J. Phys. A* **9**, 1387.
- Kim, K., M.-S. Chang, R. Islam, S. Korenblit, L.-M. Duan, and C. Monroe, 2009, *Phys. Rev. Lett.* **103**, 120502.
- Kirton, P., M. M. Roses, J. Keeling, and E. G. Dalla Torre, 2019, *Adv. Quantum Technol.* **2**, 1800043.
- Kitaev, A., 2009, *AIP Conf. Proc.* **1134**, 22.
- Kitaev, A. Y., 2001, *Phys. Usp.* **44**, 131.
- Kivelson, S. A., I. P. Bindloss, E. Fradkin, V. Oganesyan, J. M. Tranquada, A. Kapitulnik, and C. Howald, 2003, *Rev. Mod. Phys.* **75**, 1201.
- Kivelson, S. A., E. Fradkin, and V. J. Emery, 1998, *Nature (London)* **393**, 550.
- Kleinert, H., 2001, *Critical Properties of psi^4 Theories* (World Scientific Publishing, Singapore).
- Klinder, J., H. Keßler, M. R. Bakhtiari, M. Thorwart, and A. Hemmerich, 2015, *Phys. Rev. Lett.* **115**, 230403.
- Klinder, J., H. Keßler, M. Wolke, L. Mathey, and A. Hemmerich, 2015, *Proc. Natl. Acad. Sci. U.S.A.* **112**, 3290.
- Klinovaja, J., P. Stano, A. Yazdani, and D. Loss, 2013, *Phys. Rev. Lett.* **111**, 186805.
- Knight, P. L., *et al.*, 2003, *Phil. Trans. R. Soc. A* **361**, 1349.
- Koffel, T., M. Lewenstein, and L. Tagliacozzo, 2012, *Phys. Rev. Lett.* **109**, 267203.
- Kohn, W., 1964, *Phys. Rev.* **133**, A171.
- Kollár, A. J., A. T. Papageorge, V. D. Vaidya, Y. Guo, J. Keeling, and B. L. Lev, 2017, *Nat. Commun.* **8**, 14386.
- Kormos, M., M. Collura, G. Takács, and P. Calabrese, 2017, *Nat. Phys.* **13**, 246.
- Kosior, A., and K. Sacha, 2018, *Phys. Rev. A* **97**, 053621.
- Kosterlitz, J. M., 1974, *J. Phys. C* **7**, 1046.
- Kosterlitz, J. M., 2017, *Rev. Mod. Phys.* **89**, 040501.
- Kosterlitz, J. M., and D. J. Thouless, 1973, *J. Phys. C* **6**, 1181.
- Kotliar, G., P. W. Anderson, and D. L. Stein, 1983, *Phys. Rev. B* **27**, 602.
- Koziol, J., S. Fey, S. C. Kapfer, and K. P. Schmidt, 2019, *Phys. Rev. B* **100**, 144411.
- Koziol, J., A. Langheld, S. C. Kapfer, and K. P. Schmidt, 2021, [arXiv:2103.09469](https://arxiv.org/abs/2103.09469).
- Krieg, J., and P. Kopietz, 2017, *Phys. Rev. E* **96**, 042107.
- Kroeze, R. M., Y. Guo, V. D. Vaidya, J. Keeling, and B. L. Lev, 2018, *Phys. Rev. Lett.* **121**, 163601.
- Kunimi, M., and Y. Kato, 2012, *Phys. Rev. B* **86**, 060510.
- Kunz, H., and C. E. Pfister, 1976, *Commun. Math. Phys.* **46**, 245.
- Kuwahara, T., and K. Saito, 2020, *Phys. Rev. X* **10**, 031010.
- Kwaśnicki, M., 2017, *Fractional Calculus Appl. Anal.* **20**, 7.
- Kyprianidis, A., *et al.*, 2021, *Science* **372**, 1192.
- Labuhn, H., D. Barredo, S. Ravets, S. de Léséleuc, T. Macrì, T. Lahaye, and A. Browaeys, 2016, *Nature (London)* **534**, 667.
- Ladd, T. D., F. Jelezko, R. Laflamme, Y. Nakamura, C. Monroe, and J. L. O'Brien, 2010, *Nature (London)* **464**, 45.
- Laghi, D., T. Macrì, and A. Trombettoni, 2017, *Phys. Rev. A* **96**, 043605.
- Lahaye, T., C. Menotti, L. Santos, M. Lewenstein, and T. Pfau, 2009, *Rep. Prog. Phys.* **72**, 126401.
- Landa, H., S. Marcovitch, A. Retzker, M. B. Plenio, and B. Reznik, 2010, *Phys. Rev. Lett.* **104**, 043004.
- Landau, L. D., and E. M. Lifshitz, 1969, *Statistical Physics, Part 1* (Butterworth-Heinemann, Oxford).
- Landau, L. D., and E. M. Lifshitz, 1976, *Mechanics*, 3rd ed., Course of Theoretical Physics Vol. 1 (Butterworth-Heinemann, Oxford).
- Landau, L. D., and E. M. Lifshitz, 1991, *Quantum Mechanics: Non-Relativistic Theory* (Butterworth-Heinemann, Oxford).
- Landig, R., F. Brennecke, R. Mottl, T. Donner, and T. Esslinger, 2015, *Nat. Commun.* **6**, 7046.
- Landig, R., L. Hruby, N. Dogra, M. Landini, R. Mottl, T. Donner, and T. Esslinger, 2016, *Nature (London)* **532**, 476.
- Landini, M., N. Dogra, K. Kroeger, L. Hruby, T. Donner, and T. Esslinger, 2018, *Phys. Rev. Lett.* **120**, 223602.
- Lang, J., B. Frank, and J. C. Halimeh, 2018, *Phys. Rev. Lett.* **121**, 130603.
- Lang, J., F. Piazza, and W. Zwerger, 2017, *New J. Phys.* **19**, 123027.
- Larkin, A. I., and S. A. Pikin, 1969, *Sov. Phys. JETP* **29**, 891, http://www.jetp.ras.ru/cgi-bin/dn/e_029_05_0891.pdf.
- Larson, J., B. Damski, G. Morigi, and M. Lewenstein, 2008, *Phys. Rev. Lett.* **100**, 050401.
- Lashkari, N., D. Stanford, M. Hastings, T. Osborne, and P. Hayden, 2013, *J. High Energy Phys.* **04**, 22.
- Last, Y., 1996, *J. Funct. Anal.* **142**, 406.

- Latella, I., A. Pérez-Madrid, A. Campa, L. Casetti, and S. Ruffo, 2015, *Phys. Rev. Lett.* **114**, 230601.
- Lechner, W., H.-P. Büchler, and P. Zoller, 2014, *Phys. Rev. Lett.* **112**, 255301.
- Lechner, W., P. Hauke, and P. Zoller, 2015, *Sci. Adv.* **1**, e1500838.
- Lee, A.-C., D. Baillie, R. N. Bisset, and P. B. Blakie, 2018, *Phys. Rev. A* **98**, 063620.
- Lee, R. M., and N. D. Drummond, 2011, *Phys. Rev. B* **83**, 245114.
- Lee, S. K., J. Cho, and K. S. Choi, 2015, *New J. Phys.* **17**, 113053.
- Lee, W., M. Kim, H. Jo, Y. Song, and J. Ahn, 2019, *Phys. Rev. A* **99**, 043404.
- Leibfried, D., R. Blatt, C. Monroe, and D. Wineland, 2003, *Rev. Mod. Phys.* **75**, 281.
- Leibfried, D., *et al.*, 2003, *Nature (London)* **422**, 412.
- Lemmer, A., C. Cormick, C. T. Schmiegelow, F. Schmidt-Kaler, and M. B. Plenio, 2015, *Phys. Rev. Lett.* **114**, 073001.
- Léonard, J., A. Morales, P. Zupancic, T. Donner, and T. Esslinger, 2017, *Science* **358**, 1415.
- Léonard, J., A. Morales, P. Zupancic, T. Esslinger, and T. Donner, 2017, *Nature (London)* **543**, 87.
- Lepori, L., and L. Dell'Anna, 2017, *New J. Phys.* **19**, 103030.
- Lepori, L., A. Trombettoni, and D. Vodola, 2017, *J. Stat. Mech.* **033102**.
- Lepori, L., D. Vodola, G. Pupillo, G. Gori, and A. Trombettoni, 2016, *Ann. Phys. (Amsterdam)* **374**, 35.
- Lepoutre, S., J. Schachenmayer, L. Gabardos, B. Zhu, B. Naylor, E. Maréchal, O. Gorceix, A. M. Rey, L. Vernac, and B. Laburthe-Tolra, 2019, *Nat. Commun.* **10**, 1714.
- Lerose, A., J. Marino, A. Gambassi, and A. Silva, 2019, *Phys. Rev. B* **100**, 104306.
- Lerose, A., J. Marino, B. Žunkovič, A. Gambassi, and A. Silva, 2018, *Phys. Rev. Lett.* **120**, 130603.
- Lerose, A., and S. Pappalardi, 2020a, *Phys. Rev. A* **102**, 032404.
- Lerose, A., and S. Pappalardi, 2020b, *Phys. Rev. Res.* **2**, 012041.
- Lerose, A., F. M. Surace, P. P. Mazza, G. Perfetto, M. Collura, and A. Gambassi, 2020, *Phys. Rev. B* **102**, 041118.
- Lerose, A., B. Žunkovič, J. Marino, A. Gambassi, and A. Silva, 2019, *Phys. Rev. B* **99**, 045128.
- Lerose, A., B. Žunkovič, A. Silva, and A. Gambassi, 2019, *Phys. Rev. B* **99**, 121112.
- Leroux, I. D., M. H. Schleier-Smith, and V. Vuletić, 2010, *Phys. Rev. Lett.* **104**, 073602.
- Lesanovsky, I., and J. P. Garrahan, 2013, *Phys. Rev. Lett.* **111**, 215305.
- Lesanovsky, I., K. Macieszczak, and J. P. Garrahan, 2019, *Quantum Sci. Technol.* **4**, 02LT02.
- Letscher, F., O. Thomas, T. Niederprüm, M. Fleischhauer, and H. Ott, 2017, *Phys. Rev. X* **7**, 021020.
- Leuzzi, L., G. Parisi, F. Ricci-Tersenghi, and J. J. Ruiz-Lorenzo, 2008, *Phys. Rev. Lett.* **101**, 107203.
- Levi, E., R. Gutiérrez, and I. Lesanovsky, 2016, *J. Phys. B* **49**, 184003.
- Levin, Y., R. Pakter, F. B. Rizzato, T. N. Teles, and F. P. Benetti, 2014, *Phys. Rep.* **535**, 1.
- Lewenstein, M., A. Sanpera, V. Ahufinger, B. Damski, A. Sen, and U. Sen, 2007, *Adv. Phys.* **56**, 243.
- Lewin, M., and E. H. Lieb, 2015, *Phys. Rev. A* **91**, 022507.
- Lewis, H. R., 1967, *Phys. Rev. Lett.* **18**, 510.
- Lewis, Jr., H. R., 1968, *J. Math. Phys. (N.Y.)* **9**, 1976.
- Lewis, Jr., H. R., and W. B. Riesenfeld, 1969, *J. Math. Phys. (N.Y.)* **10**, 1458.
- Lewis-Swan, R. J., D. Barberena, J. R. K. Cline, D. J. Young, J. K. Thompson, and A. M. Rey, 2021, *Phys. Rev. Lett.* **126**, 173601.
- Li, J. R., J. Lee, W. Huang, S. Burchesky, B. Shteynas, F. Ç. Topi, A. O. Jamison, and W. Ketterle, 2017, *Nature (London)* **543**, 91.
- Li, W., A. Dhar, X. Deng, K. Kasamatsu, L. Barbiero, and L. Santos, 2020, *Phys. Rev. Lett.* **124**, 010404.
- Li, W., *et al.*, 2011, *Science* **334**, 1110.
- Li, W.-H., X. Deng, and L. Santos, 2021, *arXiv:2103.13780*.
- Li, Y., A. Geißler, W. Hofstetter, and W. Li, 2018, *Phys. Rev. A* **97**, 023619.
- Li, Y., L. He, and W. Hofstetter, 2013, *Phys. Rev. A* **87**, 051604.
- Lieb, E. H., and D. W. Robinson, 1972, *Commun. Math. Phys.* **28**, 251.
- Lienhard, V., S. de Léséleuc, D. Barredo, T. Lahaye, A. Browaeys, M. Schuler, L.-P. Henry, and A. M. Läuchli, 2018, *Phys. Rev. X* **8**, 021070.
- Lienhard, V., *et al.*, 2020, *Phys. Rev. X* **10**, 021031.
- Likos, C. N., 2001, *Phys. Rep.* **348**, 267.
- Likos, C. N., A. Lang, M. Watzlawek, and H. Löwen, 2001, *Phys. Rev. E* **63**, 031206.
- Likos, C. N., B. M. Mladek, D. Gottwald, and G. Kahl, 2007, *J. Chem. Phys.* **126**, 224502.
- Lilly, M. P., K. B. Cooper, J. P. Eisenstein, L. N. Pfeiffer, and K. W. West, 1999, *Phys. Rev. Lett.* **82**, 394.
- Lima, A. R. P., and A. Pelster, 2011, *Phys. Rev. A* **84**, 041604.
- Lin, R., L. Papariello, P. Morignini, R. Chitra, and A. U. J. Lode, 2019, *Phys. Rev. A* **100**, 013611.
- Lin, Y., J. P. Gaebler, T. R. Tan, R. Bowler, J. D. Jost, D. Leibfried, and D. J. Wineland, 2013, *Phys. Rev. Lett.* **110**, 153002.
- Linden, N., S. Popescu, A. J. Short, and A. Winter, 2009, *Phys. Rev. E* **79**, 061103.
- Lipkin, H. J., N. Meshkov, and A. J. Glick, 1965, *Nucl. Phys.* **62**, 188.
- Lipowsky, R., 1987, *Ferroelectrics* **73**, 69.
- Lipowsky, R., and W. Speth, 1983, *Phys. Rev. B* **28**, 3983.
- Liu, F., R. Lundgren, P. Titum, G. Pagano, J. Zhang, C. Monroe, and A. V. Gorshkov, 2019, *Phys. Rev. Lett.* **122**, 150601.
- Lourenço, J. A. S., G. Higgins, C. Zhang, M. Hennrich, and T. Macrì, 2021, *arXiv:2111.04378*.
- Lu, M., N. Q. Burdick, and B. L. Lev, 2012, *Phys. Rev. Lett.* **108**, 215301.
- Lu, Z.-K., Y. Li, D. S. Petrov, and G. V. Shlyapnikov, 2015, *Phys. Rev. Lett.* **115**, 075303.
- Luijten, E., and H. W. J. Blöte, 1996, *Phys. Rev. Lett.* **76**, 1557.
- Luijten, E., and H. W. J. Blöte, 1997, *Phys. Rev. B* **56**, 8945.
- Luijten, E., and H. W. J. Blöte, 2002, *Phys. Rev. Lett.* **89**, 025703.
- Lukin, M. D., M. Fleischhauer, R. Cote, L. M. Duan, D. Jaksch, J. I. Cirac, and P. Zoller, 2001, *Phys. Rev. Lett.* **87**, 037901.
- Lynden-Bell, D., 1999, *Physica (Amsterdam)* **263A**, 293.
- Machado, F., D. V. Else, G. D. Kahanamoku-Meyer, C. Nayak, and N. Y. Yao, 2020, *Phys. Rev. X* **10**, 011043.
- Macrì, T., F. Maucher, F. Cinti, and T. Pohl, 2013, *Phys. Rev. A* **87**, 061602.
- Macrì, T., and T. Pohl, 2014, *Phys. Rev. A* **89**, 011402.
- Macrì, T., S. Saccani, and F. Cinti, 2014, *J. Low Temp. Phys.* **177**, 59.
- Macrì, T., A. Smerzi, and L. Pezzè, 2016, *Phys. Rev. A* **94**, 010102.
- Maghrebi, M. F., Z.-X. Gong, M. Foss-Feig, and A. V. Gorshkov, 2016, *Phys. Rev. B* **93**, 125128.
- Maghrebi, M. F., Z.-X. Gong, and A. V. Gorshkov, 2017, *Phys. Rev. Lett.* **119**, 023001.
- Maier, P. G., and F. Schwabl, 2004, *Phys. Rev. B* **70**, 134430.
- Maity, S., U. Bhattacharya, and A. Dutta, 2020, *J. Phys. A* **53**, 013001.
- Majer, J., *et al.*, 2007, *Nature (London)* **449**, 443.
- Maksymov, A. O., and A. L. Burin, 2020, *Phys. Rev. B* **101**, 024201.

- Malard, M., 2013, *Braz. J. Phys.* **43**, 182.
- Maldacena, J., S. H. Shenker, and D. Stanford, 2016, *J. High Energy Phys.* **08**, 106.
- Manzano, D., 2020, *AIP Adv.* **10**, 025106.
- Marino, J., 2021, *arXiv:2108.12422*.
- Martinez, E. A., *et al.*, 2016, *Nature (London)* **534**, 516.
- Maschler, C., I. B. Mekhov, and H. Ritsch, 2008, *Eur. Phys. J. D* **46**, 545.
- Masella, G., A. Angelone, F. Mezzacapo, G. Pupillo, and N. V. Prokof'ev, 2019, *Phys. Rev. Lett.* **123**, 045301.
- Matsuda, K., L. De Marco, J.-R. Li, W. G. Tobias, G. Valtolina, G. Quémener, and J. Ye, 2020, *Science* **370**, 1324.
- Matsuta, T., T. Koma, and S. Nakamura, 2017, *Ann. Inst. Henri Poincaré* **18**, 519.
- Mattioli, M., M. Dalmonte, W. Lechner, and G. Pupillo, 2013, *Phys. Rev. Lett.* **111**, 165302.
- Matveeva, N., and S. Giorgini, 2014, *Phys. Rev. A* **90**, 053620.
- Maucher, F., N. Henkel, M. Saffman, W. Królikowski, S. Skupin, and T. Pohl, 2011, *Phys. Rev. Lett.* **106**, 170401.
- Mazza, P. P., G. Peretto, A. Lerose, M. Collura, and A. Gambassi, 2019, *Phys. Rev. B* **99**, 180302.
- Mazza, P. P., R. Schmidt, and I. Lesanovsky, 2020, *Phys. Rev. Lett.* **125**, 033602.
- Mendoza-Coto, A., D. G. Barci, and D. A. Stariolo, 2017, *Phys. Rev. B* **95**, 144209.
- Mendoza-Coto, A., R. Cenci, G. Pupillo, R. Díaz-Méndez, and E. Babaev, 2021, *Soft Matter* **17**, 915.
- Mendoza-Coto, A., L. Nicolao, and R. Díaz-Méndez, 2019, *Sci. Rep.* **9**, 2020.
- Mendoza-Coto, A., and D. A. Stariolo, 2012, *Phys. Rev. E* **86**, 051130.
- Mendoza-Coto, A., D. A. Stariolo, and L. Nicolao, 2015, *Phys. Rev. Lett.* **114**, 116101.
- Mendoza-Coto, A., R. Turcati, V. Zampronio, R. Díaz-Méndez, T. Macrì, and F. Cinti, 2021, *arXiv:2110.12299*.
- Menu, R., and T. Roscilde, 2020, *Phys. Rev. Lett.* **124**, 130604.
- Mermin, N. D., and H. Wagner, 1966, *Phys. Rev. Lett.* **17**, 1133.
- Meshkov, N., A. J. Glick, and H. J. Lipkin, 1965, *Nucl. Phys.* **62**, 199.
- Meyer, J. S., K. A. Matveev, and A. I. Larkin, 2007, *Phys. Rev. Lett.* **98**, 126404.
- Mi, X., *et al.*, 2022, *Nature (London)* **601**, 531.
- Micheli, A., G. Pupillo, H. P. Büchler, and P. Zoller, 2007, *Phys. Rev. A* **76**, 043604.
- Millán, A. P., G. Gori, F. Battiston, T. Enss, and N. Defenu, 2021, *Phys. Rev. Res.* **3**, 023015.
- Minato, T., K. Sugimoto, T. Kuwahara, and K. Saito, 2022, *Phys. Rev. Lett.* **128**, 010603.
- Mishra, C., L. Santos, and R. Nath, 2020, *Phys. Rev. Lett.* **124**, 073402.
- Mivehvar, F., S. Ostermann, F. Piazza, and H. Ritsch, 2018, *Phys. Rev. Lett.* **120**, 123601.
- Mivehvar, F., F. Piazza, T. Donner, and H. Ritsch, 2021, *Adv. Phys.* **70**, 1.
- MoECKEL, M., and S. Kehrein, 2008, *Phys. Rev. Lett.* **100**, 175702.
- Mokhberi, A., M. Hennrich, F. Schmidt-Kaler, L. F. Dimauuro, H. Perrin, and S. F. Yelin, 2020, in *Advances in Atomic, Molecular, and Optical Physics*, Vol. 69, edited by S. F. Yelin, L. F. Dimauuro, and H. Perrin (Academic Press, New York).
- Monroe, C., D. M. Meekhof, B. E. King, S. R. Jefferts, W. M. Itano, D. J. Wineland, and P. Gould, 1995, *Phys. Rev. Lett.* **75**, 4011.
- Monroe, C., *et al.*, 2021, *Rev. Mod. Phys.* **93**, 025001.
- Monthus, C., 2015, *J. Stat. Mech.* P05026.
- Morales, A., P. Zupancic, J. Léonard, T. Esslinger, and T. Donner, 2018, *Nat. Mater.* **17**, 686.
- Morgado, M., and S. Whitlock, 2020, *arXiv:2011.03031*.
- Mori, T., T. N. Ikeda, E. Kaminishi, and M. Ueda, 2018, *J. Phys. B* **51**, 112001.
- Morigi, G., and S. Fishman, 2004, *Phys. Rev. Lett.* **93**, 170602.
- Morong, W., F. Liu, P. Becker, K. S. Collins, L. Feng, A. Kyprianidis, G. Pagano, T. You, A. V. Gorshkov, and C. Monroe, 2021, *Nature (London)* **599**, 393.
- Moroni, S., and M. Boninsegni, 2014, *Phys. Rev. Lett.* **113**, 240407.
- Moses, S. A., J. P. Covey, M. T. Miecinkowski, D. S. Jin, and J. Ye, 2017, *Nat. Phys.* **13**, 13.
- Mottl, R., F. Brennecke, K. Baumann, R. Landig, T. Donner, and T. Esslinger, 2012, *Science* **336**, 1570.
- Moudgalya, S., A. Prem, R. Nandkishore, N. Regnault, and B. A. Bernevig, 2021, in *Memorial Volume for Shoucheng Zhang*, edited by X. Qi, B. Lian, E. Demler, S. Kivelson, and C. X. Liu (World Scientific, Singapore), Chap. 7, pp. 147–209.
- Mukamel, D., 2008, in *Long-Range Interacting Systems*, Proceedings of the Les Houches Summer School, Session XC, edited by T. Dauxois, S. Ruffo, and L. F. Cugliandolo (Oxford University Press, New York).
- Mukamel, D., S. Ruffo, and N. Schreiber, 2005, *Phys. Rev. Lett.* **95**, 240604.
- Müller, M., L. Liang, I. Lesanovsky, and P. Zoller, 2008, *New J. Phys.* **10**, 093009.
- Muniz, J. A., D. Barberena, R. J. Lewis-Swan, D. J. Young, J. R. K. Cline, A. M. Rey, and J. K. Thompson, 2020, *Nature (London)* **580**, 602.
- Murthy, P. A., I. Boettcher, L. Bayha, M. Holzmann, D. Kedar, M. Neidig, M. G. Ries, A. N. Wenz, G. Zürn, and S. Jochim, 2015, *Phys. Rev. Lett.* **115**, 010401.
- Muschik, C., M. Heyl, E. Martinez, T. Monz, P. Schindler, B. Vogell, M. Dalmonte, P. Hauke, R. Blatt, and P. Zoller, 2017, *New J. Phys.* **19**, 103020.
- Mussardo, G., 2009, *Statistical Field Theory: An Introduction to Exactly Solved Models in Statistical Physics*, Oxford Graduate Texts (Oxford University Press, New York).
- Myerson, A. H., D. J. Szwer, S. C. Webster, D. T. C. Allcock, M. J. Curtis, G. Imreh, J. A. Sherman, D. N. Stacey, A. M. Steane, and D. M. Lucas, 2008, *Phys. Rev. Lett.* **100**, 200502.
- Nachtergaele, B., Y. Ogata, and R. Sims, 2006, *J. Stat. Phys.* **124**, 1.
- Nadj-Perge, S., I. K. Drozdov, J. Li, H. Chen, S. Jeon, J. Seo, A. H. MacDonald, B. A. Bernevig, and A. Yazdani, 2014, *Science* **346**, 602.
- Nag, S., and A. Garg, 2019, *Phys. Rev. B* **99**, 224203.
- Nagy, D., G. Kónya, G. Szirmai, and P. Domokos, 2010, *Phys. Rev. Lett.* **104**, 130401.
- Nagy, D., G. Szirmai, and P. Domokos, 2008, *Eur. Phys. J. D* **48**, 127.
- Nagy, D., G. Szirmai, and P. Domokos, 2011, *Phys. Rev. A* **84**, 043637.
- Nakamura, M., 2000, *Phys. Rev. B* **61**, 16377.
- Nandkishore, R., and S. Gopalakrishnan, 2021, *Phys. Rev. B* **103**, 134423.
- Nandkishore, R., and D. A. Huse, 2015, *Annu. Rev. Condens. Matter Phys.* **6**, 15.
- Nandkishore, R. M., and S. L. Sondhi, 2017, *Phys. Rev. X* **7**, 041021.
- Natale, G., R. M. W. van Bijnen, A. Patscheider, D. Petter, M. J. Mark, L. Chomaz, and F. Ferlaino, 2019, *Phys. Rev. Lett.* **123**, 050402.
- Nath, R., M. Dalmonte, A. W. Glaetzle, P. Zoller, F. Schmidt-Kaler, and R. Gerritsma, 2015, *New J. Phys.* **17**, 065018.
- Nelson, D. R., and J. M. Kosterlitz, 1977, *Phys. Rev. Lett.* **39**, 1201.

- Newman, C. M., and L. S. Schulman, 1977, *J. Math. Phys. (N.Y.)* **18**, 23.
- Neyenhuis, B., J. Zhang, P. W. Hess, J. Smith, A. C. Lee, P. Richerme, Z.-X. Gong, A. V. Gorshkov, and C. Monroe, 2017, *Sci. Adv.* **3**, e1700672.
- Nezhadhighi, M. G., and M. A. Rajabpour, 2014, *Phys. Rev. B* **90**, 205438.
- Nishimori, H., and G. Ortiz, 2015, *Elements of Phase Transitions and Critical Phenomena* (Oxford University Press, New York).
- Nisoli, C., and A. R. Bishop, 2014, *Phys. Rev. Lett.* **112**, 070401.
- Noek, R., G. Vrijsen, D. Gaultney, E. Mount, T. Kim, P. Maunz, and J. Kim, 2013, *Opt. Lett.* **38**, 4735.
- Norcia, M. A., R. J. Lewis-Swan, J. R. K. Cline, B. Zhu, A. M. Rey, and J. K. Thompson, 2018, *Science* **361**, 259.
- Norcia, M. A., C. Politi, L. Klaus, E. Poli, M. Sohmen, M. J. Mark, R. Bisset, L. Santos, and F. Ferlino, 2021, [arXiv:2102.05555](https://arxiv.org/abs/2102.05555).
- Nussenzveig, H., 1973, *Introduction to Quantum Optics*, Documents on Modern Physics (Gordon and Breach, New York).
- O'Dell, D., S. Giovanazzi, G. Kurizki, and V. M. Akulin, 2000, *Phys. Rev. Lett.* **84**, 5687.
- O'Dell, D. H. J., S. Giovanazzi, and G. Kurizki, 2003, *Phys. Rev. Lett.* **90**, 110402.
- Ohl de Mello, D., D. Schäffner, J. Werkmann, T. Preuschoff, L. Kohfahl, M. Schlosser, and G. Birkel, 2019, *Phys. Rev. Lett.* **122**, 203601.
- Ojeda Collado, H. P., G. Usaj, C. A. Balseiro, D. H. Zanette, and J. Lorenzana, 2021, *Phys. Rev. Res.* **3**, L042023.
- Ortiz, C., J. Lorenzana, and C. D. Castro, 2008, *J. Phys. Condens. Matter* **20**, 434229.
- Ospelkaus, C., U. Warring, Y. Colombe, K. R. Brown, J. M. Amini, D. Leibfried, and D. J. Wineland, 2011, *Nature (London)* **476**, 181.
- Öztop, B., M. Boryduh, Ö. E. Müstecaplıoğlu, and H. E. Türeci, 2012, *New J. Phys.* **14**, 085011.
- Öztop, B., Ö. E. Müstecaplıoğlu, and H. E. Türeci, 2013, *Laser Phys.* **23**, 025501.
- Pagano, G., *et al.*, 2018, *Quantum Sci. Technol.* **4**, 014004.
- Pan, F., and J. P. Draayer, 1999, *Phys. Lett. B* **451**, 1.
- Pan, W., R. R. Du, H. L. Stormer, D. C. Tsui, L. N. Pfeiffer, K. W. Baldwin, and K. W. West, 1999, *Phys. Rev. Lett.* **83**, 820.
- Pappalardi, S., A. Russomanno, B. Žunkovič, F. Iemini, A. Silva, and R. Fazio, 2018, *Phys. Rev. B* **98**, 134303.
- Park, J. W., S. A. Will, and M. W. Zwierlein, 2015, *Phys. Rev. Lett.* **114**, 205302.
- Parker, C. V., P. Aynajian, E. H. da Silva Neto, A. Pushp, S. Ono, J. Wen, Z. Xu, G. Gu, and A. Yazdani, 2010, *Nature (London)* **468**, 677.
- Parker, N. G., C. Ticknor, A. M. Martin, and D. H. J. O'Dell, 2009, *Phys. Rev. A* **79**, 013617.
- Patrick, K., T. Neupert, and J. K. Pachos, 2017, *Phys. Rev. Lett.* **118**, 267002.
- Patscheider, A., B. Zhu, L. Chomaz, D. Petter, S. Baier, A.-M. Rey, F. Ferlino, and M. J. Mark, 2020, *Phys. Rev. Res.* **2**, 023050.
- Paul, W., 1990, *Rev. Mod. Phys.* **62**, 531.
- Pehlivan, Y., A. B. Balantekin, T. Kajino, and T. Yoshida, 2011, *Phys. Rev. D* **84**, 065008.
- Pelissetto, A., and E. Vicari, 2002, *Phys. Rep.* **368**, 549.
- Periwal, A., E. S. Cooper, P. Kunkel, J. F. Wienand, E. J. Davis, and M. Schleier-Smith, 2021, [arXiv:2106.04070](https://arxiv.org/abs/2106.04070).
- Peter, D., N. Y. Yao, N. Lang, S. D. Huber, M. D. Lukin, and H. P. Büchler, 2015, *Phys. Rev. A* **91**, 053617.
- Petter, D., G. Natale, R. M. W. van Bijnen, A. Patscheider, M. J. Mark, L. Chomaz, and F. Ferlino, 2019, *Phys. Rev. Lett.* **122**, 183401.
- Petter, D., *et al.*, 2020, [arXiv:2005.02213](https://arxiv.org/abs/2005.02213).
- Pezzè, L., and A. Smerzi, 2009, *Phys. Rev. Lett.* **102**, 100401.
- Piacente, G., I. V. Schweigert, J. J. Betouras, and F. M. Peeters, 2004, *Phys. Rev. B* **69**, 045324.
- Piazza, F., and P. Strack, 2014, *Phys. Rev. A* **90**, 043823.
- Piazza, F., P. Strack, and W. Zwerger, 2013, *Ann. Phys. (Amsterdam)* **339**, 135.
- Picco, M., 2012, [arXiv:1207.1018](https://arxiv.org/abs/1207.1018).
- Piñeiro Orioli, A., A. Signoles, H. Wildhagen, G. Günter, J. Berges, S. Whitlock, and M. Weidemüller, 2018, *Phys. Rev. Lett.* **120**, 063601.
- Pino, J. M., *et al.*, 2021, *Nature (London)* **592**, 209.
- Pino, M., 2014, *Phys. Rev. B* **90**, 174204.
- Pistorius, T., J. Kazemi, and H. Weimer, 2020, *Phys. Rev. Lett.* **125**, 263604.
- Pizzi, A., J. Knolle, and A. Nunnenkamp, 2021, *Nat. Commun.* **12**, 2341.
- Poderoso, F. C., J. J. Arenzon, and Y. Levin, 2011, *Phys. Rev. Lett.* **106**, 067202.
- Podolsky, D., 2016, *Phys. Rev. X* **6**, 031025.
- Poiblanc, D., S. Yunoki, S. Maekawa, and E. Dagotto, 1997, *Phys. Rev. B* **56**, R1645.
- Poland, D., S. Rychkov, and A. Vichi, 2019, *Rev. Mod. Phys.* **91**, 015002.
- Polchinski, J., 1984, *Nucl. Phys.* **B231**, 269.
- Polkovnikov, A., 2005, *Phys. Rev. B* **72**, 161201.
- Pomeau, Y., and S. Rica, 1994, *Phys. Rev. Lett.* **72**, 2426.
- Porras, D., and J. I. Cirac, 2004, *Phys. Rev. Lett.* **92**, 207901.
- Portmann, O., A. Gölzer, N. Saratz, O. V. Billoni, D. Pescia, and A. Vindigni, 2010, *Phys. Rev. B* **82**, 184409.
- Pozrikidis, C., 2016, *The Fractional Laplacian* (Taylor & Francis, London).
- Pruttivarasin, T., M. Ramm, I. Talukdar, A. Kreuter, and H. Häffner, 2011, *New J. Phys.* **13**, 075012.
- Pupillo, G., A. Griessner, A. Micheli, M. Ortner, D.-W. Wang, and P. Zoller, 2008, *Phys. Rev. Lett.* **100**, 050402.
- Pupillo, G., A. Micheli, M. Boninsegni, I. Lesanovsky, and P. Zoller, 2010, *Phys. Rev. Lett.* **104**, 223002.
- Pupillo, G., P. Zihler, and F. Cinti, 2020, *Phys. Rev. B* **101**, 134522.
- Pyka, K., *et al.*, 2013, *Nat. Commun.* **4**, 2291.
- Rademaker, L., and D. A. Abanin, 2020, *Phys. Rev. Lett.* **125**, 260405.
- Rajabpour, M. A., and S. Sotiriadis, 2015, *Phys. Rev. B* **91**, 045131.
- Raju, A., C. B. Clement, L. X. Hayden, J. P. Kent-Dobias, D. B. Liarte, D. Z. Rocklin, and J. P. Sethna, 2019, *Phys. Rev. X* **9**, 021014.
- Randall, J., C. E. Bradley, F. V. van der Gronden, A. Galicia, M. H. Abobeih, M. Markham, D. J. Twitchen, F. Machado, N. Y. Yao, and T. H. Taminiau, 2021, *Science* **374**, 1474.
- Ravets, S., H. Labuhn, D. Barredo, L. Béguin, T. Lahaye, and A. Browaeys, 2014, *Nat. Phys.* **10**, 914.
- Reimann, P., 2008, *Phys. Rev. Lett.* **101**, 190403.
- Ribeiro, P., J. Vidal, and R. Mosseri, 2007, *Phys. Rev. Lett.* **99**, 050402.
- Richerme, P., Z.-X. Gong, A. Lee, C. Senko, J. Smith, M. Foss-Feig, S. Michalakis, A. V. Gorshkov, and C. Monroe, 2014, *Nature (London)* **511**, 198.
- Ritsch, H., P. Domokos, F. Brennecke, and T. Esslinger, 2013, *Rev. Mod. Phys.* **85**, 553.
- Rocuzzo, S. M., A. Gallemí, A. Recati, and S. Stringari, 2020, *Phys. Rev. Lett.* **124**, 045702.
- Roos, C. F., D. Leibfried, A. Mundt, F. Schmidt-Kaler, J. Eschner, and R. Blatt, 2000, *Phys. Rev. Lett.* **85**, 5547.

- Rossotti, S., M. Teruzzi, D. Pini, D. E. Galli, and G. Bertaina, 2017, *Phys. Rev. Lett.* **119**, 215301.
- Roy, S., and D. E. Logan, 2019, *SciPost Phys.* **7**, 42.
- Rückriegel, A., A. Kreisel, and P. Kopietz, 2012, *Phys. Rev. B* **85**, 054422.
- Ruffo, S., 1994, in *Transport, Chaos And Plasma Physics*, edited by S. Benkadda, F. Doveil, and Y. Elskens (World Scientific, Singapore).
- Saccani, S., S. Moroni, and M. Boninsegni, 2012, *Phys. Rev. Lett.* **108**, 175301.
- Sachdev, S., 1999, *Quantum Phase Transitions* (Cambridge University Press, Cambridge, England).
- Safavi-Naini, A., R. J. Lewis-Swan, J. G. Bohnet, M. Gärtner, K. A. Gilmore, J. E. Jordan, J. Cohn, J. K. Freericks, A. M. Rey, and J. J. Bollinger, 2018, *Phys. Rev. Lett.* **121**, 040503.
- Safavi-Naini, A., M. L. Wall, O. L. Acevedo, A. M. Rey, and R. M. Nandkishore, 2019, *Phys. Rev. A* **99**, 033610.
- Saffman, M., T. G. Walker, and K. Mølmer, 2010, *Rev. Mod. Phys.* **82**, 2313.
- Saito, H., Y. Kawaguchi, and M. Ueda, 2007, *Phys. Rev. A* **76**, 043613.
- Sak, J., 1973, *Phys. Rev. B* **8**, 281.
- Samajdar, R., W. W. Ho, H. Pichler, M. D. Lukin, and S. Sachdev, 2021, *Proc. Natl. Acad. Sci. U.S.A.* **118**, e2015785118.
- Santos, L., G. V. Shlyapnikov, and M. Lewenstein, 2003, *Phys. Rev. Lett.* **90**, 250403.
- Santos, L. F., F. Borgonovi, and G. L. Celardo, 2016, *Phys. Rev. Lett.* **116**, 250402.
- Saratz, N., A. Lichtenberger, O. Portmann, U. Ramsperger, A. Vindigni, and D. Pescia, 2010, *Phys. Rev. Lett.* **104**, 077203.
- Sbierski, B., M. Bintz, S. Chatterjee, M. Schuler, N. Y. Yao, and L. Pollet, 2023, [arXiv:2305.03673](https://arxiv.org/abs/2305.03673).
- Scardicchio, A., and T. Thiery, 2017, [arXiv:1710.01234](https://arxiv.org/abs/1710.01234).
- Schachenmayer, J., B. P. Lanyon, C. F. Roos, and A. J. Daley, 2013, *Phys. Rev. X* **3**, 031015.
- Schachenmayer, J., A. Pikovski, and A. M. Rey, 2015a, *New J. Phys.* **17**, 065009.
- Schachenmayer, J., A. Pikovski, and A. M. Rey, 2015b, *Phys. Rev. X* **5**, 011022.
- Schaller, G., 2008, *Phys. Rev. A* **78**, 032328.
- Schauss, P., 2018, *Quantum Sci. Technol.* **3**, 023001.
- Schauß, P., M. Cheneau, M. Endres, T. Fukuhara, S. Hild, A. Omran, T. Pohl, C. Gross, S. Kuhr, and I. Bloch, 2012, *Nature (London)* **491**, 87.
- Schauß, P., J. Zeiher, T. Fukuhara, S. Hild, M. Cheneau, T. Macrì, T. Pohl, I. Bloch, and C. Gross, 2015, *Science* **347**, 1455.
- Schempp, H., G. Günter, S. Wüster, M. Weidemüller, and S. Whitlock, 2015, *Phys. Rev. Lett.* **115**, 093002.
- Schiffer, J. P., 1993, *Phys. Rev. Lett.* **70**, 818.
- Schneider, C., D. Porras, and T. Schaetz, 2012, *Rep. Prog. Phys.* **75**, 024401.
- Schnyder, A. P., S. Ryu, A. Furusaki, and A. W. W. Ludwig, 2008, *Phys. Rev. B* **78**, 195125.
- Scholl, P., *et al.*, 2020, [arXiv:2012.12268](https://arxiv.org/abs/2012.12268).
- Scholl, P., *et al.*, 2021, [arXiv:2107.14459](https://arxiv.org/abs/2107.14459).
- Schulz, H. J., 1993, *Phys. Rev. Lett.* **71**, 1864.
- Schulz, M., C. A. Hooley, R. Moessner, and F. Pollmann, 2019, *Phys. Rev. Lett.* **122**, 040606.
- Schuster, S. C., P. Wolf, S. Ostermann, S. Slama, and C. Zimmermann, 2020, *Phys. Rev. Lett.* **124**, 143602.
- Schütz, S., and G. Morigi, 2014, *Phys. Rev. Lett.* **113**, 203002.
- Schymik, K.-N., S. Pancaldi, F. Nogrette, D. Barredo, J. Paris, A. Browaeys, and T. Lahaye, 2021, [arXiv:2106.07414](https://arxiv.org/abs/2106.07414).
- Sciolla, B., and G. Biroli, 2010, *Phys. Rev. Lett.* **105**, 220401.
- Seetharam, K., A. Lerose, R. Fazio, and J. Marino, 2021, [arXiv:2101.06445](https://arxiv.org/abs/2101.06445).
- Seetharam, K., A. Lerose, R. Fazio, and J. Marino, 2022, *Phys. Rev. B* **105**, 184305.
- Sekino, Y., and L. Susskind, 2008, *J. High Energy Phys.* **08**, 065.
- Selke, W., 1988, *Phys. Rep.* **170**, 213.
- Semeghini, G., *et al.*, 2021, *Science* **374**, 1242.
- Seul, M., and D. Andelman, 1995, *Science* **267**, 476.
- Shankar, R., 1994, *Rev. Mod. Phys.* **66**, 129.
- Shenoy, S. R., and B. Chattopadhyay, 1995, *Phys. Rev. B* **51**, 9129.
- Shimshoni, E., G. Morigi, and S. Fishman, 2011, *Phys. Rev. A* **83**, 032308.
- Shiwa, Y., 2006, *J. Stat. Phys.* **124**, 1207.
- Short, A. J., 2011, *New J. Phys.* **13**, 053009.
- Sieberer, L. M., S. D. Huber, E. Altman, and S. Diehl, 2013, *Phys. Rev. Lett.* **110**, 195301.
- Siegman, A. E., 1986, *Lasers* (University Science Books, Melville, NY).
- Sierant, P., K. Biedroń, G. Morigi, and J. Zakrzewski, 2019, *SciPost Phys.* **7**, 8.
- Simon, B., M. Taylor, and T. Wolff, 1985, *Phys. Rev. Lett.* **54**, 1589.
- Smith, J., A. Lee, P. Richerme, B. Neyenhuis, P. Hess, P. Hauke, M. Heyl, D. Huse, and C. Monroe, 2016, *Nat. Phys.* **12**, 907.
- Sohmen, M., C. Politi, L. Klaus, L. Chomaz, M. J. Mark, M. A. Norcia, and F. Ferlaino, 2021, *Phys. Rev. Lett.* **126**, 233401.
- Solfanelli, A., S. Ruffo, S. Succi, and N. Defenu, 2023, *J. High Energy Phys.* **05**, 066.
- Sondhi, S. L., S. M. Girvin, J. P. Carini, and D. Shahar, 1997, *Rev. Mod. Phys.* **69**, 315.
- Sørensen, A., and K. Mølmer, 1999, *Phys. Rev. Lett.* **82**, 1971.
- Sørensen, A. S., and K. Mølmer, 2001, *Phys. Rev. Lett.* **86**, 4431.
- Sperstad, I. B., E. B. Stiansen, and A. Sudbø, 2012, *Phys. Rev. B* **85**, 214302.
- Srinivas, R., *et al.*, 2021, *Nature (London)* **597**, 209.
- Stanley, H. E., 1968, *Phys. Rev.* **176**, 718.
- Storch, D.-M., M. van den Worm, and M. Kastner, 2015, *New J. Phys.* **17**, 063021.
- Su, W. P., J. R. Schrieffer, and A. J. Heeger, 1979, *Phys. Rev. Lett.* **42**, 1698.
- Surace, F. M., and A. Lerose, 2021, [arXiv:2011.10583](https://arxiv.org/abs/2011.10583).
- Suzuki, M., 1973, *Prog. Theor. Phys.* **49**, 1106.
- Sweke, R., J. Eisert, and M. Kastner, 2019, *J. Phys. A* **52**, 424003.
- Swift, J., and P. C. Hohenberg, 1977, *Phys. Rev. A* **15**, 319.
- Syed, M., T. Enss, and N. Defenu, 2021, *Phys. Rev. B* **103**, 064306.
- Tan, W. L., *et al.*, 2021, *Nat. Phys.* **17**, 742.
- Tanzi, L., E. Lucioni, F. Famà, J. Catani, A. Fioretti, C. Gabbanini, R. N. Bisset, L. Santos, and G. Modugno, 2019, *Phys. Rev. Lett.* **122**, 130405.
- Tanzi, L., J. G. Maloberti, G. Biagioni, A. Fioretti, C. Gabbanini, and G. Modugno, 2021, *Science* **371**, 1162.
- Tanzi, L., S. M. Rocuzzo, E. Lucioni, F. Famà, A. Fioretti, C. Gabbanini, G. Modugno, A. Recati, and S. Stringari, 2019, *Nature (London)* **574**, 382.
- Thirring, W., 1970, *Z. Phys.* **235**, 339.
- Thouless, D. J., 1969, *Phys. Rev.* **187**, 732.
- Thouless, D. J., 1972, *J. Non-Cryst. Solids* **8–10**, 461.
- Titum, P., J. T. Iosue, J. R. Garrison, A. V. Gorshkov, and Z.-X. Gong, 2019, *Phys. Rev. Lett.* **123**, 115701.
- Titum, P., and M. F. Maghrebi, 2020, *Phys. Rev. Lett.* **125**, 040602.
- Torlai, G., *et al.*, 2019, *Phys. Rev. Lett.* **123**, 230504.
- Tóth, G., C. Knapp, O. Gühne, and H. J. Briegel, 2007, *Phys. Rev. Lett.* **99**, 250405.

- Tran, M. C., C.-F. Chen, A. Ehrenberg, A. Y. Guo, A. Deshpande, Y. Hong, Z.-X. Gong, A. V. Gorshkov, and A. Lucas, 2020, *Phys. Rev. X* **10**, 031009.
- Tran, M. C., A. Ehrenberg, A. Y. Guo, P. Titum, D. A. Abanin, and A. V. Gorshkov, 2019, *Phys. Rev. A* **100**, 052103.
- Tran, M. C., A. Y. Guo, Y. Su, J. R. Garrison, Z. Eldredge, M. Foss-Feig, A. M. Childs, and A. V. Gorshkov, 2019, *Phys. Rev. X* **9**, 031006.
- Tranquada, J. M., J. D. Axe, N. Ichikawa, A. R. Moodenbaugh, Y. Nakamura, and S. Uchida, 1997, *Phys. Rev. Lett.* **78**, 338.
- Trefzger, C., C. Menotti, B. Capogrosso-Sansone, and M. Lewenstein, 2011, *J. Phys. B* **44**, 193001.
- Ueda, M., 2017, in *Universal Themes of Bose-Einstein Condensation*, edited by N. P. Proukakis, D. W. Snoke, and P. B. Littlewood (Cambridge University Press, Cambridge, England), pp. 371–386.
- Uhrich, P., N. Defenu, R. Jafari, and J. C. Halimeh, 2020, *Phys. Rev. B* **101**, 245148.
- Ulm, S., *et al.*, 2013, *Nat. Commun.* **4**, 2290.
- Urban, E., T. A. Johnson, T. Henage, L. Isenhower, D. D. Yavuz, T. G. Walker, and M. Saffman, 2009, *Nat. Phys.* **5**, 110.
- Vaidya, V. D., Y. Guo, R. M. Kroeze, K. E. Ballantine, A. J. Kollár, J. Keeling, and B. L. Lev, 2018, *Phys. Rev. X* **8**, 011002.
- Vajna, S., and B. Dóra, 2014, *Phys. Rev. B* **89**, 161105.
- Vajna, S., and B. Dóra, 2015, *Phys. Rev. B* **91**, 155127.
- Valtolina, G., K. Matsuda, W. G. Tobias, J.-R. Li, L. De Marco, and J. Ye, 2020, *Nature (London)* **588**, 239.
- Vanderstraeten, L., M. Van Damme, H. P. Büchler, and F. Verstraete, 2018, *Phys. Rev. Lett.* **121**, 090603.
- van Enter, A. C. D., 1982, *Phys. Rev. B* **26**, 1336.
- van Nieuwenburg, E., Y. Baum, and G. Refael, 2019, *Proc. Natl. Acad. Sci. U.S.A.* **116**, 9269.
- Van Regemortel, M., D. Sels, and M. Wouters, 2016, *Phys. Rev. A* **93**, 032311.
- Vasiliev, A. Y., A. E. Tarkhov, L. I. Menshikov, P. O. Fedichev, and U. R. Fischer, 2014, *New J. Phys.* **16**, 053011.
- Vaterlaus, A., C. Stamm, U. Maier, M. G. Pini, P. Politi, and D. Pescia, 2000, *Phys. Rev. Lett.* **84**, 2247.
- Verdel, R., F. Liu, S. Whitsitt, A. V. Gorshkov, and M. Heyl, 2020, *Phys. Rev. B* **102**, 014308.
- Verresen, R., M. D. Lukin, and A. Vishwanath, 2021, *Phys. Rev. X* **11**, 031005.
- Vidal, G., 2003, *Phys. Rev. Lett.* **91**, 147902.
- Vidal, J., R. Mosseri, and J. Dukelsky, 2004, *Phys. Rev. A* **69**, 054101.
- Vilas, N. B., C. Hallas, L. Anderegg, P. Robichaud, A. Winnicki, D. Mitra, and J. M. Doyle, 2022, *Nature (London)* **606**, 70.
- Viyuela, O., D. Vodola, G. Pupillo, and M. A. Martin-Delgado, 2016, *Phys. Rev. B* **94**, 125121.
- Vodola, D., L. Lepori, E. Ercolessi, A. V. Gorshkov, and G. Pupillo, 2014, *Phys. Rev. Lett.* **113**, 156402.
- Vodola, D., L. Lepori, E. Ercolessi, and G. Pupillo, 2016, *New J. Phys.* **18**, 015001.
- Vojta, T., 1996, *Phys. Rev. B* **53**, 710.
- von Keyserlingk, C. W., V. Khemani, and S. L. Sondhi, 2016, *Phys. Rev. B* **94**, 085112.
- Wang, D. W., A. J. Millis, and S. Das Sarma, 2001, *Phys. Rev. B* **64**, 193307.
- Wang, W., R. Díaz-Méndez, M. Wallin, J. Lidmar, and E. Babaev, 2020, *arXiv:2011.01664*.
- Wang, Y., S. Shevate, T. M. Wintermantel, M. Morgado, G. Lochead, and S. Whitlock, 2020, *npj Quantum Inf.* **6**, 54.
- Wang, Y. K., and F. T. Hioe, 1973, *Phys. Rev. A* **7**, 831.
- Watanabe, H., and H. Murayama, 2012, *Phys. Rev. Lett.* **108**, 251602.
- Watanabe, H., and H. Murayama, 2013, *Phys. Rev. Lett.* **110**, 181601.
- Weber, S., S. de Léséleuc, V. Lienhard, D. Barredo, T. Lahaye, A. Browaeys, and H. P. Büchler, 2018, *Quantum Sci. Technol.* **3**, 044001.
- Weber, S., C. Tresp, H. Menke, A. Urvoy, O. Firstenberg, H. P. Büchler, and S. Hofferberth, 2017, *J. Phys. B* **50**, 133001.
- Weeks, J. D., 1981, *Phys. Rev. B* **24**, 1530.
- Wegner, F. J., and A. Houghton, 1973, *Phys. Rev. A* **8**, 401.
- Weidinger, S. A., M. Heyl, A. Silva, and M. Knap, 2017, *Phys. Rev. B* **96**, 134313.
- Weimer, H., M. Müller, H. P. Büchler, and I. Lesanovsky, 2011, *Quantum Inf. Process.* **10**, 885.
- Weimer, H., M. Müller, I. Lesanovsky, P. Zoller, and H. P. Büchler, 2010, *Nat. Phys.* **6**, 382.
- Wetterich, C., 1993, *Phys. Lett. B* **301**, 90.
- Wichterich, H., J. Vidal, and S. Bose, 2010, *Phys. Rev. A* **81**, 032311.
- Wilk, T., A. Gaëtan, C. Evellin, J. Wolters, Y. Miroshnychenko, P. Grangier, and A. Browaeys, 2010, *Phys. Rev. Lett.* **104**, 010502.
- Wilson, K. G., and J. Kogut, 1974, *Phys. Rep.* **12**, 75.
- Wintermantel, T. M., Y. Wang, G. Lochead, S. Shevate, G. K. Brennen, and S. Whitlock, 2020, *Phys. Rev. Lett.* **124**, 070503.
- Wright, K., *et al.*, 2019, *Nat. Commun.* **10**, 5464.
- Wu, X., X. Liang, Y. Tian, F. Yang, C. Chen, Y.-C. Liu, M. K. Tey, and L. You, 2021, *Chin. Phys. B* **30**, 020305.
- Wu, Y.-L., and S. Das Sarma, 2016, *Phys. Rev. A* **93**, 022332.
- Xu, S., 2022, *Physics* **15**, 2.
- Xue, M., S. Yin, and L. You, 2018, *Phys. Rev. A* **98**, 013619.
- Yamazaki, Y., 1977, *Phys. Lett.* **61A**, 207.
- Yan, B., S. A. Moses, B. Gadway, J. P. Covey, K. R. A. Hazzard, A. M. Rey, D. S. Jin, and J. Ye, 2013, *Nature (London)* **501**, 521.
- Yang, H., J. Cao, Z. Su, J. Rui, B. Zhao, and J.-W. Pan, 2022, *Science* **378**, 1009.
- Yang, K., *et al.*, 2019, *Phys. Rev. B* **100**, 085308.
- Yao, N. Y., C. R. Laumann, S. Gopalakrishnan, M. Knap, M. Müller, E. A. Demler, and M. D. Lukin, 2014, *Phys. Rev. Lett.* **113**, 243002.
- Yao, N. Y., and C. Nayak, 2018, *Phys. Today* **71**, No. 9, 40.
- Yong, J., T. R. Lemberger, L. Benfatto, K. Ilin, and M. Siegel, 2013, *Phys. Rev. B* **87**, 184505.
- Zeiher, J., J.-y. Choi, A. Rubio-Abadal, T. Pohl, R. van Bijnen, I. Bloch, and C. Gross, 2017, *Phys. Rev. X* **7**, 041063.
- Zeiher, J., P. Schauß, S. Hild, T. Macrì, I. Bloch, and C. Gross, 2015, *Phys. Rev. X* **5**, 031015.
- Zeiher, J., R. van Bijnen, P. Schauß, S. Hild, J.-y. Choi, T. Pohl, I. Bloch, and C. Gross, 2016, *Nat. Phys.* **12**, 1095.
- Zener, C., 1932, *Proc. R. Soc. A* **137**, 696.
- Zhang, J., G. Pagano, P. W. Hess, A. Kyprianidis, P. Becker, H. Kaplan, A. V. Gorshkov, Z.-X. Gong, and C. Monroe, 2017, *Nature (London)* **551**, 601.
- Zhang, J., *et al.*, 2017, *Nature (London)* **543**, 217.
- Zhu, S.-L., C. Monroe, and L.-M. Duan, 2006, *Phys. Rev. Lett.* **97**, 050505.
- Žunković, B., M. Heyl, M. Knap, and A. Silva, 2018, *Phys. Rev. Lett.* **120**, 130601.
- Žunković, B., A. Silva, and M. Fabrizio, 2016, *Phil. Trans. R. Soc. A* **374**, 20150160.
- Zurek, W. H., 1985, *Nature (London)* **317**, 505.
- Zurek, W. H., 1996, *Phys. Rep.* **276**, 177.
- Zurek, W. H., 2009, *Phys. Rev. Lett.* **102**, 105702.
- Zurek, W. H., and U. Dorner, 2008, *Phil. Trans. R. Soc. A* **366**, 2953.
- Zurek, W. H., U. Dorner, and P. Zoller, 2005, *Phys. Rev. Lett.* **95**, 105701.
- Zvyagin, A. A., 2016, *Low Temp. Phys.* **42**, 971.
- Zwergler, W., 2008, *Nat. Phys.* **4**, 444.